

AN ABSTRACT OF THE DISSERTATION OF

Abbas Abdollahi for the degree of Doctor of Philosophy in Civil Engineering
presented on March 21, 2017.

Title: Pore Water Pressure Response in Soil During Tsunami Loading:
Numerical Formulation and Experimentation

Abstract approved: _____

H. Benjamin Mason

Tsunami loading can cause sediment instability, which can compromise the structural integrity of coastal buildings and infrastructure. To understand the process by which a tsunami can cause sediment instability, it is necessary to understand how the pore water pressure in the soil changes during tsunami loading. Tsunami run-up causes the pore water pressure in the soil bed to increase, then during tsunami draw-down, the pore water pressure in the soil bed decreases. This rise and fall leads to a gradient of excess pore water pressure, which results in upward seepage during tsunami draw-down. If the excess pore water pressure gradient becomes large enough, significant sediment instability may occur. Although simple models have been developed to estimate the pore water pressure in hypothetical soil beds during tsunami loading, current models are generally based on the solution to the diffusion equation. As a result, they cannot incorporate the changes

in pore water pressure caused by both the weight of the overlying tsunami water and the seepage of infiltrating tsunami water. In addition, current models do not incorporate other physical phenomena, such as those that can be addressed by variation of the diffusion coefficient with depth, aired water (i.e., entrained air), zones of unsaturated soil, and varying impermeable layer depths.

Based on the changes in pore water pressure due to overlying water and seepage of infiltrating water during a tsunami, a deformation model was developed and coupled with a seepage model. The proposed seepage-deformation model is able to model the broad range of drainage conditions of a soil bed, from the fully undrained condition to the fully drained condition. A new formulation for the coefficient of consolidation as a function of Skempton's B value is also suggested. The coupled seepage-deformation model is formulated and implemented in MATLAB using the finite difference method for one-dimensional loading.

The coupled seepage-deformation model is used to perform numerical experimentation after a convergence study is performed. The convergence study is performed using two representative numerical experiments to select an appropriate grid size and time step. The numerical experimentation focuses on saturated and unsaturated soil conditions, linear and nonlinear soil constitutive models, different Skempton's B values, and de-aired and aired water for a constant depth to the impermeable layer of 10 m and using one hypothetical tsunami with a total duration of approximately 32 minutes and a maximum flow height of 5.5 m. The results of the numerical experimentation show that the excess pore water pressure head gradient induced by tsunami loading in the soil bed when de-aired water is the

pore fluid is negligible and is much less compared with the tsunami-induced excess pore water pressure head gradient developed in the soil bed when aird water is the pore fluid. The results also show that the excess pore water pressure head gradient induced in a soil bed governed by a more realistic nonlinear soil constitutive model is larger when compared to corresponding excess pore water pressure head gradient estimates in soil beds governed by a linear model. The results also show that as Skempton's B value increases from zero to one, the maximum excess pore water pressure head gradient at the ground surface reduces linearly. In addition, studying the effect of depth to impermeable layer, the tsunami height, and the entire tsunami duration (i.e., run-up and draw-down) shows that the maximum excess pore water pressure head gradient at ground surface increases linearly with an increase of tsunami height, and reduces non-linearly with an increase of tsunami duration. The results show that excess pore water pressure head gradient generally increases with an increase of the impermeable layer depth, but only up to a certain depth. The effect of depth to impermeable layer is the same when multiple tsunami heights are investigated; however, the effect deviates when tsunamis with different durations are used. Results also show that the increase of hydraulic conductivity reduces the excess pore water pressure head gradient, as expected, and the maximum excess pore water pressure head gradient at the ground surface generally reduces with an increase of the soil bulks modulus for large bulk modulus. Furthermore, the results show that an increase of gas content also increases the excess pore water pressure head gradient.

At the end of the dissertation, the potential for tsunami-induced soil liquefac-

tion based on two definitions of soil liquefaction is investigated using the coupled seepage-deformation model. More specifically, the effective stress definition of soil liquefaction, which is often used to describe earthquake-induced soil liquefaction, and the excess pore-water pressure gradient definition of soil liquefaction, which is more general and can explain tsunami-induced liquefaction, are investigated. Finally, the coupled seepage-deformation model is extended to two-dimensions. The results of the two-dimensional numerical experiments show that their one-dimensional counterparts likely underestimate the excess pore water pressure head gradient induced by tsunami loading. However, future work is needed to improve the two-dimensional implementation.

©Copyright by Abbas Abdollahi
March 21, 2017
All Rights Reserved

Pore Water Pressure Response in Soil During Tsunami Loading:
Numerical Formulation and Experimentation

by

Abbas Abdollahi

A DISSERTATION

submitted to

Oregon State University

in partial fulfillment of
the requirements for the
degree of

Doctor of Philosophy

Presented March 21, 2017
Commencement June 2017

Doctor of Philosophy dissertation of Abbas Abdollahi presented on
March 21, 2017.

APPROVED:

Major Professor, representing Civil Engineering

Head of the School of Civil and Construction Engineering

Dean of the Graduate School

I understand that my dissertation will become part of the permanent collection of Oregon State University libraries. My signature below authorizes release of my dissertation to any reader upon request.

Abbas Abdollahi, Author

ACKNOWLEDGEMENTS

This research would not have been possible without the help, support, and experience of numerous individuals. First, I offer my sincere gratitude to my adviser, Dr. Ben Mason, for providing me the opportunity to work on this research. I am indebted to him for all his support, guidance, and patience.

I was so fortunate to work with Dr. Harry Yeh as my unofficial co-adviser throughout the period of my PhD. My sincere thanks to him for all of his guidance, questions, criticisms, and support.

It is my wish to thank Dr. Malgorzata Peszynska for teaching me and helping me to finish my PhD. I was not able to explore this topic in depth without her teachings and comments.

My sincere thanks to Dr. Matthew Evans for agreeing to serve on my graduate committee and for all his support, guidance, and comments.

I would like to acknowledge Dr. Solomon Yim for agreeing to serve on my graduate committee. I learned a lot and got many ideas from his class. I am really thankful to Dr. Eric Kirby for serving on my graduate committee as my graduate council representative. I wish to acknowledge Dr. Armin Stuedlein for comments, suggestions, and relevant references for my side project. My gratitude to all of the faculty, staff, and friends at OSU's School of Civil and Construction Engineering.

I would like to express my sincere thanks to my colleague and friend Rachel Adams for her assistance in the laboratory.

Finally, last but for sure not least, I would like to thank my family deeply for

their love, support, and patience through my PhD. Without the endless support of my parents, Mohammad Kazem and Yasamin, from overseas the successful completion of this thesis would not have been possible. I would like to express my love to my brother, Amir, who always encouraged me through my education at OSU.

The work was supported by the Oregon State University College of Engineering and the Cascadia Lifeline Project (CLiP). The financial support is gratefully acknowledged.

TABLE OF CONTENTS

| | <u>Page</u> |
|---|-------------|
| 1 Introduction | 1 |
| 1.1 Definition of soil liquefaction | 2 |
| 1.2 Contributions | 6 |
| 1.3 Organization and convention | 8 |
| 2 Background | 20 |
| 2.1 Tsunami waves | 20 |
| 2.2 Soil mechanics concepts | 22 |
| 2.2.1 Effective stress | 23 |
| 2.2.2 Pore water pressure parameters | 29 |
| 2.2.3 The Mandel-Cryer effect | 31 |
| 2.3 Soil instability | 32 |
| 2.3.1 Wave-induced residual liquefaction | 33 |
| 2.3.2 Wave-induced momentary liquefaction | 36 |
| 2.3.3 Rapid draw-down in embankment dams | 47 |
| 2.4 Literature synthesis | 52 |
| 3 Proposed deformation model | 58 |
| 3.1 Description | 59 |
| 3.2 Discussion | 64 |
| 3.2.1 Defining model parameters | 64 |
| 3.2.2 Model assumptions and limitations | 67 |
| 3.2.3 Model performance | 70 |
| 4 Numerical modeling framework | 72 |
| 4.1 Seepage model | 72 |
| 4.1.1 Description | 73 |
| 4.1.2 Discussion | 74 |
| 4.2 Coupled seepage-deformation model | 84 |
| 4.2.1 Description | 84 |
| 4.2.2 Assumptions and limitations | 87 |
| 4.3 Numerical formulation | 89 |

TABLE OF CONTENTS (Continued)

| | <u>Page</u> |
|---|-------------|
| 5 Numerical experimentation | 97 |
| 5.1 Hypothetical tsunami waveforms | 98 |
| 5.2 Numerical experimentation plan | 103 |
| 5.3 Numerical convergence | 109 |
| 5.4 Numerical experimentation results | 120 |
| 5.4.1 Fully saturated soil model | 120 |
| 5.4.2 Unsaturated soil model | 135 |
| 6 Analysis and discussion | 139 |
| 6.1 Depth to the impermeable layer | 140 |
| 6.2 Tsunami properties | 145 |
| 6.2.1 Tsunami height | 147 |
| 6.2.2 Tsunami duration | 152 |
| 6.3 Hydraulic conductivity | 165 |
| 6.4 Soil bulk modulus | 169 |
| 6.5 Effects of entrained air bubbles | 173 |
| 6.6 Initiation of liquefaction | 180 |
| 6.7 Extension to two-dimensions | 187 |
| 6.7.1 Two-dimensional formulation | 187 |
| 6.7.2 Numerical convergence and preliminary results | 190 |
| 7 Summary and conclusions | 210 |
| 7.1 Summary | 211 |
| 7.2 Recommendations for future work | 219 |
| Bibliography | 223 |
| Appendices | 236 |
| A Pore water pressure and pore water pressure head gradient for cases in Table 5.2 | 237 |

LIST OF FIGURES

| Figure | Page |
|--|------|
| 2.1 Schematic showing the concept of effective stress using two sand grains. Modified from Figure 5-1 in Scott (1963, pg. 164). | 26 |
| 2.2 Time series of period-averaged excess pore-pressure at depth z during progressive wave loading [modified from Figure 3.11 in Sumer (2014, pg. 55)]. | 35 |
| 2.3 Variation of the shear stress and strain in the soil as a function of horizontal distance during standing wave loading [modified from Figure 3 in Kirca et al. (2013, pg. 493)]. | 39 |
| 4.1 The van Genuchten (1980) soil-water characteristic curve developed by Equation 4.2 with $\alpha' = 1.027 \times 10^{-4} \text{ Pa}^{-1}$ and $n' = 3.304$, which are typical model parameters for poorly graded sands (Lu and Likos, 2004), we also assume that $S_r = 0$ | 75 |
| 4.2 The van Genuchten (1980) relative permeability developed by Equation 4.3 with $\alpha' = 1.027 \times 10^{-4} \text{ Pa}^{-1}$ and $n' = 3.304$, which are typical model parameters for poorly graded sands (Lu and Likos, 2004). | 77 |
| 4.3 A schematic of the seepage-deformation model. | 85 |
| 4.4 Algorithm for the fully implicit cell-centered finite difference approach used to solve Equation 4.1. | 90 |
| 4.5 Graphical depiction of the finite difference cell centered spatial domain. | 92 |
| 5.1 The variation of a typical tsunami height with time in the shoreline for (a) non-dimensional and (b) dimensional conditions. The tsunami wave data is from Carrier et al. (2003) model. The slope of the beach, ψ , is assumed 1/100 and the length scale, L , is 40 km. | 102 |

LIST OF FIGURES (Continued)

| <u>Figure</u> | <u>Page</u> |
|---------------|---|
| 5.2 | A schematic of the numerical experimentation algorithm. Two soil bed conditions are considered: saturated and unsaturated, two soil constitutive models are considered: linear and nonlinear, and two pore water conditions are considered: de-aired water and aired water. In addition, analyses where the B value is systematically changed are performed for the fully saturated soil bed condition with the linear soil constitutive model. The arrows in the schematic depict the extent of the performed numerical experimentation. 104 |
| 5.3 | Variation of shear modulus with depth for fully saturated condition. 107 |
| 5.4 | Initial condition at equilibrium hydrostatic condition for the unsaturated soil condition when the ground water table is at 3 m below the ground surface: a) pore water pressure distribution with depth, and b) degree of saturation distribution with depth. 111 |
| 5.5 | Convergence studies for case I for a) 10 minutes , b) 20 minutes, c) 28 minutes, d) 29 minutes. 113 |
| 5.6 | Convergence studies for case I, for the depth between 0 to 3 m for a) 10 minutes, b) 20 minutes, c) 28 minutes , d) 29 minutes. . . . 114 |
| 5.7 | Convergence studies for case I for pressure head gradient with depth for a) 10 minutes, b) 20 minutes, c) 28 minutes, d) 29 minutes. . . . 116 |
| 5.8 | Convergence studies for case I for pressure head gradient with depth, for the depth between 0 to 3 m for a) 10 minutes, b) 20 minutes, c) 28 minutes, d) 29 minutes. 117 |
| 5.9 | Convergence studies for case II for a) 10 minutes, b) 20 minutes, c) 25 minutes, d) 30 minutes. 118 |
| 5.10 | Convergence studies for case II for pressure head gradient with depth for a) 10 minutes, b) 20 minutes, c) 25 minutes, d) 30 minutes. . . . 119 |
| 5.11 | Convergence studies for pressure head gradient with time for different grid size, a) case I when ground water table is 3 m below the ground surface, and b) case II when the ground water table is at ground surface. 121 |

LIST OF FIGURES (Continued)

| <u>Figure</u> | <u>Page</u> |
|--|-------------|
| 5.12 Case S-LE-UW: a) total pore water pressure at different times with depth for the fully saturated soil condition, assuming aired water, and considering the linear soil constitutive model; b) excess pore water pressure head gradient at different times with depth for the fully saturated soil condition, assuming aired water, and considering the linear soil constitutive model. | 122 |
| 5.13 Case S-LE-UW: the excess pore water pressure head gradient at different depths with time for the fully saturated soil condition, assuming aired water, and considering the linear soil constitutive model. | 122 |
| 5.14 Maximum excess pore water pressure head gradient at the ground surface for the fully saturated soil condition for different cases using the linear soil constitutive model and assuming that the impermeable layer depth is at 10 m below ground surface. The values are normalized with the maximum value, which occurs for Case S-LE-B(0) and is equal to 0.1628. | 125 |
| 5.15 The variation of excess pore water pressure head gradient at different times with depth. Comparison of the results from the Yeh and Mason (2014) solution with numerical results from the proposed seepage deformation model shows good agreement. Note that, linear constitutive soil model is used. In addition, for the seepage deformation model, we assume $\alpha = 1$ and $B = 0$, and $\nu_u = 0.5$ | 128 |
| 5.16 Case S-NI-UW: a) pore water pressure changes with depth at different times for the fully saturated soil condition considering the nonlinear soil constitutive model and with aired water as the pore fluid; b) excess pore water pressure head gradient changes with depth at different times for the fully saturated soil conditions considering the nonlinear soil constitutive model and with aired water as the pore fluid. | 129 |
| 5.17 Case S-NI-UW: excess pore water pressure head gradient changes with time at different depths for fully saturated soil conditions considering the nonlinear soil constitutive model and with aired water as the pore fluid. | 131 |

LIST OF FIGURES (Continued)

| <u>Figure</u> | <u>Page</u> |
|--|-------------|
| 5.18 Maximum excess pore water pressure head gradient at the ground surface for the fully saturated soil condition for different cases, considering the nonlinear soil constitutive model, and the impermeable layer depth is at 10 m below the ground surface. The values are normalized with the maximum value, which occurs for Case S-NI-B(0) and is equal to 0.2125. | 132 |
| 5.19 Comparison of the maximum excess pore water pressure head gradient at the ground surface from the linear soil constitutive model and the nonlinear soil constitutive model. The values are normalized with the maximum value, which occurs for Case S-NI-UW and is equal to 0.1864. | 133 |
| 5.20 The linear variation of the maximum excess pore water pressure head gradient at the ground surface with B value for the fully saturated soil condition using linear and nonlinear soil constitutive models. The impermeable layer depth is at 10 m below ground surface. | 134 |
| 5.21 Case UN-NI-UW(3m): a) pore water pressure changes with depth at different times for unsaturated soil conditions when the groundwater table is at 3 m, considering the nonlinear soil constitutive model and aird water as the pore fluid; b) pressure head gradient changes with depth at different times for unsaturated soil conditions when the groundwater table is at 3 m, considering the nonlinear soil constitutive model and aird water as the pore fluid. | 136 |
| 5.22 Case UN-NI-UW(3m): excess pore water pressure head gradient changes with time at different depths for unsaturated soil conditions when the groundwater table is at 3m, considering the nonlinear soil constitutive model and aird water as the pore fluid. | 137 |
| 5.23 Maximum excess pore water pressure head gradients during the tsunami draw-down for different groundwater table depths. The values are normalized with the maximum value, which occurs for Case UN-NI-UW-(3m) and is equal to 0.2054. | 138 |

LIST OF FIGURES (Continued)

| <u>Figure</u> | <u>Page</u> |
|---|-------------|
| 6.1 Excess pore water pressure head gradient with depth at different times and for different impermeable layer depths, z_i . The analyses are based on the nonlinear soil constitutive model, a) 20 min after the start of tsunami, b) 25 min after the start of tsunami, and c) 30 min after the start of tsunami. | 143 |
| 6.2 Maximum excess pore water pressure head gradient at the ground surface for the fully saturated soil condition using linear and nonlinear soil constitutive models with aired water for different impermeable layer depths. | 144 |
| 6.3 Maximum excess pore water pressure head gradient during tsunami draw-down for different water table depths and for different impermeable layer depths. The values are normalized with the maximum value, which occurs for Case 30-UN-NI-UW(1m) and is equal to 0.3076. Note that the first number refers to the depth of impermeable layer and for the cases that do not start with a number, the depth of the impermeable layer is 10 m. | 146 |
| 6.4 Three hypothetical tsunamis with different maximum flow heights developed using the Carrier et al. (2003) approach at the shoreline. The tsunami duration is constant for all three hypothetical tsunamis and equal to the duration of the hypothetical tsunami shown in Figure 5.1b (i.e., ≈ 32 min). The beach slopes, ψ , of the large, medium, and small height hypothetical tsunamis are 1/70, 1/100 and 1/160, respectively, and the length scales, L , are 57.1, 40, and 25 km for the large, medium, and small height hypothetical tsunamis, respectively. | 148 |
| 6.5 The variation maximum excess pore water pressure head gradient at the ground surface for tsunamis with different heights. | 149 |
| 6.6 The variation maximum excess pore water pressure head gradient at the ground surface with wave amplitude for different impermeable layer depths. | 150 |
| 6.7 The variation of excess pore water pressure head gradient with depth for a 10 m impermeable layer depth and for different wave heights. . | 151 |

LIST OF FIGURES (Continued)

| <u>Figure</u> | <u>Page</u> |
|---|-------------|
| 6.8 The variation of normalized maximum excess pore water pressure head gradient at the ground surface with the impermeable layer depth for waves with different amplitudes but the same duration. | 152 |
| 6.9 Three hypothetical tsunamis with different durations developed using the Carrier et al. (2003) approach at the shoreline. The maximum tsunami flow height is constant for all three hypothetical tsunamis and equal to the maximum flow height of the hypothetical tsunami shown in Figure 5.1b (i.e., ≈ 5.5 m). The beach slopes, ψ , of the long, medium, and short duration hypothetical tsunamis are 1/200, 1/100 and 1/50, respectively, and the length scales, L , are 80, 40, and 20 km for the long, medium, and short duration hypothetical tsunamis, respectively. | 154 |
| 6.10 The variation maximum excess pore water pressure head gradient at the ground surface for waves with different durations. | 155 |
| 6.11 The variation maximum excess pore water pressure head gradient at the ground surface with tsunami duration for different impermeable layer depths. | 156 |
| 6.12 The variation of excess pore water pressure head gradient with depth for different tsunamis with different durations but similar amplitudes at times T_1 and T_2 , where $T_1 = 0.64T_d$, and $T_2 = 0.96T_d$. T_d is the duration of tsunami. Note that T_1 occurs during run-up and T_2 occurs during the draw-down. | 158 |
| 6.13 The variation of normalized maximum excess pore water pressure head gradient at the ground surface with the impermeable layer depth for waves with different durations but the same wave height. | 159 |
| 6.14 The variation of normalized maximum excess pore water pressure head gradient with the impermeable layer depth, z_i , that is normalized with $\sqrt{C_{v0}T_d}$ | 161 |
| 6.15 The variation of excess pore water pressure head gradient at different depths with the rate of tsunami loading for the short duration tsunami and for the condition when the impermeable layer depth is 10 m, a) short duration tsunami, b) long duration tsunami. | 163 |

LIST OF FIGURES (Continued)

| <u>Figure</u> | <u>Page</u> |
|--|-------------|
| 6.16 The variation of the derivative of pressure head gradient with respect to depth at different depths with the rate of tsunami loading for the condition when the impermeable layer depth is 10 m, a) short duration tsunami, b) long duration tsunami. | 166 |
| 6.17 Variation of the maximum excess pore water pressure head gradient with the hydraulic conductivity during tsunami draw-down. Two types of tsunamis are considered: 1) a medium duration, medium flow height tsunami, and 2) a medium duration, large flow height tsunami. The minimum value of the x -axis corresponds to $k_h = 0.005$ cm/s and maximum value of the x -axis corresponds to $k_h = 1$ cm/s. | 168 |
| 6.18 Maximum pressure head gradient at the ground surface for the fully saturated condition using nonlinear constitutive model, and the impermeable layer depth is at 50 m below ground surface. | 171 |
| 6.19 Maximum pressure head gradient at the ground surface for the fully saturated condition using linear constitutive model, and the impermeable layer depth is at 50 m below ground surface. | 172 |
| 6.20 Maximum pressure head gradient at the ground surface for the fully saturated condition using Carslaw and Jaeger (1959) analytical solution. The diffusion coefficient is normalised with the maximum value of the $C_{v,max}^* = 100000$ cm ² /s. | 174 |
| 6.21 Calibration of the diffusion coefficient. The dotted line shows the relation between the diffusion coefficient and G/G_{max} where $G_{max} = 70$ MPa for the linear soil constitutive model, A/A_{max} where $A_{max} = 500$ for the nonlinear soil constitutive model. Note that the minimum value for G/G_{max} is 0.00125. | 175 |
| 6.22 Variation of the gas content with depth, extrapolated from Bonjean et al. (2004) and Michallet et al. (2009). | 177 |
| 6.23 Effects of entrained air bubbles: a) the variation of the pore water pressure with depth at different times for the nonlinear soil constitutive model; b) the variation of the pore water pressure head gradient with depth at different times for nonlinear model. Note that the air content distribution with depth is shown in Figure 6.22. | 178 |

LIST OF FIGURES (Continued)

| <u>Figure</u> | <u>Page</u> |
|---|-------------|
| 6.24 Variation of the excess pore water pressure head gradient with normalized fluid bulk modulus. Maximum bulk modulus is for pure water $K_{w,max} = 2.2 \text{ GPa}$. The solid line shows the maximum excess pore water pressure head gradient at the surface during draw-down and the dashed line shows the maximum absolute value of the excess pore water pressure head gradient during run-up. | 179 |
| 6.25 Six different tsunamis that are used to study the effect of tsunami-induced liquefaction. | 181 |
| 6.26 Case 5 from Table 6.2: variation of excess pore water pressure head gradient with depth at different times. | 182 |
| 6.27 Case 5 from Table 6.2: variation of pore water pressure and total stress with depth at the end of the tsunami. | 184 |
| 6.28 Case 4 from Table 6.2: variation of pore water excess pore water pressure head gradient with depth at different times. | 185 |
| 6.29 Case 4 from Table 6.2: variation of pore water pressure and total stress with depth at 7.3 min after the start of the tsunami. | 186 |
| 6.30 Schematic of rotated coordinate system for two-dimensional numerical experiments: Tsunami run-up on the plane slope. | 191 |
| 6.31 Hypothetical tsunami flow height-time series at the shoreline used for the two-dimensional numerical experiments. | 193 |
| 6.32 Pore water pressure response of the two-dimensional soil bed subjected to the tsunami loading shown in Figure 6.31 at the initial condition. | 194 |
| 6.33 Pore water pressure response of the two-dimensional soil bed subjected to the tsunami loading shown in Figure 6.31 at $t=100 \text{ s}$ | 195 |
| 6.34 Pore water pressure response of the two-dimensional soil bed subjected to the tsunami loading shown in Figure 6.31 at $t=200 \text{ s}$ | 196 |
| 6.35 Pore water pressure response of the two-dimensional soil bed subjected to the tsunami loading shown in Figure 6.31 at $t=300 \text{ s}$ | 197 |

LIST OF FIGURES (Continued)

| <u>Figure</u> | <u>Page</u> |
|--|-------------|
| 6.36 Pore water pressure response of the two-dimensional soil bed subjected to the tsunami loading shown in Figure 6.31 at $t=400$ s. . . . | 198 |
| 6.37 Pore water pressure response of the two-dimensional soil bed subjected to the tsunami loading shown in Figure 6.31 at $t=500$ s. . . . | 199 |
| 6.38 Pore water pressure response of the two-dimensional soil bed subjected to the tsunami loading shown in Figure 6.31 at the end of the tsunami loading. | 200 |
| 6.39 Pore water pressure at a depth of 1.2 m underground as a function of the horizontal distance at different times. | 201 |
| 6.40 Pore water pressure at a depth of 4.2 m underground as a function of horizontal distance at different times. | 202 |
| 6.41 Convergence studies for two dimensional model at shoreline and at $t=600$ s. | 204 |
| 6.42 Convergence studies for two dimensional model at $x=800$ m and at $t=600$ s. | 205 |
| 6.43 Pore water pressure at the shoreline for different times from two-dimensional analysis. | 207 |
| 6.44 Vertical (i.e., z direction in Figure 6.30) excess pore water pressure head gradient at the shoreline for different times from two-dimensional analysis. | 208 |
| 6.45 Comparison of the vertical (i.e., z direction in Figure 6.30) excess pore water pressure head gradient induced by the tsunami at the shoreline based on the one-dimensional and two-dimensional models, where for the two-dimensional model, $x=400$ m. | 209 |

LIST OF TABLES

| Table | Page |
|--|------|
| 1.1 List of symbols. | 13 |
| 2.1 Disturbing forces, restoring forces, and typical wavelengths for different ocean wave types. Adapted from Table 7.1 in Garrison and Ellis (2016, pg. 127). | 21 |
| 2.2 A table of compressibility values for different materials. C is the overall compressibility of the material, and C_s is the compressibility of the solid phase. Both C and C_s are reported in $\text{kg}/\text{cm}^2 \times 10^{-6}$, and $\alpha = 1 - (C_s/C)$. Adapted from Table 3 in Skempton (1984, pg. 114). | 27 |
| 2.3 Details of the testing program performed by Chowdhury et al. (2006) to investigate wave-induced liquefaction. | 43 |
| 2.4 Summary of important studies on loading of a soil bed by a fluid. | 53 |
| 5.1 Assumed constant modeling parameters used for the numerical experimentation. | 103 |
| 5.2 The numerical experimentation cases, with defined nomenclature, shown in Figure 5.2. Note that for the cases that B value are not selected manually, B , α , and ν_u are estimated from poroelasticity. | 108 |
| 5.3 Summary of convergence studies with four different grids for Case I and Case II. Δz is the cell size, mz is the total number of cells, Δt is the time increment, and N is the total number of time increments. | 110 |
| 6.1 Different cases used to study the effect of impermeable layer depth, z_i . Note that the nomenclature used here is similar to §5.2. The first number of each case shows the depth of the impermeable layer in meters. | 141 |
| 6.2 The maximum excess pore water pressure head gradient at the ground surface, $(\partial h/\partial z)_{z=0}$, caused by the different tsunamis shown in Figure 6.25. Note that Case 4 did not converge, which indicates that tsunami-induced liquefaction occurred. | 180 |

LIST OF TABLES (Continued)

| <u>Table</u> | | <u>Page</u> |
|--------------|---|-------------|
| 6.3 | Summary of convergence studies with four different grids for the two-dimensional model. Δz is the cell size in the z -direction, Δx is the cell size in the x -direction, mz is the total number of cells in the z -direction, mx is the total number of cells in the x -direction, Δt is the time increment, and N is the total number of time increments. . | 203 |

LIST OF APPENDIX FIGURES

| <u>Figure</u> | <u>Page</u> |
|--|-------------|
| A.1 Case S-LE-B(0): a) total pore water pressure at different time with depth for the saturated condition, assuming $B=0$, and considering linear constitutive model; b) pressure head gradient at different time with depth for the saturated condition, assuming $B=0$, and considering linear constitutive model. | 238 |
| A.2 Case S-LE-B(0): pressure head gradient changes with time at different depth for fully saturated linear model and $B=0$ | 238 |
| A.3 Case S-LE-B(0.5): a) total pore water pressure at different time with depth for the saturated condition, assuming $B=0.5$, and considering linear constitutive model; b) pressure head gradient at different time with depth for the saturated condition, assuming $B=0.5$, and considering linear constitutive model. | 239 |
| A.4 Case S-LE-B(0.5): pressure head gradient changes with time at different depth for fully saturated linear model and $B=0.5$ | 239 |
| A.5 Case S-LE-B(0.6): a) total pore water pressure at different time with depth for the saturated condition, assuming $B=0.5$, and considering linear constitutive model; b) pressure head gradient at different time with depth for the saturated condition, assuming $B=0.6$, and considering linear constitutive model. | 240 |
| A.6 Case S-LE-B(0.6): pressure head gradient changes with time at different depth for fully saturated linear model and $B=0.6$ | 240 |
| A.7 Case S-LE-B(0.7): a) total pore water pressure at different time with depth for the saturated condition, assuming $B=0.7$, and considering linear constitutive model; b) pressure head gradient at different time with depth for the saturated condition, assuming $B=0.7$, and considering linear constitutive model. | 241 |
| A.8 Case S-LE-B(0.7): pressure head gradient changes with time at different depth for fully saturated linear model and $B=0.7$ | 241 |

LIST OF APPENDIX FIGURES (Continued)

| <u>Figure</u> | <u>Page</u> |
|--|-------------|
| A.9 Case S-LE-B(0.8): a) total pore water pressure at different time with depth for the saturated condition, assuming $B=0.8$, and considering linear constitutive model; b) pressure head gradient at different time with depth for the saturated condition, assuming $B=0.8$, and considering linear constitutive model. | 242 |
| A.10 Case S-LE-B(0.8): pressure head gradient changes with time at different depth for fully saturated linear model and $B=0.8$ | 242 |
| A.11 Case S-LE-B(0.9): a) total pore water pressure at different time with depth for the saturated condition, assuming $B=0.9$, and considering linear constitutive model; b) pressure head gradient at different time with depth for the saturated condition, assuming $B=0.9$, and considering linear constitutive model. | 243 |
| A.12 Case S-LE-B(0.9): pressure head gradient changes with time at different depth for fully saturated linear model and $B=0.9$ | 243 |
| A.13 Case S-LE-B(0.95): a) total pore water pressure at different time with depth for the saturated condition, assuming $B=0.95$, and considering linear constitutive model; b) pressure head gradient at different time with depth for the saturated condition, assuming $B=0.95$, and considering linear constitutive model. | 244 |
| A.14 Case S-LE-B(0.95): pressure head gradient changes with time at different depth for fully saturated linear model and $B=0.95$ | 244 |
| A.15 Case S-LE-PW: a) total pore water pressure at different time with depth for the saturated condition, assuming pure water, and considering linear constitutive model; b) pressure head gradient at different time with depth for the saturated condition, assuming pure water, and considering linear constitutive model. | 245 |
| A.16 Case S-LE-PW: pressure head gradient changes with time at different depth for fully saturated linear model and pure water. | 245 |

LIST OF APPENDIX FIGURES (Continued)

| <u>Figure</u> | <u>Page</u> |
|---|-------------|
| A.17 Case S-LE-UW: a) total pore water pressure at different time with depth for the saturated condition, assuming aired water, and considering linear constitutive model; b) pressure head gradient at different time with depth for the saturated condition, assuming aired water, and considering linear constitutive model. | 246 |
| A.18 Case S-LE-UW: pressure head gradient changes with time at different depth for fully saturated linear model and aired water. | 246 |
| A.19 Case S-NI-B(0): a) total pore water pressure at different time with depth for the saturated condition, assuming $B=0$, and considering nonlinear constitutive model; b) pressure head gradient at different time with depth for the saturated condition, assuming $B=0$, and considering nonlinear constitutive model. | 247 |
| A.20 Case S-NI-B(0): pressure head gradient changes with time at different depth for fully saturated nonlinear model and $B=0$ | 247 |
| A.21 Case S-NI-B(0.5): a) total pore water pressure at different time with depth for the saturated condition, assuming $B=0.5$, and considering nonlinear constitutive model; b) pressure head gradient at different time with depth for the saturated condition, assuming $B=0.5$, and considering nonlinear constitutive model. | 248 |
| A.22 Case S-NI-B(0.5): pressure head gradient changes with time at different depth for fully saturated nonlinear model and $B=0.5$ | 248 |
| A.23 Case S-NI-B(0.8): a) total pore water pressure at different time with depth for the saturated condition, assuming $B=0.8$, and considering nonlinear constitutive model; b) pressure head gradient at different time with depth for the saturated condition, assuming $B=0.8$, and considering nonlinear constitutive model. | 249 |
| A.24 Case S-NI-B(0.8): pressure head gradient changes with time at different depth for fully saturated nonlinear model and $B=0.8$ | 249 |

LIST OF APPENDIX FIGURES (Continued)

| <u>Figure</u> | <u>Page</u> |
|--|-------------|
| A.25 Case S-NI-B(0.95): a) total pore water pressure at different time with depth for the saturated condition, assuming $B=0.95$, and considering nonlinear constitutive model; b) pressure head gradient at different time with depth for the saturated condition, assuming $B=0.95$, and considering nonlinear constitutive model. | 250 |
| A.26 Case S-NI-B(0.95): pressure head gradient changes with time at different depth for fully saturated nonlinear model and $B=0.95$. . . | 250 |
| A.27 Case S-NI-UW: a) total pore water pressure at different time with depth for the saturated condition, assuming aired water, and considering nonlinear constitutive model; b) pressure head gradient at different time with depth for the saturated condition, assuming aired water, and considering nonlinear constitutive model. | 251 |
| A.28 Case S-NI-UW: pressure head gradient changes with time at different depth for fully saturated nonlinear model and aired water. . . . | 251 |
| A.29 Case S-NI-PW: a) total pore water pressure at different time with depth for the saturated condition, assuming pure water, and considering nonlinear constitutive model; b) pressure head gradient at different time with depth for the saturated condition, assuming pure water, and considering nonlinear constitutive model. | 252 |
| A.30 Case S-NI-PW: pressure head gradient changes with time at different depth for fully saturated with nonlinear model and pure water. . . . | 252 |
| A.31 Case UN-NI-PW(1m): a) pore water pressure changes with depth at different time for partially saturated condition when the water table is at 1 m, nonlinear model and pure water; b) pressure head gradient changes with depth at different time for partially saturated condition when the water table is at 1 m with nonlinear model and pure water. | 253 |
| A.32 Case UN-NI-PW(3m): pressure head gradient changes with time at different depth for when the water table is at 1 m with nonlinear model and pure water. | 253 |

LIST OF APPENDIX FIGURES (Continued)

| <u>Figure</u> | <u>Page</u> |
|--|-------------|
| A.33 Case UN-NI-PW(3m): a) pore water pressure changes with depth at different time for partially saturated condition when the water table is at 3 m, nonlinear model and pure water; b) pressure head gradient changes with depth at different time for partially saturated condition when the water table is at 3 m with nonlinear model and pure water. | 254 |
| A.34 Case UN-NI-PW(3m): pressure head gradient changes with time at different depth for when the water table is at 3 m with nonlinear model and pure water. | 254 |
| A.35 Case UN-NI-UW(1m): a) pore water pressure changes with depth at different time for partially saturated condition when the water table is at 1 m, nonlinear model and aired water; b) pressure head gradient changes with depth at different time for partially saturated condition when the water table is at 1 m nonlinear model and aired water. | 255 |
| A.36 Case UN-NI-UW(1m): pressure head gradient changes with time at different depth for when the water table is at 1 m with nonlinear model and aired water. | 255 |
| A.37 Case UN-NI-UW(3m): a) pore water pressure changes with depth at different time for partially saturated condition when the water table is at 3 m, nonlinear model and aired water; b) pressure head gradient changes with depth at different time for partially saturated condition when the water table is at 3 m nonlinear model and aired water. | 256 |
| A.38 Case UN-NI-UW(3m): pressure head gradient changes with time at different depth for when the water table is at 3 m with nonlinear model and aired water. | 256 |

Chapter 1: Introduction

Tsunamis have the ability to cause significant sediment instability due to relatively large bed shear stresses, which motivates erosion, and due to the rapid draw-down of water. We focus on the second phenomenon; that is, the potential for sediment instability caused by the rapid draw-down of the tsunami water. To understand the potential for sediment instability caused by the rapid draw-down of tsunami water, it is critical to understand how pore water pressure is generated and diffused within a soil bed. Herein, we focus on homogeneous beds of beach sands. When considering pore water pressure generation caused by tsunami loading, it is important to understand two simultaneously-occurring phenomena: the generation of pore water pressure caused by overlying water weight, and the infiltration of water into the soil bed. Accordingly, to perform numerical experimentation of tsunami loading on a homogeneous soil bed, it is critical to numerically formulate a coupled seepage-deformation model. Within this dissertation, we present a seepage-deformation model, which is implemented in MATLAB, and then we use the seepage-deformation model to perform numerical experiments examining pore water pressure changes in hypothetical soil beds during hypothetical tsunami loading. The problem we investigate is unique, because tsunami loading is transient, which creates a partially drained scenario; accordingly, classic soil mechanics procedures, which are primarily focused on either drained loading scenarios (i.e.,

slow loading of coarse-grained soils) or undrained loading scenarios (i.e., loading of fine-grained soils or rapid loading of coarse-grained soils), are not entirely applicable. In addition, tsunami loading is unique because of the time scale. The draw-down of water during tsunami loading is much quicker than rapid draw-down of water in embankment dams.

1.1 Definition of soil liquefaction

Soil liquefaction caused by earthquake motion is a well-studied phenomenon within the field of geotechnical earthquake engineering. Many definitions of earthquake-induced soil liquefaction exists, but for practice in the United States, the definition from Youd et al. (2001, pg. 818) is ubiquitous: “the transformation of a granular material from a solid to a liquefied state as a consequence of increased pore water pressure and reduced effective stress.” Idriss and Boulanger (2008) provides a recent treatment of earthquake-induced soil liquefaction. Notably, in the coastal engineering field, earthquake-induced liquefaction falls under the category of residual liquefaction, because excess pore water pressures residually build-up in the soil during earthquake shaking. Earthquake-induced liquefaction occurs because of cyclic deformation of soil, which causes soil contraction in loose soils subjected to undrained loading. Evidently, earthquake-induced soil liquefaction occurs some depth below the ground surface and usually in relatively loose deposits of clean, fully saturated sand. Residual liquefaction is also caused by ocean waves (Seed and Rahman, 1978).

Soil liquefaction can also be induced by rapid draw-down of water on the ground surface. Within the geotechnical engineering field, this phenomenon is referred to as static liquefaction (Kramer and Seed, 1988). In the coastal engineering field, the phenomenon is often referred to as momentary liquefaction (Sakai et al., 1992). A definition of momentary liquefaction, which is caused by progressive ocean waves, is given by Sakai et al. (1992, pg. 202): “Under the wave trough phase, the pore water pressure does not decrease as much as the wave pressure on the bed surface, and also there is a time lag in the pore water pressure. As a result, the pore water pressure becomes larger than the static pressure at the wave trough phase, and the effective vertical stress decreases. Since the static effective stress near the seabed surface in calm water is small, there is a chance that the decrease of vertical effective stress due to waves becomes larger than the static effective stress at the wave trough phase; and therefore the seabed is momentarily liquefied at the wave trough phase. This liquefaction is repeated periodically by waves ...” Sumer and Fredsøe (2002) and Sumer (2014) give more thorough literature reviews of momentary liquefaction research.

Herein, we focus on the potential for sediment instability during tsunami loading; accordingly, we consider the potential of momentary liquefaction within a soil bed caused by tsunami loading. Note that although we are interested in momentary liquefaction, we are primarily interested in the pore water pressure response in soil beds during tsunami loading. Momentary liquefaction is a limiting condition; i.e., significant sediment instability occurs during momentary liquefaction. Recently, Yeh and Mason (2014) provided a thorough description of momentary liquefaction

caused by tsunami loading. In addition, Mason and Yeh (2016, pg. 1912) provides a definition of soil liquefaction, which is relevant for both earthquake and tsunami loading: “liquefaction is the critical condition when the action-reaction transfer at grain-to-grain contacts vanishes due to the effect of water pressure gradients in the pore spaces.” The primary details of the Mason and Yeh (2016) argument, changed slightly in organization to be more relevant for this dissertation, are given in the succeeding paragraph.

For a fully saturated element of soil, the weight of the soil element is $W = \rho_{sat}gV_T$, where ρ_{sat} is the mass density of the fully saturated soil bed and V_T is the total volume of the soil element. The weight of the soil element is used to calculate the total stress, σ . For a small soil element with dimensions of dx , dy , and dz : $V_T = dx dy dz$ and $A' = dx dy$, where A' is the area of the soil element with respect to the vertical direction (i.e., the z -direction). The effective stress, σ' , is defined by $\sigma = p_w + \sigma'$ (Terzaghi, 1943), where p_w is the total pore water pressure in the soil element. Force equilibrium in the vertical direction yields,

$$\sigma A' = (p_w + \sigma')A' = \rho_{sat}gV_T, \quad (1.1)$$

therefore,

$$\sigma dx dy = (p_w + \sigma')dx dy = \rho_{sat}g dx dy dz, \quad (1.2)$$

and,

$$\sigma = p_w + \sigma' = \rho_{sat}gz. \quad (1.3)$$

Taking the limit of Equation 1.3 as $dz \rightarrow 0$ yields,

$$\frac{d}{dz}(p_w + \sigma') = \rho_{sat}g, \quad (1.4)$$

and further rearrangement yields,

$$\frac{d\sigma'}{dz} = \rho_{sat}g - i_t\rho_w g, \quad (1.5)$$

where i_t is the total pore water pressure head gradient,

$$i_t = \frac{1}{\rho_w g} \frac{dp_w}{dz}. \quad (1.6)$$

Locally, soil liquefies when $d\sigma'/dz \rightarrow 0$, which is the state when forces do not transmit through the sediment skeleton. Setting $d\sigma'/dz = 0$ in Equation 1.5 and solving for i_t yields,

$$i_{cr,t} = \frac{\rho_{sat}}{\rho_w}, \quad (1.7)$$

where $i_{cr,t}$ is the critical total pore water pressure head gradient when liquefaction occurs. Herein, we assume a beach sand with a grain specific gravity, $G_s = 2.65$ and an initial porosity, $\phi_0 = 0.4$, which gives $\rho_{sat} = 1,990 \text{ kg/m}^3$, and $i_{cr,t} = 1.99 \approx 2$ (assuming that $\rho_w = 1,000 \text{ kg/m}^3$). Subtracting the gravitational gradient from Equation 1.7 results in the excess pore water pressure head gradient required to cause soil liquefaction,

$$i_{cr} = i_{cr,t} - 1 = \frac{\rho_{sat}}{\rho_w} - 1. \quad (1.8)$$

Accordingly, based on the assumed beach sand, the critical excess pore water pressure head gradient is $i_{cr} \approx 1$.

As previously mentioned, earthquake-induced liquefaction is often defined as the condition when the effective stress goes to zero as the total pore water pressure increases; i.e., the effective stress definition of soil liquefaction. The definition of liquefaction provided by Equation 1.8 is more general than the effective stress definition. Liquefaction occurs when either the effective stress definition or Equation 1.8 is met; however, liquefaction occurs at different times and different depths based on the two definitions (i.e, the pore water pressure is not large enough to induce liquefaction, but the pore water pressure gradient is large enough to make the local effective stress zero), which is the key point provided by Mason and Yeh (2016).

Based on the preceding discussion, it is clear that calculating the excess pore water pressure head gradient, $\partial h/\partial z$, is important for understanding tsunami-induced liquefaction potential. That is, if $\partial h/\partial z \geq i_{cr}$, then soil liquefaction is expected to occur.

1.2 Contributions

The principal contributions of this thesis are:

- The change of pore water pressure due to soil deformation induced by total stress is considered.
- As the classical deformation models can not model the deformation induced

by fluid, herein, a new deformation model is developed that models the deformation of porous media loaded by fluid.

- The concept of generation of pore water pressure by the overlying weight of fluid is developed, explained, and implemented in the developed deformation model.
- The concept of a partial drainage condition from loading of porous media by fluid is developed, explained, and implemented in the deformation model.
- A modified form of the coefficient of consolidation is developed from the proposed deformation model.
- The general seepage model is coupled with the developed deformation model.
- Tsunami loading on both offshore and onshore soil beds (i.e., fully saturated and partially saturated zones) is studied. Note that previous researchers focused on tsunami loading on offshore soil beds (i.e., fully saturated zones).
- The finite difference model allows for variable switching; accordingly, the seepage equation can be solved for the total pore water pressure as the unknown or the degree of saturation as the unknown.
- The effect of entrained air in water on the pore water pressure induced by tsunami loading is studied.
- Previous research by Yeh and Mason (2014) only considered a B value of zero and a constant shear modulus of the soil bed subjected to tsunami loading.

The current research considers the entire range of B values between zero and one.

- The soil model can be linear or nonlinear. In other words, the soil stiffness can be constant with depth and time, or can change (i.e., linear or nonlinear model).
- Effects of the tsunami duration and the tsunami height on the pore water pressure induced by the tsunami loading are investigated.
- The effect of depth to the impermeable layer on the excess pore water pressure head gradient for different tsunami loadings, for linear and nonlinear soil models, is investigated.
- The effects of soil bulk modulus, and hydraulic conductivity on excess pore water pressure head gradient are investigated.
- Tsunami-induced liquefaction based on two definitions of soil liquefaction is investigated.
- The model is extended to two-dimensions.

1.3 Organization and convention

Chapter 2 presents a background for the rest of the dissertation. In particular, tsunamis, soil mechanics concepts, and soil instability concepts (specifically, residual and momentary wave-induced liquefaction and rapid draw-down in embank-

ment dams) are discussed. Chapter 2 ends with a brief literature synthesis, which highlights the important points for understanding the coupled seepage-deformation model we developed and the subsequent numerical experimentation.

Chapter 3 presents the deformation model. As a start, the model developed by Fredlund et al. (2012) to estimate changes in volumetric strain as a function of net stress and matric suction is presented, but then the Fredlund et al. (2012) model is changed based on physical arguments to make it suitable for estimating deformation caused by tsunami loading. The hallmarks of the changed model include the incorporation of α (Biot, 1941), which is a parameter related to the compressibility of the soil bed and the compressibility of the soil grains, and the incorporation of B (Skempton, 1954; Bishop, 1954), which is a parameter related to the compressibility of the voids within a soil bed (i.e., air plus pore fluid, usually water), the compressibility of the soil skeleton (i.e., the arrangement of soil grains), and the porosity of the soil bed, $\phi = V_v/V_T$, where V_v is the volume of the voids within the soil bed, and V_T is the total volume of the soil bed. After presentation of the modified deformation model, we explain the assumptions, limitations, and modeling inputs in detail.

Chapter 4 presents the seepage model (Richards, 1931). The seepage model has been well developed and utilized within the fields of engineering, geosciences, and applied mathematics, among others. A primary contribution of Chapter 4 is the coupling of the deformation model presented in Chapter 3 to the seepage model. Herein, we couple the two models through the porosity; more specifically, the the increment of volumetric strain, $\delta\epsilon_v$, calculated at each time step with the

deformation model described in Chapter 3 is set equal to the increment of porosity, $\delta\phi$, at each time step. The increment of porosity is then used to update the porosity value in the seepage model at each time step. The numerical formulation of the coupled seepage-deformation model follows Newton's method and is implemented in MATLAB. The numerical formulation allows for variable switching; accordingly, the seepage equation can be solved for the total pore water pressure as the unknown or the degree of saturation as the unknown.

Chapter 5 contains the one-dimensional numerical experimentation that was performed using the coupled seepage-deformation model. An idealized tsunami flow height-time series was created using the Carrier et al. (2003) method, which presents a solution to the nonlinear shallow water wave equations. The idealized tsunami flow height-time series is inputted as the ground surface boundary condition to idealized soil beds. We investigate soil beds with two saturation conditions: fully saturated and unsaturated. For the unsaturated soil condition, we examined two unsaturated zone depths: one meter and three meters. We investigate two soil constitutive models: linear and nonlinear. Note that the definition of linear and nonlinear is based on shear modulus. For the nonlinear soil constitutive model, the soil bed's shear modulus varies as a function of depth and is function of effective stress; in contrast, the soil bed's shear modulus remains constant for the linear soil constitutive model. We investigate two pore fluids: aird water and de-aired water. The difference between the bulk moduli of the pore fluids is significant (i.e., the ratio between the bulk modulus of de-aired water to aird water, considering approximately 3% entrapped air, is ≈ 550). A numerical convergence study is

performed using two critical cases; namely, the case of an unsaturated soil bed (with a depth of the unsaturated zone of three meters) governed by a nonlinear soil constitutive model with aird water as the pore fluid and a fully saturated soil bed governed by a nonlinear soil constitutive model with aird water as the pore fluid. The numerical convergence study shows that convergence is readily achieved for the one-dimensional case with a modest grid spacing when the total pore water pressure, p_w is investigated. As described in §1.1, the excess pore water pressure head gradient, $\partial h/\partial z$, is also important for considering sediment instability due to tsunami loading. Convergence is more difficult to achieve for the case of gradients, because the calculation of the gradient is directly influenced by the mesh size. However, convergence is achieved for $\partial h/\partial z$ at the ground surface, which is one of the primary parameters-of-interest herein. Convergence of $\partial h/\partial z$ was impossible to achieve near the infiltration front for unsaturated soil conditions. As a result, we focus on the trends of $\partial h/\partial z$ for the unsaturated soil conditions herein. After the convergence study, we described all the numerical experimentation performed for the aforementioned soil bed cases using the hypothetical tsunami. The numerical experimentation focuses on the total pore water pressure and the excess pore water pressure head gradient recorded as a function of depth and time.

Chapter 6 contains further analysis and discussion of the numerical experimentation. First, the sensitivity of the pore water pressure response of the soil beds subjected to tsunami loading is examined as a function of the impermeable layer depth. For the numerical experimentation performed in Chapter 5, the impermeable layer depth was fixed at 10 m; however, when deeper and shallower

impermeable layer depths are considered, the pore water pressure response does change. Second, the sensitivity of the pore water pressure response in the hypothetical soil beds to the tsunami parameters — in particular, tsunami duration and tsunami height — is examined. Third, the sensitivity of the pore water pressure response in the hypothetical soil beds to the soil properties is examined. In particular, changes in hydraulic conductivity, which affect changes in the diffusion coefficient, C_v , are examined, and changes in the bulk modulus of the soil bed are examined. Fourth, the affect of entrapped air within the soil bed on the pore water pressure response is examined using the results of a field study. Fifth, the conditions required to initiate momentary liquefaction within the hypothetical soil beds are discussed. Finally, a two-dimensional formulation is developed and presented.

Chapter 7 contains the conclusions for the dissertation. In addition, a minor discussion of future research ideas is given.

Throughout the dissertation, we assume that the downward vertical axis (i.e., the z -direction) is positive, where downward is defined with respect to the gravity vector. As previously mentioned, the total pore water pressure, p_w , and the excess pore water pressure head gradient, $\partial h/\partial z$, are critically important for understanding the potential of sediment instability during tsunami loading. The total pore water pressure is given as the hydrostatic pore water pressure plus any excess pore water pressure caused by the tsunami loading. Herein, the term “pore water pressure” is always taken to mean total pore water pressure and term “pore water pressure

head gradient” is always taken to mean excess pore water pressure head gradient, unless otherwise stated. Following the choice of the positive z -direction, when the pore water pressure head gradient is positive, upward seepage of the pore water occurs. Conversely, when the pore water pressure head gradient is negative, downward seepage of the pore water occurs. In general, the value of $\partial h/\partial z$ is negative during tsunami run-up and positive during tsunami draw-down, though there is a phase lag between the pore water pressure response at the end of tsunami run-up and the beginning of tsunami draw-down, which depends on the tsunami and soil properties.

The use of symbols is pervasive throughout this dissertation, and because we have combined ideas from different fields, the chosen symbols can become confusing. Table 1.1 contains a comprehensive list of the symbols, and their definitions, used throughout.

Table 1.1: List of symbols.

| | |
|-----------|--|
| A | Fitting parameter which shows soil stiffness |
| a | A_s/A' |
| A' | Area of soil element perpendicular to z axis |
| A_g | Area of gas-solid contact |
| A_{uns} | Fitting parameter |
| A_s | Area of solid contact |
| A_{sk} | Skempton’s pore water pressure parameter |
| a_v | Coefficient of compressibility |

Table 1.1 Continued: List of symbols.

| | |
|---------------|--|
| A_w | Area of liquid-solid contact |
| a_0 | Parameter used in Gaussian wave |
| B | Skempton's pore water pressure coefficient |
| b | Parameter defined in Carrier et al. (2003) |
| C | Compressibility of soil bed |
| C_H | Empirical coefficient in Hazen (1892) formula |
| C_s | Compressibility of soil grains |
| C_{uns} | Fitting parameter |
| C_v | Coefficient of consolidation |
| C_w | Water compressibility |
| C_v^* | Diffusion coefficient |
| $C_{v,max}^*$ | Maximum diffusion coefficient assumed in computation |
| C_{v0} | Coefficient of consolidation at ground surface at initial time |
| D | Depth of interest |
| d | Soil grain diameter |
| dx | Soil element dimension along x axis |
| dy | Soil element dimension along y axis |
| dz | Soil element dimension along z axis |
| d_{50} | Mean grain diameter |
| E | Modulus of elasticity |
| e | Void ratio |

Table 1.1 Continued: List of symbols.

| | |
|------------|--|
| e_0 | Initial void ratio |
| G | Shear modulus |
| g | Gravitational acceleration |
| G_{max} | Maximum shear modulus assumed assumed in computation |
| G_s | Grain specific gravity |
| G_1 | Function defined in Carrier et al. (2003) |
| h | Excess pore water pressure head |
| H_{dr} | Drainage length in theory of consolidation |
| i_{cr} | Critical excess pore water pressure head gradient |
| i_t | Total pore water pressure head gradient |
| $i_{t,cr}$ | Critical pore water pressure head gradient |
| K | Bulk modulus of soil bed |
| k_{ab} | Absolute permeability |
| k_r | Relative permeability |
| K_f | Fluid bulk modulus (in this study, $K_f = K_w$) |
| k_g | Parameter used in Gaussian wave |
| k_h | Hydraulic conductivity |
| k_i | Intrinsic permeability |
| K_u | Undrained soil bulk modulus |
| $kvis$ | Parameter used to show the model in finite difference form |
| K_w | Water bulk modulus |

Table 1.1 Continued: List of symbols.

| | |
|--------|--|
| K'_w | Aired water bulk modulus |
| L | Length scale |
| m_v | Coefficient of volume compressibility |
| m_z | Number of cells in z direction |
| m' | $m' = 1 - 1/n'$ |
| N | Number of time steps |
| n_2 | Fitting parameter |
| n' | Fitting parameter |
| P | Total load |
| p_a | Pore air pressure |
| p_b | Wave associated pressure at the surface of seabed |
| p_e | Excess pore water pressure |
| p_g | Pore gas pressure |
| p_m | Oscillatory pore water pressure in seabed |
| p_s | Stress in solid |
| p_w | Total pore water pressure |
| p_0 | Absolute fluid pressure |
| P_1 | Function defined in Carrier et al. (2003) |
| Q | Parameter used to show the model in finite difference form |
| q | Parameter defined in Carrier et al. (2003) |
| q_v | Darcy velocity |

Table 1.1 Continued: List of symbols.

| | |
|----------|---|
| R | Residual |
| Re | Reynolds number |
| S | Degree of saturation |
| S_e | Effective degree of saturation |
| S_r | Residual saturation |
| T | Transmissibility (i.e., parameter used to show the model in finite difference form) |
| t | Time |
| T_d | Tsunami duration |
| T_v | Time factor in theory of consolidation |
| T_{xx} | Parameter used to show the model in finite difference form |
| T_{zz} | Parameter used to show the model in finite difference form |
| u | Solid displacement |
| u_1 | Parameter defined in Carrier et al. (2003) |
| v | Depth averaged horizontal velocity of tsunami |
| v_p | Flow velocity in porous media |
| V_s | Shear wave velocity |
| V_T | Total volume of soil element |
| V_{T0} | Initial total volume of soil element |
| V_v | Volume of void in an element |
| W | Weight of soil element |
| z_i | Depth to impermeable layer |

Table 1.1 Continued: List of symbols.

| | |
|----------------|---|
| z_w | Depth of the ground water |
| α | Biot coefficient |
| α_y | Pore water pressure coefficient in Zen and Yamazaki (1990a) model |
| α' | Fitting parameter |
| γ_b | Buoyant unit weight of soil |
| γ_d | Soil dry unit weight |
| γ_s | Unit weight of soil grain |
| γ_{sat} | Saturated unit weight of soil |
| γ_w | Water unit weight |
| δ | Increment |
| ϵ | Axial strain (i.e., strain in z direction here) |
| ϵ_v | Volumetric strain |
| ζ | Parameter defined in Carrier et al. (2003) |
| η | Wave height |
| Θ | Normalized water content |
| θ_r | Residual volumetric water content |
| θ_s | Saturated volumetric water content |
| θ_w | Volumetric water content |
| κ'' | Fitting parameter |
| Λ | Parameter defined in Carrier et al. (2003) |
| λ | Integration variable |

Table 1.1 Continued: List of symbols.

| | |
|--------------|--|
| μ | Dynamic viscosity of fluid |
| μ_w | Dynamic viscosity of water |
| ν | Drained Poisson ratio |
| ν_u | Undrained Poisson ratio |
| ξ | Parameter defined in Carrier et al. (2003) |
| ρ | Fluid density |
| ρ_b | Mass density of soil grain |
| ρ_d | Dry mass density of soil |
| ρ_{sat} | Saturated mass density of soil |
| ρ_w | Water density |
| σ | Total stress |
| σ' | Effective stress based on Terzaghi (1943) definition |
| σ_r | Reference stress |
| σ_1 | Major principal stress |
| σ_3 | Minor principal stress |
| ϕ | Soil porosity |
| ϕ_0 | Initial soil porosity |
| χ | Bishop effective stress parameter |
| ψ | Slope of beach |

Chapter 2: Background

2.1 Tsunami waves

We are focused on pore water pressure changes in soils during tsunami loading; therefore, a brief introduction to tsunamis is warranted. The reader is encouraged to consult *Tsunamis* for a recent and more comprehensive discussion of tsunamis (Bernard and Robinson, 2009). The work herein particularly hinges on the work of Carrier et al. (2003), which provides a method for predicting tsunami wave heights and wave velocities spatially and temporally given an initial waveform. The Carrier et al. (2003) method is explained further in Chapter 5, when the input tsunamis for the numerical experimentation are described.

Tsunami is a Japanese word written with two characters: *tsu* means harbor and *nami* means wave. Tsunamis are created by disturbing forces; namely, submarine landslides, volcanic eruptions, and faulting of the sea floor, which induces earthquakes. Herein, we focus on earthquake-induced tsunamis. Earthquake-induced tsunamis have different restoring forces and typical wavelengths than other ocean wave types; for comparison purposes, Table 2.1 shows characteristics of different ocean wave types.

Earthquake-induced tsunamis have large source areas (Okal, 2009). For instance, the 2011 Great East Japan Tsunami was generated by a moment mag-

Table 2.1: Disturbing forces, restoring forces, and typical wavelengths for different ocean wave types. Adapted from Table 7.1 in Garrison and Ellis (2016, pg. 127).

| Wave type | Disturbing force | Restoring force | Typical wavelength |
|-----------|--|-----------------------------|------------------------------|
| Capillary | Usually wind | Cohesion of water molecules | ≤ 1.73 cm |
| Wind | Wind over ocean | Gravity | ≈ 60 to 150 m |
| Seiche | Atmospheric pressure, storm surge, tsunami | Gravity | Function of ocean basin size |
| Tsunami | Faulting of seafloor, volcanic eruption, landslide | Gravity | ≈ 200 km |
| Tidal | Gravitational attraction, rotation of earth | Gravity | Half earth's circumference |

nitude 9.0 earthquake that had an approximately 150 km wide by 300 km long rupture zone (Ammon et al., 2011). Unlike storm-generated waves, which have periods of less than tens of seconds and are characterized by many cycles, tsunami waves are characterized by a single cycle or a few cycles. Tsunami wave periods are approximately a few minutes to tens of minutes. A typical tsunami inundates several hundred meters, and in some cases, it extends more than a few kilometers. For instance, inundation distances on the island of Sri Lanka during the 2004 Indian Ocean Earthquake and Tsunami ranged from 200 m to 3 km (Wijetunge, 2006). During the 2011 Japan Great East Earthquake and Tsunami, the maximum inundation height on the Sendai Plain was 19.5 m, and the tsunami bore propagated more than 5 km inland (Mori et al., 2011).

The wavelength of earthquake-induced tsunami waves is large compared to the

water depth, which causes them to behave like shallow water waves, even in the open ocean (Okal, 2009). The rate of loss of wave energy is inversely related to the wavelength (Dean and Dalrymple, 1991); therefore, due to the large wavelength of tsunamis, they lose little energy during propagation, and they are typically more powerful (in terms of damage potential to coastal buildings and infrastructure) than storm waves. As tsunamis propagate towards coastlines, their kinetic energy is converted to potential energy and the wave height increases (i.e., shoaling). During shoaling from deep to shallow water, the asymmetry of the wave profile increases (Adeyemo, 1968).

Shallow water wave theory assumes that the water is incompressible and inviscid, and that the vertical acceleration and wave dispersion are negligible (Stoker, 1957; Whitham, 1974). Multiple researchers have solved the shallow water wave equations using numerical and analytical approaches (e.g., Carrier and Greenspan, 1958; Casulli, 1990; Harbitz, 1992; Bradford and Sanders, 2002). As previously mentioned, herein we use the Carrier et al. (2003) tsunami run-up and draw-down model is used to estimate the tsunami inundation and draw-down, which is described in §5.1.

2.2 Soil mechanics concepts

Three concepts from soil mechanics are important for understanding the later chapters of this dissertation: effective stress, pore water pressure parameters, and the Mandel-Cryer effect. A brief discussion of each concept is presented within this

section. The reader is encouraged to consult seminal soil mechanics texts for more information (e.g., Terzaghi, 1943; Taylor, 1948; Scott, 1963; Santamarina et al., 2001; Mitchell and Soga, 2005).

2.2.1 Effective stress

Soil is a three phase material (i.e., solid, liquid, gas), and accordingly, understanding the response of soil to different loadings is a notoriously difficult problem (Jaeger and Nagel, 1992). Even considering the fully saturated soil condition, where the liquid is water, is complex, because the solid phase and the water phase respond differently to different loadings. For instance, the water phase usually has negligible shear resistance, so any resistance to shearing within a soil bed must be developed within the solid phase. It is therefore paramount to understand the stresses in the soil skeleton. As stated by Santamarina et al. (2001, pg. 82), “The concept of effective ‘skeletal’ stress permits computing the load-deformation response of the granular skeleton, including shear strength and volume change, independently of the pore fluid pressure. Therefore, the effective stress concept unifies the interpretation of the drained and undrained behavior of granular materials.” The unification of drained and undrained behavior of granular materials is particularly important when considering tsunami-induced pore water pressures in soil beds.

An understanding of the concept of effective stress is provided by Scott (1963), which follows the work of Skempton (1984) closely (n.b., Skempton’s original paper

was published in 1960, but we are referencing a later copy, which is published in an edited collection). Given the importance of the concept of effective stress for the work herein, we will briefly summarize the salient effective stress concepts given by Scott (1963) in the succeeding paragraph.

The effective stress concept, as discussed by Scott (1963), is shown schematically in Figure 2.1; i.e., a phase diagram showing two sand grains in contact with the relevant forces and areas noted. A force balance in the vertical direction produces,

$$P = p_s A_s + p_w A_w + p_g A_g, \quad (2.1)$$

where P is the total load, p_s , p_w , and p_g are the stresses in the solid, liquid (i.e., the pore water pressure), and gas phases, respectively. Dividing Equation 2.1 by the gross area, A' , gives,

$$\sigma = ap_s + (1 - a)p_w + (1 - a - b)(p_g - p_w), \quad (2.2)$$

where σ is the total stress ($\sigma = P/A'$), $a = A_s/A'$, and $b = A_w/A'$. If the soil bed is fully saturated, then Equation 2.2 reduces to,

$$\sigma = ap_s + (1 - a)p_w. \quad (2.3)$$

Scott (1963, pg. 165) argues that for sands, $a \approx 0$, because the contact area between adjacent grains is small. In addition, as stated by Scott (1963, pg. 165), the value of p_s is usually large, so the quantity ap_s is not zero, and it is equal to

the *effective stress*, σ' ; i.e., $ap_s = \sigma'$. In the end, the foregoing discussion leads to the popular computation of effective stress proposed by Terzaghi,

$$\sigma = \sigma' + p_w. \quad (2.4)$$

Equation 2.4 is credited to Terzaghi (i.e., from his 1923 paper written in German). Note that in 1913 Paul Fillunger stated that the pore liquid pressure does not have any influence on the strength of the porous solid and his work is the basis for the new theory of porous media. See De Boer (2012) for more historical discussions and original references.

Skempton (1984) performed experiments on soil, concrete, and rock, and he developed modified effective stress expressions. Skempton (1984) showed that Equation 2.3 is not valid. For a deformable bed the Skempton (1984) effective stress equation is,

$$\sigma = \sigma' + \left(1 - \frac{C_s}{C}\right) p_w, \quad (2.5)$$

where C is the compressibility of the soil bed, and C_s is the compressibility of the soil grains. Table 2.2 shows compressibility values of different materials determined and compiled by Skempton (1984). For many soils near the surface, the ratio C_s/C approaches zero, as shown in Table 2.2, because the soil bed is much more compressible than the individual soil grains. Accordingly, for many common geotechnical engineering problems, $C_s/C \rightarrow 0$, and the Skempton (1984) effective stress equation (Equation 2.5) collapses to the familiar form given by Terzaghi (Equation 2.4). In Table 2.2, $\alpha = 1 - (C_s/C)$; accordingly, Equation 2.5 can also

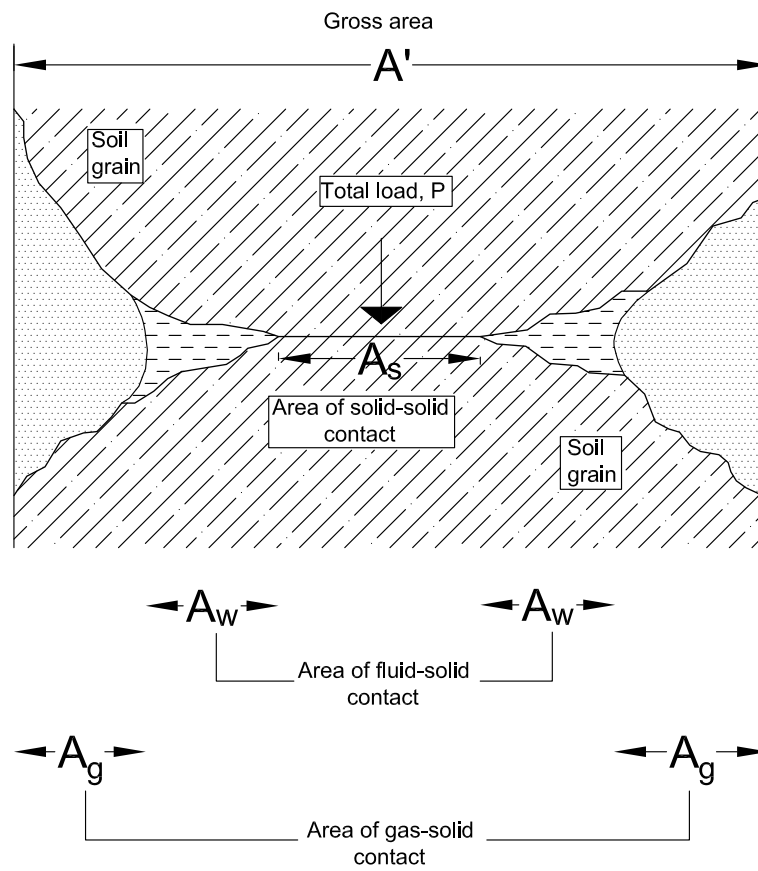


Figure 2.1: Schematic showing the concept of effective stress using two sand grains. Modified from Figure 5-1 in Scott (1963, pg. 164).

Table 2.2: A table of compressibility values for different materials. C is the overall compressibility of the material, and C_s is the compressibility of the solid phase. Both C and C_s are reported in $\text{kg/cm}^2 \times 10^{-6}$, and $\alpha = 1 - (C_s/C)$. Adapted from Table 3 in Skempton (1984, pg. 114).

| Material | C | C_s | C_s/C | α |
|-------------------------------|-------|-------|---------|----------|
| Quartzitic sandstone | 5.8 | 2.7 | 0.46 | 0.54 |
| Quincy granite (100 ft deep) | 7.5 | 1.9 | 0.25 | 0.75 |
| Vermont marble | 17.5 | 1.4 | 0.08 | 0.92 |
| Concrete (approx. value) | 20 | 2.5 | 0.12 | 0.88 |
| Dense sand | 1800 | 2.7 | 0.0015 | 0.9985 |
| Loose sand | 9000 | 2.7 | 0.0003 | 0.9997 |
| London Clay (over-cons.) | 7500 | 2.0 | 0.00025 | 0.99975 |
| Gosport Clay (normally-cons.) | 60000 | 2.0 | 0.00003 | 0.99997 |

be written as,

$$\sigma = \sigma' + \alpha p_w. \quad (2.6)$$

Compressibility is defined as the inverse of bulk modulus; that is, the bulk modulus of the soil grains, K_s , is defined as $K_s = 1/C_s$, and the bulk modulus of the soil bed, K , is defined as $K = 1/C$. It follows that,

$$\alpha = 1 - (K/K_s). \quad (2.7)$$

The bulk modulus of the soil bed, K , is,

$$K = \frac{2(1 + \nu)G}{3(1 - 2\nu)}, \quad (2.8)$$

where G is the soil's shear modulus and ν is the drained Poisson's ratio of the soil

bed. (Biot, 1941, pg. 158) defined α as,

$$\alpha = \frac{2(1 + \nu)G}{3(1 - 2\nu)H}, \quad (2.9)$$

where $1/H$ is the compressibility of the soil bed caused by a change in water pressure (Biot, 1941). For a fully saturated clay, Biot (1941, pg. 163) assumed that the bulk modulus of the soil grains is much larger than the bulk modulus of the soil bed; i.e., $\alpha = 1$ in Equation 2.9, which again leads to the typical form of effective stress given in Equation 2.4.

As stated by Nur and Byerlee (1971), the exact value of the parameter α is controversial for different soil types. Terzaghi, in his 1923 paper (see De Boer, 2012), suggested that α should be equal to the porosity, but he experimentally found that $\alpha \approx 1$. He interpreted this to imply that grain boundaries and grain contacts have an effective porosity of approximately one. Hubbert (1960) attempted to prove theoretically that $\alpha = 1$, but Laubscher (1960) questioned the validity of the Hubbert proof. As discussed by Nur and Byerlee (1971), the strain due to a pore is very localized and decreases with distance from the pore; accordingly for sufficiently small pores, the strain is equal to the strain of the solid with no pores. Therefore, as the number of pores approaches zero, the effect of the pores on strain also approaches zero. Note that all the above experiments and discussions are relevant for slow rate of loading conditions (i.e., stable, equilibrium conditions).

2.2.2 Pore water pressure parameters

The functional form about pore water pressure is given by Skempton (1954) as,

$$\Delta p_w = B[\Delta\sigma_3 + A_{sk}(\Delta\sigma_1 - \Delta\sigma_3)], \quad (2.10)$$

where A_{sk} and B are the pore water pressure parameters, which are often referred to as “Skempton’s pore water pressure parameters,” and Δp_w , $\Delta\sigma_1$, and $\Delta\sigma_3$ are the changes in pore water pressure, major principal total stress, and minor principal total stress, respectively. The pore water pressure parameters A_{sk} and B in Equation 2.10 are determined experimentally using undrained triaxial testing (Bishop and Henkel, 1962).

Herein, we focus on the pore water pressure parameter B , which is defined by considering the consolidation phase of the undrained triaxial test (Bishop and Henkel, 1962). Assuming isotropic consolidation, the soil specimen is subjected to a cell pressure equal to $\Delta\sigma_1 = \Delta\sigma_3$. Accordingly, Equation 2.10 reduces to,

$$\Delta p_w = B\Delta\sigma_3. \quad (2.11)$$

Skempton (1954) showed that for the fully saturated condition, the B value can be estimated as,

$$B = \frac{1}{1 + \frac{\phi C_w}{C}}, \quad (2.12)$$

where C_w is the compressibility of water and ϕ is the porosity of the soil bed. When water is assumed to be incompressible, which is a typical assumption made

by geotechnical engineers when examining the consolidation of a fully saturated clay layer, then the B value is one. We noted that Skempton's pore water pressure parameter B is an important parameter in the developed deformation model (see Chapter 3).

Herein, because the focus is on both saturated and unsaturated conditions, a modified functional form of the B value is needed. Yang (2005) developed the following relationship for the B value as a function of degree of saturation,

$$B = \frac{1/K - 1/K_s}{1/K - (1 + \phi)/K_s + \phi/K_w + \phi(1 - S)/p_0}, \quad (2.13)$$

where S is degree of saturation, K_w is the water bulk modulus, and p_0 is the absolute fluid pressure (i.e., the total fluid pressure plus one atmosphere). We use the expression for the B value given by Yang (2005) herein.

In the field, measuring B values reliably is difficult; in contrast, in the laboratory, B values can be easily measured using triaxial testing devices (Bishop and Henkel, 1962). The shear resistance of water is negligible and soil skeleton resists the shear stress when the shear wave passes soil medium, accordingly as stated by Naesgaard et al. (2007) the shear wave velocity is independent of the B value. However, the P-wave velocity (i.e., velocity of compression waves) is related to B value (e.g., Kokusho, 2000; Yang, 2002; Nakazawa et al., 2004; Naesgaard et al., 2007). Note that the soil below the ground water table is not always saturated, and accordingly $B < 1$ (e.g., Nakazawa et al., 2004).

2.2.3 The Mandel-Cryer effect

To understand the Mandel-Cryer effect, it is important to consider soil consolidation. Clearly, consolidation is occurring to soil beds subjected to tsunami loading, and pore water pressures within the soil bed change as a result. When considering a fine-grained soil (i.e., clay), after applying the pressure increment and during the primary consolidation, the total stress is shared by the free pore water pressure (Barden, 1965), by the plastic resistance of the highly viscous adsorbed double layer, and by the solid-solid contact (i.e., grain bond). The viscous double layer and the grain bonds are the components of effective stress. In contrast to the preceding clay behavior, for sands, only the grain bond components are important for the consolidation process.

After primary consolidation, secondary compression will occur. Terzaghi (1943) showed that secondary compression is a result of two independent processes. One process is caused by the gradual readjustment of clay particles to a more stable equilibrium position. The second process is caused by the gradual lateral displacements within a soil bed that occur because of shear stress. During secondary compression, the pore water pressure is almost zero and the pressure increment is shared by the grain bonds and the double layer. Over longer periods of time, the pressure increment is gradually transferred from the double layer to the grain bonds. For sand, the pressure increment is only resisted by the grain bonds.

For non-porous materials with open drainage, the excess pore water pressure resulting from external loading reduces to zero monotonically. In contrast, in a

poroelastic medium, a change of excess pore water pressure in one part of the medium does not result in the monotonic response of the entire medium. In other words, the excess pore water pressure increases in parts of the medium for a certain time, before the overall decrease of excess pore water pressure within the medium becomes dominant (Holzbecher, 2016). Mandel (1953) described such behavior. Mandel's problem consists of a rectangular soil sample sandwiched between two rigid, frictionless plates with drainage allowed towards the two sides in the lateral direction. At the initial time ($t = 0$), a uniform vertical load is applied to the soil, and the load remains constant. With time, the excess pore water pressure near the side edges will dissipate; however, Mandel showed that between the drained ends and the center, the excess pore water pressure will continue to rise for some duration. After Mandel, Cryer (1963) showed similar behavior at the center of a sphere consolidating under hydrostatic pressure.

In short, during consolidation, the increase in excess pore water pressure near the central axis of a soil specimen, and the increase of the hydraulic gradient is called the Mandel-Cryer effect. Physically speaking, the Mandel-Cryer effect accelerates the consolidation process.

2.3 Soil instability

Soil instability is a large topic within several fields including soil mechanics and geotechnical engineering. Herein, we focus on soil instability caused by wave-induced residual and momentary liquefaction. The amount of work that has been

completed by others on this topic is substantial, and Sumer (2014) provides a recent and comprehensive literature review. Herein, we only focus on describing a few studies that motivated our understanding of the work presented in Chapters 3 to 6. In addition to discussions about wave-induced residual and momentary liquefaction, §2.3.3 contains a discussion about the rapid draw-down of water in embankment dams, which is a phenomenon related to momentary liquefaction caused by tsunamis.

2.3.1 Wave-induced residual liquefaction

Wave-induced residual liquefaction can occur during progressive wave loading (e.g., Sumer et al., 1999). Under the crest of the progressive wave, the pore water pressure within the soil bed increases, and under the trough of the progressive wave, the pore water pressure within the soil bed decreases (see Figure 10.1 in Sumer and Fredsøe, 2002). Accordingly, the soil-water interface undergoes temporal shear deformations during progressive wave loading, and the shear strain in the soil bed changes periodically. The periodic shear strain can result in the contraction of the soil bed, if the soil is relatively loosely packed, which generates excess pore water pressures within the soil bed. The excess pore water pressures can become large enough to cause the effective stress within the soil bed to approach zero and induce liquefaction, which is called residual liquefaction. The residual liquefaction mechanism described for progressive wave loading is the same as earthquake-induced residual liquefaction (Idriss and Boulanger, 2008).

Sumer et al. (1999) and Sumer et al. (2006) performed experiments in a wave flume to investigate residual liquefaction caused by progressive wave loading. Using the results from the Sumer et al. (1999) and Sumer et al. (2006) experiment, Sumer (2014) showed that transition from a non-liquefied state to a liquefied state is characterized by a sudden discontinuity (see Figure 3.8 in Sumer, 2014). Sumer (2014) stated that the discontinuous transition may be linked to the change in the state of the soil from a solid state to a liquid state during the residual liquefaction process, and that the liquefied layer of sediment and the water column form a two-layer system.

Figure 2.2, from Sumer (2014), shows how progressive waves build up excess pore water pressure until liquefaction occurs (i.e. A to D in Figure 2.2). The built up excess pore water pressure leads to an upward flow of pore water. Sumer (2014) stated that the accumulated pressure is largest at the impermeable base and smallest at the surface of the soil bed. As the pore water pressure is dissipating, the soil grains settle down through the water, and compaction occurs (i.e. D to G in Figure 2.2). Note that here the term “compaction” is defined as the process of densifying the soil bed. During compaction, the soil bed’s porosity reduces as air and water are expelled, and the soil particles are pressed together into a close state of contact (e.g., Olson, 1963; Sumer, 2014). Sumer (2014) found that compaction starts from the bottom of the soil bed and progresses towards the top, and he also showed that the initial bed surface settles downward and as a result, the compaction process causes ripples at the bed surface. During the compaction process, the soil bed’s relative density increases, and additionally, the relative

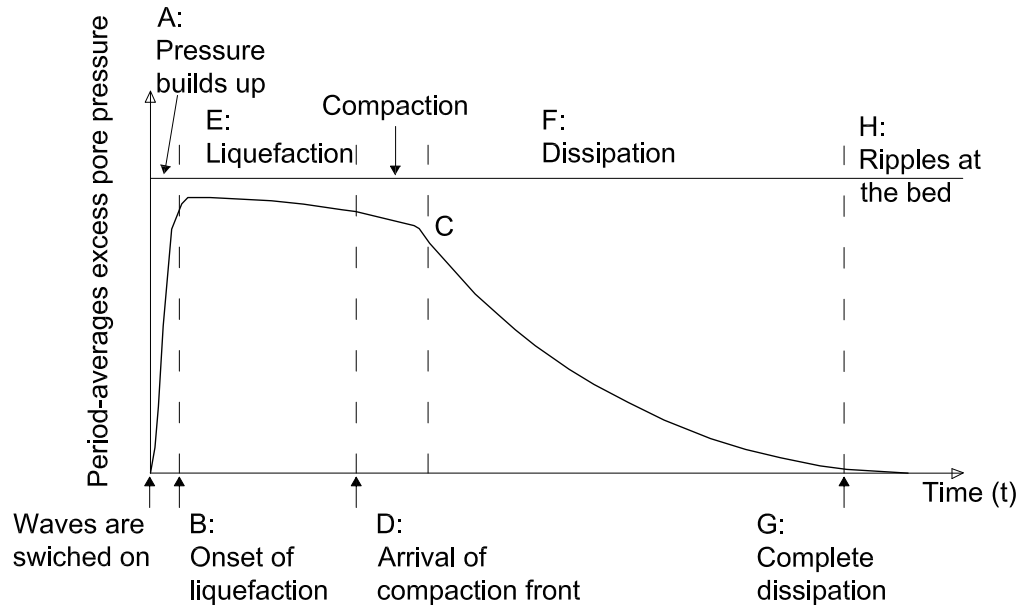


Figure 2.2: Time series of period-averaged excess pore-pressure at depth z during progressive wave loading [modified from Figure 3.11 in Sumer (2014, pg. 55)].

density increases with increasing progressive wave amplitude. Note that during the compaction phase shown in Figure 2.2, the progressive waves are still being applied and switching off the progressive waves would result in a faster dissipation of excess pore water pressure.

Although wave propagation in oceans is complicated, for the sake of simplicity, it is often assumed that linear wave theory governs (e.g., Dean and Dalrymple, 1991). Ocean waves produce periodical pressure over sea floors. The ocean waves are irregular, and the superposition of regular (i.e., sinusoidal) waves is used to

model the irregular waves. Ocean waves can induce liquefaction via a different mechanism than earthquakes (i.e., momentary liquefaction), or via a similar mechanism (i.e., residual liquefaction). The effective stress oscillation during ocean wave loading can induce densification in the sea bed. Bjerrum (1973) related the high relative density of the sea floor in the North Sea to the large number of cycles of shear stress caused by the ocean waves, and Miyamoto and Sekiguchi (2003) found that sediments that have experienced wave-induced liquefaction have less potential to liquefy under the residual liquefaction mechanism. As stated earlier, during progressive wave loading, wave-induced liquefaction is controlled by two liquefaction mechanisms, and the increase of relative density can result in an increase of the momentary liquefaction potential; however, the focus of this section is on residual liquefaction. The foregoing Bjerrum (1973) observation is caused by the pre-shearing of the sediment grains, which are rearranged in a more dense and stable condition during ocean wave loading. There are important exceptions to the observation that wave-induced liquefaction always causes densification and reduces liquefaction potential; namely, 1) when the soil is softened or loosened; 2) when there is slow sedimentation; and 3) when the seabed is active (Sumer, 2014). In addition, sometimes the storm waves are bigger than usual and they come onshore.

2.3.2 Wave-induced momentary liquefaction

Sumer (2014) defined momentary liquefaction as the phenomenon when the excess

pore water pressure is lower on the top of a soil bed as compared to at some depth within the soil bed, which is a condition that leads to an upward flow of pore water. If the upward flow of pore water reaches a critical velocity, then sediment instability can occur, which is a process often referred to as fluidization (Lowe, 1975) and is related to momentary liquefaction (Sakai et al., 1992). Momentary liquefaction can occur under the wave trough, because a downward pressure head gradient is developed under the trough of a progressive wave (Sumer, 2014). The downward pressure gradient applies uplift forces to sediment particles, because of both skin friction forces and pressure difference forces (recall that we assume the vertical axis is positive downward). Under the wave trough, the pressure gradient is positive and downward; however, the seepage force is upward. If the downward gradient exceeds the submerged unit weight of the sediment, then momentary liquefaction occurs. Note that the preceding discussion of momentary liquefaction is based on the assumption that pore water flow occurs one-dimensionally.

During progressive wave or standing wave loading, residual liquefaction and momentary liquefaction occur simultaneously. Note that standing waves are created when progressive waves hit a rigid wall and reflect. The superposition of the original wave with the reflected wave creates the standing wave. Putnam (1949) investigated the wave-induced flow through a sediment bed during standing wave loading. Putnam (1949) presented his results as a flow net. Putnam (1949) flow net results showed that the pore water instantaneously infiltrates into the soil bed under the wave crest, and it ex-filtrates from the ground surface under the wave trough.

Recently, Kirca et al. (2013) performed experiments to understand the mechanism of liquefaction induced by standing waves, and the results were also compared with the results from similar experiments using progressive waves. The experiments were performed in a wave flume with a 26.5 m length and a 0.6 m width. The water depth was 0.3 m, and the soil dimensions were 0.4 m, 0.6m, and 0.78 m (depth, width, and length). The standing wave heights ranged from 5.9 cm to 12 cm and the progressive wave heights ranged from 6.2 cm to 11.1 cm. The experiments were conducted on silt with a mean grain diameter, d_{50} , of 0.070 mm, and a specific gravity of 2.67.

The shear stress under the standing wave is shown in Figure 2.3. Kirca et al. (2013) stated that under the node, cyclic shear deformation occurs and this process builds up the excess pore water pressure. Similar to observations from progressive wave loading of soil beds, the pore pressure generation in soil beds due to standing wave loading is followed by dissipation and compaction (see Figure 12 in Kirca et al., 2013, pg. 498). Excess pore water dissipation occurs within the entire soil bed, from nodes to anti-nodes, until total dissipation is reached. Sumer (2014) stated that the shear deformation under the nodes is maximum and under anti-nodes is zero. The building up of excess pore water pressures by cyclic deformation induces an upward flow of pore water. The resulting excess pore water pressure gradient is small under the nodes and increases from the nodes towards the anti-nodes.

Sumer (2014) also showed that the rate of spreading of excess pore water pressure is a function of the diffusion coefficient (i.e., the coefficient of consolidation,

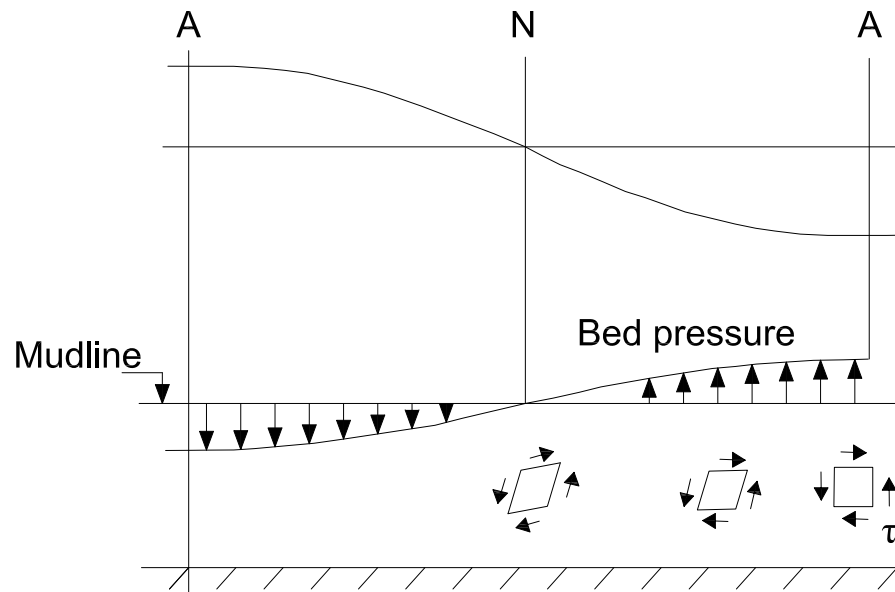


Figure 2.3: Variation of the shear stress and strain in the soil as a function of horizontal distance during standing wave loading [modified from Figure 3 in Kirca et al. (2013, pg. 493)].

C_v). It was shown that the number of waves required for the accumulated pore pressure at the nodal section to reach the maximum pressure is equal to that experienced by progressive waves for the same wave height.

Zen and Yamazaki (1990a) developed an apparatus to study wave-induced liquefaction and densification (see Figure 3 in Zen and Yamazaki, 1990a, pg. 93). Toyoura sand specimens, with different relative densities, were tested. The specific gravity and the mean grain diameter of Toyoura sand were 2.674 and 0.181 mm, respectively. The sand was poured to a height of 2.1 m within a test cylinder, which had an inner diameter of 200 mm. Regular sine wave loading with wave periods between 2 s and 15 s was used to load the sand specimens.

The Zen and Yamazaki (1990a) results show the pore water pressure response at different depths. The pore water pressure attenuates with depth during sine wave loading, as expected. The phase lags of the pore water pressure as function of depth is also presented by Zen and Yamazaki (1990a). The relative density of the sand also increased during testing. The vertical strain decreased with depth, and thus, the increase of relative density also decreases with depth. The densification of the deposit intensified in locations where liquefaction occurred. Zen and Yamazaki (1990a) showed that the change in the vertical effective stress was equal to the oscillatory excess pore water pressure in the seabed, and they further noted that the wave oscillations caused oscillations of effective stress. When the effective stress increased, the sediment bed densified, and *vice versa*. The effective stress varied periodically in accordance with the pressure changes on the surface of the deposit. Accordingly, the effective stress was decreased by the amount that in-

duces liquefaction. When the effective stress increases, the sediment settles down, and when effective stress decreases, the vertical strain decreases. As the loading amplitude increases, the sediment liquefies. As liquefaction happens, the sediment particles are suspended, and the reconstitution of the soil skeleton occurs. As a result, the soil skeleton deposits in a denser and more stable condition. The described circulation occurs several times until the density of the deposit comes to a steady state.

To qualify the observations described in the preceding paragraph, Zen and Yamazaki (1990b) derived the following equation,

$$\alpha_y \frac{\partial p_m}{\partial t} = C_v \frac{\partial^2 p_m}{\partial z^2} + \frac{\partial p_b}{\partial t}, \quad (2.14)$$

which they developed from the conservation of mass equation,

$$\frac{k_h}{\gamma_w} \frac{\partial^2 p_m}{\partial z^2} = -m_v \frac{\partial \sigma'_v}{\partial t} + \phi C_w \frac{\partial p_m}{\partial t}, \quad (2.15)$$

where k_h is hydraulic conductivity, γ_w , is water unit weight, $\alpha_y = 1 + [(\phi C_w)/m_v]$, ϕ is the soil porosity, C_w is the compressibility of pore water including air, m_v is the coefficient of volume compressibility, C_v is the coefficient of consolidation, σ'_v is the vertical effective stress in soil, and p_m and p_b are the oscillatory pore pressure in the seabed and the wave associated pressure at the surface of the seabed, respectively. Porosity is defined as $\phi = V_v/V_T$, where V_v is the volume of the void space and V_T is the total or bulk volume of material, including the solid and void components. Void ratio is defined as $e = V_v/V_s$ where V_s is the volume of the solids. Void ratio

and porosity are related as $\phi = e/(1 + e)$.

Zen and Yamazaki (1990b) used a finite difference approach to solve the dimensionless form of Equation 2.14. Comparisons of the solutions of Equation 2.14 with the measurement data from the tests showed good agreement. Note that, if the compressibility of water is neglected, then α is equal to one and Equation 2.14 is similar to Terzaghi's one-dimensional consolidation equation (Terzaghi, 1943). The only difference is the one additional term is added, which is related to the pore pressure generation by the waves. Note that Equation 2.14 with $\alpha_y = 1$ is also the same functional form that Seed et al. (1976) used to describe residual liquefaction caused by earthquake loading.

Further study was performed by Chowdhury et al. (2006) to investigate wave-induced liquefaction. The studies were performed on river sand from Australia with a specific gravity of 2.65, a mean grain diameter, d_{50} , of 0.25 mm, and a permeability of 2.9×10^{-3} m/s to 6.2×10^{-4} m/s for loose to nearly dense sand, respectively. A large-scale, one-dimensional experiment was developed to study the momentary liquefaction of the sea floor; namely, a large cylindrical wave tank with a diameter of 800 mm and a height of 2.5 m. Two types of tests were performed: one series with aired water, which models the unsaturated situation due to the presence of air, and one series with de-aired water and circulation of carbon dioxide to model fully saturated condition. A static pressure of 50 kPa, which is equal to about a 5 m water depth, was used. In the first four tests the small wave amplitude of 9 kPa with the wave periods of 3 s, 9 s, 15 s, 21 s, 27 s, and 33 s with 500 wave cycles were used to test. The details of the testing program

Table 2.3: Details of the testing program performed by Chowdhury et al. (2006) to investigate wave-induced liquefaction.

| Test No. | Relative density (%) | Water | Flushed with Co2 | Initial saturation (%) |
|----------|----------------------|-------------|------------------|------------------------|
| 1 | 78 | Aired water | No | 96 |
| 2 | 78 | De-aired | Yes | 99 |
| 3 | 40 | Aired water | No | 96 |
| 4 | 40 | De-aired | Yes | 99 |
| 5 | 40 | Aired water | No | 96 |

are shown in the Table 2.3.

Similar to Zen and Yamazaki (1990a,b), Chowdhury et al. (2006) found that the pore pressure changes amplitude reduces with depth, and also the phase lag of the pore water pressure with respect to the soil surface increases with depth. Thus, the depth of momentary liquefaction increases with decreasing wave period, and the potential of momentary liquefaction is decreased when the wave period becomes large. Chowdhury et al. (2006) showed that momentary liquefaction is more likely to occur in dense sand rather than in loose sand. Note that this finding is contrary to similar observations made for residual liquefaction, wherein loose sand has a higher liquefaction potential. Numerical studies by Chowdhury (2004) showed that the observed differences is caused by the higher permeability of loose sand, and that mechanical properties (e.g., modulus of elasticity), and hydraulic properties do not play a significant role. As the fraction of applied bed pressure that propagates to the sediment bed decreases, the depth of momentary liquefaction increases. In other words, as stated by Chowdhury et al. (2006), the depth of momentary liquefaction increases with decrease in permeability, degree of saturation, and wave period.

In the fifth test of Chowdhury et al. (2006), the sinking of an object on the surface of the sand bed was tested. Chowdhury et al. (2006) found that the object would sink if the specific gravity of the object was more than the specific gravity of liquefied sand. When the sand liquefies the object sinks, but because of the downward gradient and the seepage force, the instantaneous depth of burial is much lower than the momentary liquefaction depth. It is also shown by Chowdhury et al. (2006) that the rate of sinking of the object decreases with the continuous number of waves of a particular amplitude and frequency. The Chowdhury et al. (2006) results show that the object settles down into the soil during the wave loading phase and maintains a steady position during the unloading phase (see Figure 11 in Chowdhury et al., 2006). Chowdhury et al. (2006) stated that the degree of saturation plays an important role, especially at small wave periods, and they also found that the influence of the degree of saturation is higher deeper within the sand bed. Furthermore, they stated that the pore water pressure response is higher when the degree of saturation is higher. Note that the difference between high saturation and low saturation during the Chowdhury et al. (2006) fifth test is 3% (i.e. 96% to 99%). It should be noted that the sinking test was also performed under low saturation conditions.

Another way of investigating momentary liquefaction is to use solitary waves. Merxhani and Liang (2012) investigated the seabed response to a solitary wave numerically, by solving Biot's equation (Biot, 1941) using a finite element approach. Their work showed that for a horizontal seabed, the solitary wave does not induce momentary liquefaction. Sumer (2014) stated that momentary liquefaction does

not occur by solitary wave, because solitary waves have no troughs. Sumer et al. (2011) measured the pore water pressure under a plunging solitary wave on a slope of 1:14, and found that both the downward pressure gradient and the upward pressure gradient are caused by the delay in sediment response to the fluid loading. They attributed this delay to the infiltration and ex-filtration of pore water into and out of the sediment bed. The Sumer et al. (2011) results show that the downward pressure gradient near the hydraulic jump is highest, but the sediment does not reach liquefaction.

Young et al. (2009) studied the liquefaction potential of coastal slopes under solitary waves using numerical studies for a full-scale simulation of a 10 m solitary wave over a 1:15 and 1:5 sloped beach of fine sand. Young et al. (2009, pg., 17) stated:

The results show that the soil near the bed surface, particularly along the seepage face, is at risk to liquefaction failure. The depth of the seepage face increases and the width of the seepage face decreases with increasing bed slope. The rate of bed surface loading and unloading due to wave run-up and draw-down, respectively, also increases with increasing bed slope. Consequently, the case with the steeper slope is more susceptible to liquefaction failure due to the higher hydraulic gradient. The analysis also suggests that the results are strongly influenced by the soil permeability and relative compressibility between the pore fluid and solid skeleton, and that a coupled solid/fluid formulation is needed for the soil solver. Finally, the results show the

draw-down pore-pressure response is strongly influenced by nonlinear material behavior for the full-scale simulation.

Young et al. (2009) used the hybrid Boussinesq-nonlinear shallow water equations to model the solitary wave, and they also applied a coupled model consisting of balance equations enforcing the conservation of mass and linear momentum for the solid/fluid mixture for the modeling of the porous media. The primary equations Young et al. (2009) used are,

$$\nabla \cdot (\sigma' - \alpha p_e \mathbf{1}) + \rho_b \mathbf{g}, \quad (2.16a)$$

$$\nabla \cdot \frac{\partial \mathbf{u}}{\partial t} + \nabla \cdot \mathbf{q}_v + \frac{\phi}{K_f} \frac{\partial p_e}{\partial t} = 0, \quad (2.16b)$$

where σ' is the effective stress, $\alpha = 1 - K/K_s$ is Biot's coefficient, K is the drained bulk modulus of solid skeleton, K_s is the bulk modulus of the solid constituent, p_e is the excess pore water pressure, ρ_b is the buoyant density of the solid matrix, \mathbf{q}_v is the Darcy velocity, K_f is the effective bulk modulus of the pore-fluid and \mathbf{u} is the displacement of the solid matrix. The effective bulk modulus of the pore-fluid K_f is given by Verruijt (1969), as

$$\frac{1}{K_f} = \frac{1}{K_w} + \frac{1 - S}{p_0}, \quad (2.17)$$

where S is the degree of saturation, p_0 is the absolute fluid pressure, and K_f is the bulk modulus of fluid (i.e., water). Note that the bulk modulus of pure water is large (i.e., ≈ 2.2 GPa). Young et al. (2009) neglected the compressibility of the

solid constituent relative to the bulk skeleton (i.e., $\alpha \approx 1$), and they assumed that the effective modulus for the pore fluid is $K_f = 4$ MPa, which corresponds to 97% saturation (i.e., 3% air in the water). (Young et al., 2009, pg. 20) mentioned that, “If the pore space is absolutely saturated, then the effective bulk modulus of the pore fluid is simply equal to the bulk modulus K_w of pure water (i.e., ~ 2.2 GPa). Even a small amount of entrained air (either as free air or dissolved air) can lead to a drastic reduction in the effective modulus, and cause a large increase in the apparent compressibility of the pore fluid.” The assumption of pure water conditions diminishes the right term in Equation 2.16b, which reduces Equation 2.16 to Terzaghi’s one-dimensional consolidation equation.

Young et al. (2009) used two different soil constitutive models, a linear elastic model and a non-associative Mohr-Coulomb model (Young et al., 2009), to estimate the pore water pressure induced by solitary waves. The results showed that the non-associative Mohr-Coulomb model predicted significantly larger negative pore water pressures with much less dissipation with depth than the linear elastic model. Therefore, Young et al. (2009) showed that the hydraulic gradient for the linear elastic model is higher and the hydraulic gradient penetrates to a shallower depth.

2.3.3 Rapid draw-down in embankment dams

The momentary liquefaction phenomenon is similar to the rapid draw-down condition in the embankment dams (Bishop, 1954), and accordingly, it is instructive to provide a modest background discussion before describing the proposed deforma-

tion model in Chapter 3. The rapid draw-down condition occurs following a long steady-state condition, when the water level upstream or in the dam reservoir is lowered quickly. During rapid draw-down, the pore water pressure in the embankment dam does not have enough time to dissipate completely, and thus, the rapid removal of the water load results in an undrained unloading condition. The condition can be considered undrained, because the unloading process occurs quickly; in contrast, if the unloading occurs gradually, then the condition is drained.

The rapid draw-down condition can be analyzed by two approaches: the total stress method (e.g., Lowe and Karafiath, 1960; Duncan et al., 1990; Fredlund et al., 2011; VandenBerge et al., 2013; VandenBerge, 2014), and the effective stress method. The effective stress method is more relevant when comparing rapid draw-down in embankment dams to tsunami loading, because the pore water pressure changes due to the transient water level are estimated. Methods for predicting the pore water pressure changes during rapid draw-down using the effective stress method are classified into three groups (VandenBerge, 2014): the \bar{B} method, the uncoupled transient seepage analysis, and the fully coupled transient seepage/stress analysis. The fully coupled transient seepage/stress analysis is the most relevant for understanding pore water pressure changes during tsunami loading.

For the total stress method, the undrained strength of the soil is related to the effective stress in the embankment, and the effect of pore water pressure is accounted for in the reduction of undrained strength of the compacted soil (e.g., Lowe and Karafiath, 1960; Duncan et al., 1990; VandenBerge et al., 2013; VandenBerge, 2014). The total stress method is easier to implement in practice, and it

results in more conservative design and consequently higher costs (Fredlund et al., 2011). In the United States, the total stress method is often adopted for the design of dams and levees. Note that rapid draw-down in embankment occurs with the rate of 0.1 m/day to 0.5 m/day (e.g., Alonso and Pinyol, 2009), but tsunami loading (i.e., run-up and draw-down) occurs in few minutes (e.g., Fritz et al., 2012; Yeh and Sato, 2016).

For the \bar{B} method, Bishop (1954) applied the pore water pressure coefficients defined by Skempton (1954) to the problems of determining the effective stress in embankment dams during their construction and during rapid draw-down.

For the uncoupled transient seepage analysis, the pore-pressure is estimated by applying only the hydraulic boundary condition to the system (i.e. the hydraulic boundary condition is the pore water pressure at the soil surface, which is equal to the pressure that is induced from the water depth on the ground surface). For the uncoupled transient seepage analysis the effect of total stress induced by the weight of the tsunami on the soil deformation is neglected.

As an example, Yeh and Mason (2014) used uncoupled transient seepage analysis to estimate the tsunami-induced pore water pressure in soil beds during tsunami run-up and draw-down by neglecting the soil deformation caused by the total stress induced by the overlying tsunami water weight. More specifically, Yeh and Mason (2014) considered the pore water pressure that is induced by diffusion of pore water pressure from the soil surface. To calculate $\partial h/\partial z$ for idealized tsunami loading, Yeh and Mason (2014) considered a soil bed as a homogeneous, elastic halfspace,

and solved the diffusion equation,

$$\frac{\partial p_e}{\partial t} = C_v \frac{\partial^2 p_e}{\partial z^2}, \quad \text{for } z \geq 0, \quad (2.18)$$

where p_e is the excess pore water pressure in the soil bed (i.e., the pore water pressure in excess of the hydrostatic pore water pressure) and C_v is the diffusion coefficient. Equation 2.18 is the same as Terzaghi's one-dimensional consolidation equation (Terzaghi, 1943). By considering the initial condition for $p_e(z, t)$,

$$p_e(z, 0) = 0, \quad (2.19)$$

and the boundary condition,

$$p_e(0, t) = f(t), \quad (2.20)$$

where $f(t)$ is given, in the case examined by Yeh and Mason (2014), as the tsunami wave height-time series, the solution for $p_e(z, t)$ is given by (Carslaw and Jaeger, 1959),

$$p_e(z, t) = \frac{z}{2\sqrt{\pi C_v}} \int_0^t \frac{f(\lambda)}{(t-\lambda)^{2/3}} d\lambda. \quad (2.21)$$

It is apparent from Equation 2.21 that $p_e(z, t)$ calculated by the Yeh and Mason (2014) method only depends on the diffusion coefficient (which is assumed to remain constant) and the tsunami wave height-time series.

Following Equation 2.21, the functional form of $\partial h/\partial z$ given by Yeh and Mason (2014, pg. 136) for the initial condition (Equation 2.19) and boundary condition

(Equation 2.20) is,

$$\begin{aligned} \frac{\partial h}{\partial z} = & \frac{1}{2\sqrt{\pi C_v}} \int_0^t f(\lambda) \frac{\exp[-z^2/4C_v(t-\lambda)]}{(t-\lambda)^{3/2}} d\lambda - \\ & - \frac{z^2}{4C_v\sqrt{\pi C_v}} \int_0^t f(\lambda) \frac{\exp[-z^2/4C_v(t-\lambda)]}{(t-\lambda)^{5/2}} d\lambda. \end{aligned} \quad (2.22)$$

Note that Yeh and Mason (2014) misprinted Equation 2.22 in the original reference, and it is corrected in a *corrigendum* printed on page 757 of the 64th volume of *Géotechnique*, and Yeh and Mason (2014) considered the opposite sign convention for the z -direction than was considered herein, so their form of Equation 2.22 (and Equation 2.21) is slightly different. Clearly, as $z \rightarrow 0$, Equation 2.22 reduces to,

$$\left. \frac{\partial h}{\partial z} \right|_{z=0} \sim \frac{1}{2\sqrt{\pi C_v}} \int_0^t \frac{f(\lambda)}{(t-\lambda)^{3/2}} d\lambda. \quad (2.23)$$

For the fully coupled transient seepage/stress analysis, the effect of total stress changes on the pore water pressure is included. Pariseau et al. (1997), Berilgen (2007), Pinyol et al. (2008) and Alonso and Pinyol (2010) employed the coupled transient analysis to analyze the pore water pressure during rapid draw-down. For a rapid draw-down analysis, it is usually assumed that the dam is initially in a steady state condition, and then sudden rapid draw-down of water occurs. In contrast, tsunami draw-down occurs directly after tsunami run-up, and the pore water pressure in the soil bed always changes during run-up and draw-down. In addition, tsunamis can have large flow heights and can inundate large areas. Accordingly, the water load caused by the tsunami is not negligible and should

be considered in the analysis. Herein, we use the coupled transient seepage/stress analysis to predict the pore water pressure distributions and the excess pore water pressure gradient distributions during tsunami run-up and draw-down.

2.4 Literature synthesis

Many researchers (e.g., Mei and Foda, 1981; Sakai et al., 1991; Gratiot et al., 2000; Liu et al., 2007) have studied the changes in pore water pressure within a soil bed due to wave loading. Table 2.4 shows a summary of some approaches for wave-induced pore water pressure changes in soil beds, and the advantages and disadvantages of each approach. Note that the approaches shown in Table 2.4 were particularly beneficial for the work presented herein.

Several points need to be discussed from previous research regarding the loading of soil beds by a fluid to understand the work presented in Chapters 3 to 6. The first point is related to the difference between the consolidation of sand and clay. For sand, there is no double layer between the soil grains; therefore, the total load of the overlying weight is resisted by the grain-to-grain bonds and the pore water pressure within the medium. In contrast, clay particles are surrounded by double layers, and as a result, clay particles slide on each other during loading.

The second point is related to the Mandel-Cryer effect, which shows that when a total stress is applied to the soil bed, the total stress is not resisted fully by the pore water. In other words, the total stress is shared between the soil skeleton and the pore water after the total stress is applied. For clay, the load resisted by

Table 2.4: Summary of important studies on loading of a soil bed by a fluid.

| Researchers | Approach | Advantages | Disadvantages (assumptions) | Comment |
|-------------------------|--|--|--|----------------------------------|
| Zen and Yamazaki (1990) | Modified Terzaghi equation | Simple and easy to apply total stress effect considered | Uncoupled linear elastic soil skeleton saturated region | Wave induced liquefaction 1-D |
| Young et al. (2009) | Modified Biot (1941) | Coupled linear elastic elastoplastic total stress effect is considered | Saturated region with dissolved air | Solitary wave 2-D |
| Merxhani et al. (2012) | Biot (1941) | Simple coupled linear elastic soil skeleton total stress effect is considered | Linear elastic saturated region horizontal seabed | Wave induced liquefaction 2-D |
| Cheng (2014) | Superposition | Simple and easy to apply coupled total stress effect is considered | Saturated region linear elastic soil skeleton | Rock mechanics 1-D |
| Yeh and Mason (2014) | Terzaghi equation | Simple and easy to apply | Uncoupled linear elastic soil skeleton total stress effect is not considered saturated region | Wave induced liquefaction 1-D |
| Current study | General seepage equation nonlinear stress deformation | Coupled nonlinear and linear soil skeleton total stress effect is considered saturated and unsaturated region | Complicated atmospheric air pressure non-hysteresis SWRC model | 1D-2D |

the pore water is much larger when compared to sand. The preceding observation results from the compressibility of the clay being larger than the compressibility of sand, because of the chemical properties of the clay. Skempton (1984) showed that Terzaghi's effective stress definition is very suitable for clay, but is not applicable for concrete and rock. Note that, Skempton (1984) showed, based on laboratory experiments, that for a dense sand $\alpha \approx 0.998$ (see Table 2.2), which shows that Terzaghi's effective stress model works with the assumption of very slow loading rate and for the tested sand.

The third point is related to experiments, either physical or numerical, investigating the pore water pressure changes in soil beds due to fluid loading. To separate residual liquefaction from momentary liquefaction, it is strongly recommended to model and experiment the loading by a fluid one-dimensionally. Admittedly, in one-dimensional experiments, residual liquefaction occurs simultaneously with momentary liquefaction; however, the effect of residual liquefaction is much less in one-dimensional experiments as compared with two-dimensional experiments. In short, it is experimentally difficult to separate the pore water pressure induced by the residual liquefaction mechanism (cyclic deformation) from the pore water pressure induced by the momentary liquefaction mechanism, and this is especially true when two-dimensional experiments are performed.

To belabor the third point further, for a progressive wave in a flume, the cyclic stress is always applied to the soil bed, and based on the wave amplitude, a very small gradient may be applied because of the momentary liquefaction mechanism. For the standing waves the cyclic deformation is largest under the node and is

smaller under the anti-node. Note that soil bed behavior under the anti-node is similar to soil bed behavior during cyclic triaxial testing. Wave flume results show that for standing wave loading (Kirca et al., 2013) and progressive wave loading (Sumer, 2014), after some time, although the waves are running, only pore water pressure dissipation occurs. The preceding observation is caused by the fact that soil is densified during the wave loading, and Sumer (2014) stated that soil beds that have experienced wave-induced liquefaction have less potential to liquefy (an observations that is very similar to the post-earthquake behavior of soil beds, where the liquefaction potential reduces during subsequent aftershocks). In summary, one-dimensional experiments are the best experiments to model momentary liquefaction.

The fourth point is related to the Chowdhury et al. (2006) one-dimensional experiments, which showed a very important result for the work we present herein. Recall that Chowdhury et al. (2006) found that momentary liquefaction is more likely to occur in dense sand beds rather than loose sand beds. Recall that for the dense sands, the grain-to-grain contact forces are larger; therefore, more of the total load is resisted by the soil skeleton. In addition, Chowdhury et al. (2006) found that the depth of momentary liquefaction increases with the decrease of permeability, saturation, and wave period. The preceding findings are opposite of what is observed during residual liquefaction. The results of the Chowdhury et al. (2006) experiments also support the idea that for progressive wave loading and standing wave loading of a soil bed, the mechanism of sediment instability is predominantly a residual liquefaction mechanism rather than a momentary lique-

faction mechanism. Now consider two-dimensional experiments again. During the two-dimensional experiments, the soil bed is densified, and based on the Chowdhury et al. (2006) results, the potential of momentary liquefaction should increase; however, the two-dimensional flume results do not show any liquefaction after some time.

The fifth point is related to solitary wave loading of soil beds. Recall that Merxhani and Liang (2012) showed that there is no liquefaction within a level seabed subjected to solitary waves. Moreover, Sumer et al. (2011) and Young et al. (2009) experimented on steep slopes, and found that the steeper slopes were more susceptible to liquefaction than the shallower slopes. Accordingly, the preceding results are related to the third point and show that the liquefaction behavior of sloped soil beds is two-dimensional. In addition, Young et al. (2009) stated that the relative compressibility between the pore fluid and the soil skeleton is needed to understand the behavior of sloped soil beds during solitary wave loading, because the load is shared between the soil and fluid with respect to their relative stiffnesses; i.e., the stiffer material gets more load. Note also that the bulk modulus of pure water reduces significantly with few amount of entrapped air in water.

The final point relates to the *alpha* value. When studying the loading of a soil bed by a fluid, the soil bed evidently behaves somewhere within the range of saturated clay-like material to rock-like material. Clay behavior is governed by Terzaghi's effective stress approach (i.e., $\alpha \approx 1$), and in contrast, for rock-like materials, α can be as low as 0.5 (Skempton, 1984; Detournay and Cheng, 1993). With regards to α values, sand behavior is in between clay-like behavior and rock-

like behavior, and the α value for sands depends on the relative density of the sand, the entrained air in the pore water, and the sand particle size.

Chapter 3: Proposed deformation model

Understanding how the pore water pressure changes in a soil bed during tsunami loading requires an understanding of how the soil bed deforms (i.e., a deformation model) and how the overlying water seeps into the soil bed (i.e., a seepage model) during the tsunami loading. In Chapter 3, we aim to describe and discuss the proposed deformation model. The description focuses on the derivation of the proposed deformation model. The discussion focuses on defining the parameters needed for the deformation model, listing the assumptions and limitations of the proposed deformation model, and then showcasing the proposed deformation model performance with some simple examples.

Importantly, as alluded to in the previous paragraph, partial drainage occurs when a soil bed is loaded by a tsunami. Herein, to incorporate the partial drainage scenario into the numerical formulation, the pore water pressure induced by tsunami loading is classified in two parts: 1) the pore water pressure induced by the weight of the overlying tsunami water, and 2) the pore water pressure induced by seepage. Skempton's B value is used to "tune" the model from the undrained condition to the partially drained condition and to the fully drained condition.

3.1 Description

We assume a uni-axial strain condition to model the tsunami-induced deformation of a soil bed (n.b., the axial direction is the z -direction herein). For the fully saturated condition, the constitutive equations linking the total vertical stress to the vertical strain and the total pore water pressure (i.e., the pore water coupled constitutive equation) and linking the total vertical stress to the volumetric water content (i.e., the water content coupled constitutive equation) are given, respectively (Detournay and Cheng, 1993),

$$\sigma = \frac{2G(1 - \nu)}{1 - 2\nu} \epsilon - \alpha p_w, \quad (3.1a)$$

$$\sigma = \frac{2G(1 - \nu_u)}{1 - 2\nu_u} \epsilon - \alpha M \delta\theta_w. \quad (3.1b)$$

In Equation 3.1, ν_u is the undrained Poisson's ratio, G is the soil bed's shear modulus, ϵ is the axial strain, $\delta\theta_w$ is the increment of water content (which shows the variation of fluid volume per unit volume of porous media), and M is Biot's modulus and is the inverse of specific storage coefficient at constant volumetric strain, $\epsilon_{v,}$; i.e.,

$$\frac{1}{M} = \left. \frac{\partial\theta_w}{\partial p_w} \right|_{d\epsilon_v=0}. \quad (3.2)$$

An undrained assumption implies that the pore water pressure changes instantaneously as a function of time during the tsunami loading; i.e., the total stress due to the weight of tsunami water instantaneously transfers to the pore water pressure in the soil below. When the undrained assumption is made, the volumet-

ric water content, $\delta\theta_w$, in Equation 3.1b goes to zero. Because the tsunami run-up and draw-down occurs very quickly, this assumption is justified; however, as it is shown later in this section, the proposed deformation model also incorporates the partial drainage condition. Setting θ_w equal to zero in Equation 3.1b, and then combining Equations 3.1a and 3.1b and solving for p_w yields,

$$p_w = -\frac{B(1 + \nu_u)}{3(1 - \nu_u)}\sigma_{zz}, \quad (3.3)$$

where B is the Skempton's B value, which can be formulated in terms of elastic coefficients from the theory of poroelasticity as (Detournay and Cheng, 1993),

$$B = \frac{3(\nu_u - \nu)}{\alpha(1 - 2\nu)(1 + \nu_u)}. \quad (3.4)$$

What is needed, moving forward, is a deformation model that also works for unsaturated soil conditions. Fredlund et al. (2012, pg. 678) suggested a deformation model for unsaturated soil conditions, which is similar to the Fredlund and Morgenstern (1976) deformation model and ultimately a modification of the Biot (1941) deformation model for saturated soil conditions. The suggested model by Fredlund et al. (2012), which is used to estimate the deformation of an unsaturated soil bed in a uni-axial direction, is given as,

$$\delta\epsilon_v = \frac{(1 + \nu)(1 - 2\nu)}{E(1 - \nu)}\delta(\sigma - p_a) + \frac{(1 + \nu)}{H(1 - \nu)}\delta(p_a - p_w). \quad (3.5)$$

In Equation 3.5, ϵ_v is the volumetric strain, ν is the drained Poisson's ratio,

E is the modulus of elasticity of the soil bed, σ is the total vertical stress, p_a is the pore-air pressure, p_w is the pore water pressure, and $1/H$ is a measure of the compressibility of the soil for a change in water pressure (Biot, 1941). For unsaturated soil conditions, H is the elastic modulus of the soil skeleton with respect to the suction (i.e., matric suction herein). Note that the uni-axial assumption implies that the volumetric strain is the vertical strain. We chose the Fredlund et al. (2012) deformation model as a starting point for our proposed deformation model, because it is a two-state constitutive model, it is applicable for sands, it is relatively simple to implement, and it is closely related to the Biot (1941) poroelasticity equations. Herein, we assume that p_a is equal to zero. Accordingly, Equation 3.5 reduces to,

$$\delta\epsilon_v = \frac{(1 + \nu)(1 - 2\nu)}{E(1 - \nu)}\delta\sigma - \frac{(1 + \nu)}{H(1 - \nu)}\delta p_w. \quad (3.6)$$

Recall, from §2.2.2, that Skempton (1984) investigated the effective stress in soils, concrete, and rock, and he developed a general expression for the effective stress,

$$\sigma' = \sigma - \alpha p_w, \quad (3.7)$$

where α is explained in § 2.2.1. Note that the the effective stress is larger when $\alpha < 1$. In other words, the soil skeleton resists more load when $\alpha < 1$. Considering Equation 3.1 and Equation 3.6 results in,

$$\delta\epsilon_v = \underbrace{\frac{(1 + \nu)(1 - 2\nu)}{E(1 - \nu)}\delta\sigma}_{\text{(A)}} - \underbrace{\frac{\alpha(1 + \nu)}{H(1 - \nu)}\delta p_w}_{\text{(B)}}, \quad (3.8)$$

which yields a smooth transition from saturated condition to unsaturated condition.

From Equation 3.8, it is apparent that as α decreases, the increment of volumetric strain due to the change of pore water pressure also decreases. In fact, for the loading of a porous media by fluid, the \textcircled{A} term is the deformation increment induced by the weight of the fluid, and the \textcircled{B} term is the deformation increment induced by the change of total pore water pressure. Note that the deformation increment induced by \textcircled{A} results in hydrostatic pore water pressure, and the deformation induced by \textcircled{B} results in pore water pressure changes because of total pore water pressure.

Equation 3.8 implies that the entire weight of the overlying water is converted into pore water pressure within the soil bed (i.e., the typical “incompressible water” assumption used by geotechnical engineers when considering the consolidation of fully saturated clays). Accordingly, Equation 3.8 is not an acceptable deformation model when considering tsunami-induced pore water pressure changes in typical beach sands, because the effects of the compressibility of the pore water are not considered (i.e., differing B values are not considered). Therefore, to forward a more general form of deformation model, we have employed Skempton’s B value (Skempton, 1954) to link the change in pore water pressure with the change in total stress on the soil bed due to the overlying water weight. Recall, from §2.2.2, that Skempton’s B value is a function of the bulk moduli of the soil skeleton and the voids.

Therefore, combining Equation 3.8 and 3.3 results in,

$$\boxed{\delta\epsilon_v = \frac{B(1+\nu)(1-2\nu)(1+\nu_u)}{3E(1-\nu)(1-\nu_u)}\delta\sigma - \frac{\alpha(1+\nu)}{H(1-\nu)}\delta p_w}. \quad (3.9)$$

Herein, we use a functional form of H given by Krahn (2004), which is the bulk modulus of the soil skeleton (for the uni-axial saturated assumption),

$$H = \frac{E}{(1-2\nu)}. \quad (3.10)$$

Combining Equation 3.9 with Equation 3.10 yields,

$$\delta\epsilon_v = \frac{(1+\nu)(1-2\nu)}{E(1-\nu)} \left[\frac{B(1+\nu_u)}{3(1-\nu_u)}\delta\sigma - \alpha\delta p_w \right]. \quad (3.11)$$

Furthermore, recalling that $E = 2G(1+\nu)$, where G is the shear modulus of the soil, leads to,

$$\boxed{\delta\epsilon_v = \frac{(1-2\nu)}{2G(1-\nu)} \left[\frac{B(1+\nu_u)}{3(1-\nu_u)}\delta\sigma - \alpha\delta p_w \right]}, \quad (3.12)$$

which is the final functional form of the proposed deformation model with all the simplifying assumptions and appropriate modifications.

Equation 3.12 is the suggested equation for saturated condition. For unsaturated condition, Equation 3.9, which is more general form, is suggested.

3.2 Discussion

3.2.1 Defining model parameters

The final functional form of the proposed deformation model for fully saturated conditions, Equation 3.12, shows that several parameters are needed to define the model; namely, the drained Poisson's ratio, ν , the undrained Poisson's ratio, ν_u , the shear modulus, G , the pore water pressure parameter, B , and the coefficient α . The definitions of α and B are given in §2.2.1 and §2.2.2, respectively.

It should be noted that there are different theories in the field of unsaturated soil mechanics related to the concept of effective stress. Many researchers have studied single state variables to understand unsaturated soil behavior (e.g., Khalili and Khabbaz, 1998; Murray, 2002; Lu and Likos, 2006). Bishop (1959) developed an effective stress model for unsaturated soil, and he defined χ to combine the effects of the net stress, $\sigma - p_a$, with the matric suction, $p_a - p_w$. Similarly, many other researchers have studied two state variables (e.g., Fredlund and Morgenstern, 1977; Alonso et al., 1990; Fredlund et al., 2012), and they believe that both the net stress and the matric suction should be considered as two independent state variables.

Herein, we use Equation 3.9 to estimate tsunami-induced deformation of soil beds, which is written in terms of two independent state variables. Accordingly, the choice of Equation 3.9 for a deformation model informs our choice of a relationship to predict the soil bed's shear modulus or shear moduli.

The shear modulus (and thus, modulus of elasticity) of unsaturated soils is

significantly influenced by matric suction (e.g., Vanapalli et al., 1996; Vanapalli and Mohamed, 2007; Oh et al., 2009). Multiple researchers (e.g., Oh et al., 2009; Sawangsuriya et al., 2009; Vanapalli and Oh, 2010) have presented models for describing the dependence of the shear modulus on state variables. Herein, we use the Sawangsuriya et al. (2009) empirical models. The first empirical model forwarded by Sawangsuriya et al. (2009) is based on the two independent state variables, net stress and matric suction, and is given by,

$$G = A_{uns} f''(e) (\sigma - p_a)^{n_1} + C_{uns} \left(\frac{\theta_w}{\theta_s} \right)^{\kappa''} (p_a - p_w), \quad (3.13)$$

and the second empirical model forwarded by Sawangsuriya et al. (2009) is based on the single independent state variable model, and is given as,

$$G = A_{uns} f''(e) \left[(\sigma - p_a) + \left(\frac{\theta_w}{\theta_s} \right)^{\kappa''} (p_a - p_w) \right]^{n_2}, \quad (3.14)$$

where $f''(e)$ is a void ratio function, which is defined as $(0.3 + 0.7e^2)^{-1}$, and n_1 , n_2 , κ'' , C_{uns} , and A_{uns} are curve fitting parameters. Note that,

$$\sigma' = (\sigma - p_a) + \left(\frac{\theta_w}{\theta_s} \right)^{\kappa''} (p_a - p_w) = (\sigma - p_a) + \chi(p_a - p_w), \quad (3.15)$$

and χ can be expressed as,

$$\chi = \left\{ \frac{1}{1 + [\alpha' (p_a - p_w)]^{n'}} \right\}^{1 - \frac{1}{n'}}, \quad (3.16)$$

where θ_s is saturated water content, α' , and n' are curve fitting parameters. Note that herein G can be calibrated based on either a single independent state variable model or a two independent state variables model. Herein, we chose the single independent state variable model to calibrate G , because it is easier to apply and matches with the fully saturated soil condition models for predicting G (e.g., Hardin and Richart, 1963; Janbu, 1963). Our choice of the single independent state variable model for G does not conflict with our two independent state variable assumption for the proposed deformation model. With the preceding considerations, Equation 3.14 can be simplified to,

$$G = A_{uns} f''(e) (\sigma')^{n_2}. \quad (3.17)$$

Lu and Kaya (2013) incorporated the void ratio function into the coefficient, A_{uns} , and presented the coefficients and curve fitting parameters for a variety of soils, including sand. Accordingly, Equation 3.17 further reduces to,

$$G = A'' (\sigma')^{n_2}. \quad (3.18)$$

Equation 3.17 is similar to the equation given by Hardin and Richart (1963) to calculate the shear modulus of sandy soil, and Equation 3.19 is similar to Janbu tangent modulus defined by Janbu (1963), which is ultimately why we chose the Sawangsuriya et al. (2009) shear modulus model. Herein, we chose $n_2 = 0.5$, which matches the assumption by Hardin and Richart (1963) and Janbu (1963) for sands. Given that $n_2 = 0.5$ for fully saturated soil conditions, the value of A''

in Equation 3.18 can be tuned to develop reasonable shear modulus versus depth profiles. Note that the dimensions on the right side and left side of Equation 3.18 do not match each other. In other words, as shown by Janbu (1963), it is better to normalize the effective stress with a reference stress, σ_r , which we have assumed to be 1 atm to conform with Janbu (1963). Therefore, Equation 3.18 becomes,

$$G = A\sigma_r \left(\frac{\sigma'}{\sigma_r} \right)^{n_2}. \quad (3.19)$$

Herein, we used the guidance of Sawangsuriya et al. (2009) and Lu and Kaya (2013) to select appropriate ranges for A and extend the concept to unsaturated soil conditions. However, the selection of appropriate A values for beach sands, and especially for unsaturated soil conditions, is a topic that deserves future study.

3.2.2 Model assumptions and limitations

The uni-axial strain assumption is a simplification; however, it is an appropriate assumption, because for the case of tsunami loading of an isotropic porous medium, the deformation in the x and y directions is negligible compared to the deformation in the z -direction.

Equation 3.1 is the constitutive relation, reported by Detournay and Cheng (1993), that links the total vertical stress to vertical strain and total pore water pressure. Equation 3.1 is justified for quasi-static processes, as described by Detournay and Cheng (1993); however, herein for the sake of simplicity, we have used

it for dynamic loading (i.e., loading by tsunami). Equation 3.1 is similar to the Biot (1941) poroelasticity equations. To develop Equation 3.1, it is assumed that the solid and fluid phases are fully connected, that the stress and strain relationship is linear and reversible, and that the porous medium is isotropic. In addition, the shear stress between the fluid phase and the solid skeleton as well as the fluid's viscosity are neglected in Equation 3.1.

Multiple researchers (e.g., Tadepalli and Fredlund, 1991; Krahn, 2004; Zhang et al., 2005) have used the deformation model shown in Equation 3.5 to model rainfall-induced soil deformation. Fredlund and Morgenstern (1976) stated that Equation 3.5 can be used for engineering practice; however, Equation 3.5 has some limitations. For example, it is independent of suction, stress history, and time. Note that most deformation models, like the Fredlund et al. (2012) deformation model, are developed for fine-grained soils like clays.

We assume that $p_a = 0$, and the implication of this assumption is that air is not entrapped at the flow front in the soil; therefore, we assume that air entrapment as a pressurized separate region does not affect the soil bed during tsunami loading. Notably, this is a modeling simplification, and it is unclear how much the results of the numerical experimentation presented herein are affected by this simplification. The incorporation of air entrapped within the soil presents significant modeling challenges, and it should be the focus of future research.

The B value is evidently important for our proposed deformation model. In geotechnical laboratories, the B value is estimated for small soil samples in equilibrium conditions and in undrained conditions; e.g., the triaxial compression test.

During triaxial compression testing, high back pressures are used, and when the confining pressure is increased, the experimenter waits for equilibrium conditions to be achieved and then measures the pore water pressure inside the specimen (Bishop and Henkel, 1962). The situation when soil beds are loaded by tsunamis is different from the preceding description of triaxial compression testing; primarily, tsunami loading is transient, the soil bed is large, and partial drainage occurs. However, to reduce complexities, we assume that at each time step, the soil bed is in equilibrium (i.e., the pore water pressure induced by the weight of the overlying tsunami water is applied to the soil bed instantaneously). Also, as an additional simplification, we assume that the tsunami loading occurs relatively rapidly; therefore, we assume that the generation of pore water pressure by the overlying tsunami water weight is an undrained condition.

Defining H for unsaturated soils and for soils other than fully saturated clays is problematic, and to our knowledge, this problem has not received much attention in the soil mechanics and geotechnical engineering literature. We have used Equation 3.10, which defines H as the bulk modulus of the soil skeleton (for the uni-axial assumption). Assuming that Equation 3.10 is valid results in a smooth, continuous functional form of the proposed deformation model when the soil condition changes from fully saturated to unsaturated. However, as stated by Krahn (2004), Equation 3.10 is fundamentally only correct for the fully saturated soil condition. The mechanics of unsaturated soil is notoriously complicated; accordingly, we deem the assumptions needed for Equation 3.10 to hold acceptable, but acknowledge that more work needs to be completed, because the definition of H

is more complex for unsaturated soil conditions (Vu and Fredlund, 2006). However, researchers using SIGMA/W have shown, by comparing their results with the results from Vu and Fredlund (2006), that by assuming that G is function of effective stress reasonable results can be obtained (Geo-Slope, 2013). In addition, Wong et al. (1998) used a similar assumption for H when examining both fully saturated and unsaturated soil conditions.

3.2.3 Model performance

We aim to discuss the proposed deformation model performance for fully saturated conditions in §3.2.3. In Equation 3.12, if $B = 0$,

$$\delta\epsilon_v = -\frac{\alpha(1-2\nu)}{2G(1-\nu)}\delta p_w, \quad (3.20)$$

and no pore water pressure is induced by the overlying tsunami water weight. Notably, as $B \rightarrow 0$, which means that the fluid bulk modulus is negligible compared to the soil bulk modulus. In other words, if the pore fluid is highly compressible (i.e., $K_f/K \ll 1$), then the pore water pressure only changes due to infiltration. Equation 3.20 shows an unrealistic condition, because the pore fluid is highly compressible compared to the soil skeleton, which is not true for the phenomena we examine herein.

Assuming that both the fluid and solid constituents are incompressible (or

$K/K'_s \ll 1$ and $K/K_f \ll 1$) requires that $B = 1$, $\alpha = 1$, and $\nu_u = 0.5$; i.e.,

$$\delta\epsilon_v = \frac{(1 - 2\nu)}{2G(1 - \nu)}(\delta\sigma - \delta p_w), \quad (3.21)$$

which is similar to the undrained condition; therefore, under the preceding condition, the pore water pressure in the soil bed generated by the overlying tsunami water weight is equal to the total stress induced by tsunami (i.e., all the weight of the tsunami load is resisted by the pore fluid phase). In Equation 3.21, the term $(1 - 2\nu)/[2G(1 - \nu)]$ is referred to as the coefficient of volume change, m_v (Lambe and Whitman, 1969). Equation 3.21 is the typical relationship used in geotechnical engineering for estimating the volume change of fully saturated clay subjected to loading. Recall that our focus herein is on a one-dimensional deformation model.

More realistically, the value of B is between zero and one, but closer to one for most sands. In Equation 3.12, as the B value increases, the pore water pressure induced by the weight of the overlying tsunami water increases. In fact, $[B(1 + \nu_u)]/[3(1 - \nu_u)]$ multiplied by the total vertical stress gives the pore water pressure induced by the overlying tsunami water weight.

Finally, note that in the general form, with the effect of air pressure, the proposed deformation model is given as,

$$\delta\epsilon_v = \frac{B(1 + \nu)(1 - 2\nu)(1 + \nu_u)}{3E(1 - \nu)(1 - \nu_u)}\delta(\sigma - p_a) + \frac{\alpha(1 + \nu)}{H(1 - \nu)}\delta(p_a - p_w). \quad (3.22)$$

Future work should focus on Equation 3.22.

Chapter 4: Numerical modeling framework

Recall that understanding how the pore water pressure changes in a soil bed during tsunami loading requires an understanding of how the soil bed deforms (i.e., a deformation model) and how the overlying water seeps into the soil bed (i.e., a seepage model) during the tsunami loading. In Chapter 4, we aim to describe and discuss the seepage model, which is governed by the Richards' equation (Richards, 1931). In addition, we aim to describe and discuss how the seepage model is coupled to the proposed deformation model described in Chapter 3, and how we numerically formulate the coupled seepage-deformation model using a finite difference approach. Throughout Chapter 4, assumptions and known modeling limitations are noted.

4.1 Seepage model

Fluid flow in fully saturated and unsaturated porous media has been the subject of extensive study (e.g., Peaceman, 1977; Helmig, 1997; Lu and Likos, 2004; Fredlund et al., 2012). Herein, we describe the seepage model, which is based on Richards' equation (Richards, 1931). After a brief description of the seepage model, we define the seepage model parameters that we used for the tsunami inundation problem, and we discuss model assumptions and limitations.

4.1.1 Description

The differential equation governing the flow in soil beds (neglecting source or sink terms) can be written as (Richards, 1931),

$$\boxed{\frac{\partial}{\partial t}(\rho\phi S) - \nabla \cdot \left[\frac{\rho k_{ab} k_r}{\mu} (\nabla p_w - \rho g \nabla D) \right]} = 0, \quad (4.1)$$

which is known as Richards' equation and is similar to the equation shown by Peaceman (1977, pg. 16). In Equation 4.1, ρ is the mass density of water, ϕ is the porosity of the porous medium, S is the fluid (water herein) saturation of the porous medium (i.e., the ratio of the volume of water within the voids to the volume of voids, or equivalently, the ratio of the volumetric water content to the porosity), k_{ab} is the absolute permeability of the porous medium, k_r is the relative permeability of the porous medium, μ is the dynamic viscosity of fluid (water herein, μ_w), g is the acceleration due to gravity, D is the depth-of-interest within the porous medium (i.e., for vertical flow, $D = z$), and ∇ is the gradient operator. We assume that $\rho = 1000 \text{ kg/m}^3$, $k_{ab} = 1 \times 10^{-11} \text{ m}^2$ (i.e., a hypothetical value for fine sand), $\mu_w = 1 \times 10^{-3} \text{ Pa}\cdot\text{s}$, and $g = 9.806 \text{ m/s}^2$. How we determine the other model parameters in Equation 4.1 is discussed in §4.1.2.1.

4.1.2 Discussion

4.1.2.1 Defining model parameters

Equation 4.1 is clearly a function of the porosity of the soil bed, ϕ . The increment of porosity is assumed to be equal to the increment of volumetric strain (the limitations of this assumption are explained in §4.2.2), which is estimated with the deformation model explained in Chapter 3. In short, ϕ is the coupling term that connects the deformation model (Equation 3.12) to the seepage model (Equation 4.1).

The value of the degree of saturation, S , in Equation 4.1 changes as a function of the pore water pressure. The change in the degree of saturation is usually defined as a function of the matric suction, $p_a - p_w$, with a soil-water characteristic curve (e.g., Lu and Likos, 2004). Recall that p_a is assumed to be zero herein, so the matric suction is defined as $-p_w$. We have used the van Genuchten (1980) soil-water characteristic curve model to link changes in saturation to changes in matric suction. van Genuchten (1980) presented the following expressions for the soil-water characteristic curve,

$$S_e = \frac{S - S_r}{1 - S_r} = \left\{ \frac{1}{1 + [\alpha I (p_a - p_w)]^{n'}} \right\}^{1-1/n'}, \quad (4.2a)$$

$$\Theta = S_e = \frac{\theta_w - \theta_r}{\theta_s - \theta_r}, \quad (4.2b)$$

where S_r is the residual saturation, S_e is the effective degree of saturation, θ_w is

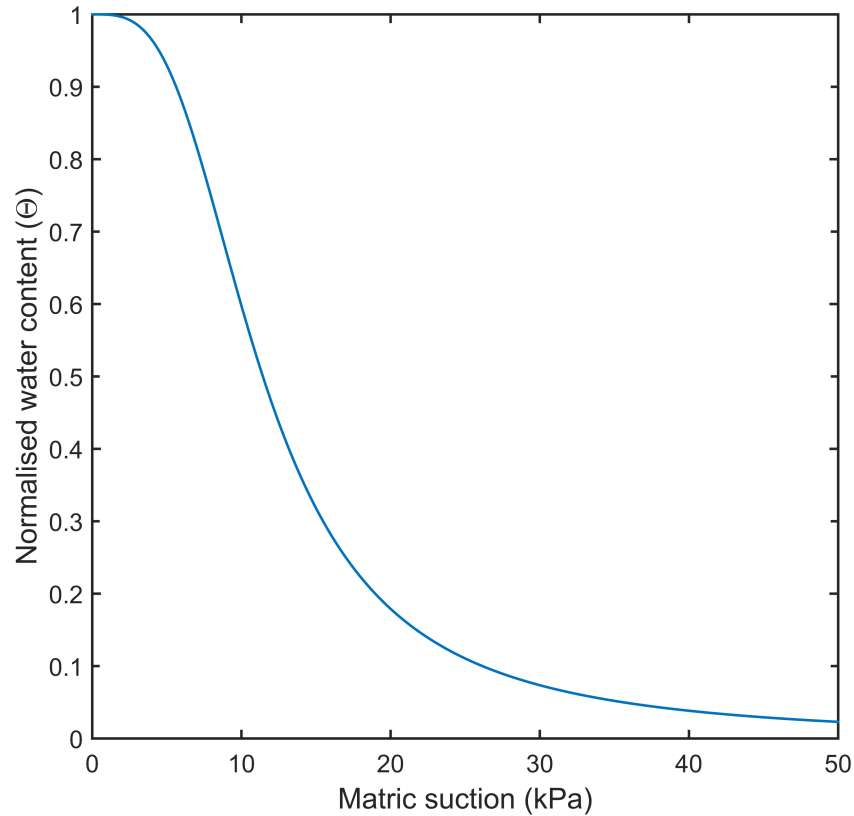


Figure 4.1: The van Genuchten (1980) soil-water characteristic curve developed by Equation 4.2 with $\alpha' = 1.027 \times 10^{-4} \text{ Pa}^{-1}$ and $n' = 3.304$, which are typical model parameters for poorly graded sands (Lu and Likos, 2004), we also assume that $S_r = 0$.

the volumetric water content, θ_r is the residual water content, θ_s is the volumetric water content in the saturated condition, Θ is the normalized water content, α' is the inverse of the air-entry pressure, and n' is the curve fitting parameter. We focus on poorly graded beach sand herein, so $\alpha' = 1.027 \times 10^{-4} \text{ Pa}^{-1}$ and $n' = 3.304$ are selected (Lu and Likos, 2004). Figure 4.1 shows the soil-water characteristic curve generated based on the aforementioned fitting parameters α' and n' .

The relative permeability, k_r , varies between zero (i.e., a dry soil) and one (i.e.,

a fully saturated soil). Herein, we use the van Genuchten (1980) model to estimate the relative permeability,

$$k_r = \frac{\{1 - [\alpha'(p_a - p)]^{n'-1} [1 + (\alpha'(p_a - p))^{n'}]^{-m'}\}^2}{\{1 + [\alpha'(p_a - p)]^{n'}\}^{\frac{m'}{2}}}, \quad (4.3)$$

where $m' = 1 - 1/n'$. Note that Mualem (1976) first derived the relative permeability model, and the relative permeability in the form of Equation 4.3 is suggested by van Genuchten (1980) (developed after van Genuchten (1980) substituted his soil-water characteristic curve into the Mualem (1976) permeability model). Recall that hydraulic conductivity, relative permeability, and intrinsic permeability can be related by,

$$k_h = \frac{\rho g k_i}{\mu_w}, \quad k_i = k_r k_{ab}, \quad (4.4)$$

where k_{ab} is the absolute permeability, k_i is the intrinsic permeability for phase i , k_r is the relative permeability, k_h is the hydraulic conductivity, and μ_w is the dynamic viscosity of the fluid. Figure 4.2 shows the relative permeability curve generated based on the aforementioned fitting parameters α' and n' .

4.1.2.2 Model input assumptions and limitations

Equation 4.1 describes fluid (herein, water) flow through a porous media; however, herein we neglect the air flow through the porous media. In other words, we assume that the air pressure within the porous media is always atmospheric (note that this assumption is consistent with the $p_a = 0$ assumption made for the deformation

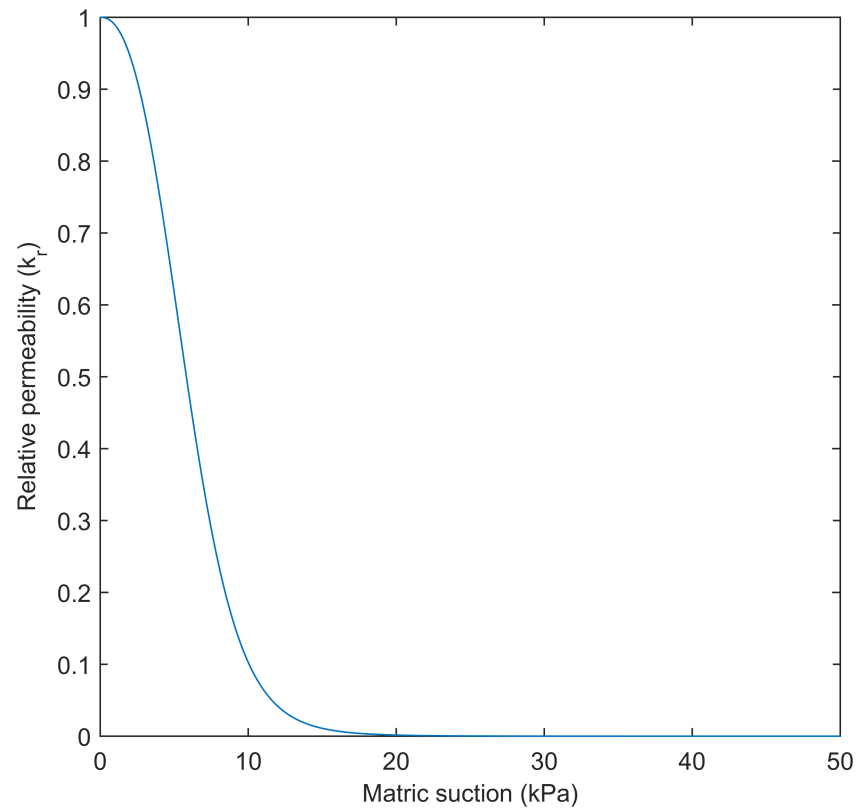


Figure 4.2: The van Genuchten (1980) relative permeability developed by Equation 4.3 with $\alpha' = 1.027 \times 10^{-4} \text{ Pa}^{-1}$ and $n' = 3.304$, which are typical model parameters for poorly graded sands (Lu and Likos, 2004).

model in Chapter 3). The assumption of no air flow is accepted here for the sake of simplicity; however, in reality, air is entrapped in the porous media, and the air pressure within the soil bed is not atmospheric. A similar more general two-phase system needs to be solved for air flow through porous media (e.g., Peszyńska et al., 2002; Lu and Likos, 2004; Peszyńska and Yi, 2008; Fredlund et al., 2012).

In addition to considering the air pressure as atmospheric, we have made other assumptions:

1. Herein, we kept the fluid density constant for the results shown in Chapters 5 and 6; however, the developed numerical formulation of Equation 4.1 easily allows for changes in fluid density. Regardless, incorporating the effects of changes in fluid density is expected to have a negligible effect, because water's bulk modulus is large.
2. It is assumed that fluid flows through the porous skeleton according to Darcy's law (Bear, 1988). Darcy's law is based on experimental observations of one-dimensional water flow through packed sands at low velocity and steady state condition. Notably, fluid flow through porous media deviates from Darcy's law for turbulent flow and high velocity flow (e.g., Firoozabadi and Katz, 1979; Guppy et al., 1982; Martins et al., 1990; Zeng and Grigg, 2006). According to Bear (1988), Darcy's law is valid when the Reynolds number (i.e., $Re = (\rho v_p d_{50}) / \mu_w$, where v_p is the seepage velocity, d_{50} is mean grain diameter, and μ_w is water viscosity) does not exceed values between 1 and 10. Therefore, for the worst case scenario considered herein, $\rho_w = 1000$

kg/m³, $d_{50} = 0.1$ mm, and $\mu_w = 1 \times 10^{-3}$ Pa·s, the maximum hydraulic conductivity is 0.001 m/s, and the maximum pressure head gradient is 2 (i.e., $dh/dz = 2$), then the velocity can be estimated from $v_p = k_h(dh/dz)$ if based on Darcy's law. Therefore, the Reynolds number with the aforementioned assumptions is ≈ 0.2 , which is well within the range that Bear (1988) considers valid for Darcy's law. It must be noted that modest changes to the physical quantities defined above yields the same conclusion; i.e., for the problem of upward seepage caused by tsunami inundation and draw-down, the seepage velocities are well within the validity of Darcy's law. The seepage flow induced by tsunami loading is transient and in reality, a more complex model is needed. However, Mongan (1985) validated the application of Darcy's law to transient flow for most ground water flow conditions. Herein, for the sake of simplicity, we accept Darcy's law.

3. The absolute permeability, k_{ab} , changes as a function of the size of the pores, the porosity, and the tortuosity of the porous medium (Bear, 1988). However, porosity changes within a soil bed are typically small for tsunami loading, so for the sake of simplicity, it is assumed that absolute permeability is constant and does not change with the change of porosity.
4. Realistically, the variation of matric suction during wetting is different from the variation of matric suction during drying (Pham et al., 2005); i.e., the relationship between matric suction and degree of saturation is hysteretic. However, we assume that the variation of matric suction with the degree

of saturation is not hysteretic. We made this assumption for the sake of simplicity; though, as stated in Chapter 3, the effects of entrapped air on the pore water response of soil beds subjected to tsunami loading should be considered in future work.

5. Suction has two components: matric suction and osmotic suction. Osmotic suction is a function of the amount of dissolved salts in the pore water, and matric suction is related to the interaction between the soil matrix, pore air, and pore water (Lu and Likos, 2004; Fredlund et al., 2012). The summation of osmotic suction and matric suction is called the total suction. Herein, we neglect the osmotic suction, so the focus is only on the matric suction, and the soil-water characteristic curve is only a function of the matric suction.
6. In this study a unique soil water characteristic curve is investigated, and the residual saturation is neglected (i.e., $S_r = 0$), which simplifies the soil-water characteristic curve. In addition, we neglect any effects caused by the dissolution of air in water when pore water pressures are high and the evaporation of water when matric suction is high, which simplifies the computations considerably.

4.1.2.3 Model performance

Similar to §3.2.3, in this section we examine the “performance” of Equation 4.1 with a simple example. In this case, we review the assumptions necessary to re-

duce Equation 4.1 to Terzaghi's one-dimensional consolidation equation; i.e., the one-dimensional diffusion equation. By doing this, we will develop an estimate for calculating the coefficient of volume change, m_v , and the coefficient of consolidation, C_v , using the seepage model.

To start, if we assume that the fluid flow is isothermal, then the fluid viscosity and fluid density are constant, and Equation 4.1 reduces to,

$$\frac{\partial(\phi S)}{\partial t} - \nabla \cdot \left[\frac{k_{ab} k_r}{\mu_w} (\nabla p_w - \rho_w g \nabla D) \right] = 0. \quad (4.5)$$

For a fully saturated condition, $S = 1$ and $k_r = 1$; accordingly, Equation 4.5 reduces to,

$$\frac{\partial \phi}{\partial t} - \nabla \cdot \left[\frac{k_{ab}}{\mu_w} (\nabla p_w - \rho_w g \nabla D) \right] = 0. \quad (4.6)$$

Furthermore, assuming that the absolute permeability is constant reduces Equation 4.6 to,

$$\frac{\partial \phi}{\partial t} = \frac{\partial \phi}{\partial p_w} \frac{\partial p_w}{\partial t} = \frac{k_{ab}}{\mu_w} \nabla \cdot (\nabla p_w - \rho_w g \nabla D). \quad (4.7)$$

By neglecting the hydrostatic pressure and the gravity term, Equation 4.7 can be written in terms of the excess pore water pressure, p_e ,

$$\frac{\partial \phi}{\partial p_e} \frac{\partial p_e}{\partial t} = \frac{k_{ab}}{\mu_w} \nabla^2 p_e, \quad (4.8)$$

where the excess pore water pressure is defined as the total pore water pressure minus the hydrostatic pore water pressure. Assuming that the excess pore water pressure only dissipates in one-dimension (i.e., the z -direction) reduces Equation 4.8

to,

$$\frac{\partial \phi}{\partial p_e} \frac{\partial p_e}{\partial t} = \frac{k_{ab}}{\mu_w} \frac{\partial^2 p_e}{\partial z^2}. \quad (4.9)$$

The hydraulic conductivity, k_h , is equal to,

$$k_h = \frac{\rho_w g k_{ab}}{\mu_w}. \quad (4.10)$$

Note that the subscript ‘‘h’’ denotes the hydraulic conductivity and not specifically the horizontal or vertical hydraulic conductivity. Accordingly, Equation 4.9 can be written as,

$$\frac{\partial \phi}{\partial p_e} \frac{\partial p_e}{\partial t} = \frac{k_h}{\rho_w g} \frac{\partial^2 p_e}{\partial z^2}. \quad (4.11)$$

Herein, we assume that the porosity, ϕ , is defined based on the initial total volume of the soil, V_{T0} ; accordingly, Equation 4.11 reduces to,

$$\frac{\partial V_v}{V_{T0} \partial p_e} \frac{\partial p_e}{\partial t} = \frac{k_h}{\rho_w g} \frac{\partial^2 p_e}{\partial z^2}. \quad (4.12)$$

If the volume changes within the solid phase is neglected (i.e., there is no deformation of the sand grains), then Equation 4.12 further reduces to,

$$\frac{\partial(eV_s)}{V_{T0} \partial p_e} \frac{\partial p_e}{\partial t} = \frac{V_s}{V_{T0}} \frac{\partial e}{\partial p_e} \frac{\partial p_e}{\partial t} = \frac{k_h}{\rho_w g} \frac{\partial^2 p_e}{\partial z^2}. \quad (4.13)$$

From soil mechanics, $V_s = V_{T0}/(1 + e_0)$, where e_0 is the initial void ratio; therefore,

$$\frac{1}{1 + e_0} \frac{\partial e}{\partial p_e} \frac{\partial p_e}{\partial t} = \frac{k_h}{\rho_w g} \frac{\partial^2 p_e}{\partial z^2}, \quad (4.14)$$

where $\partial e/\partial p_e$ is equivalent to the coefficient of compressibility, a_v , (Taylor, 1948) for the assumptions outlined in §4.1.2.3.

The coefficient of consolidation, C_v , is defined as (Terzaghi, 1943),

$$C_v = \frac{k_h(1+e)}{a_v\rho_w g}. \quad (4.15)$$

Note that as the excess pore water pressure dissipates the load transfers from the pore water to the soil skeleton (i.e. $\Delta p_e = -\Delta\sigma'_z$, where σ'_z is the effective stress in the z -direction). Equation 4.15 is the familiar form of the coefficient of consolidation in geotechnical engineering (Taylor, 1948). The coefficient of volume compressibility, m_v , is defined as $m_v = a_v/(1+e_0)$; therefore, Equation 4.15 reduces to,

$$C_v = \frac{k_h}{m_v\rho_w g}. \quad (4.16)$$

Note that comparing Equation 4.16 with 4.11 shows that $m_v = \partial\phi/\partial p_e$ for the foregoing assumptions.

Note that Equation 4.16 is routinely given in classical soil mechanics textbooks (e.g., Taylor, 1948). Herein, based on Equation 3.12, for fully saturated soil conditions, we write the coefficient of volume compressibility, m_v , as,

$$m_v = \frac{\alpha(1+\nu)(1-2\nu)}{E(1-\nu)}. \quad (4.17)$$

Furthermore, from the theory of elasticity (Detournay and Cheng, 1993), the value

of α is given as,

$$\alpha = \frac{3(\nu_u - \nu)}{B(1 - 2\nu)(1 + \nu_u)}. \quad (4.18)$$

Therefore, from Equation 4.16 the coefficient of consolidation can be estimated as,

$$C_v = \frac{k_h E(1 - \nu)B(1 + \nu_u)}{3\rho g(1 + \nu)(\nu_u - \nu)}. \quad (4.19)$$

Equation 4.19 shows the general form of coefficient of consolidation. If we assume that $B = 1$ and $\nu_u = 0.5$, then Equation 4.19 reduces to (Lambe and Whitman, 1969),

$$C_v = \frac{k_h E(1 - \nu)}{\rho g(1 + \nu)(1 - 2\nu)}, \quad (4.20)$$

which is similar to the coefficient of consolidation given in classical soil mechanics textbooks (e.g., Taylor, 1948) for a fully saturated clay.

4.2 Coupled seepage-deformation model

4.2.1 Description

The coupled seepage-deformation model is primarily defined by the proposed deformation model (Equation 3.12) and the seepage model (Equation 4.1). Figure 4.3 schematically shows the coupled seepage-deformation model.

The modeling parameters for the proposed deformation model, Equation 3.12, are determined as follows,

- The drained Poisson's ratio, ν , is assumed to be 0.3, which is a typical value

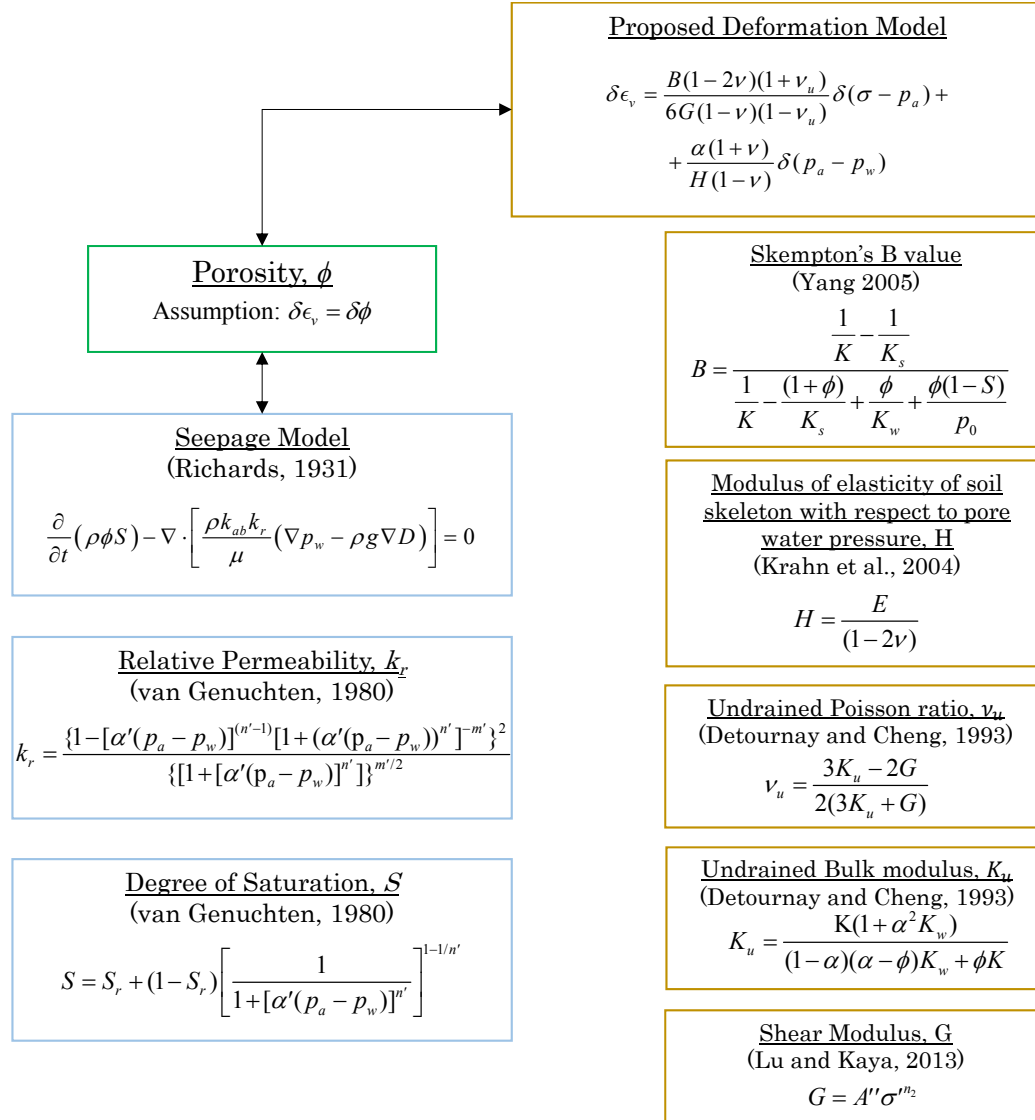


Figure 4.3: A schematic of the seepage-deformation model.

for sand experiencing significant loading (Lambe and Whitman, 1969);

- The bulk modulus of the soil grains, K_s , is assumed to be 36 GPa (Stoll and Kan, 1981);
- The shear modulus, G , is estimated using Equation 3.17, and for the linear soil constitutive model, G is assumed to be a constant value (i.e., $G = 35$ MPa);
- The modulus of elasticity, E , is estimated by $E = 2G(1 + \nu)$, and for the linear soil constitutive model, E is a constant value (i.e., $E = 91$ MPa);
- The B value is estimated from Equation 2.13 (when required, sometimes the B value is manually selected);
- The soil bed's bulk modulus, K , is estimated from Equation 2.8;
- The parameter α is estimated from Equation 2.7;
- The undrained bulk modulus, K_u , is estimated using the functional form from Detournay and Cheng (1993), which is based on the theory of elasticity; i.e., $K_u = [K(1 + \alpha^2 K_f)] / [(1 - \alpha)(\alpha - \phi)K_f + \phi K]$; and,
- The undrained Poisson's ratio, ν_u , is estimated using the functional form from Detournay and Cheng (1993), which is based on the theory of elasticity; i.e., $\nu_u = (3K_u - 2G) / [2(3K_u + G)]$.

The modeling parameters for the seepage model, Equation 4.1, are determined as follows,

- The parameters ρ_w , k_{ab} , μ_w , g , and D are modeling constants, and recall from §4.1.1 that $\rho_w = 1000 \text{ kg/m}^3$, $k_{ab} = 1 \times 10^{-11} \text{ m}^2$, $\mu_w = 1 \times 10^{-3} \text{ Pa}\cdot\text{s}$, and $g = 9.806 \text{ m/s}^2$;
- The relative permeability, k_r , is estimated from Equation 4.3;
- The degree of saturation, S , and the matric suction, $-p_w$, are estimated from Equation 4.2; and
- **The porosity, ϕ , is calculated from Equation 3.12.**

Note that the last bullet item is bold, because it is the critical link that couples the seepage model and the proposed deformation model. When the pore fluid is de-aired water, the fluid bulk modulus is equal to the de-aired water bulk modulus and when the pore fluid is aired water, the fluid bulk modulus is equal to the aired water bulk modulus.

4.2.2 Assumptions and limitations

As mentioned in §4.1.2.1, the seepage model (Equation 4.1) and the deformation model (Equation 3.12) are coupled by the porosity, ϕ . Recall that the coupling requires a fundamental assumption: that the increment of volumetric strain, $\delta\epsilon_v$ (calculated with the deformation model, Equation 3.12) is equal to the increment of porosity, $\delta\phi$ (inputted into the seepage model, Equation 4.1). Note that volumetric strain is defined as the ratio of volume change to the initial volume of soil (i.e.,

$\epsilon_v = V_v/V_{T0}$, and $\delta\epsilon_v = \delta V_v/V_{T0}$), so in terms of porosity,

$$\delta\phi = \frac{\delta V_v V_T - \delta V_T V_v}{V_T^2} = \frac{\delta V_v}{V_T} - \frac{\delta V_T V_v}{V_T^2} = \frac{\delta V_v}{V_T} - \frac{\phi \delta V_T}{V_T}. \quad (4.21)$$

From soil mechanics, $V_s = V_T/(1 + e)$; accordingly, with the assumption that $\delta V_T = \delta V_v$, the increment of porosity becomes,

$$\delta\phi = \left(\frac{1 - \phi}{V_T} \right) \delta V_v = \frac{1}{(1 + e)^2} \frac{\delta V_v}{V_s} = \frac{\delta e}{(1 + e)^2}. \quad (4.22)$$

The difference between the assumption that we make (i.e., $\delta\phi = \delta\epsilon_v$) and the more realistic condition is that we consider the variation of volume change with respect to the initial volume of the soil bed and not the instantaneous volume of the soil bed. Further, the assumption $\delta\phi = \delta\epsilon_v$ implies that,

$$\delta e = \frac{\delta V_v}{V_s} = \frac{\delta V_v(1 + e)}{V_{T0}} = \delta\epsilon_v(1 + e), \quad \therefore \quad \delta\epsilon_v = \frac{\delta e}{(1 + e)}. \quad (4.23)$$

Accordingly, the $\delta\phi = \delta\epsilon_v$ assumption is consistent with the typical assumption used in soil mechanics when examining the volume change behavior of soils (Terzaghi, 1943).

Recall, from §2.3.1, that during progressive wave and standing wave loading, the pore water pressure in a soil bed also increases because of cyclic deformation. Herein, we neglect the cyclic deformation within the soil bed induced by the tsunami; accordingly, we ignore residual liquefaction and we focus only on momentary liquefaction. For long waves, like tsunamis, the preceding assumption is

acceptable, because the tsunami wave frequency is small, and as a consequence, the pore water pressure induced by cyclic deformation within the soil bed is also small. Note that herein, we also neglect the shear stress induced by the flow.

4.3 Numerical formulation

Developing solutions to estimate the tsunami-induced pore water pressure changes in unsaturated or fully saturated porous media requires an efficient numerical formulation. Herein, we use a finite difference approach to solve Equation 4.1. The finite difference approach is first developed for the one-dimensional case. The solution algorithm is then modified to couple the deformation model, as described in §4.2. Note that the numerical formulation is extended, in a simple way, to the two-dimensions, in §6.7.

Numerical solutions for Equation 4.1 have been extensively developed and documented within the engineering, geosciences, and applied mathematics literature, among other fields. Herein, we use a fully implicit cell-centered finite difference approach described by Peaceman (1977) and Helmig (1997) and further developed by Peszyńska et al. (2002) and Peszyńska and Yi (2008) to solve Equation 4.1, and we implement the solution in MATLAB. A graphical depiction of the solution algorithm is given in Figure 4.4. Although many researchers have solved Equation 4.1 (e.g., Zarba et al., 1990; Woodward and Dawson, 2000), and its solution is implemented in many commercial software packages, such as GeoStudio and Comsol, we can not directly use the the other solutions, because we need to couple

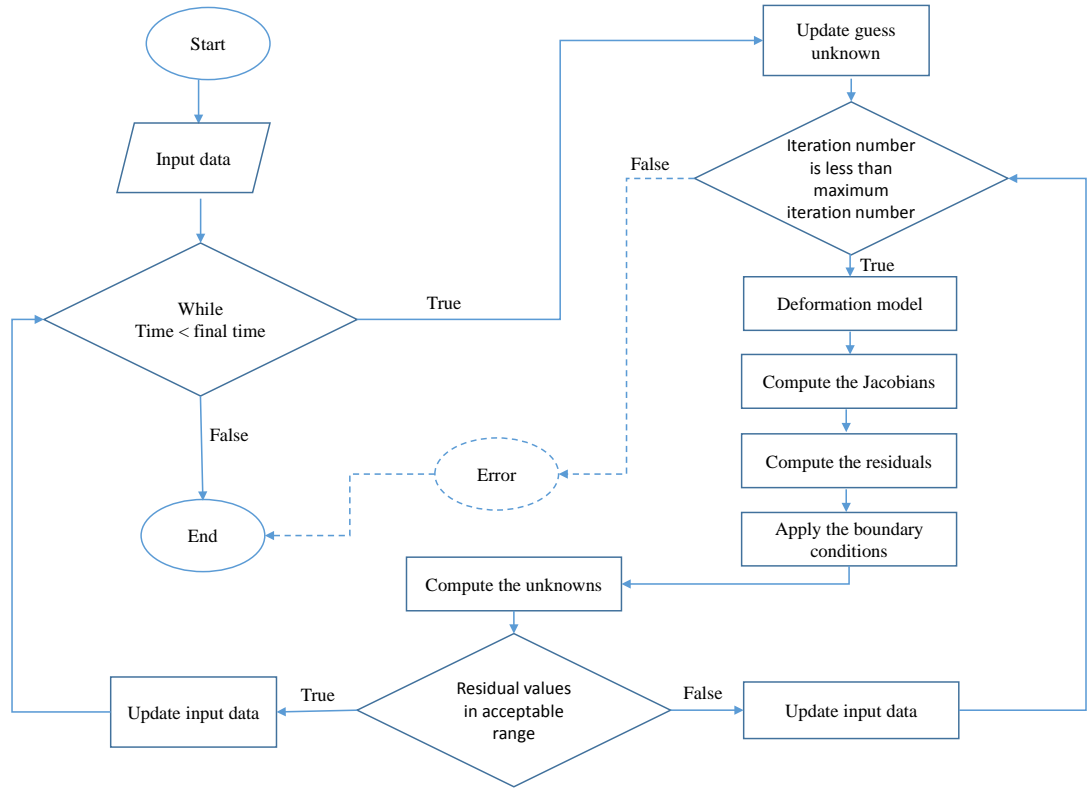


Figure 4.4: Algorithm for the fully implicit cell-centered finite difference approach used to solve Equation 4.1.

Equation 4.1 with the proposed deformation model, and the other solutions do not explicitly consider the boundary and initial conditions required for tsunami loading (i.e., the solutions have not been analyzed outside of smooth regimes).

To understand the solution algorithm shown in Figure 4.4, it is first instructive to understand the physical process that is being modeled. At the initial condition, the water table can be at the ground surface or below. Then the tsunami inundation occurs. During tsunami inundation, the ground surface experiences relatively high pore water pressure; therefore, saturation starts from the ground

surface. With respect to the soil bed, there are two two limiting initial conditions: 1) the fully saturated soil condition, and 2) the unsaturated soil condition where the matric suction within the soil bed is large. When the soil bed is fully saturated, or if the degree of saturation of the soil bed is relatively high, then Equation 4.1 can be solved by assuming that the pore water pressure is the primary unknown. Conversely, when the degree of saturation is small, Equation 4.1 can be solved by assuming that the degree of saturation is the primary unknown.

The first step of the solution algorithm, as shown in Figure 4.4, is selecting the number of grids, the time step, the time range, the method of averaging, the type of boundary conditions, the values of the boundary conditions, and the primary unknown (or automatic status), and then defining the initial condition. At the initial time, the soil properties — such as soil porosity, soil-water characteristic curve fitting parameters, hydraulic conductivity, and total stress at the initial condition — are defined and computed.

As mentioned previously, the initial condition can be defined based on either the pore water pressure or the degree of saturation, which can be estimated from each other from the soil-water characteristic curve shown in Figure 4.1 (n.b., when the soil bed is fully saturated, the pore water pressure cannot be estimated from the degree of saturation, because the degree of saturation is 100%). The choice of solving for pressure or saturation can be applied automatically to the solution algorithm.

To perform the computations, the spatial domain must be defined, and it is discretized by a uniform grid of size Δz , with cell centers denoted by z_j . The

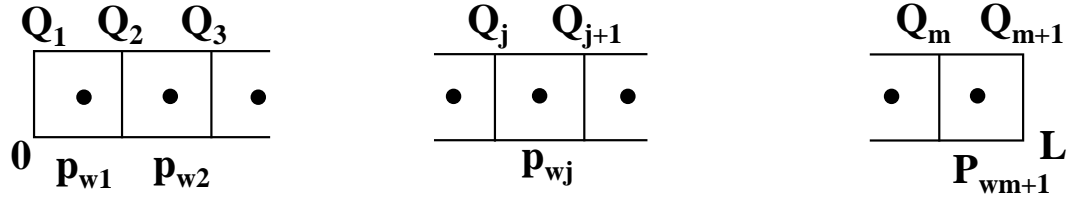


Figure 4.5: Graphical depiction of the finite difference cell centered spatial domain.

subscript j defines the assigned cell number and is $j = 1, \dots, mz$. The spatial domain is depicted graphically in Figure 4.5. The time domain is also discretized into subintervals of variable size ΔT_n , where $n = 1, \dots, N$ and N is the total number of time steps.

After all the input data are defined, the computations are performed for the defined time range. At the initial time step, the “guess unknowns” are equal to the values from the initial conditions. For subsequent time steps, the guess values are equal to the guess values from the previous time step. Accordingly, at each time step, the iterative computations begin. If the number of iterations is greater than the maximum defined limit, then “Error” is printed and the algorithm ends without acceptable results (i.e., the residual values are not within an acceptable range). If the number of iterations is less than the maximum defined limit, then the computations continue. Based on the updated guess values from the previous time step or the previous iteration, the hydraulic conductivity (and the related Jacobians), either degree of saturation or pore water pressure (and related Jacobians), and porosity (and related Jacobians) are computed. Then, the entire matrix of Jacobians and matrix of residuals are calculated. The Jacobians are computed analytically. For instance, when pore water pressure is the primary unknown, the

Jacobians, J , are calculated as,

$$J = \left(\frac{\partial R_j}{\partial p_{w,j}}, \frac{\partial R_j}{\partial p_{w,j+1}}, \frac{\partial R_j}{\partial p_{w,j-1}} \right), \quad (4.24)$$

where R is the residual value, which is calculated as,

$$R = \frac{(\rho_{w_j} \phi_j S_j)^n - (\rho_{w_j} \phi_j S_j)^{n-1}}{\Delta t} - \frac{1}{\Delta z_j} [Q_{j+1/2}^n - Q_{j-1/2}^n] = 0, \quad (4.25a)$$

$$Q_{j+1/2}^n = \rho_{w_{j+1/2}} k_{r_{j+1/2}} T_{j+1/2} [p_{w_{j+1}}^n - p_{w_j}^n - \rho_{w_{j+1/2}} g (D_{j+1} - D_j)], \quad (4.25b)$$

$$Q_{j-1/2}^n = \rho_{w_{j-1/2}} k_{r_{j-1/2}} T_{j-1/2} [p_{w_j}^n - p_{w_{j-1}}^n - \rho_{w_{j-1/2}} g (D_j - D_{j-1})], \quad (4.25c)$$

and the transmissibility, T , functions are computed as,

$$T_{j+1/2} = \frac{2}{\frac{\Delta z_j}{kvis_j} + \frac{\Delta z_{j+1}}{kvis_{j+1}}}, \quad (4.26a)$$

$$T_{j-1/2} = \frac{2}{\frac{\Delta z_j}{kvis_j} + \frac{\Delta z_{j-1}}{kvis_{j-1}}}, \quad (4.26b)$$

$$kvis = \frac{k_{ab}}{\mu_w}. \quad (4.26c)$$

Two types of boundary conditions are considered: the Neumann boundary condition, and 2) the Dirichlet boundary condition. For the Neumann boundary condition, the pore water flow at the boundary is specified. For this problem, no flow is allowed at the impermeable boundary, so $\partial p_w / \partial z$ at the impermeable layer

is zero. For the Dirichlet boundary condition, the value of the pore water pressure or the degree of saturation is defined at the boundary. For instance, for this problem, the pore water pressure (in terms of head) at the ground surface, $z = 0$, is equal to the height of the tsunami. Notably, the aforementioned Jacobian and residual matrices do not include the effects of the boundary conditions. Therefore, the Jacobians and residual values at the boundaries are calculated and are added to the matrices at the appropriate indices; more specifically, at the boundaries (1) and $(nx + 1)$,

$$T(1) = \frac{2}{\frac{\Delta z_1}{kvis_1}}, \quad (4.27a)$$

$$T(mz + 1) = \frac{2}{\frac{\Delta z_{nx}}{kvis_{mz}}}. \quad (4.27b)$$

After the Jacobian and residual matrices are built, the guess unknowns are calculated. If the residual values are within an acceptable range, which is defined by the user, then the computed values are the final results for the time step and the values are used as initial guess values for the next time step. If the residual values are not within an acceptable range, then at least one more iteration is needed. Note that at each iteration, all the important values — such as hydraulic conductivity, pore water pressure, degree of saturation, and total stress — are updated. Based on the preceding discussion, at each iteration the fundamental computations are

$$\text{Jacobian}(R)^{itr} \delta^{itr} = -R^{itr}, \quad (4.28)$$

which is solved for δ , and

$$p_w^{itr} = \delta^{itr} + p_w^{itr-1}. \quad (4.29)$$

Notably, when the primary unknown is the degree of saturation, the computations are analogous.

When performing the computations, the harmonic average was used to define the values of absolute permeability and dynamic viscosity for each cell at each iteration during each time step (Equation 4.26). Similarly, arithmetic averaging was used to estimate the average density for each cell at each iteration during each time step as,

$$\rho_{w_{j+1/2}} = \frac{\rho_{w_j} + \rho_{w_{j+1}}}{2}, \quad (4.30a)$$

$$\rho_{w_{j-1/2}} = \frac{\rho_{w_{j-1}} + \rho_{w_j}}{2}. \quad (4.30b)$$

Either arithmetic averaging or upwinding averaging can be used to handle the edge nonlinearities for the permeability. If arithmetic averaging is used, then,

$$k_{r_{j+1/2}} = \frac{k_r(S_j^n) + k_r(S_{j+1}^n)}{2}, \quad (4.31a)$$

$$k_{r_{j-1/2}} = \frac{k_{r_{j-1}} + k_{r_j}}{2}. \quad (4.31b)$$

If the upwinding averaging is used, then the methodology is more complex. If the potential difference,

$$p_w^n_{j+1} - p_w^n_j - \rho_{w_{j+1/2}} g, (D_{j+1} - D_j), \quad (4.32)$$

is negative, which means that the pore water flow is from the left to the right in Figure 4.5, then the upwinding average is,

$$k_{rj+1/2} = k_r(S_j^n). \quad (4.33)$$

In contrast, if Equation 4.32 is positive, which indicates that the pore water flow is from the right to the left in Figure 4.32, then the upwinding average is,

$$k_{rj+1/2} = k_r(S_{j+1}^n). \quad (4.34)$$

Peszyńska and Yi (2008) stated that the upwinding averaging method is more generally applicable (i.e., to multiple rock types with different compressibilities), and it provides additional stability; however, the upwinding averaging method is associated with a lower likelihood of numerical convergence.

Chapter 5: Numerical experimentation

One of our overarching objectives, as stated in Chapter 1, is to use the coupled seepage-deformation model we created to perform numerical experimentation using hypothetical, but realistic, tsunami loading and soil models. In Chapter 5, we first describe the tsunami models, the soil models, and the experimental plan. Then, we present the results of the numerical experiments. Notably, the presented results are focused on two saturation conditions (fully saturated and unsaturated) and two soil constitutive models (linear and nonlinear).

In Chapter 5, we rely on numerical descriptions of total pore water pressure, p_w , and excess pore water pressure head gradient, $\partial h/\partial z$. Note that the total pore water pressure, p_w , is the summation of the hydrostatic pore water pressure and any excess pore water pressure caused by the tsunami loading. Herein, whenever we mention pore water pressure, we mean total pore water pressure and whenever we mention pore water pressure head gradient, we mean excess pore water pressure head gradient, unless otherwise noted. Recall that the z -direction is defined vertically, with $z = 0$ at the ground surface and the positive z -direction being downward (i.e., into the soil bed). The value of total pore water pressure, p_w is always reported as a positive value, and based on the definition of the z -direction, negative $\partial h/\partial z$ values indicate infiltration of water into the soil bed, and positive $\partial h/\partial z$ values indicate ex-filtration of water out of the soil bed.

5.1 Hypothetical tsunami waveforms

The hypothetical tsunami is generated using the solution to the nonlinear shallow-water wave equations given by Carrier et al. (2003). To create the hypothetical tsunami, we implemented the Carrier et al. (2003) solution. Given the importance of the tsunami loading to the pore water pressure response of the hypothetical soil beds investigated in Chapter 5, we briefly describe the Carrier et al. (2003) method below.

For a plane beach with slope of ψ , the nonlinear shallow water wave equations are, (e.g., Stoker, 1957; Whitham, 1974),

$$\frac{\partial \eta}{\partial t} + \frac{\partial}{\partial x}[v(x\psi + \eta)] = 0, \quad (5.1a)$$

$$\frac{\partial v}{\partial t} + v \frac{\partial v}{\partial x} + g \frac{\partial \eta}{\partial x} = 0, \quad (5.1b)$$

where v is the depth averaged horizontal velocity in the x -direction, and η is the water surface departure from its quiescent position. The x -direction runs in the onshore-offshore direction, and the origin is at the quiescent shoreline, with the positive x -direction pointing offshore. Carrier et al. (2003) used the non-dimensional parameters,

$$\hat{v} = \frac{v}{\sqrt{g\psi L}}, \quad \hat{\eta} = \frac{\eta}{\psi L}, \quad \hat{x} = \frac{x}{L}, \quad \hat{t} = t \sqrt{\frac{\psi g}{L}}, \quad (5.2)$$

where L is the length scale and can be assumed as the distance from the shoreline to the middle of the initial wave condition (i.e., Gaussian wave here), and $\hat{(\)}$

are the dimensionless parameters. Using the non-dimensional parameters defined in Equation 5.2, Carrier et al. (2003) rewrote the nonlinear shallow water wave equations as,

$$\frac{\partial \hat{\eta}}{\partial \hat{t}} + \frac{\partial}{\partial \hat{x}} [\hat{v}(\hat{x} + \hat{\eta})] = 0, \quad (5.3a)$$

$$\frac{\partial \hat{v}}{\partial \hat{t}} + \hat{v} \frac{\partial \hat{v}}{\partial \hat{x}} + \frac{\partial \hat{\eta}}{\partial \hat{x}} = 0. \quad (5.3b)$$

Using further transformation, the nonlinear shallow wave equations are written in the form,

$$\frac{\partial}{\partial \hat{q}} (\hat{q}\hat{v}) + \frac{\partial}{\partial \hat{\Lambda}} \left(\hat{\eta} + \frac{\hat{v}^2}{2} \right) = 0, \quad (5.4a)$$

$$\frac{\partial \hat{v}}{\partial \hat{\Lambda}} + \frac{\partial}{\partial \hat{q}} \left(\hat{\eta} + \frac{\hat{v}^2}{2} \right) = 0, \quad (5.4b)$$

where,

$$\hat{\Lambda} = \hat{t} - \hat{v}, \quad \hat{\xi}^2 = \hat{q} = \hat{x} + \hat{\eta}. \quad (5.5)$$

Finally, Carrier et al. (2003) showed that Equation 5.4 can be transformed further to produce the cylindrical wave equation,

$$4\hat{\xi} \frac{\partial^2 \hat{\zeta}}{\partial \hat{\Lambda}^2} - \frac{\partial}{\partial \hat{\xi}} \left(\hat{\xi} \frac{\partial \hat{\zeta}}{\partial \hat{\xi}} \right) = 0, \quad (5.6)$$

where

$$\frac{\partial \hat{\zeta}}{\partial \hat{\Lambda}} = \hat{\eta} + \frac{\hat{v}^2}{2}, \quad (5.7a)$$

$$\hat{u}_1 = -\frac{1}{2\hat{\xi}} \frac{\partial \hat{\zeta}}{\partial \hat{\xi}}, \quad (5.7b)$$

$$\hat{\eta} = \frac{\partial \hat{\zeta}}{\partial \hat{\Lambda}} - \frac{1}{8\hat{\xi}^2} \left(\frac{\partial \hat{\zeta}}{\partial \hat{\xi}} \right)^2. \quad (5.7c)$$

Carrier et al. (2003) gave the following solution to the Equation 5.6,

$$\hat{\zeta}(\hat{\xi}, \hat{\Lambda}) = 2 \left[\int_0^\infty \hat{F}_1(b) \hat{G}_1(b, \hat{\xi}, \hat{\Lambda}) db + \int_0^\infty \hat{P}_1(b) \frac{\partial \hat{G}_1(b, \hat{\xi}, \hat{\Lambda})}{\partial \hat{\Lambda}} db \right]. \quad (5.8)$$

In Equation 5.8, $\hat{F}_1(b)$ and $\hat{P}_1(b)$ are the initial conditions, and $\hat{G}_1(b, \hat{\xi}, \hat{\Lambda})$ is the Green function developed by Carrier et al. (2003).

For the hypothetical tsunami, we assume that the initial wave shape is Gaussian with initial zero velocity [i.e., Figure 3 in Carrier et al. (2003, pg. 84)]; thus,

$$\hat{F}_1(b) = a_0 \exp[-k_g(b^2 - b_0^2)^2], \quad \hat{P}_1(b) = 0, \quad (5.9)$$

where $a_0 = 0.017$, $b_0 = 1.3$, and $k_g = 4.0$ (Carrier et al., 2003, pg. 83).

Equation 5.8 is solved with the Gaussian wave initial conditions (Equation 5.9) to yield $\hat{\zeta}(\hat{\xi}, \hat{\Lambda})$. The solution, $\hat{\zeta}(\hat{\xi}, \hat{\Lambda})$, is then converted to the physical, but non-dimensional, $\hat{x} - \hat{t}$ domain by computing the partial derivatives $\partial \hat{\zeta} / \partial \hat{\xi}$ and $\partial \hat{\zeta} / \partial \hat{\Lambda}$, computing \hat{u} and $\hat{\eta}$ with Equation 5.7, and computing \hat{x} and \hat{t} with Equation 5.5. Evidently, the transformation from the user-chosen $\hat{\xi} - \hat{\Lambda}$ domain to the $\hat{x} - \hat{t}$ domain is nonlinear, which creates difficulties in determining final tsunami flow heights and tsunami flow velocities. The difficulties are exacerbated near the shoreline ($\hat{x} = 0$), because the Jacobians used for the transformation of Equation 5.3 to Equation 5.4

approach zero. The transformation between the $\hat{\xi} - \hat{\Lambda}$ and the $\hat{x} - \hat{t}$ domain, in terms of tsunami flow height for the Gaussian wave, is shown in Figure 4 and Figure 5 of Carrier et al. (2003, pg. 85).

Notwithstanding the aforementioned difficulties, Figure 5.1a shows the dimensionless tsunami flow height-time series at the shoreline ($\hat{x} = 0$) for the hypothetical tsunami. The dimensionless tsunami-flow height-time series was smoothed with a median filter, but it still has some irregularities, which impact the results shown in § 5.4 and Chapter 6 — especially when the pore water pressure head gradient is investigated.

Figure 5.1b shows the dimensioned tsunami flow height-time series at the shoreline ($x = 0$ m) for the hypothetical tsunami. Figure 5.1a was dimensioned using Equation 5.2 to create Figure 5.1b; specifically, we chose a length scale, L , of 40 km and a beach slope, ψ , of 1/100 to create the hypothetical tsunami. Note that the tsunami run-up occurs in about twenty-five minutes and the tsunami draw-down occurs in about seven minutes. The dimensioned tsunami in Figure 5.1b is similar to real measured tsunami (e.g., Fritz et al., 2012; Koshimura and Hayashi, 2012; Yeh and Sato, 2016). The effect of tsunami duration on pore water pressure generation in the soil bed is discussed in more detail in §6.2.2. The pressure induced by the tsunami is applied as a boundary condition to the ground surface; i.e., the Dirichlet boundary condition.

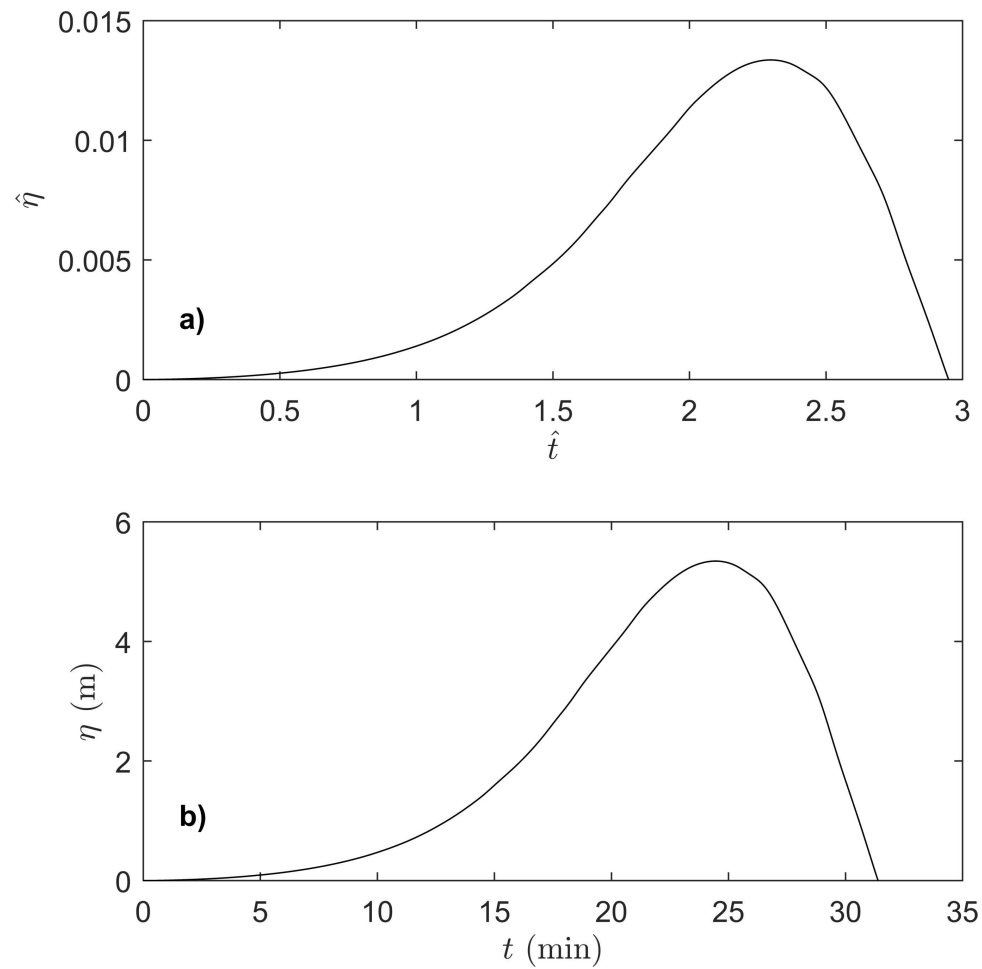


Figure 5.1: The variation of a typical tsunami height with time in the shoreline for (a) non-dimensional and (b) dimensional conditions. The tsunami wave data is from Carrier et al. (2003) model. The slope of the beach, ψ , is assumed 1/100 and the length scale, L , is 40 km.

Table 5.1: Assumed constant modeling parameters used for the numerical experimentation.

| Parameter | Symbol | Value |
|--------------------------------|-----------|--|
| Soil grain specific gravity | G_s | 2.65 |
| Absolute permeability | k_{ab} | $1 \times 10^{-11} \text{ m}^2$ |
| Initial soil bed porosity | ϕ_0 | 0.4 |
| Residual saturation | S_r | 0 |
| Dynamic viscosity of water | μ | $1 \times 10^{-3} \text{ Pa}\cdot\text{s}$ |
| Mass density of water | ρ_w | $1000 \text{ kg}/\text{m}^3$ |
| Bulk modulus of soil grains | K_s | 36 GPa |
| Drained Poisson's ratio | ν | 0.3 |
| Bulk modulus of de-aired water | K_w | 2.2 GPa |
| Bulk modulus of 3% aired water | K'_w | 4 MPa |
| Gravitational acceleration | g | $9.806 \text{ m}/\text{s}^2$ |
| Fitting parameter | A | 500 |
| Fitting parameter | n_2 | 0.5 |
| Fitting parameter | α' | $1.027 \times 10^{-4} \text{ Pa}^{-1}$ |
| Fitting parameter | n' | 3.304 |

5.2 Numerical experimentation plan

Figure 5.2 shows the numerical experimentation plan used to produce the results in Chapter 5. We are focused on poorly-graded beach sands, and for the results presented in Chapter 5, we have assumed a constant depth to bedrock of 10 m. The effect of impermeable layer depth on the pore water pressure response of the soil bed is examined more thoroughly in §6.1. Most of the modeling parameters needed for the coupled seepage deformation model are described in §4.2.1; however, we expand the discussion of some of the important modeling parameters within this section. For convenience, Table 5.1 shows the modeling parameters assumed for this study that are modeling constants.

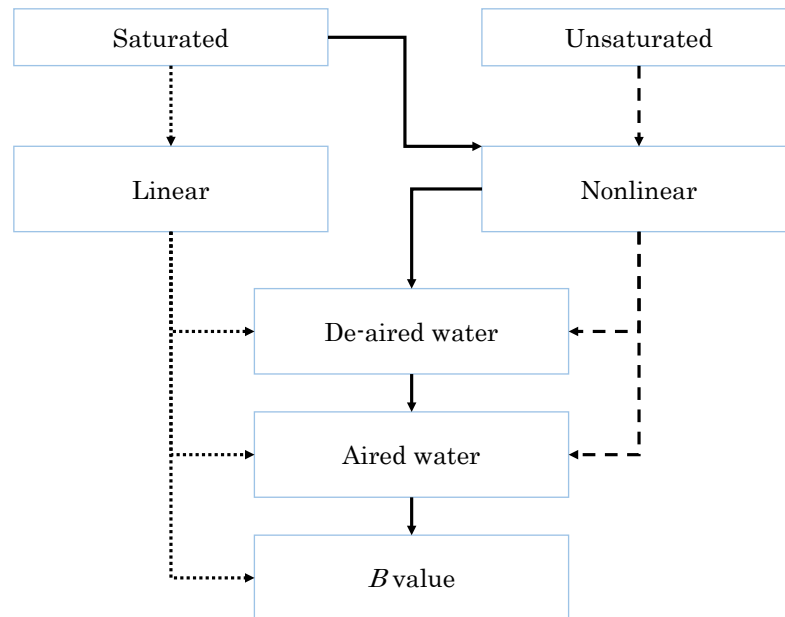


Figure 5.2: A schematic of the numerical experimentation algorithm. Two soil bed conditions are considered: saturated and unsaturated, two soil constitutive models are considered: linear and nonlinear, and two pore water conditions are considered: de-aired water and aired water. In addition, analyses where the B value is systematically changed are performed for the fully saturated soil bed condition with the linear soil constitutive model. The arrows in the schematic depict the extent of the performed numerical experimentation.

We have assumed that the specific gravity of soil grains, G_s , is 2.65 (Mitchell and Soga, 2005). The corresponding unit weight of the soil grains, γ_s , is ≈ 26.0 kN/m³, which corresponds to a mass density of the soil grains, ρ_s , of $\approx 2,650$ kg/m³. We have assumed that the initial porosity of the soil beds, ϕ_0 , is 0.4 (Santamarina et al., 2001), which corresponds to an initial void ratio of the soil bed, e_0 , of 2/3. Accordingly, the dry unit weight (γ_d), saturated unit weight (γ_{sat}), and buoyant unit weight (γ_b) of the hypothetical soil bed are approximately 15.6 kN/m³, 19.5 kN/m³, and 9.70 kN/m³, respectively. The preceding unit weights correspond to dry (ρ_d), saturated (ρ_{sat}), and buoyant (ρ_b) mass densities of the soil bed of approximately 1,590 kg/m³, 1,990 kg/m³, and 989 kg/m³, respectively.

We consider two soil bed conditions: fully saturated (i.e., $z_w = 0$ m) and unsaturated. Note that z_w is the depth of the water table from the ground surface. For the unsaturated condition, we consider $z_w = 1$ m and $z_w = 3$ m. The $z_w = 3$ m unsaturated conditions is chosen to bound the parameter space and for trend examination; realistically, $z_w = 3$ m is likely low for most beaches.

We consider two soil constitutive models: linear and nonlinear. For the linear soil constitutive model, it is assumed that the soil's shear modulus, G , is a constant value of 35 MPa for the entire 10 m soil bed. For a fully saturated condition, the shear wave velocity of the soil bed, V_s is calculated as $V_s = \sqrt{G/\rho_{sat}}$ (Achenbach, 1975); accordingly, $V_s = 133$ m/s for the soil bed. Recall that the shear modulus, G , is estimated from Equation 3.19. Note that assuming a constant shear modulus for a 10 m soil bed is admittedly a modeling limitation, because the soil's shear modulus is stress dependent (e.g., Seed and Idriss, 1970; Ishihara, 1996).

For the nonlinear soil constitutive model, the soil's shear modulus is not constant; rather, it is modeled as a function of the effective stress according to Equation 3.19. Figure 5.3 shows the soil's assumed initial shear modulus (and shear wave velocity) profile for the fully saturated condition considering a nonlinear soil constitutive model. The assumed initial shear modulus values are similar to the values measured by Abdoun et al. (2013) for uniform sand deposits. Note from Figure 5.3 that for the condition where the impermeable layer is at 10 m below the ground surface, the shear modulus is approximately 35 MPa at the depth of 5 m, which is the value assumed for the linear soil constitutive model for the condition where the depth to the impermeable depth is 10 m. Also note that for the unsaturated soil condition, only the nonlinear soil constitutive model is investigated.

Two types of pore fluid are considered during the numerical experimentation: de-aired water and aired water. The bulk modulus of the de-aired water, K_w , is assumed to be 2.2 GPa (Young et al., 2009). The aired water is considered to have 3% entrained air, which follows the work of Young et al. (2009), and the corresponding bulk modulus of the de-aired water, K'_w , is assumed to be 4 MPa (Young et al., 2009). The ratio K_w/K'_w is 550; therefore, the difference in the response of the soil bed to tsunami loading when the pore fluid is de-aired versus aired is significant.

All of the performed numerical experiments for Chapter 5 are shown in Table 5.2, which also shows the nomenclature used throughout Chapter 5. Only selected results are shown within Chapter 5, but the variation of pore water pressure and pore water pressure head gradient with depth and time for all the cases

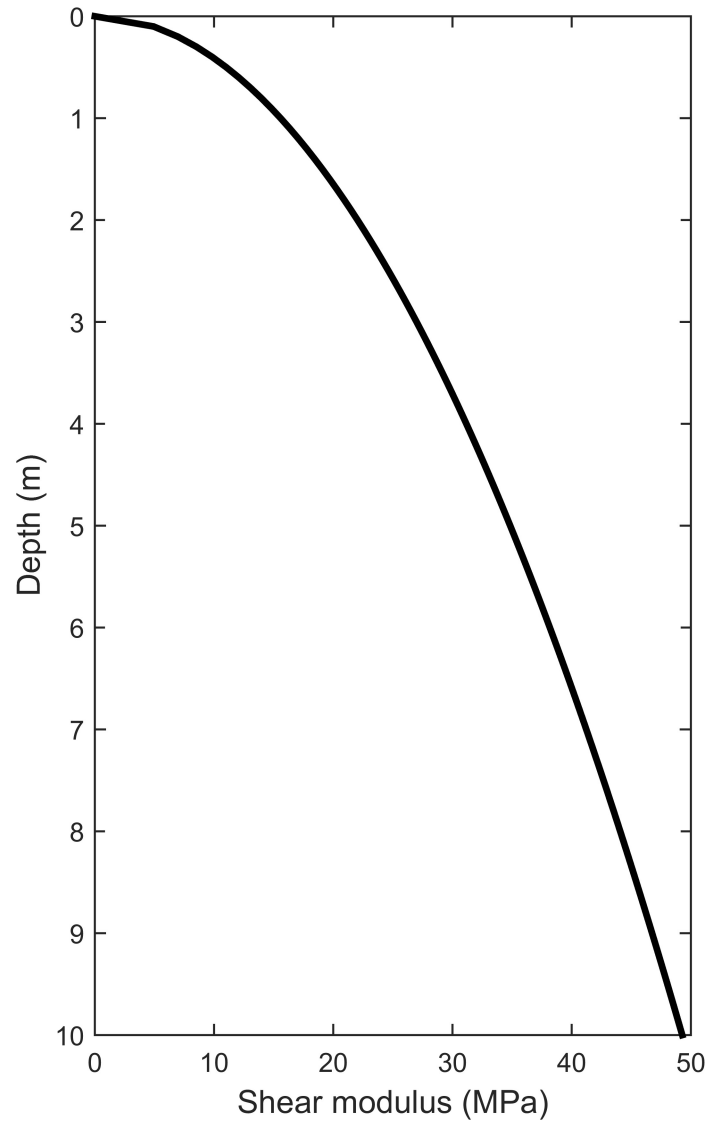


Figure 5.3: Variation of shear modulus with depth for fully saturated condition.

Table 5.2: The numerical experimentation cases, with defined nomenclature, shown in Figure 5.2. Note that for the cases that B value are not selected manually, B , α , and ν_u are estimated from poroelasticity.

| Case | Constitutive | | | Water | | |
|--------------|--------------|------|----------|---------|----------|-----------|
| | Model | B | α | ν_u | Type | z_w (m) |
| S-LE-B(0) | LE | 0 | 1 | 0.5 | - | 0 |
| S-LE-B(0.5) | LE | 0.5 | 1 | 0.5 | - | 0 |
| S-LE-B(0.6) | LE | 0.6 | 1 | 0.5 | - | 0 |
| S-LE-B(0.7) | LE | 0.7 | 1 | 0.5 | - | 0 |
| S-LE-B(0.8) | LE | 0.8 | 1 | 0.5 | - | 0 |
| S-LE-B(0.9) | LE | 0.9 | 1 | 0.5 | - | 0 |
| S-LE-B(0.95) | LE | 0.95 | 1 | 0.5 | - | 0 |
| S-LE-PW | LE | 1 | - | - | De-aired | 0 |
| S-LE-UW | LE | 1 | - | - | Aired | 0 |
| S-NI-B(0) | NI | 0 | 1 | 0.5 | - | 0 |
| S-NI-B(0.5) | NI | 0.5 | 1 | 0.5 | - | 0 |
| S-NI-B(0.8) | NI | 0.8 | 1 | 0.5 | - | 0 |
| S-NI-B(0.95) | NI | 0.95 | 1 | 0.5 | - | 0 |
| S-NI-PW | NI | 1 | - | - | De-aired | 0 |
| S-NI-UW | NI | 1 | - | - | Aired | 0 |
| UN-NI-PW(1m) | NI | - | - | - | De-aired | 1 |
| UN-NI-UW(1m) | NI | - | - | - | Aired | 3 |
| UN-NI-PW(3m) | NI | - | - | - | De-aired | 1 |
| UN-NI-UW(3m) | NI | - | - | - | Aired | 3 |

shown in Table 5.2 are given in in Appendix A For each case, the first letter(s) corresponds to the soil bed condition: saturated (S) versus unsaturated (UN). The second two letters correspond to the soil constitutive model: linear (LE) versus nonlinear (NI). The pore water conditions is given as de-aired (PW) or aired (UW), or for the cases that the B value is systematically changed, the letter B is used followed by the specific B value in parentheses. For the cases with an unsaturated soil condition, the parenthetical values denote the depth of the ground water table.

5.3 Numerical convergence

For the numerical experimentation, we must decide what cell sizes and time steps use for the finite difference approach described in §4.3. Additionally, a numerical convergence study is performed for the one-dimensional case to verify the numerical formulation.

For the one-dimensional numerical convergence study, two cases are chosen: *Case I* investigates the convergence for unsaturated conditions (i.e., the ground water table located 3 m below the ground surface), and *Case II* investigates the convergence for fully saturated conditions (i.e., the ground water table is located at the ground surface).

For both Case I and Case II, a nonlinear soil constitutive model is assumed, and the pore water is considered to be aired (i.e., 3% air in the pore water). The convergence cases were selected to be “worst cases” for both the unsaturated and fully saturated conditions; that is, convergence is achieved more easily for the other cases we examine. Note that Case I corresponds to Case UN-NI-UW(3m) and Case II corresponds to Case S-NI-UW in Table 5.2, but the nomenclature Case I and Case II is used specifically in §5.3 for clarity.

To perform the convergence study, we assume that the soil bed is initially in equilibrium conditions; therefore, the initial pore water pressure distribution is linear and hydrostatic. For Case I (i.e., the unsaturated condition), the pore water pressure distribution and the degree of saturation distribution versus depth at the initial condition is shown in Figure 5.4 (e.g., Fredlund and Rahardjo, 1993; Lu and

Table 5.3: Summary of convergence studies with four different grids for Case I and Case II. Δz is the cell size, mz is the total number of cells, Δt is the time increment, and N is the total number of time increments.

| | Δz (m) | mz | Δt (s) | N |
|---------------|----------------|------|----------------|--------|
| Grid 1 | 0.5 | 20 | 0.3193 | 5900 |
| Grid 2 | 0.1 | 100 | 0.0639 | 29499 |
| Grid 3 | 0.05 | 200 | 0.0319 | 58998 |
| Grid 4 | 0.025 | 400 | 0.016 | 117996 |

Likos, 2004; Fredlund et al., 2012). The saturation is estimated from soil-water characteristic curve (i.e. Equation 4.2). To perform the convergence study, we use the soil properties given in Table 5.1 and the hypothetical tsunami shown in Figure 5.1b. The pressure induced by the hypothetical tsunami is applied as a boundary condition at the ground surface.

The convergence studies for Case I and Case II are performed using four different grids, which are shown in Table 5.3. Grid 1 is the “coarsest” grid, and the Grid 4 is the “finest” grid. The time step, Δt , varies linearly with cell size, Δz , as described by Peszyńska and Yi (2008).

Figure 5.5 shows the results of the convergence study for Case I in terms of pore water pressure versus depth. Over most of the soil bed depth, the different grids shown in Table 5.3 produce the same results. The notable exception is near the infiltration front. To examine the convergence near the infiltration front more thoroughly, Figure 5.6 shows the results from Figure 5.5, but zoomed-in to a depth range of 0 to 3 m. By examining Figure 5.6, it is evident that model convergence is being achieved for the estimation of pore water pressures with depth when $\Delta z < 0.1$ m. Figure 5.5c shows pore water pressure 28 minutes after tsunami, and

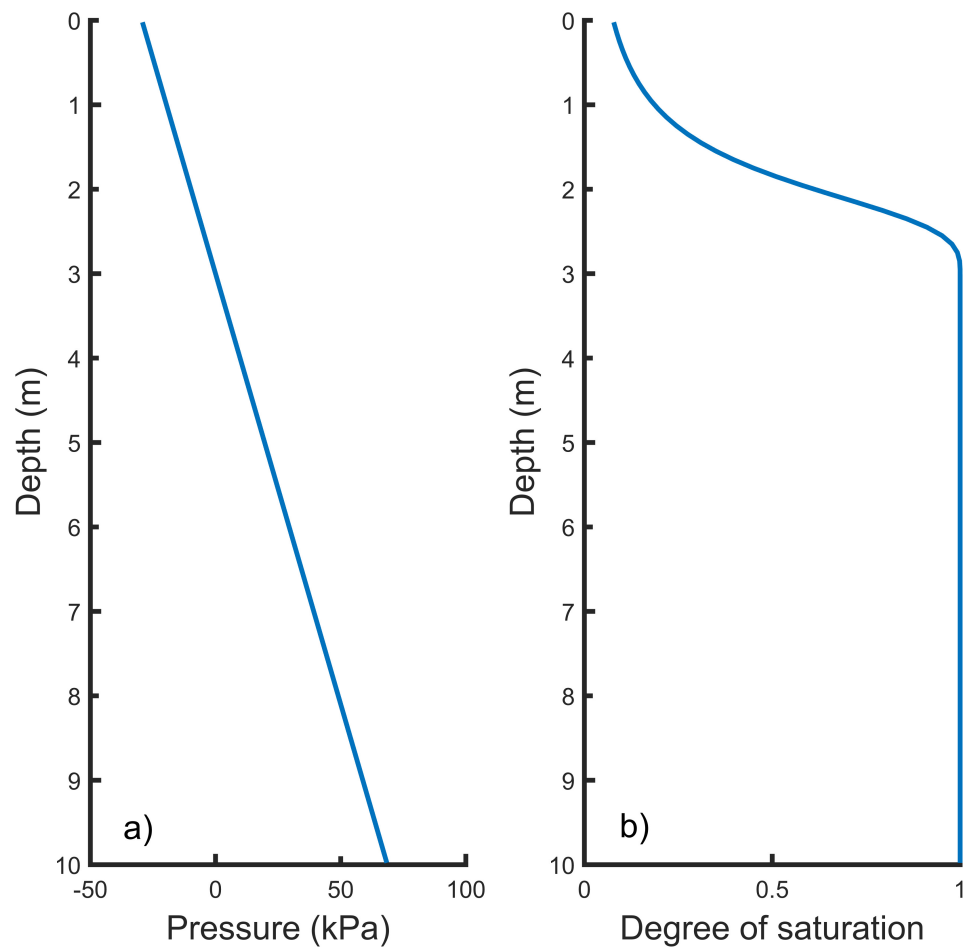


Figure 5.4: Initial condition at equilibrium hydrostatic condition for the unsaturated soil condition when the ground water table is at 3 m below the ground surface: a) pore water pressure distribution with depth, and b) degree of saturation distribution with depth.

Figure 5.5d shows pore water pressure 29 minutes after tsunami. The importance of the effect of grid size can be seen in Figures 5.5c and 5.5d. As we see for Grid 1, the soil bed is fully saturated after 28 minutes, and the pore water pressure is larger when compared with Grids 2, 3, and 4. In Figure 5.5d, we see that for the very fine grid, the soil bed is not fully saturated. Note that the sudden increase in pore water pressure after the soil bed becomes fully saturated is caused by our assumption to neglect air pressure. That is, when we assume that air pressure is zero, the pore water pressure increases suddenly after the soil becomes saturated. Studying the effect of air pressure on the pore water pressure response in soil beds subjected to tsunami loading is suggested for future study.

Figure 5.7 shows the results of the convergence study for Case I in terms of the excess pore water pressure head gradient, $\partial h/\partial z$, versus depth. Recall that $\partial h/\partial z$ is important for determining whether liquefaction is occurring (Yeh and Mason, 2014; Mason and Yeh, 2016), as discussed in §1.1. The value of $\partial h/\partial z$ is consistent between all grid sizes considered in Table 5.3 for most depths, with the notable exception of the infiltration front. Figure 5.8 shows the results from Figure 5.7 zoomed-in over a depth range of 0 to 3 m. It can be seen, from Figure 5.8, that the value of $\partial h/\partial z$ does not converge as Δz gets smaller; in fact, it is apparent that a discontinuity exist at the infiltration front. The discontinuity is expected. When examining Figure 5.6, it can be seen that the pore water pressure at the depth of the infiltration front resembles “cusp-like” behavior, and the cusp becomes more defined as Δz decreases; accordingly, as Δz decreases, the definition of $\partial h/\partial z$ approaches non-existence. It is clear, from examining Figures 5.8a and 5.8c, that the

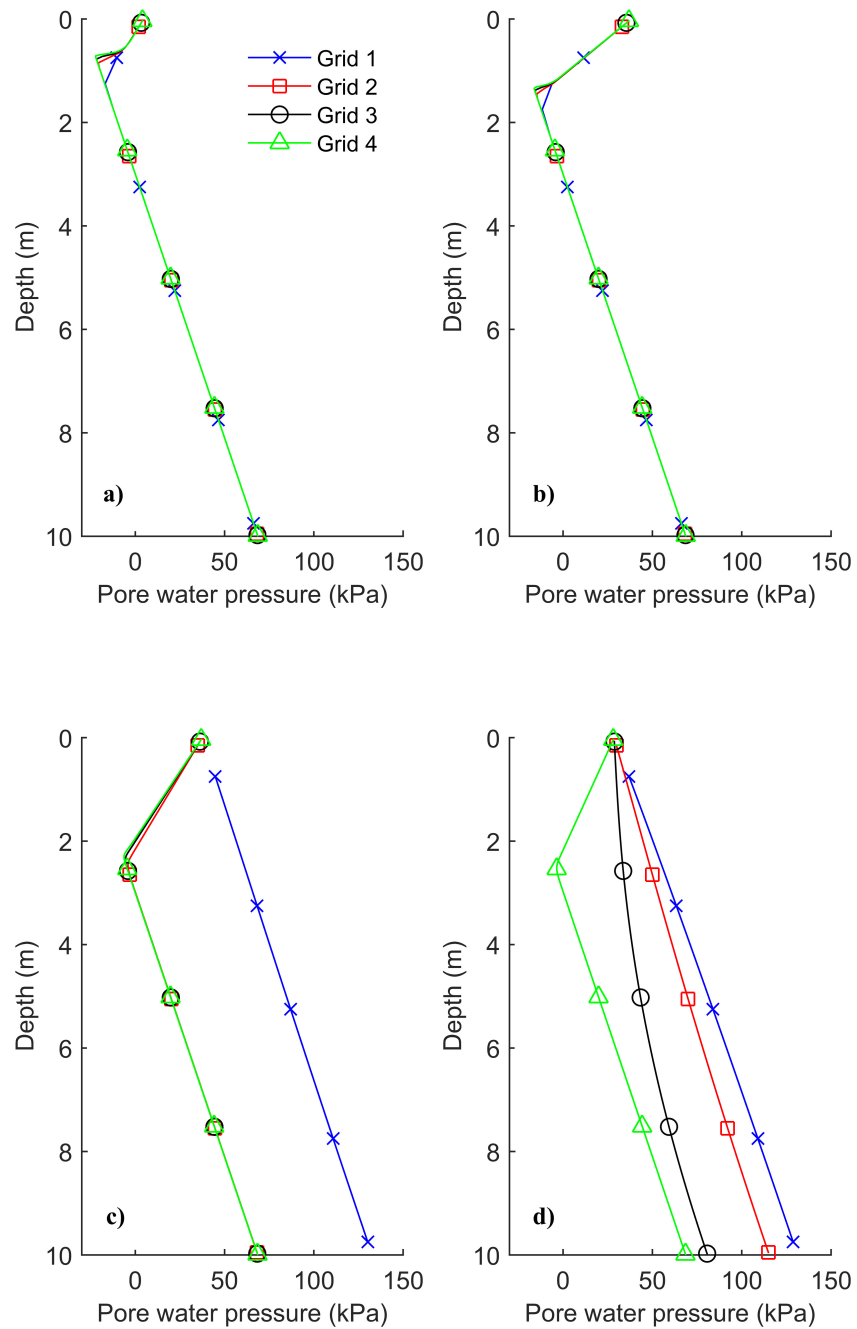


Figure 5.5: Convergence studies for case I for a) 10 minutes , b) 20 minutes, c) 28 minutes, d) 29 minutes.

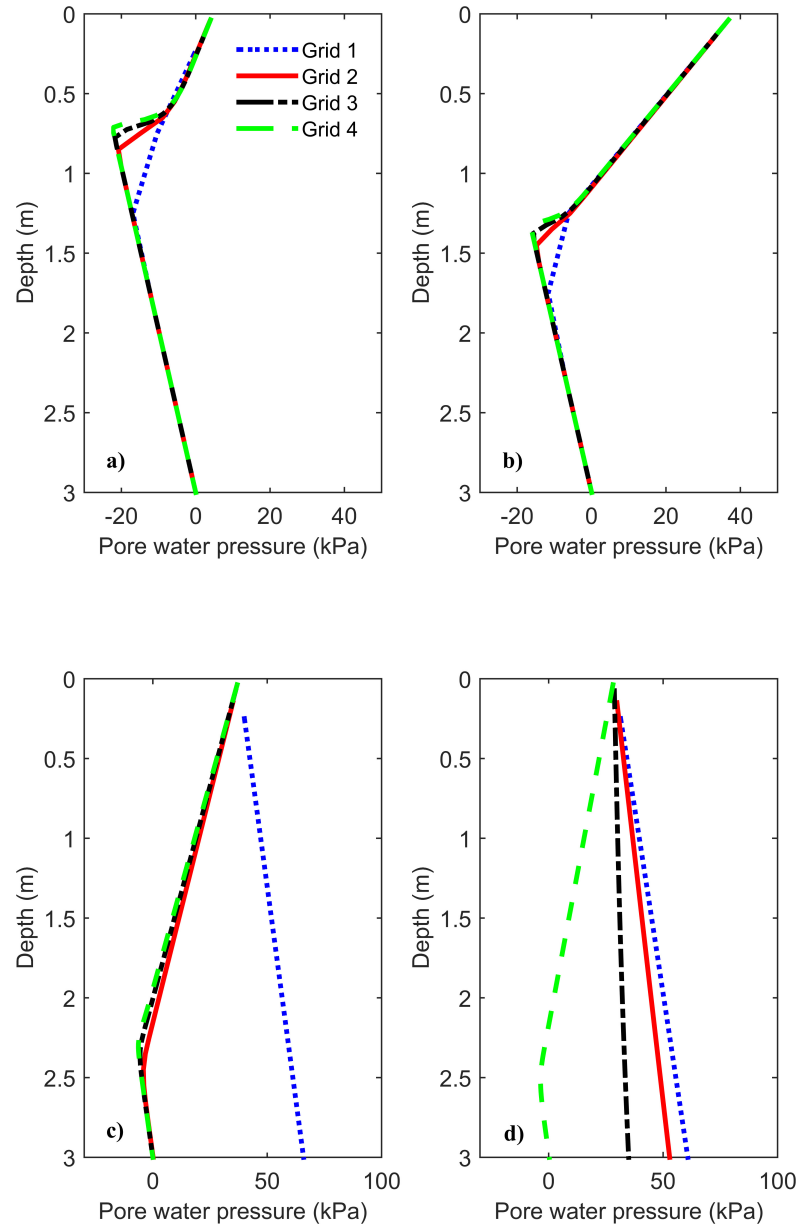


Figure 5.6: Convergence studies for case I, for the depth between 0 to 3 m for a) 10 minutes, b) 20 minutes, c) 28 minutes , d) 29 minutes.

discontinuity is more pronounced near the beginning of the tsunami inundation, as the infiltration front is progressing downward, and as the unsaturated soil becomes saturated, the discontinuity becomes less pronounced. Regardless, for the unsaturated soil conditions examined herein, the value of $\partial h/\partial z$ does not converge near the infiltration front, and accordingly, we examine the trends of the results for the unsaturated soil conditions within this dissertation.

Figure 5.9 shows the results of the convergence study for the fully saturated soil condition (i.e., case II). As we see, for the fully saturated soil condition, the pore water pressure predicted using different grid size all match very well. In fact, the pore water pressure induced by tsunami loading is not sensitive to the grid sizes we investigated for the fully saturated soil conditions. Likewise, Figure 5.10 shows the results of the convergence study for case II in terms of $\partial h/\partial z$. We see that for case II, the $\partial h/\partial z$ results are generally not sensitive to the grid sizes we selected. However, we see that after 30 minutes of tsunami loading, the value of $\partial h/\partial z$ computed using Grid 1 underestimates the value of $\partial h/\partial z$ induced by tsunami loading, and especially at the ground surface.

Recall that the excess pore water pressure head gradient at the ground surface, $(\partial h/\partial z)|_{z=0}$, is important for determining liquefaction potential (Yeh and Mason, 2014; Mason and Yeh, 2016); therefore, it is instructive to examine convergence of $(\partial h/\partial z)|_{z=0}$ versus time for Case I (Figure 5.11a) and Case II (Figure 5.11b). From Figure 5.11, it is apparent that convergence is achieved as the cell size decreases, and in fact, Grids 2, 3, and 4 all yield similar results (especially for Case II). For Case I, $(\partial h/\partial z)|_{z=0}$ has a large negative value initially, which is caused by the

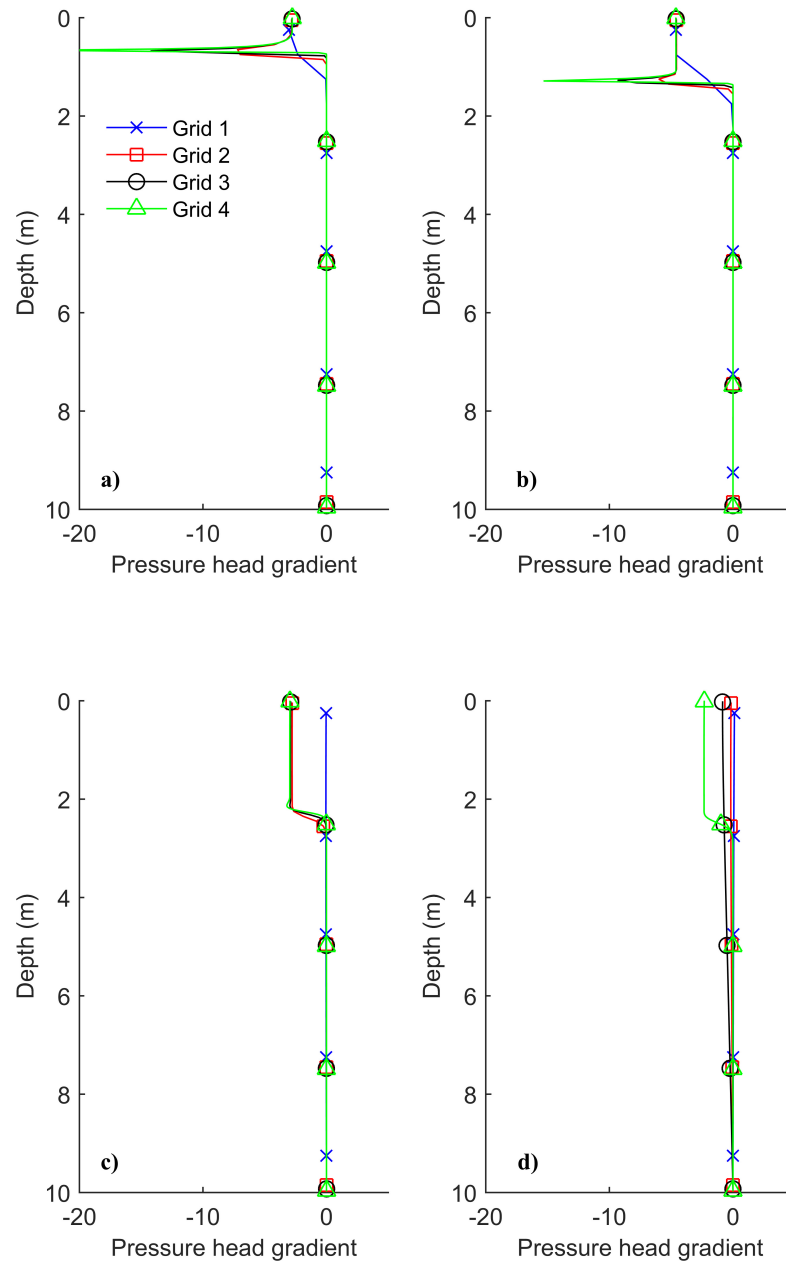


Figure 5.7: Convergence studies for case I for pressure head gradient with depth for a) 10 minutes, b) 20 minutes, c) 28 minutes, d) 29 minutes.

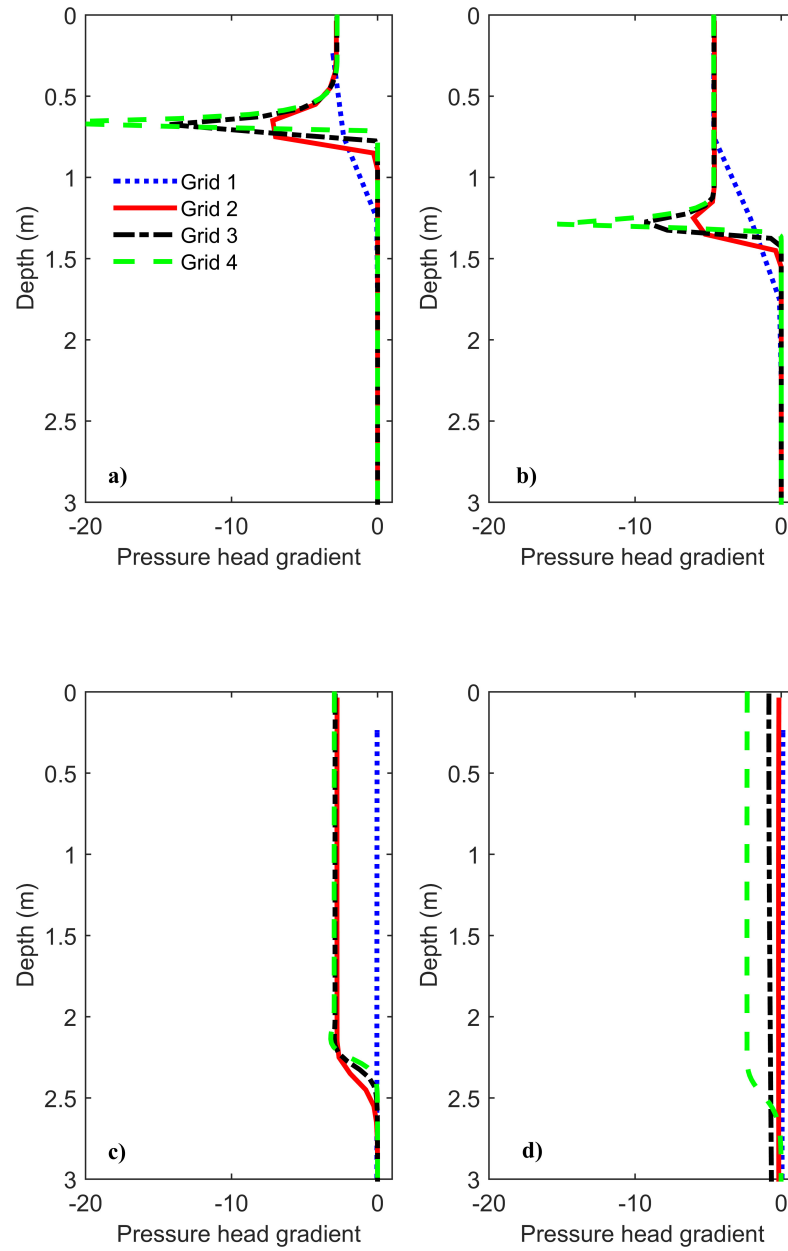


Figure 5.8: Convergence studies for case I for pressure head gradient with depth, for the depth between 0 to 3 m for a) 10 minutes, b) 20 minutes, c) 28 minutes, d) 29 minutes.

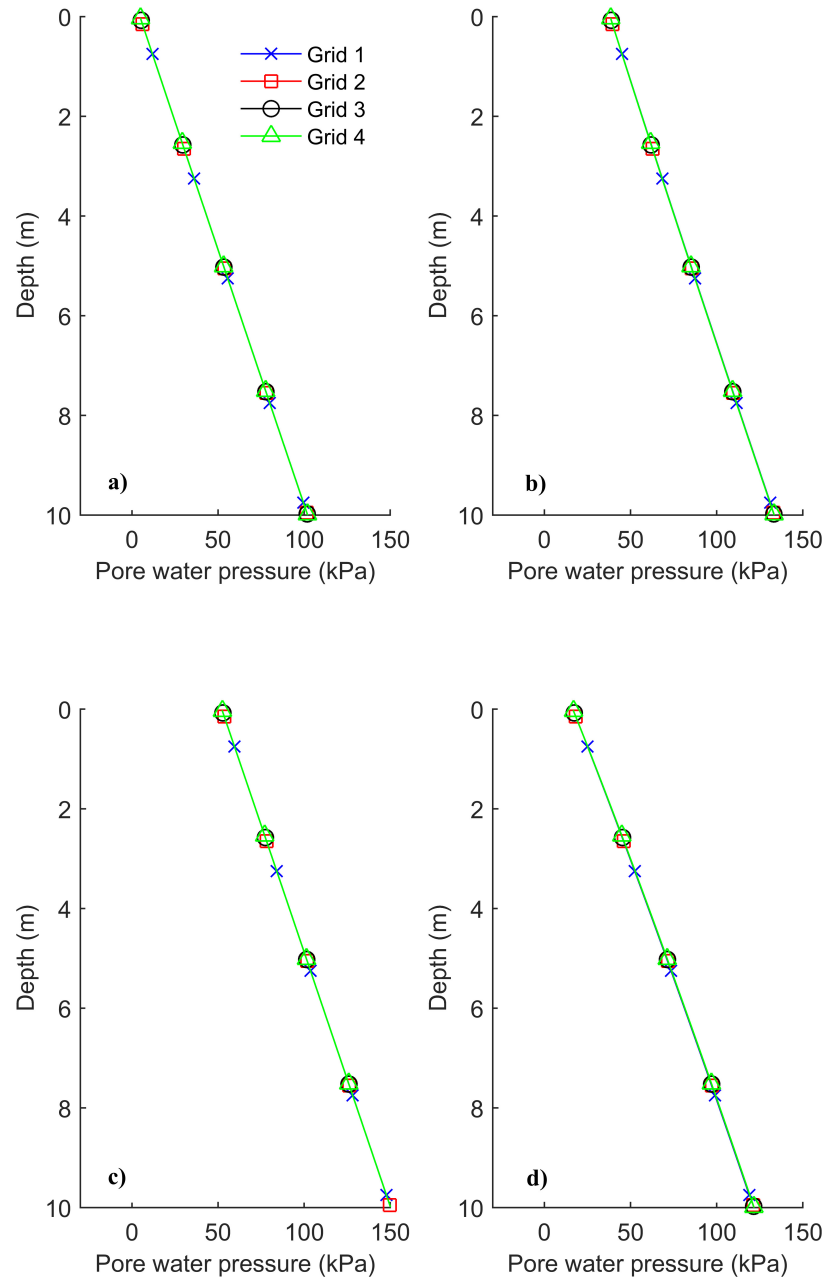


Figure 5.9: Convergence studies for case II for a) 10 minutes, b) 20 minutes, c) 25 minutes, d) 30 minutes.

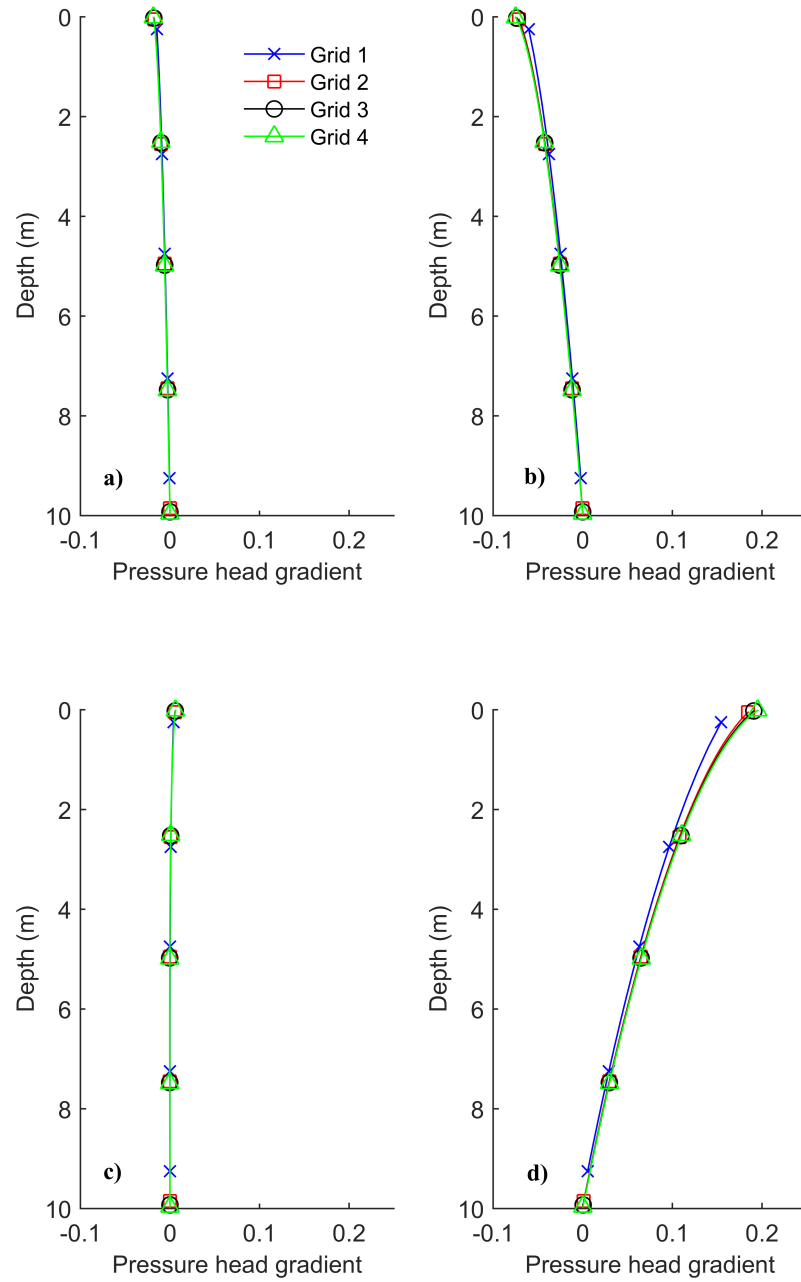


Figure 5.10: Convergence studies for case II for pressure head gradient with depth for a) 10 minutes, b) 20 minutes, c) 25 minutes, d) 30 minutes.

infiltration front; recall that this same observation was made in Figure 5.8.

Based on the results of the one-dimensional numerical convergence study, we decided to use Grid 2 to produce the results shown in § 5.4 and one-dimensional results in Chapter 6; i.e., $\Delta z = 0.1$ m and $\Delta t = 0.0639$ s.

5.4 Numerical experimentation results

The results of the numerical experimentation, shown in Figure 5.2 and Table 5.2, are shown in §5.4. As previously mentioned, the results are primarily considered in terms of total pore water pressure, p_w and excess pore water pressure head gradient, $\partial h/\partial z$. In addition, only selected results are shown in §5.4, but all the results are given in Appendix A.

5.4.1 Fully saturated soil model

The fully saturated soil condition is investigated by considering two soil constitutive models: linear and nonlinear.

5.4.1.1 Linear constitutive model

Figures 5.12 and 5.13 show the results of the hypothetical tsunami (Figure 5.1b) inundating the fully saturated soil model with a linear constitutive model and aired water (i.e., 3% entrained air) as the pore fluid. In other words, Case S-LE-UW (Table 5.2) is examined.

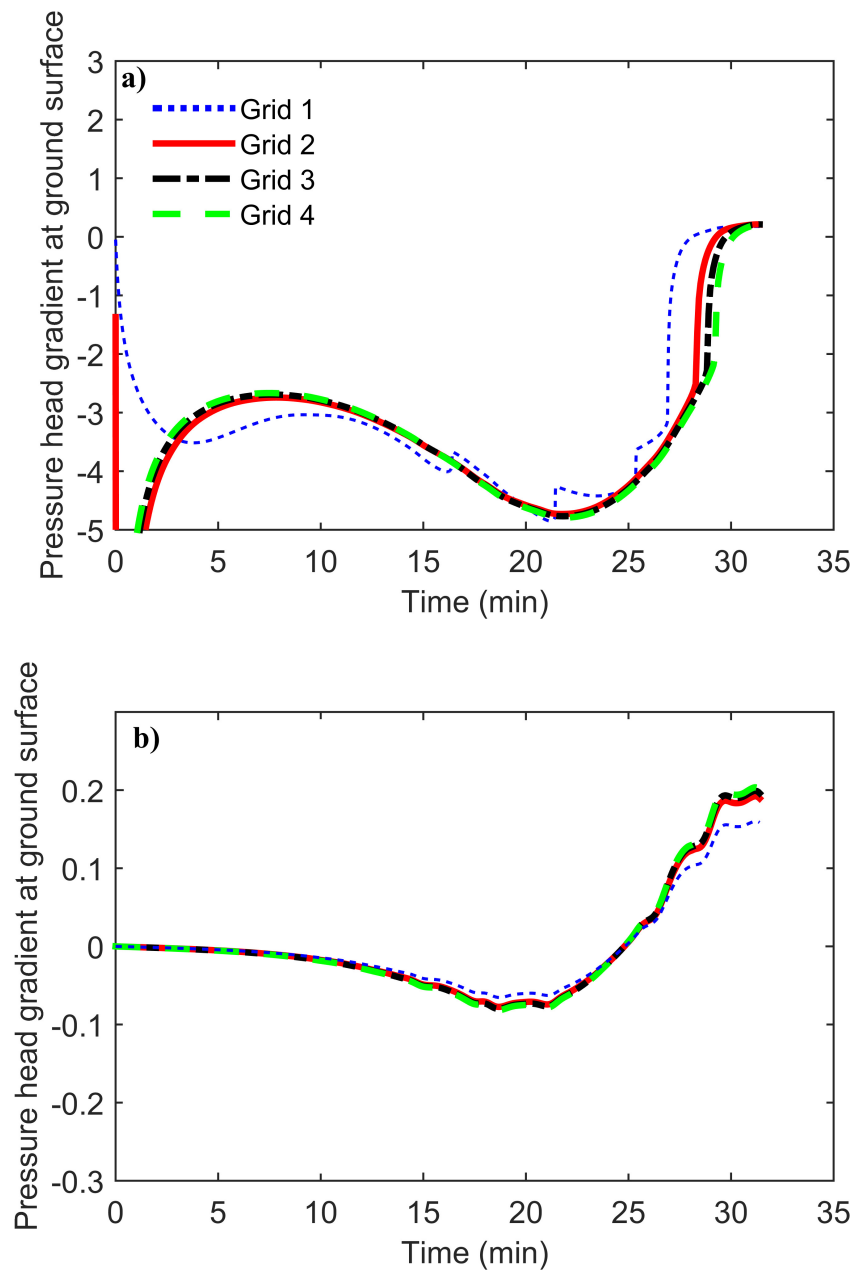


Figure 5.11: Convergence studies for pressure head gradient with time for different grid size, a) case I when ground water table is 3 m below the ground surface, and b) case II when the ground water table is at ground surface.

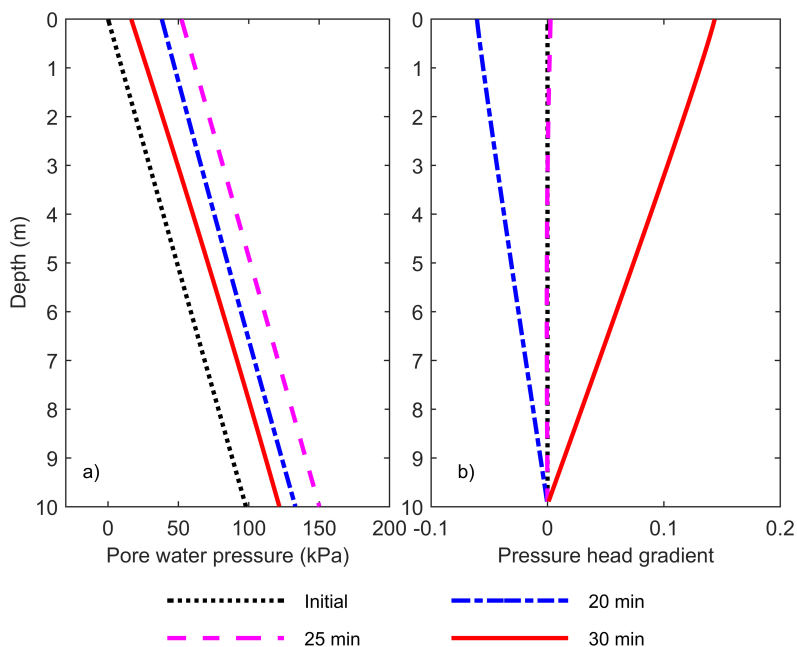


Figure 5.12: Case S-LE-UW: a) total pore water pressure at different times with depth for the fully saturated soil condition, assuming aird water, and considering the linear soil constitutive model; b) excess pore water pressure head gradient at different times with depth for the fully saturated soil condition, assuming aird water, and considering the linear soil constitutive model.

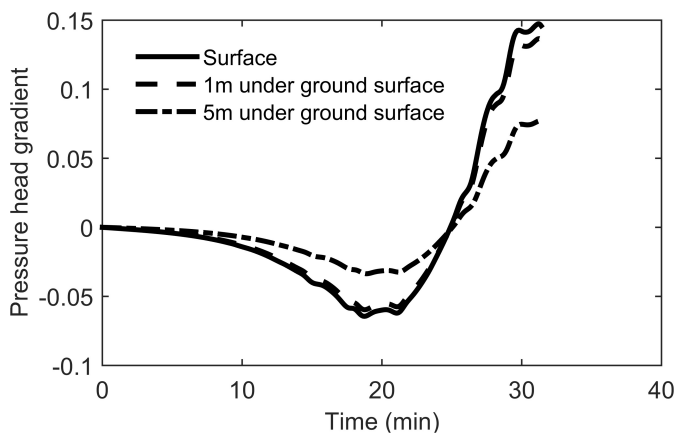


Figure 5.13: Case S-LE-UW: the excess pore water pressure head gradient at different depths with time for the fully saturated soil condition, assuming aird water, and considering the linear soil constitutive model.

Figure 5.12a shows the total pore water pressure, p_w , versus depth during tsunami run-up and draw-down. Recall from Figure 5.1b that 20 min is during the middle of the tsunami run-up, 25 min is near the beginning of tsunami draw-down, and 30 min is near the end of tsunami draw-down. Figure 5.12a primarily shows that the total pore water pressure increases as the tsunami run-up is occurring, and decreases relatively rapidly as the tsunami draw-down is occurring. The pressure profiles shown in Figure 5.12a appear parallel, but they are not. The subtle differences can best be examined in Figure 5.12b, which shows $\partial h/\partial z$ versus depth for different times. Recall that a positive values of $\partial h/\partial z$ indicates upward flow (defined in relation to the gravity vector); accordingly, downward flow of pore water occurs during tsunami run-up, and upward flow of pore water occurs during tsunami draw-down, which is observed in Figure 5.12b. The depth profiles of $\partial h/\partial z$ are nearly linear, with the value being zero at the bedrock (i.e., the Neumann boundary condition), and the largest value is computed at the ground surface. The linearity of the $\partial h/\partial z$ versus depth profiles is a function of the lowered bulk modulus of the aired water. The largest value of $\partial h/\partial z$ occurs at the end of draw-down, as expected, but it is not large enough to cause significant momentary liquefaction or enhanced scour.

Figure 5.13 shows $\partial h/\partial z$ versus time at the ground surface, one meter below the ground surface, and five meters below the ground surface. It can be seen that the $\partial h/\partial z$ values calculated at the ground surface and at a depth one meter below the ground surface are nearly identical, which is indicative of the $\partial h/\partial z$ versus depth profiles being linear, as previously discussed. In addition, Figure 5.13

shows that the increase in $\partial h/\partial z$ is more significant during the tsunami draw-down period than the tsunami run-up period, which indicates that the tsunami draw-down occurs relatively rapidly compared to the tsunami run-up, as shown in Figure 5.1.

We created a normalized bar chart to compare multiple cases. The bar chart, shown in Figure 5.14, shows the normalized maximum $\partial h/\partial z$ numerically determined at the ground surface for all the S-LE Cases (fully saturated condition, linear soil constitutive model) shown in Table 5.3. Notably, the maximum values of $\partial h/\partial z$ occur at the end of tsunami draw-down for all the cases examined.

Examining the bar heights for Case S-LE-PW and Case S-LE-UW in Figure 5.14 shows the differences in the response of soil beds saturated with de-aired water (PW) and aired water (UW). The difference between the two cases is significant; in fact, the maximum $\partial h/\partial z$ recorded at the ground surface when aired water is the pore fluid is significantly larger than the same measure when de-aired water is the pore fluid. The drastic difference shows the importance of the bulk modulus of water.

As explained in §2.2.2, the B value depends on the fluid bulk modulus, and because de-aired water has a larger bulk modulus than aired water, soil beds saturated with de-aired water also have larger B values. The B value can be selected manually without regard to the solid and fluid bulk moduli, and different B values result in different excess pore water pressure head gradient profiles. The reduced results for the numerical experiments investigating different B values are also shown in Figures 5.14. For the numerical experimentation performed when the

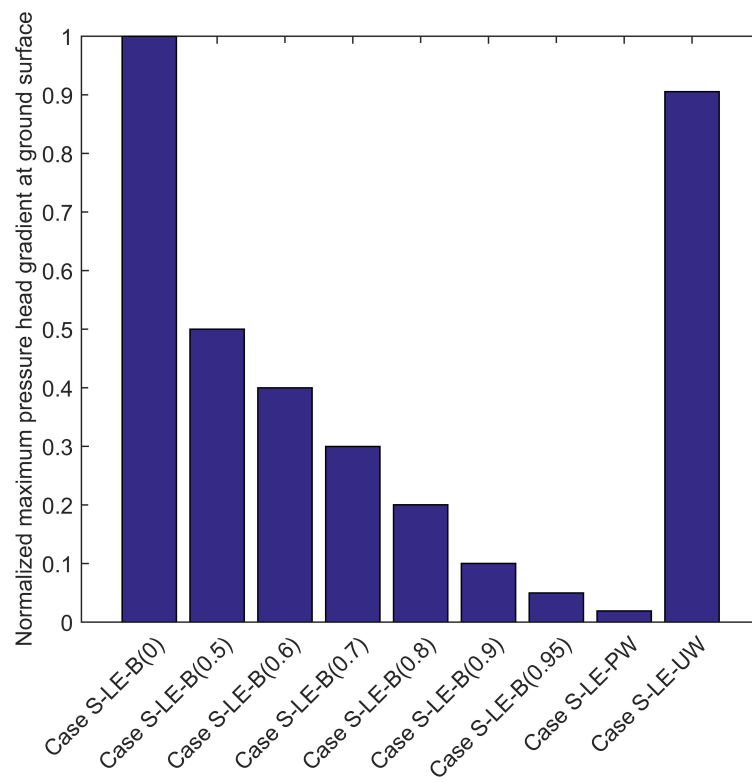


Figure 5.14: Maximum excess pore water pressure head gradient at the ground surface for the fully saturated soil condition for different cases using the linear soil constitutive model and assuming that the impermeable layer depth is at 10 m below ground surface. The values are normalized with the maximum value, which occurs for Case S-LE-B(0) and is equal to 0.1628.

B value was selected manually, it is assumed that the poroelasticity parameters are not affected by the effective stress or porosity; that is, it is assumed that $\nu_u = 0.5$ and $\alpha = 1$.

Recall that when $B = 0$, the pore water pressure changes are only due to seepage; accordingly, no pore water pressure changes are instantaneously induced within the soil bed by the weight of the overlying tsunami water. Thus, the $B = 0$ assumption is referred to as the “uncoupled” assumption. Yeh and Mason (2014) use the uncoupled assumption to investigate pore water pressure changes in soil beds due to hypothetical tsunami loadings.

If we assume that $\alpha = 1$, $B = 0$, and $\nu = 0.3$, the coefficient of compressibility, m_v , is estimated as $m_v = 8.16 \times 10^{-9} \text{ Pa}^{-1}$ from Equation 4.17, which results in $C_v = 12,200 \text{ cm}^2/\text{s}$; i.e.,

$$C_v = \frac{k_{ab}}{\mu_w m_v} = \frac{10^{-11} \text{m}^2}{10^{-3}(\text{Pa} \cdot \text{s}) \times 8.16 \times 10^{-9} \text{Pa}^{-1}} = 12,200 \text{ cm}^2/\text{s}. \quad (5.10)$$

Note that the value of C_v calculated in Equation 5.10 represents the shear modulus of 35 MPa at the depth of 5 m. As discussed in §5.2, the shear modulus increases with depth; therefore, C_v also increases with depth and it follows that C_v is less at the ground surface. Herein, our goal is to show that the uncoupled approach (Yeh and Mason, 2014) matches with the current model results when $B = 0$. Note that Equation 4.19 can not be used here to calculate C_v . In fact, because the uncoupled approach is an unrealistic condition, when we assume $B = 0$, we calculated $C_v = 0$, which is not true for fully saturated soil conditions.

Figure 5.15 shows the excess pore water pressure head gradient versus depth at different times using the uncoupled analytical approach (Yeh and Mason, 2014) and the proposed seepage deformation model when $B = 0$ with linear constitutive soil model. Comparison of the results of excess pore water pressure head gradient from the Yeh and Mason (2014) model with the proposed seepage-deformation model solution shows good agreement — specifically when the depth to impermeable layer is very large (i.e., 100 m herein, which approaches the infinite halfspace assumption used by Yeh and Mason (2014)).

As the B value increases from zero to one, the amount of pore water pressure within the soil bed induced by the overlying tsunami water weight increases, which results in lower values of $\partial h/\partial z$. For the limiting condition, when $B = 1$, the value of $\partial h/\partial z$ becomes negligible; accordingly, when $B = 1$, the overlying tsunami water weight induces a change in excess pore water pressure within the soil bed almost equal to the weight of the overlying tsunami water, which is the typical assumption employed when investigating consolidation of soft clays (Terzaghi, 1943).

5.4.1.2 Nonlinear constitutive model

Figure 5.16 shows the variation of pore water pressure and $\partial h/\partial z$ with depth for the fully saturated soil condition at different times. To create the figure, the nonlinear soil constitutive model is used with aird water as the pore fluid; i.e., the S-NI-UW Case from Table 5.2 is investigated.

Comparing Figure 5.12 with Figure 5.16 shows the difference between the lin-

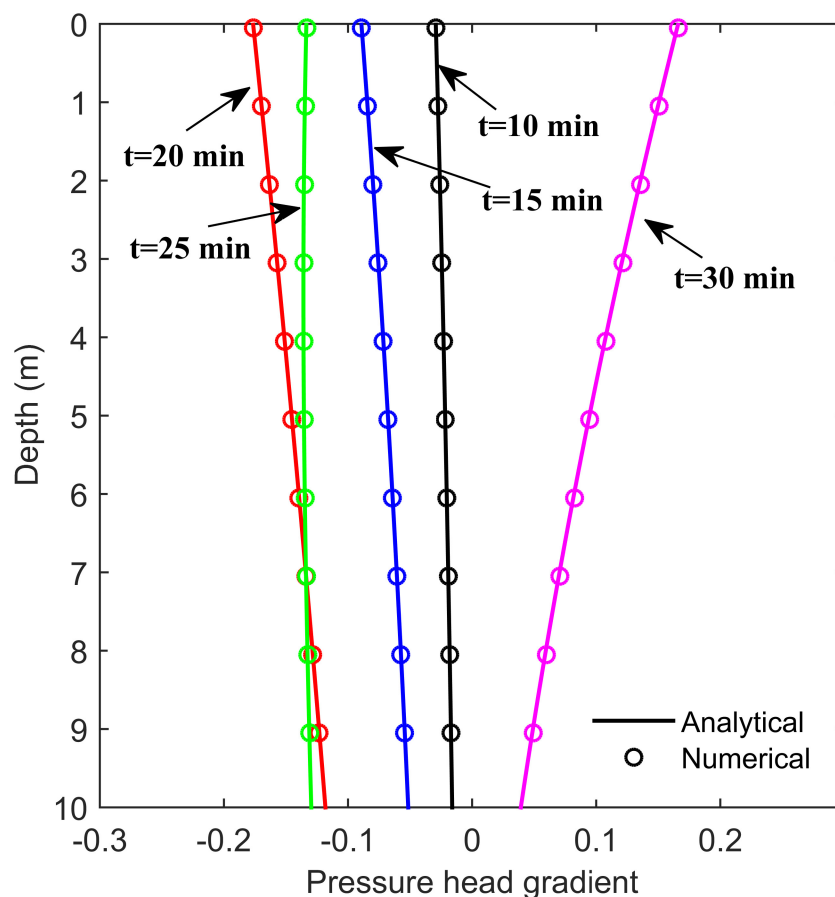


Figure 5.15: The variation of excess pore water pressure head gradient at different times with depth. Comparison of the results from the Yeh and Mason (2014) solution with numerical results from the proposed seepage deformation model shows good agreement. Note that, linear constitutive soil model is used. In addition, for the seepage deformation model, we assume $\alpha = 1$ and $B = 0$, and $\nu_u = 0.5$.

ear and nonlinear soil constitutive models in terms of the pore water pressure response in the soil bed due to the hypothetical tsunami loading. At first glance, Figures 5.12a and 5.16a look the same, and they are very similar; however, there are subtle differences in the two figures best examined by investigating the differences in $\partial h/\partial z$, which are shown in Figures 5.12b and 5.16b for the linear and nonlin-

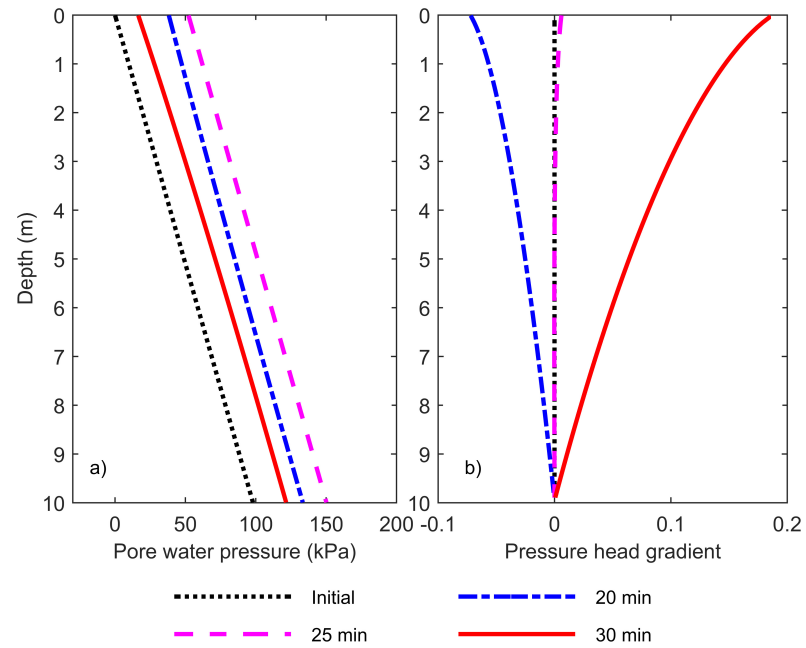


Figure 5.16: Case S-NI-UW: a) pore water pressure changes with depth at different times for the fully saturated soil condition considering the nonlinear soil constitutive model and with aired water as the pore fluid; b) excess pore water pressure head gradient changes with depth at different times for the fully saturated soil conditions considering the nonlinear soil constitutive model and with aired water as the pore fluid.

ear soil constitutive models, respectively. Primarily, the nonlinear soil constitutive model leads to values of $\partial h/\partial z$ that are nonlinear near the soil bed surface.

Figure 5.17 shows the variation of $\partial h/\partial z$ with time at the ground surface, one meter below the ground surface, and five meters below the ground surface for Case S-NI-UW. Figure 5.17 shows that $\partial h/\partial z$ reduces and becomes negative during the tsunami run-up, then $\partial h/\partial z$ increases and becomes positive during tsunami draw-down, as expected based on similar observations from Figure 5.13. From Figure 5.17, it can also be seen that $\partial h/\partial z$ recorded at the ground surface and one meter below the ground surface are relatively similar, though less similar than shown for the S-LE-UW Case shown in Figure 5.13. In addition, the values of $\partial h/\partial z$ near the soil surface during tsunami draw-down are larger when the nonlinear soil constitutive model is employed, but the values of $\partial h/\partial z$ are smaller at a depth of five meters when the nonlinear soil constitutive model is employed. The preceding observation highlights the effect of the shear modulus on the pore water pressure response of a soil bed subjected to tsunami loading. It is evident that careful measurements of the soil's shear modulus (and other elastic moduli) must be made to yield better predictions of $\partial h/\partial z$ and thus, better predictions of sediment instability during tsunami loading.

Figure 5.18 shows the maximum values of $\partial h/\partial z$ for the nonlinear soil constitutive model cases shown in Table 5.2. By examining the figure, it can be seen that the maximum value of $\partial h/\partial z$ is almost negligible for the case when de-aired water is the pore fluid as compared to the case when aired water is the pore fluid; more specifically, the maximum values of $\partial h/\partial z$ at the ground surface during tsunami

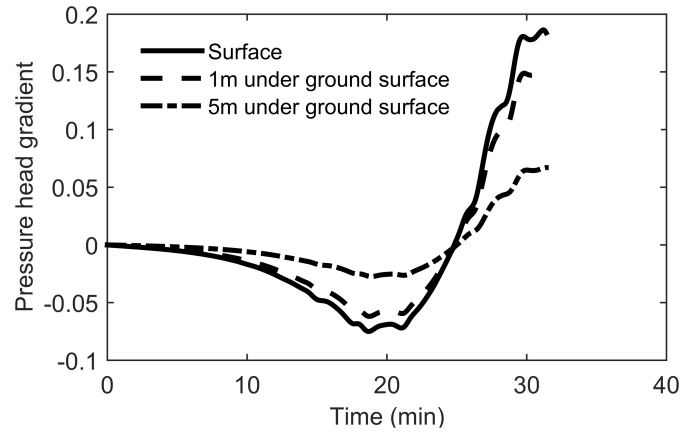


Figure 5.17: Case S-NI-UW: excess pore water pressure head gradient changes with time at different depths for fully saturated soil conditions considering the nonlinear soil constitutive model and with aired water as the pore fluid.

draw-down for the cases when de-aired water and aired water are the pore fluids are 0.0032 and 0.1864, respectively.

Figure 5.18 also shows the maximum values of $\partial h/\partial z$ for manually selected B values for the nonlinear soil constitutive model cases shown in Table 5.2. Similar to the linear soil constitutive model cases, for when the B value is defined manually, it is assumed that $\nu_u = 0.5$ and $\alpha = 1$. Figure 5.18 shows that assuming $B = 0.95$ (and is constant with depth), $\nu_u = 0.5$, and $\alpha = 1$, results in a maximum values of $\partial h/\partial z$ of 0.0099, which is almost negligible. Note that for other realistic conditions, the B value can be smaller than 0.95, ν_u can be smaller than 0.5, and α can be smaller than one. As it is shown in Figure 5.19 for either de-aired water or aired water, comparing the excess pore water pressure head gradient at the ground surface for the linear constitutive model with the nonlinear constitutive model shows that the excess pore water pressure head gradient for the nonlinear

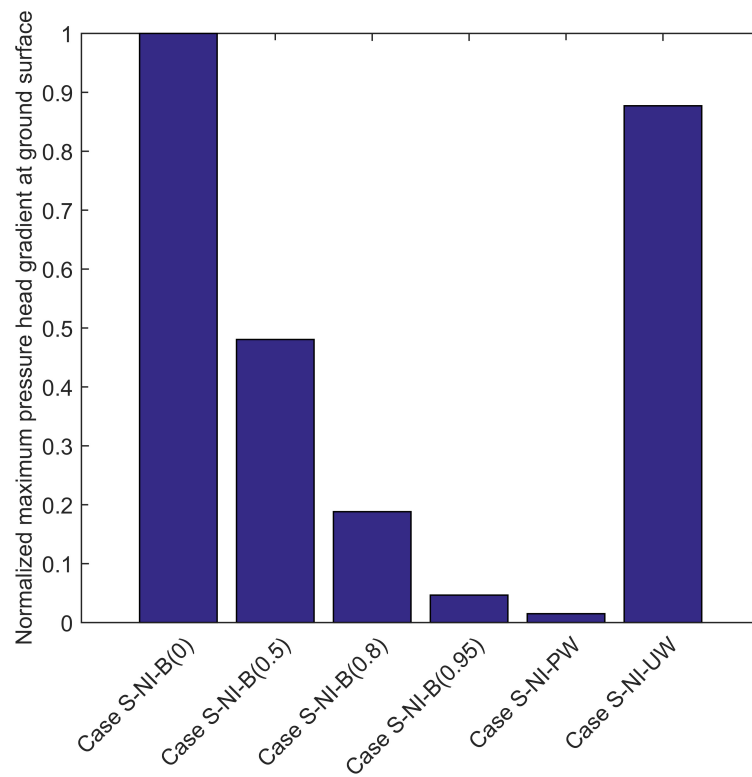


Figure 5.18: Maximum excess pore water pressure head gradient at the ground surface for the fully saturated soil condition for different cases, considering the nonlinear soil constitutive model, and the impermeable layer depth is at 10 m below the ground surface. The values are normalized with the maximum value, which occurs for Case S-NI-B(0) and is equal to 0.2125.

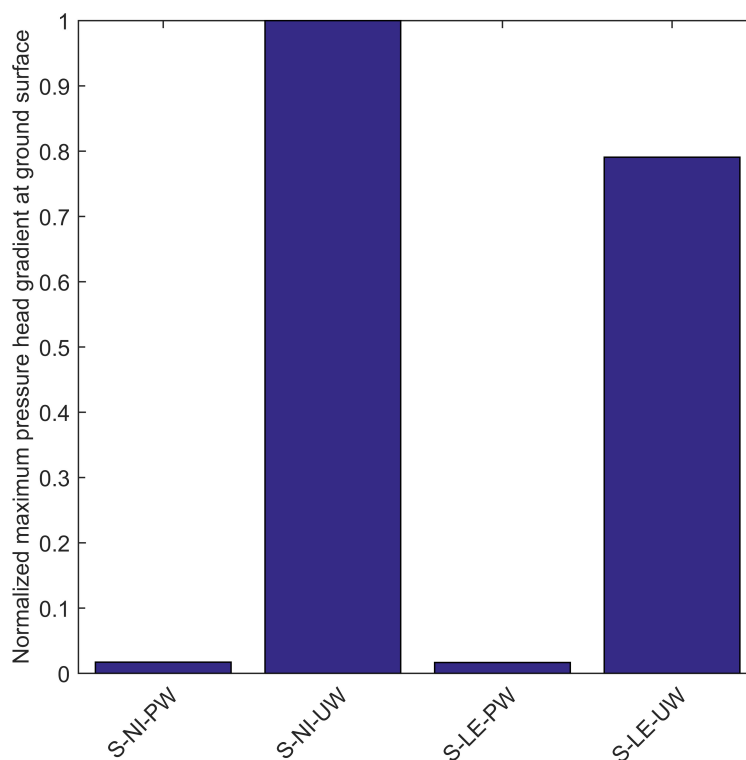


Figure 5.19: Comparison of the maximum excess pore water pressure head gradient at the ground surface from the linear soil constitutive model and the nonlinear soil constitutive model. The values are normalized with the maximum value, which occurs for Case S-NI-UW and is equal to 0.1864.

constitutive model is larger. The difference is more for when aird water is the pore fluid. The maximum excess pore water pressure head gradient at the ground surface for when de-aired water is the pore fluid is very small for both the linear and nonlinear soil constitutive models.

Figure 5.20 shows that the maximum excess pore water pressure head gradient reduces linearly with the reduction of B value. As seen in Figure 5.20, the variation of the surface excess pore water pressure head gradient linearly changes

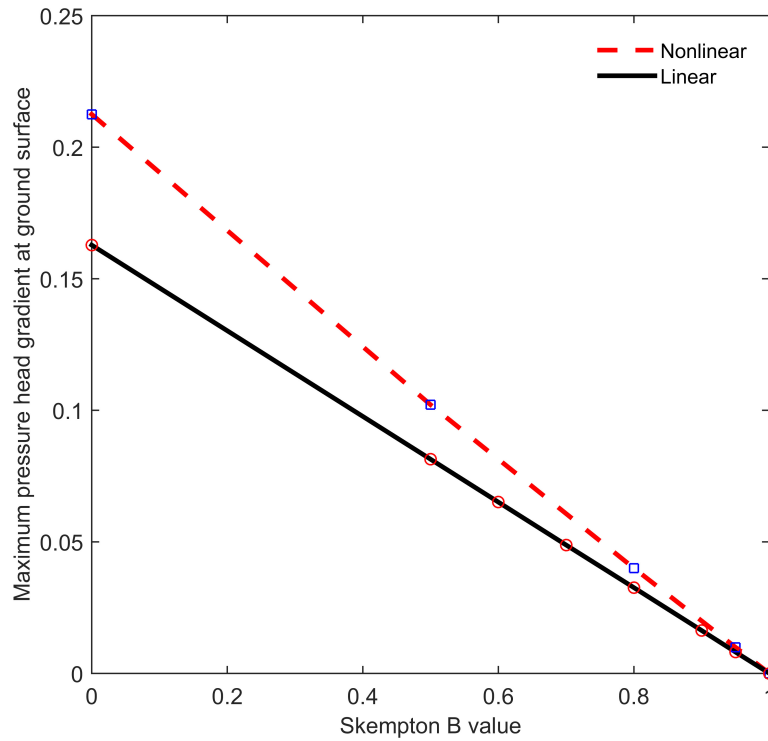


Figure 5.20: The linear variation of the maximum excess pore water pressure head gradient at the ground surface with B value for the fully saturated soil condition using linear and nonlinear soil constitutive models. The impermeable layer depth is at 10 m below ground surface.

with changes in the B value for both the linear soil constitutive model and the nonlinear soil constitutive model. As the B value decreases, the nonlinear soil constitutive model results in more excess pore water pressure head gradient at the ground surface compared with the linear soil constitutive model. Assuming de-aired water results in negligible excess pore water pressure head gradients at the ground surface for both soil constitutive models.

5.4.2 Unsaturated soil model

Two series of numerical experiments are performed for the one-dimensional unsaturated soil models: de-aired water and aired water. The groundwater table is set at one meter and three meters below the ground surface. Note that because the behavior of partially saturated soil is more complex, only the nonlinear soil constitutive model is used to perform numerical experiments on the unsaturated soil conditions.

The results of the analyses for case UN-NI-UW(3m) are shown in Figure 5.21 and 5.22. For the unsaturated soil condition, the absolute value of the excess pore water pressure head gradient during the run-up is very large compared with the same value when the saturated soil condition is modeled. In the unsaturated region, the pore water pressure head is negative, and at the initial condition, the pore water pressure head for the one-meter and three-meter water level are -1 m and -3 m, respectively. When tsunami run-up occurs, a significant negative excess pore water pressure head gradient results. Sometime after the tsunami loading commences, because of infiltration of water into the unsaturated zone, the soil becomes fully saturated (neglecting the residual water content). Similar to the fully saturated soil condition, the excess pore water pressure head gradient is more for the aired water case compared with the de-aired water case. Figure 5.23 shows the maximum excess pore water pressure head gradient at ground surface during tsunami draw-down for different water table depths with de-aired water and aired water. The excess pore water pressure head gradient for three meters of

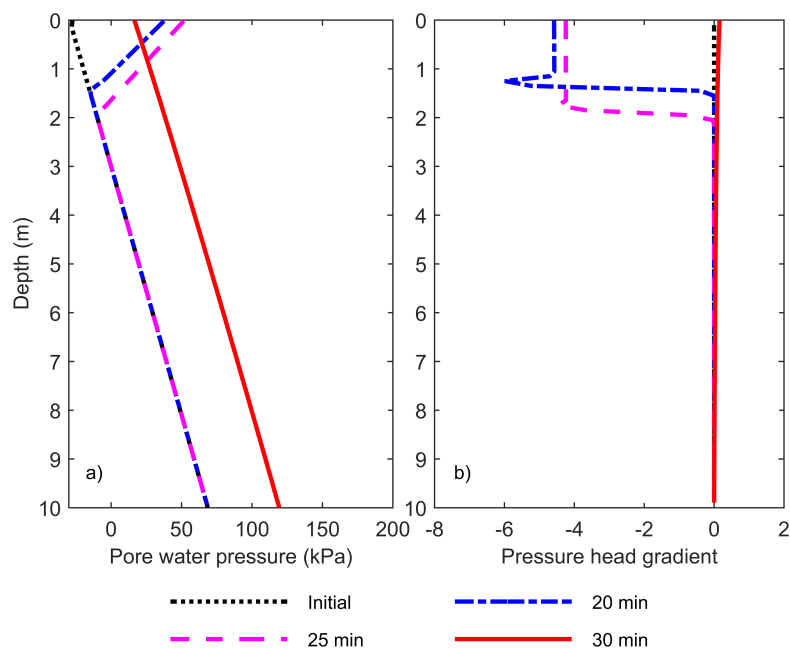


Figure 5.21: Case UN-NI-UW(3m): a) pore water pressure changes with depth at different times for unsaturated soil conditions when the groundwater table is at 3 m, considering the nonlinear soil constitutive model and aired water as the pore fluid; b) pressure head gradient changes with depth at different times for unsaturated soil conditions when the groundwater table is at 3 m, considering the nonlinear soil constitutive model and aired water as the pore fluid.

unsaturated soil is more than the excess pore water pressure head gradient for one meter of unsaturated soil. However, the excess pore water pressure head gradient for one meter of unsaturated soil is larger than the pressure head gradient for a fully saturated soil. Accordingly, as the groundwater table becomes lower, the maximum excess pore water pressure head gradient at the ground surface increases.

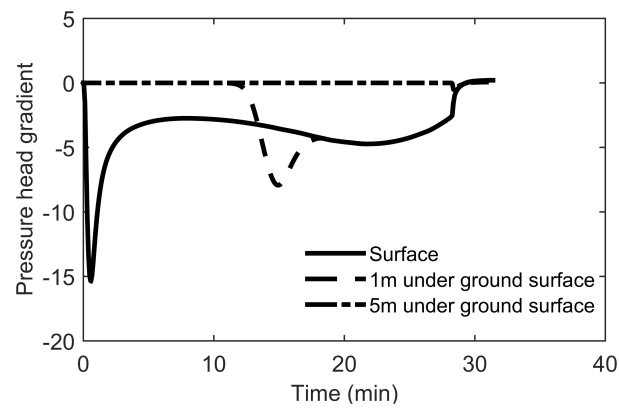


Figure 5.22: Case UN-NI-UW(3m): excess pore water pressure head gradient changes with time at different depths for unsaturated soil conditions when the groundwater table is at 3m, considering the nonlinear soil constitutive model and aird water as the pore fluid.

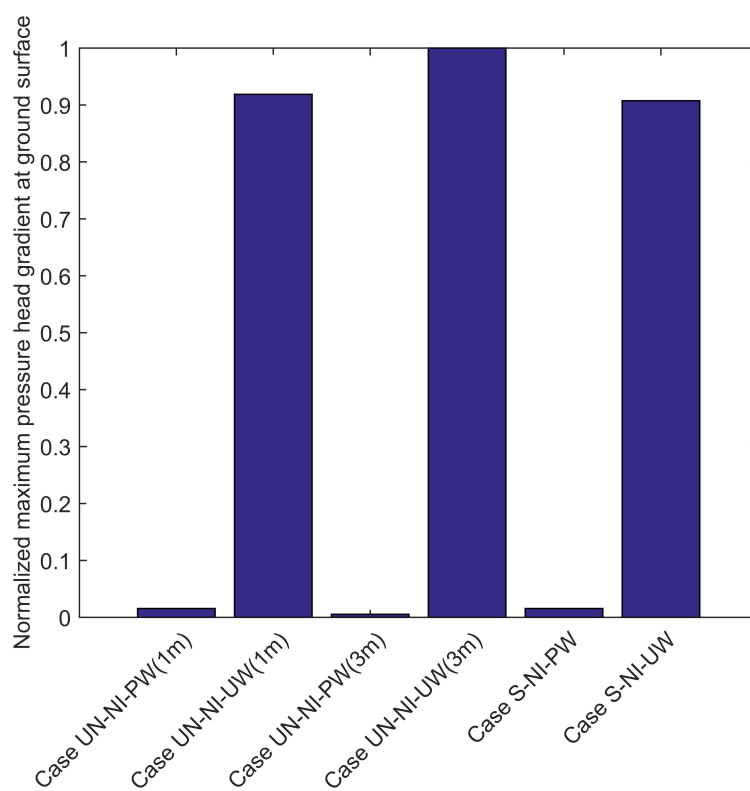


Figure 5.23: Maximum excess pore water pressure head gradients during the tsunami draw-down for different groundwater table depths. The values are normalized with the maximum value, which occurs for Case UN-NI-UW-(3m) and is equal to 0.2054.

Chapter 6: Analysis and discussion

In Chapter 6, we continue numerical experimentation using the coupled seepage-deformation model, but we investigate problems of interest more thoroughly. In §6.1, the effect of the depth to the impermeable layer on the pore water pressure and the excess pore water pressure head gradient induced by tsunami loading is investigated. In this section, we consider fully saturated and unsaturated soil conditions, linear and nonlinear soil constitutive models, and aird water and deaired water (see Table 6.1). In §6.2, the effect of tsunami properties (duration and amplitude) on the tsunami-induced pore water pressure response of soil beds is studied. All the cases in §6.2 assume fully saturated soil conditions, a nonlinear soil constitutive model, and aird water as the pore fluid. Note that in §6.2, the effect of different depths of the impermeable layer on the tsunami-induced pore water pressure response of soil beds is also investigated. In §6.3, the effect of hydraulic conductivity on the excess pore water pressure head gradient induced by tsunami loading is investigated. All cases in this section assume fully saturated soil conditions, a nonlinear soil constitutive model, aird water as the pore fluid, and a depth to the impermeable layer of 10 m. In §6.4, the effect of soil stiffness on the excess pore water pressure head gradient induced by tsunami loading is investigated. Both linear and nonlinear soil constitutive models are used in this section, and we assume fully saturated soil conditions with aird water as the pore

fluid. For the linear soil constitutive model, different constant shear moduli are studied. For the nonlinear soil constitutive model, different A values are investigated. Recall that A is related to the soil stiffness for the nonlinear soil constitutive model. In §6.4, we also calibrate the diffusion coefficient and find the equivalent value of diffusion coefficient for different values of soil stiffness for both the linear and nonlinear soil constitutive models. Section 6.5 has two parts. In the first part, the effect of different gas contents in water is investigated. In the second part, the pore water pressure induced by tsunami loading in a field scenario with measured entrained air bubbles is investigated. In §6.5, the nonlinear soil constitutive model is used. In §6.6, tsunami-induced liquefaction is studied. For all cases in §6.6, we assume that the soil bed is fully saturated, the nonlinear soil constitutive model is used, aird water is the pore fluid, and the depth to the impermeable layer is 10 m.

6.1 Depth to the impermeable layer

Soil beds are highly spatially variable, and one of the most highly variable properties is the depth of the impermeable layer (i.e., depth to bedrock). Recall that at the impermeable layer, $\partial h/\partial z$ is zero (i.e., the Neumann boundary condition). In §6.1, the effect of the impermeable layer depth on the the excess pore water pressure head gradient for both fully saturated and unsaturated soil conditions is investigated. Table 6.1 shows the details of the examined cases in §6.1.

Figure 6.1 shows temporal contours of $\partial h/\partial z$ versus depth for a fully saturated

Table 6.1: Different cases used to study the effect of impermeable layer depth, z_i . Note that the nomenclature used here is similar to §5.2. The first number of each case shows the depth of the impermeable layer in meters.

| Case | Constitutive Model | Water Type | $z_w(m)$ | $z_i(m)$ |
|-----------------|---------------------------|-------------------|----------|----------|
| 3-S-NI-UW | NI | Aired | 0 | 3 |
| 5-S-NI-UW | NI | Aired | 0 | 5 |
| 20-S-NI-UW | NI | Aired | 0 | 20 |
| 30-S-NI-UW | NI | Aired | 0 | 30 |
| 50-S-NI-UW | NI | Aired | 0 | 50 |
| 80-S-NI-UW | NI | Aired | 0 | 80 |
| 100-S-NI-UW | NI | Aired | 0 | 100 |
| 20-S-LE-UW | LE | Aired | 0 | 20 |
| 30-S-LE-UW | LE | Aired | 0 | 30 |
| 50-S-LE-UW | LE | Aired | 0 | 50 |
| 80-S-LE-UW | LE | Aired | 0 | 80 |
| 100-S-LE-UW | LE | Aired | 0 | 100 |
| 30-UN-NI-UW(1m) | NI | Aired | 0 | 30 |
| 50-UN-NI-UW(1m) | NI | Aired | 0 | 50 |
| 30-UN-NI-UW(3m) | NI | Aired | 0 | 30 |
| 50-UN-NI-UW(3m) | NI | Aired | 0 | 50 |

soil condition, with aird water, and a nonlinear soil constitutive model subjected to the hypothetical tsunami shown in Figure 5.1. The depth to the impermeable layer, z_i , is varied from 3 m (i.e., a shallow soil bed) to 50 m (i.e., a very deep soil bed). By examining Figure 6.1, it is obvious that $\partial h/\partial z$ is sensitive to the depth of the impermeable layer.

Figure 6.1a shows $\partial h/\partial z$ 20 minutes after the start of tsunami, which is during the middle of tsunami run-up. During this time, $\partial h/\partial z$ is negative, which indicates a downward flow of pore water (i.e., infiltration), and $\partial h/\partial z$ reduces as the depth of impermeable layer increases.

Figure 6.1b shows $\partial h/\partial z$ 25 minutes after the start of tsunami, which is at the beginning of tsunami draw-down. During this time, $\partial h/\partial z$ starts to increase, and the values are still negative for the deeper soil beds, but are positive for the shallower soil beds. Accordingly, during this time, we see a delay between the variation of tsunami height and pore water pressure response of the soil bed. The delay increases from the ground surface to the impermeable layer, and the delay increases with the increase of impermeable layer depth.

Figure 6.1c shows $\partial h/\partial z$ 30 minutes after the start of tsunami, which is close to the end of tsunami draw-down. The value of $\partial h/\partial z$ is positive for all the soil bed depths, and $\partial h/\partial z$ increases with the increase of impermeable layer depth. Comparing $\partial h/\partial z$ for $z_i = 30$ and $z_i = 50$ shows that the $\partial h/\partial z$ values are very close to each other, especially for the shallower depth.

Figure 6.2 shows how the maximum excess pore water pressure head gradient at the ground surface, $(\partial h/\partial z)|_{z=0}$, changes as a function of depth to the impermeable

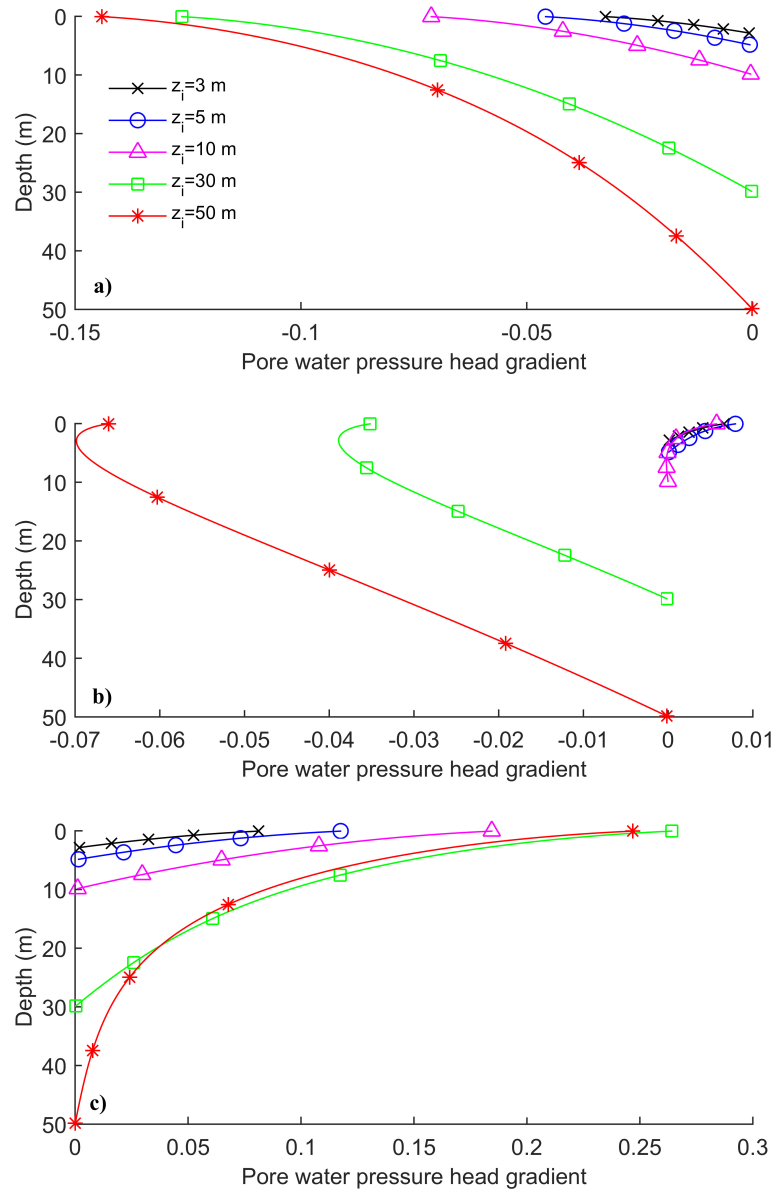


Figure 6.1: Excess pore water pressure head gradient with depth at different times and for different impermeable layer depths, z_i . The analyses are based on the nonlinear soil constitutive model, a) 20 min after the start of tsunami, b) 25 min after the start of tsunami, and c) 30 min after the start of tsunami.

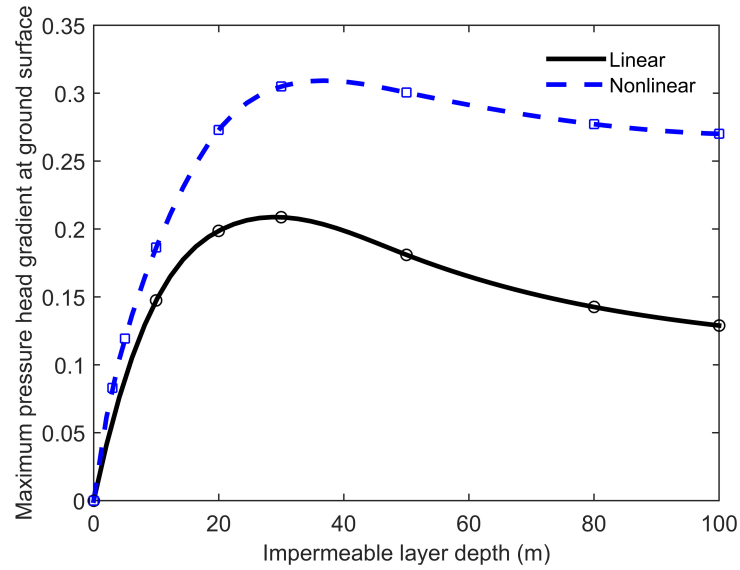


Figure 6.2: Maximum excess pore water pressure head gradient at the ground surface for the fully saturated soil condition using linear and nonlinear soil constitutive models with aired water for different impermeable layer depths.

layer during tsunami draw-down for the hypothetical tsunami shown in Figure 5.1 (i.e., 30 min after the start of the tsunami). Two soil constitutive models, linear and nonlinear, are considered, and the pore fluid, which fully saturates the soil bed, is assumed to be aired water. As seen in Figure 6.2, the maximum $(\partial h/\partial z)|_{z=0}$ values are consistently larger for the nonlinear soil constitutive model as compared to the linear soil constitutive model.

Figure 6.2 also shows that the maximum $(\partial h/\partial z)|_{z=0}$ increases as the impermeable layer depth increases up to about an impermeable layer depth of 30 m for both the linear and nonlinear soil constitutive models. For impermeable layer depths larger than 30 m, the maximum $(\partial h/\partial z)|_{z=0}$ value slightly decreases, and the decrease is more pronounced for the linear soil constitutive model. The devia-

tion from asymptotic behavior (i.e., post-peak reduction) is caused by the increase of soil stiffness with depth (i.e., the increase of shear modulus, G , shown in Figure 5.3, and the accompanying increase in the soil's bulk modulus, as shown in Equation 2.8), and the corresponding reduction in the B value (as shown in Equation 2.13).

Figure 6.3 shows the effect of the impermeable layer depth on the maximum $(\partial h/\partial z)|_{z=0}$ estimated for unsaturated soil conditions 30 min after the start of the hypothetical tsunami shown in Figure 5.1 (i.e., near the end of tsunami draw-down). When the ground water table is 1 m below the ground surface, the maximum $(\partial h/\partial z)|_{z=0}$ value increases with the increase of impermeable layer depth during the tsunami draw-down. When the ground water table is 3 m below the ground surface, the maximum $(\partial h/\partial z)|_{z=0}$ value reduces with an increase of impermeable layer depth.

6.2 Tsunami properties

Estimating the response of a soil bed to any natural hazard relies heavily on understanding the hazard. To understand the pore water pressure response in a soil bed subjected to tsunami loading, it is critical to understand the tsunami height and tsunami duration, which is the focus of §6.2. All investigated cases in §6.2 assume a fully saturated soil condition with aird water as the pore fluid. The nonlinear soil model is used, and the depth to impermeable layer varies.

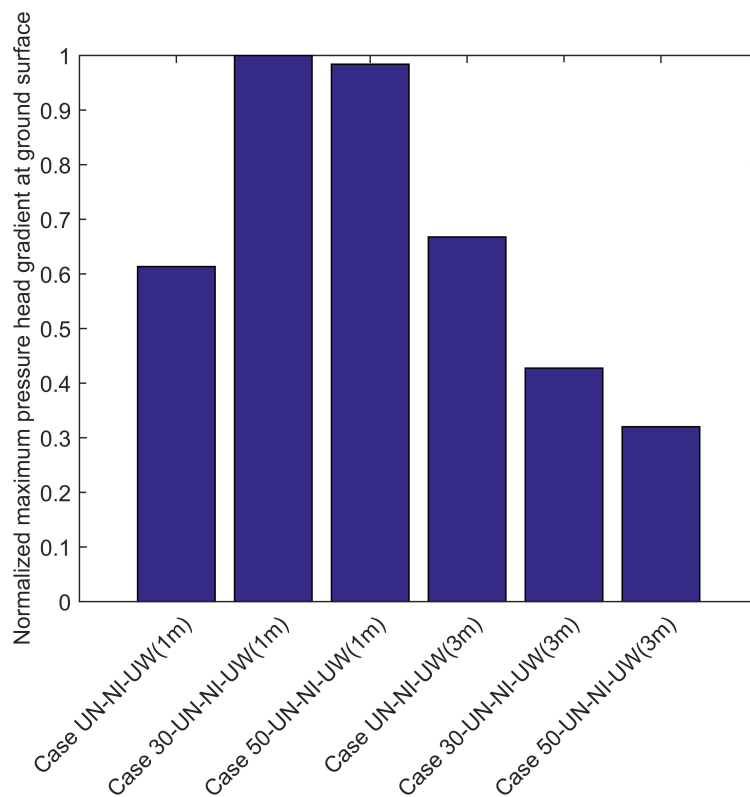


Figure 6.3: Maximum excess pore water pressure head gradient during tsunami draw-down for different water table depths and for different impermeable layer depths. The values are normalized with the maximum value, which occurs for Case 30-UN-NI-UW(1m) and is equal to 0.3076. Note that the first number refers to the depth of impermeable layer and for the cases that do not start with a number, the depth of the impermeable layer is 10 m.

6.2.1 Tsunami height

To investigate the effect of tsunami height on the excess pore water pressure head gradient, three hypothetical tsunamis with different maximum flow heights, but the same durations, are created. The three hypothetical tsunamis, which are shown in Figure 6.4, are created by scaling the dimensionless tsunami flow height-time series shown in Figure 5.1a with the scaling relationships shown in Equation 5.2. The three hypothetical tsunamis, labeled “large height” ($\psi = 1/160$, $L = 25$ km), “medium height” ($\psi = 1/100$, $L = 40$ km), and “small height” ($\psi = 1/70$, $L = 57.1$ km), are shown in Figure 6.4. Note that the medium height tsunami shown in Figure 6.4 is the same as the hypothetical tsunami shown in Figure 5.1.

Figure 6.5 shows the maximum $(\partial h/\partial z)|_{z=0}$ values for the three hypothetical tsunamis as a function of the impermeable layer depth. Note that the maximum $(\partial h/\partial z)|_{z=0}$ value occurs at the end of tsunami draw-down. As expected, the maximum values of $(\partial h/\partial z)|_{z=0}$ increase with an increase of tsunami height. Figure 6.5 also shows that the value of maximum $(\partial h/\partial z)|_{z=0}$ is relatively stable when the depth of impermeable layer is relatively large (i.e., greater than ≈ 30 m for the specific tsunami case examined).

Figure 6.6 shows the maximum $(\partial h/\partial z)|_{z=0}$ as a function of wave height for impermeable layer depths, z_i , of 10, 30, and 50 m. It can be seen that the relationship between the wave height and the maximum $(\partial h/\partial z)|_{z=0}$ is relatively linear for the cases shown on Figure 6.6. In addition, Figure 6.6 also shows that the maximum $(\partial h/\partial z)|_{z=0}$ is nearly the same when the impermeable layer depth, z_i ,

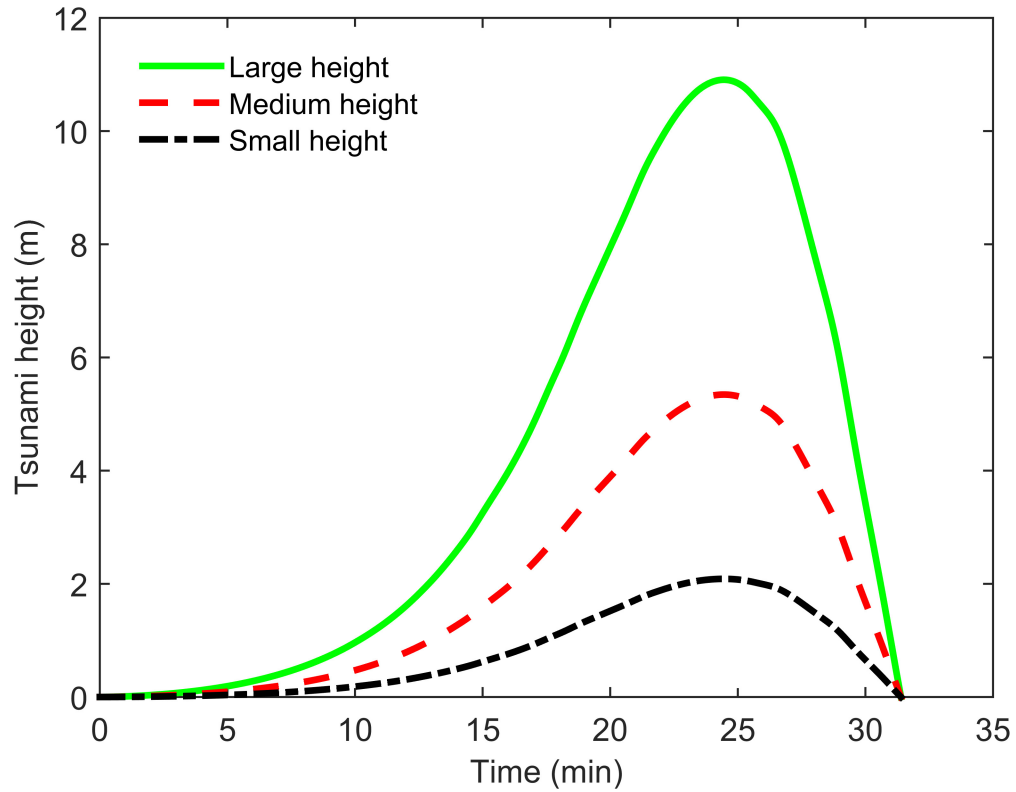


Figure 6.4: Three hypothetical tsunamis with different maximum flow heights developed using the Carrier et al. (2003) approach at the shoreline. The tsunami duration is constant for all three hypothetical tsunamis and equal to the duration of the hypothetical tsunami shown in Figure 5.1b (i.e., ≈ 32 min). The beach slopes, ψ , of the large, medium, and small height hypothetical tsunamis are $1/70$, $1/100$ and $1/160$, respectively, and the length scales, L , are 57.1, 40, and 25 km for the large, medium, and small height hypothetical tsunamis, respectively.

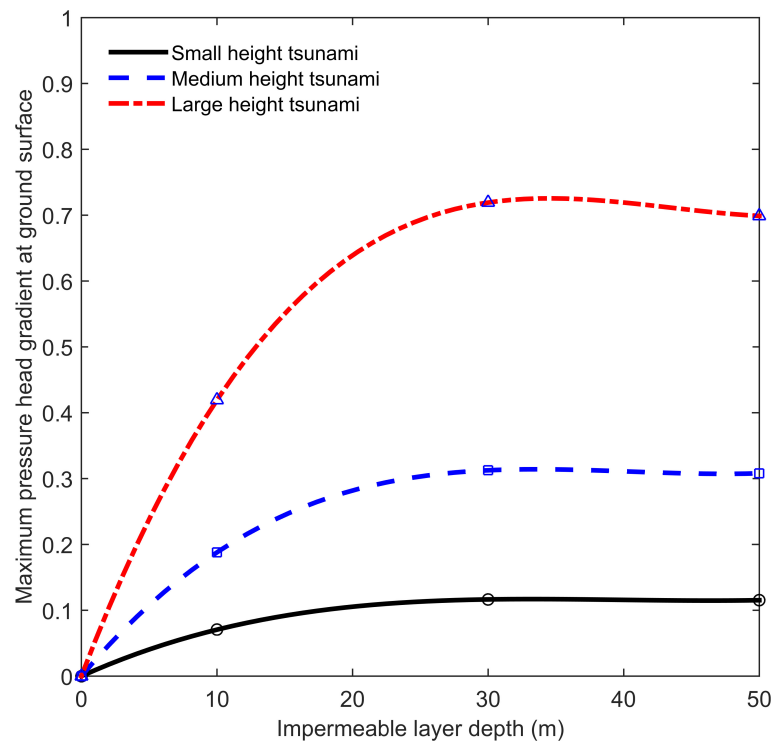


Figure 6.5: The variation maximum excess pore water pressure head gradient at the ground surface for tsunamis with different heights.

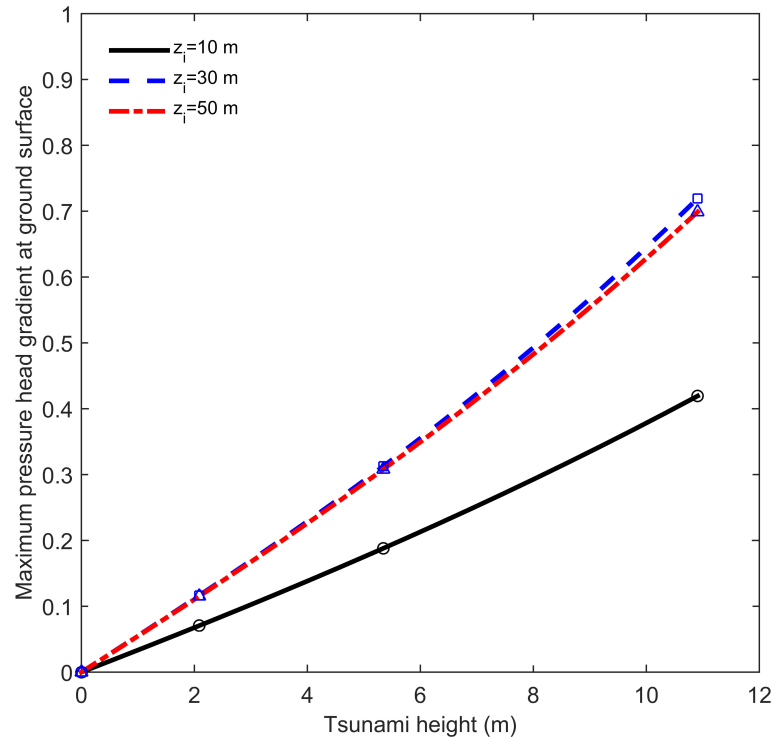


Figure 6.6: The variation maximum excess pore water pressure head gradient at the ground surface with wave amplitude for different impermeable layer depths.

is 30 or 50 m, regardless of the tsunami wave height.

The variation of $\partial h/\partial z$ with depth for different wave heights considering a 10 m impermeable layer depth is shown in Figure 6.7. The maximum and minimum $\partial h/\partial z$ values at all depth are caused by the large height tsunamis. For all depths, the small height tsunami has the lowest absolute value of $\partial h/\partial z$.

Figure 6.8 shows the variation of the maximum $(\partial h/\partial z)|_{z=0}$ normalized with respect to the maximum $\partial h/\partial z$ with the impermeable layer depth. The shape of the all three curves in Figure 6.4 are the same, which indicates that effect of impermeable layer depth on the maximum $\partial h/\partial z$ induced by tsunamis with

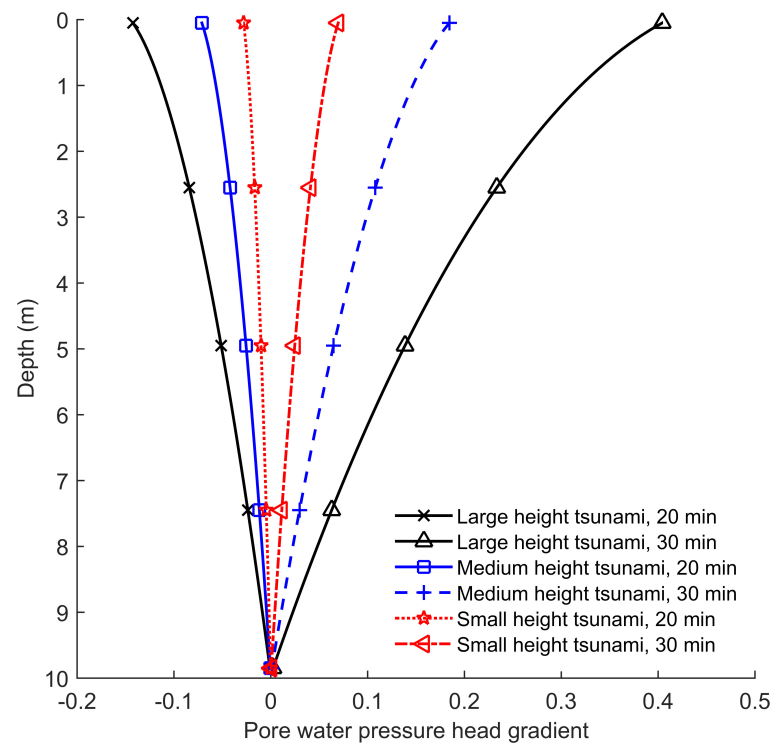


Figure 6.7: The variation of excess pore water pressure head gradient with depth for a 10 m impermeable layer depth and for different wave heights.

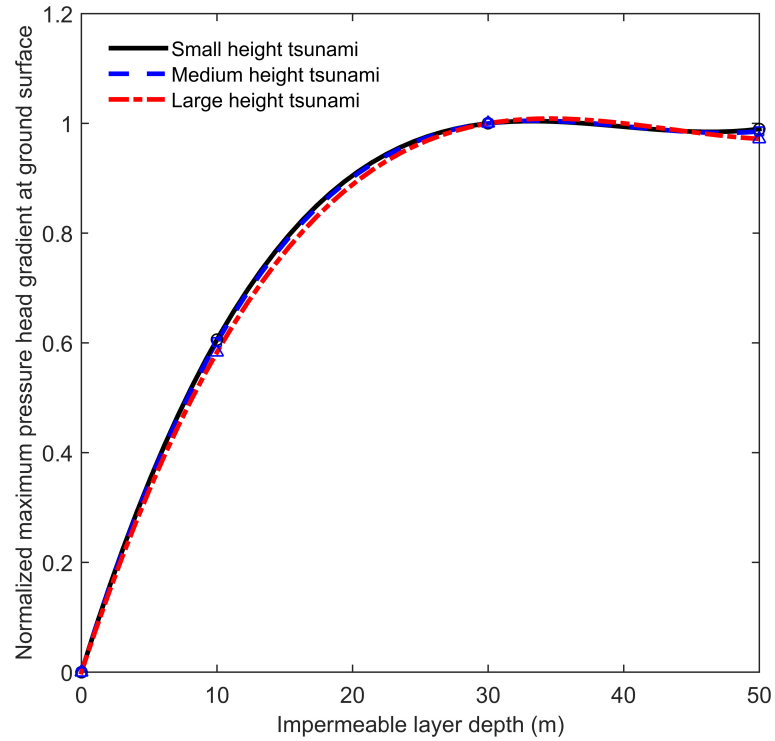


Figure 6.8: The variation of normalized maximum excess pore water pressure head gradient at the ground surface with the impermeable layer depth for waves with different amplitudes but the same duration.

different heights loading the soil bed is similar.

6.2.2 Tsunami duration

To investigate the effect of tsunami duration on $\partial h/\partial z$, three hypothetical tsunamis with different durations, but the same maximum flow heights, are created. The three hypothetical tsunamis, which are shown in Figure 6.9, are created by scaling the dimensionless tsunami flow height-time series shown in Figure 5.1a with the scaling relationships shown in Equation 5.2. The three hypothetical tsunamis,

labeled “long duration” ($\psi = 1/200$, $L = 80$ km), “medium duration” ($\psi = 1/100$, $L = 40$ km), and “short duration” ($\psi = 1/50$, $L = 20$ km), are shown in Figure 6.9. Note that the medium duration tsunami shown in Figure 6.9 is the same as the hypothetical tsunami shown in Figure 5.1b (and the same as the medium height tsunami shown in Figure 6.4). The long duration hypothetical tsunami shown in Figure 6.4 has an unusually long duration, but it is used to understand the mechanism of sediment instability and the response trends for the extreme case.

For the numerical experimentation in this section, we assume nonlinear constitutive model with aired water. Figure 6.10 shows the maximum $(\partial h/\partial z)|_{z=0}$ as a function of the impermeable layer depth and tsunami duration. The short duration tsunami produces the largest maximum $(\partial h/\partial z)|_{z=0}$, which occurs at the end of the tsunami draw-down, and the long duration tsunami produces the smallest maximum $(\partial h/\partial z)|_{z=0}$, which also occurs at the end of the tsunami draw-down. Recall that the trend is reversed when the tsunami flow height is varied, as shown in Figure 6.5; i.e., the large height tsunami creates the largest maximum $(\partial h/\partial z)|_{z=0}$. The short duration tsunami has a shorter draw-down period, so the velocity of the retreating water is quicker, and as a result, the release in total stress from the ground surface caused by the overlying water weight is also quicker. The preceding physical description leads to a larger sediment instability potential, as discussed by Sakai et al. (1992) and Yeh and Mason (2014), among other researchers.

Figure 6.10 also shows that the value of the maximum $(\partial h/\partial z)|_{z=0}$ reaches an asymptotic value when the impermeable layer depth becomes larger than approximately 30 m. Recall that the same observation was made when the variation of

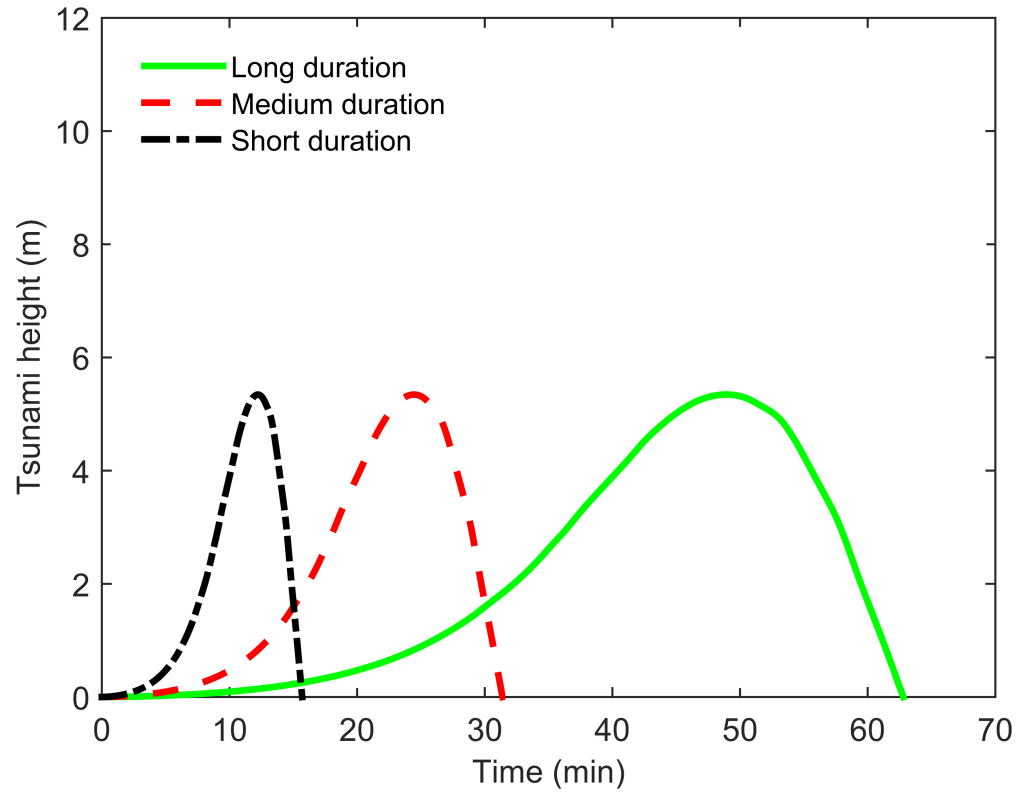


Figure 6.9: Three hypothetical tsunamis with different durations developed using the Carrier et al. (2003) approach at the shoreline. The maximum tsunami flow height is constant for all three hypothetical tsunamis and equal to the maximum flow height of the hypothetical tsunami shown in Figure 5.1b (i.e., ≈ 5.5 m). The beach slopes, ψ , of the long, medium, and short duration hypothetical tsunamis are $1/200$, $1/100$ and $1/50$, respectively, and the length scales, L , are 80, 40, and 20 km for the long, medium, and short duration hypothetical tsunamis, respectively.

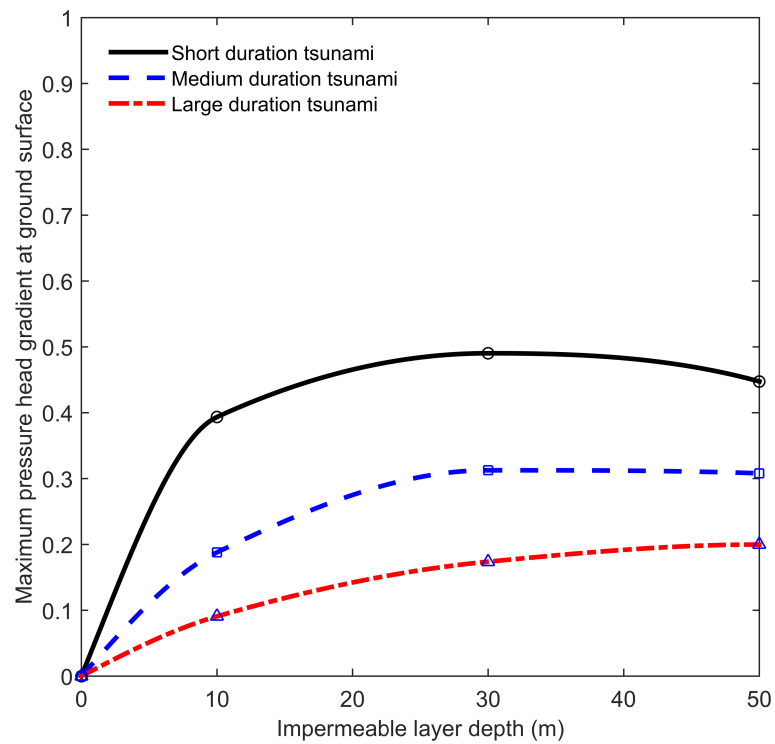


Figure 6.10: The variation maximum excess pore water pressure head gradient at the ground surface for waves with different durations.

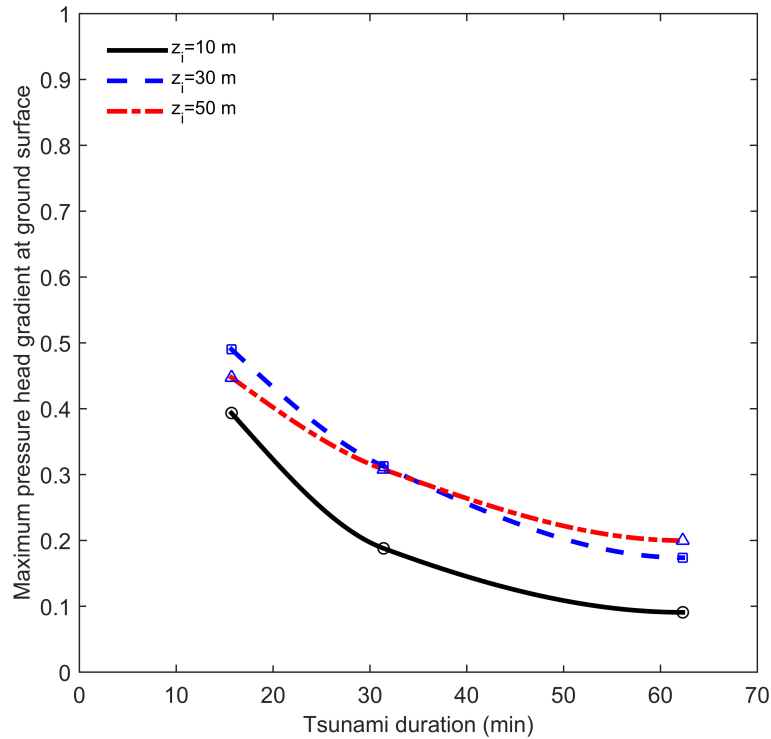


Figure 6.11: The variation maximum excess pore water pressure head gradient at the ground surface with tsunami duration for different impermeable layer depths.

tsunami flow height was investigated, as shown in Figure 6.5.

Figure 6.11 shows the maximum $(\partial h/\partial z)|_{z=0}$ versus impermeable layer depth for different tsunami durations. As the tsunami duration increases, the maximum $(\partial h/\partial z)|_{z=0}$ reaches an asymptotic value, which is nearly equivalent for the $z_i = 30$ m and $z_i = 50$ m cases. As the tsunami duration decreases, the curves show a significant increase in maximum $(\partial h/\partial z)|_{z=0}$. Figure 6.11 lends more credence to the observation also gleaned from Figures 6.5 and 6.10; i.e., that large height, short duration tsunamis are the most likely to cause sediment instability.

As an aside, following the preceding observation, Figures 6.4 and 6.9 show the

scaling factors required to create the different flow height and different duration hypothetical tsunamis, respectively. Note that the scaling factor trends for beach slope are reversed; i.e., a large height tsunami requires a steeper beach slope than a small height tsunami, whereas a long duration tsunami requires a shallower beach slope than a short duration tsunami (assuming, of course, that duration is fixed for the variable height tsunamis and amplitude is fixed for the variable duration tsunamis). The trends can be seen clearly by examining the scaling relationships shown in Equation 5.2. For the same dimensionless hypothetical shoreline tsunami (i.e., Figure 5.1a), it is apparent that to create a larger height tsunami, the beach slope, ψ , and length scale, L , should be increased, and to create a shorter duration tsunami, the beach slope, ψ , should be increased, but the length scale, L , should be decreased. Accordingly, the solutions to the nonlinear shallow-water wave equations, which govern tsunami propagation, dictate that if the tsunami height increases, the tsunami duration also increases given that the beach slope is constant. Note that the Carrier et al. (2003) method should only be used for relatively shallow beach slopes.

Figures 6.4 and 6.9 show the maximum $(\partial h/\partial z)|_{z=0}$, which is important for understanding sediment instability potential. Figure 6.12 shows the $\partial h/\partial z$ versus depth at different times (i.e., tsunami run-up and draw-down) for the three hypothetical tsunamis with different durations. Because the three hypothetical tsunamis have different durations, it is impossible to compare the same temporal contours for all three tsunamis; accordingly, we chose temporal contours, $T_1 = 0.64T_d$ and $T_2 = 0.96T_d$, where T_d is the total tsunami duration. T_1 occurs

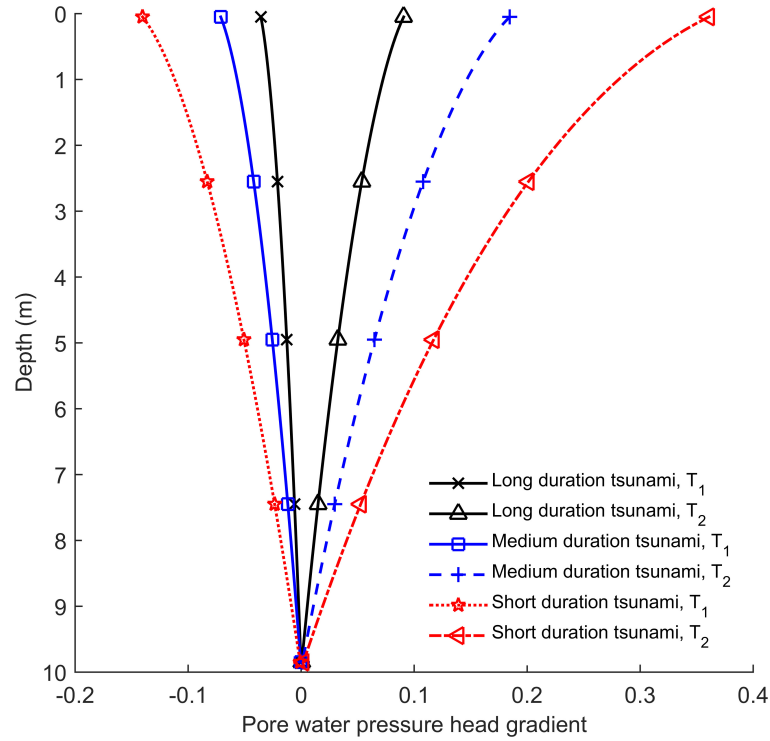


Figure 6.12: The variation of excess pore water pressure head gradient with depth for different tsunamis with different durations but similar amplitudes at times T_1 and T_2 , where $T_1 = 0.64T_d$, and $T_2 = 0.96T_d$. T_d is the duration of tsunami. Note that T_1 occurs during run-up and T_2 occurs during the draw-down.

during tsunami run-up, and T_2 occurs during tsunami draw-down. The short duration tsunami creates the largest $\partial h/\partial z$ during the draw-down phase. The short duration tsunami also leads to the smallest $\partial h/\partial z$ recorded during the tsunami run-up phase.

Normalizing the maximum $(\partial h/\partial z)|_{z=0}$ with the maximum $(\partial h/\partial z)|_{z=0}$ from Figure 6.10 results in three different curves (i.e., they do not match with each other) unlike the Figure 6.8 for the waves with the same amplitude as shown in Figure 6.13. This means that effect of impermeable layer depth on maximum

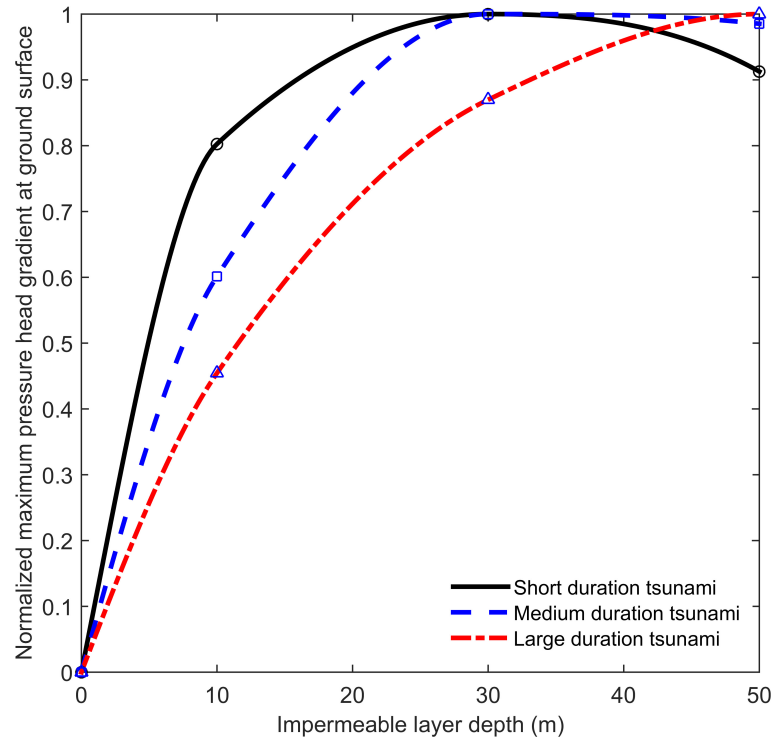


Figure 6.13: The variation of normalized maximum excess pore water pressure head gradient at the ground surface with the impermeable layer depth for waves with different durations but the same wave height.

$(\partial h/\partial z)|_{z=0}$ induced by tsunamis with different duration is not similar.

From the discussions in §6.2.1 and §6.2.2, it is apparent that the tsunami flow height and tsunami duration has a large effect on the expected $\partial h/\partial z$ values. Figure 6.8 and 6.13 show that the effect of impermeable layer is different on tsunamis with different properties (i.e., tsunami duration and height). Therefore, we need to incorporate the tsunami characteristics in $\partial h/\partial z$ and impermeable layer. Figure 6.14 shows the normalized maximum $(\partial h/\partial z)|_{z=0}$ versus the normalized impermeable layer depth. The maximum $(\partial h/\partial z)|_{z=0}$ is normalized by the maximum

$(\partial h/\partial z)|_{z=0}$ recorded over a range of impermeable layer depths (i.e., maximum normalizing values taken from Figures 6.5 and 6.10). The impermeable layer depth is normalized by $\sqrt{C_{v0}T_d}$, where $C_{v0}=2,117 \text{ cm}^2/\text{s}$ (i.e., $12.7 \text{ m}^2/\text{min}$), as determined from Equation 4.19, and T_d is the tsunami duration. C_{v0} is the initial coefficient of consolidation at ground surface. The results in Figure 6.14 shows that the normalized maximum $(\partial h/\partial z)|_{z=0}$ versus impermeable layer depth estimated from all the hypothetical tsunamis with small, medium, and large tsunami flow heights, and short, medium and long durations, is well normalized by $\sqrt{C_{v0}T_d}$. From examining Figure 6.14, it is apparent that the maximum $(\partial h/\partial z)|_{z=0}$ is observed within the range of $z_i/\sqrt{C_{v0}T_d}$ equal to 1.5 and greater. Given that C_{v0} can range from ≈ 0.05 to $70 \text{ m}^2/\text{min}$ for beach sands (Yeh et al., 2004), and T_d can range from ≈ 5 min to 40 min, it is apparent that the depth of impermeable layer that leads to the maximum $(\partial h/\partial z)|_{z=0}$ also varies widely. It has already been observed that short duration tsunamis and smaller values of C_{v0} create larger maximum values of $(\partial h/\partial z)|_{z=0}$; accordingly, based on Figure 6.14, the “critical” depth of impermeable layer (i.e., the smallest depth that creates the largest maximum $(\partial h/\partial z)|_{z=0}$; $z_i/\sqrt{C_{v0}T_d} \approx 1.5$) also decreases as T_d and C_{v0} decrease, which is a realistic situation for many plane beaches subject to tsunamis.

Note that in classical soil mechanics, the dimensionless time factor, T_v , is defined as $T_v = (C_v \cdot t)/(H_{dr}^2)$, where H_{dr} is the length of the longest drainage path (Taylor, 1948). For one way drainage (which is the case we assume), H_{dr} is equal to the entire thickness of the sand layer; accordingly, herein, $H_{dr} = z_i$. Note that T_v has values between zero and infinity. At the start of consolidation $T_v = 0$, and

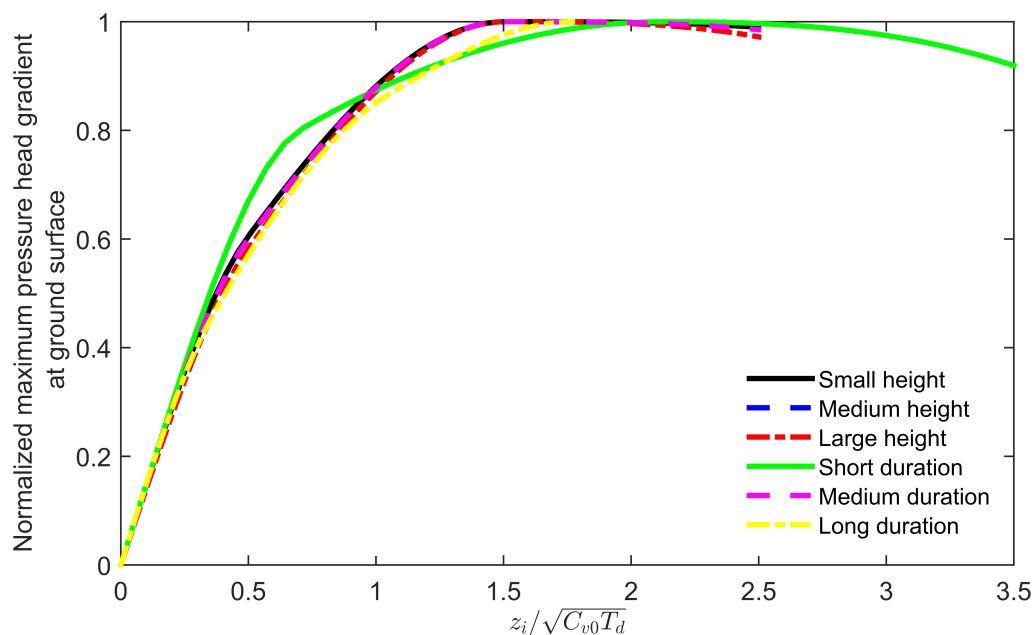


Figure 6.14: The variation of normalized maximum excess pore water pressure head gradient with the impermeable layer depth, z_i , that is normalized with $\sqrt{C_{v0}T_d}$

when the layer is completely consolidated $T_v \rightarrow \infty$. Comparing T_v with $z_i/\sqrt{C_{v0}T_d}$ shows that

$$z_i/\sqrt{C_{v0}T_d} \propto \sqrt{1/T_v}. \quad (6.1)$$

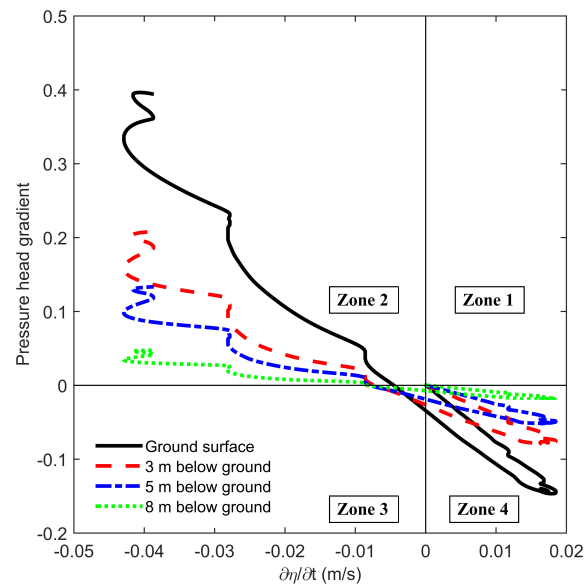
At the start of consolidation, $T_v = 0$ and $z_i/\sqrt{C_{v0}T_d} \rightarrow \infty$; accordingly, $\partial h/\partial z$ is large at the start of consolidation. In contrast, when the soil bed is completely consolidated, $T_v \rightarrow \infty$; therefore, $z_i/\sqrt{C_{v0}T_d} \approx 0$, which results in $\partial h/\partial z = 0$. Similar trends can be observed in Figure 6.14; i.e., as $z_i/\sqrt{C_{v0}T_d}$ increases, the maximum $(\partial h/\partial z)|_{z=0}$ also increases.

Recall that the sediment instability potential increases as the tsunami draw-down occurs more quickly. We examine the time derivative of the tsunami flow

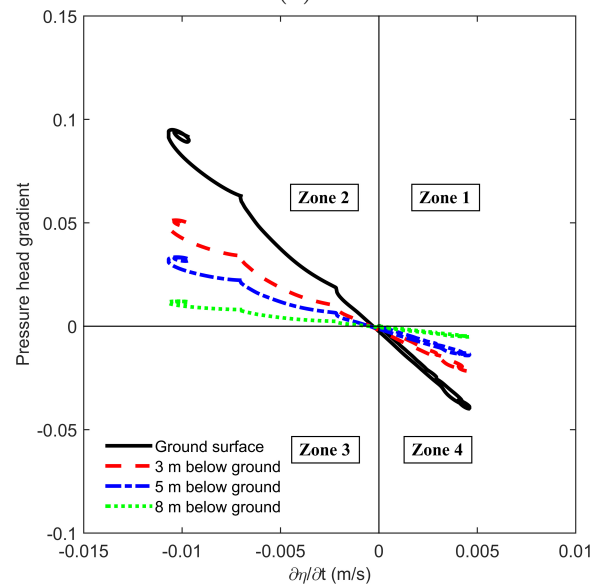
height, $\partial\eta/\partial t$, versus $\partial h/\partial z$, which is shown in Figure 6.15a, to examine this concept. To understand Figure 6.15a, it is instructive to first examine the plot for the ground surface. Initially, the tsunami run-up starts occurring, and $\partial\eta/\partial t$ is positive, but $\partial h/\partial z$ is negative. This corresponds to the initial part of the ground surface curve shown in Zone 4 of Figure 6.15a. As time progresses, the tsunami run-up phase ends, and $\partial\eta/\partial t$ becomes zero. Notice that when $\partial\eta/\partial t = 0$ at the end of run-up, that $\partial h/\partial z$ does not equal zero; accordingly, there is a lag between the tsunami flow height-time series and $\partial h/\partial z$, as expected. Zone 3 allows us to see this phase of the process — when tsunami draw-down is occurring, but $\partial h/\partial z$ is still negative. Finally, in Zone 2, $\partial\eta/\partial t > 0$ and $\partial h/\partial z$ is also positive, which indicates an upward flow of pore water during tsunami draw-down. The curve ends in Zone 2 at the end of tsunami draw-down. If we examined progressive wave loading, instead of tsunami loading, then the curve would venture through Zone 1 during the wave trough, before starting the process again.

Figure 6.15a and 6.15b also show how the relationship between $\partial\eta/\partial t$ and $\partial h/\partial z$ as a function of depth below the ground surface for short duration tsunami and long duration tsunami, respectively. It can be seen that the general shape of the curves remains the same as a function of depth, but the “slope” of the curves becomes more shallow, which indicates that $\partial h/\partial z$ reduces significantly as a function of depth, as expected based on the boundary condition at the impermeable layer. The time lag between the tsunami flow height time series and $\partial h/\partial z$ increases with depth.

Notably, the curves in Figure 6.15a are not smooth, which results from the



(a)



(b)

Figure 6.15: The variation of excess pore water pressure head gradient at different depths with the rate of tsunami loading for the short duration tsunami and for the condition when the impermeable layer depth is 10 m, a) short duration tsunami, b) long duration tsunami.

tsunami height-time series not being smooth. As mentioned in § 5.1, when employing the Carrier et al. (2003) method, grid interpolation methods are needed to determine the final waveform in the physical $\hat{x} - \hat{t}$ domain, which leads to non-smooth curves. Note that this is a technical problem and it is not mathematical problem. In fact, the Carrier et al. (2003) method is an analytical solution. In addition, because we are assuming that $\hat{x} = 0$ (i.e., shoreline location), the waveforms become more difficult to interpolate.

Taking one more partial derivative of the excess pore water pressure head gradient yields, $\partial^2 h / \partial z^2$. Figure 6.16a and 6.16b show $\partial^2 h / \partial z^2$ versus $\partial \eta / \partial t$ for the short duration and long duration tsunami when the impermeable layer depth is 10 m. Recall that η also defines the pore water pressure at the ground surface (i.e., the total weight of the overlying tsunami water). Accordingly, the slopes of the curves shown in Figure 6.16a are proportional to the diffusion coefficient, C_v ; i.e.,

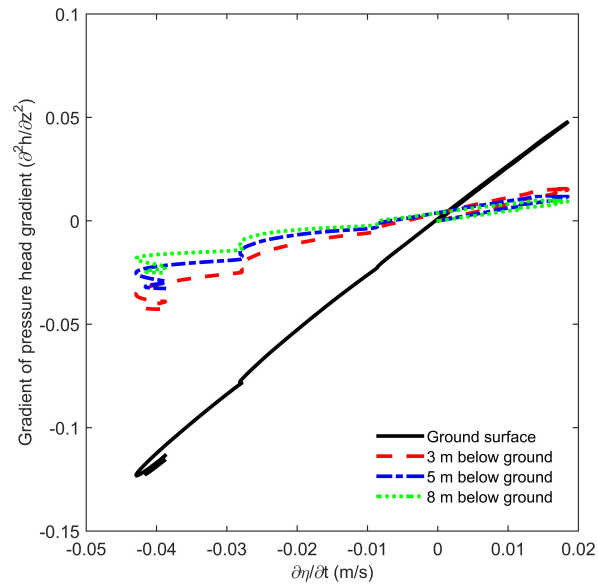
$$C_v \propto \frac{\partial \eta}{\partial t} / \frac{\partial^2 h}{\partial z^2} . \quad (6.2)$$

Note that both Figure 6.16a and 6.16b have the same slope (i.e., $\frac{\partial \eta}{\partial t} / \frac{\partial^2 h}{\partial z^2} \approx 0.37 \text{ m}^2/\text{s} = 3,700 \text{ cm}^2/\text{s}$) for the ground surface which means that the estimated coefficient of consolidation from both figures are the same. Note that this value is comparable with the C_{v0} estimated in §6.2.2. C_{v0} is the coefficient of consolidation estimated at the initial time at the ground surface, and the value of C_{v0} estimated here is the average coefficient of consolidation, which is estimated from the results of the soil constitutive model. We should note that C_v is not exactly equal to

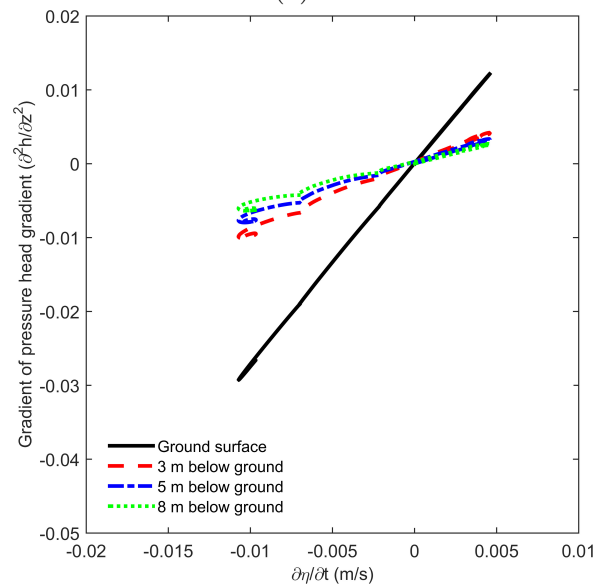
$\frac{\partial \eta}{\partial t} / \frac{\partial^2 h}{\partial z^2}$, because $\partial \eta / \partial t$ shows the changes of pore water pressure at the ground surface and is not the derivative of pore water pressure with respect to time under the ground. We should also note that taking the derivative of pore water pressure with respect to z two times numerically also reduces the accuracy of the result. From Figure 6.16, it can be seen that the slope of the curve is relatively shallow at the ground surface compared to the curves at deeper depths, which does not indicate that C_v is smaller at the ground surface, because $\partial \eta / \partial t$ represents the variation of the pore water pressure head with time at the ground surface and not underground.

6.3 Hydraulic conductivity

It is clear that the pore water pressure response of a soil bed subjected to tsunami loading is a function of the hydraulic conductivity, k_h , and $\partial h / \partial z$ is particularly sensitive to changes in k_h . As the value of k_h decreases, the absolute value of $\partial h / \partial z$ increases. For a fine sand, such as a beach sand, Terzaghi et al. (1996) reports the hydraulic conductivity to be ≈ 0.001 to 0.1 cm/s. A fine beach sand from South Beach, Oregon has a d_{10} of ≈ 0.015 cm, where d_{10} is the particle size for which 10% of the soil in a given batch is finer. Hazen's formula (Hazen, 1892), $k_h = C_H d_{10}^2$, also gives an estimate of hydraulic conductivity. C_H is an empirical coefficient, which is usually assumed to be 100 (Carrier, 2003), d_{10} is given in cm, and k_h is calculated in cm/s; accordingly, Hazen's formula yields an estimate of $k_h \approx 0.02$ cm/s, which is in the middle of the range of k_h reported by Terzaghi et al. (1996)



(a)



(b)

Figure 6.16: The variation of the derivative of pressure head gradient with respect to depth at different depths with the rate of tsunami loading for the condition when the impermeable layer depth is 10 m, a) short duration tsunami, b) long duration tsunami.

for a fine sand. Note that although Carrier (2003) has shown a wide range of C_H values reported by multiple researchers, herein we use the simple Hazen (1892) model to estimate the range of hydraulic conductivity for sand and compare that to the range from Terzaghi et al. (1996), because we need a reasonable range of values for hydraulic conductivity to perform the sensitivity analysis.

Based on the preceding discussion, to examine the sensitivity of the pore water pressure response to the hydraulic conductivity, we select the hydraulic conductivity range from 0.005 to 1 cm/s, which reasonably bounds the parameter space discussed above. Figure 6.17 shows the variation of the maximum $(\partial h/\partial z)_{z=0}$ as a function of the hydraulic conductivity for two hypothetical tsunamis: 1) the medium duration, medium height hypothetical tsunami (i.e., the “medium height” tsunami in Figure 6.4), and 2) the medium duration large height hypothetical tsunami (i.e., the “large height” tsunami in Figure 6.4). Note that the nonlinear soil constitutive model with aird water as the pore fluid is used, and the depth to the impermeable layer is 10 m for all cases. Figure 6.17 is plotted in terms of $\log_{10}(k_h)$, which shows the trend more clearly. From examining Figure 6.17, it is evident that the maximum $(\partial h/\partial z)_{z=0}$ reduces significantly with small increases of hydraulic conductivity, which is an observation that is true for both hypothetical tsunamis. For relatively large hydraulic conductivities (i.e., $k_h \gtrsim 0.1$ cm/s), the amplitude of the tsunami loading does not affect the value of the maximum $(\partial h/\partial z)_{z=0}$. However, for values of k_h smaller than approximately 0.1 cm/s, the deviation in the maximum $(\partial h/\partial z)_{z=0}$ becomes significant for the tsunamis with different amplitudes.

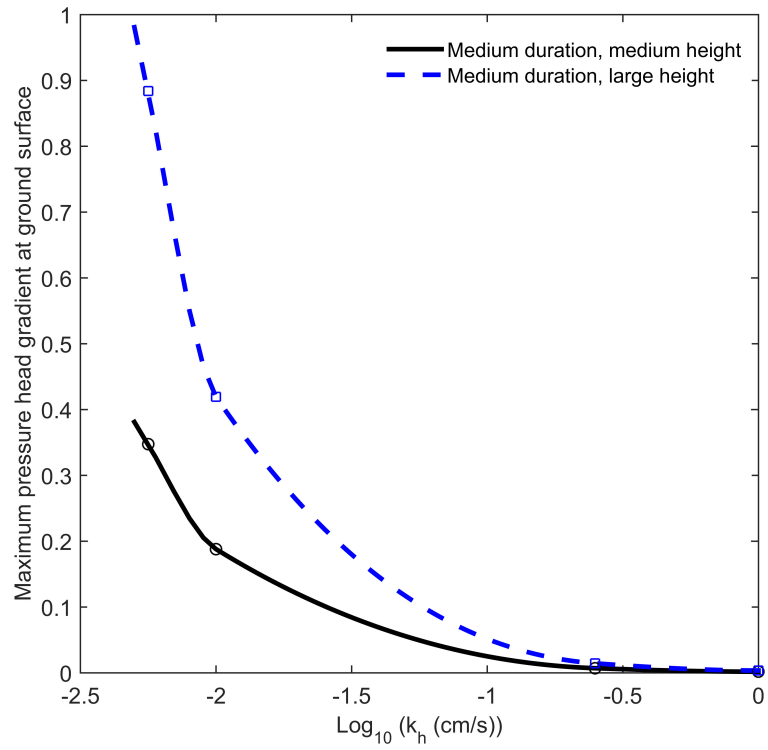


Figure 6.17: Variation of the maximum excess pore water pressure head gradient with the hydraulic conductivity during tsunami draw-down. Two types of tsunamis are considered: 1) a medium duration, medium flow height tsunami, and 2) a medium duration, large flow height tsunami. The minimum value of the x -axis corresponds to $k_h = 0.005$ cm/s and maximum value of the x -axis corresponds to $k_h = 1$ cm/s.

6.4 Soil bulk modulus

During tsunami run-up and draw-down, the pore water pressure changes at the ground surface, as shown many times in Chapters 5 and 6. It can be assumed that the pore water pressure diffuses from the top of the soil bed into the soil. In §6.4, we try to calibrate the diffusion equation. In other words, we attempt to find a diffusion coefficient that can predict the maximum excess pore water pressure head gradient at ground surface. The reason we calibrate the diffusion equation in this manner is because we try to find a simple way to predict the excess pore water pressure head gradient induced by tsunami loading.

Note that analytical solutions are available for the diffusion equation (Carslaw and Jaeger, 1959) (e.g., recall Equation 2.21 §2.3.3). We copy the diffusion equation here for convenience,

$$\frac{\partial p_w}{\partial t} = C_v^* \frac{\partial^2 p_w}{\partial z^2}, \quad (6.3)$$

where C_v^* is the diffusion coefficient. It should be noted that C_v^* is different than the coefficient of consolidation, C_v ; however, the diffusion equation shown in Equation 6.3 is similar to Terzaghi's one-dimensional consolidation equation.

Herein, the diffusion coefficient is calibrated for the maximum pore water pressure head gradient at the ground surface for three scenarios: 1) the fully saturated soil condition with a nonlinear soil constitutive model and the impermeable layer located at 50 m; 2) the fully saturated soil condition with a linear soil constitutive model with the impermeable layer located at 50 m; 3) the fully saturated soil conditions with a nonlinear soil constitutive model with the impermeable layer located

at 10 m. For all scenarios, aird water is assumed to be the pore fluid.

To calibrate the diffusion equation, first a sensitivity analysis is performed for the different scenarios. The variation of the maximum absolute value of excess pore water pressure head gradient at the ground surface with respect to different values of soil parameters is investigated. The variation of the maximum excess pore water pressure head gradient at the ground surface with different values of A (i.e., the nonlinear soil constitutive model) for the condition where the impermeable layer depth is 50 m is shown in Figure 6.18. The negative excess pore water pressure head gradient corresponds to downward seepage flow (i.e., during tsunami run-up) and the positive excess pore water pressure head gradient corresponds to the upward seepage flow (i.e., during tsunami draw-down). Different values of A are used to estimate the excess pore water pressure head gradient, and $A_{max} = 500$.

Recall that the parameter A is used to tune the shear stiffness of the soil bed. As A increases, the coefficient of volume compressibility, m_v , reduces and the B value also reduces. As a result, the absolute value of the maximum excess pore water pressure head gradient increases first and then reduces with an increase of A . The aforementioned increase and reduction of the maximum excess pore water pressure head gradient can be related to two competing effects that occur with the change of the B value and m_v as soil stiffness changes.

The variation of the minimum and maximum excess pore water pressure head gradient at the ground surface with G/G_{max} during the tsunami loading for the linear soil constitutive model and for the condition where the impermeable layer is at 50 m is shown in Figure 6.19. G_{max} is the maximum shear modulus in the

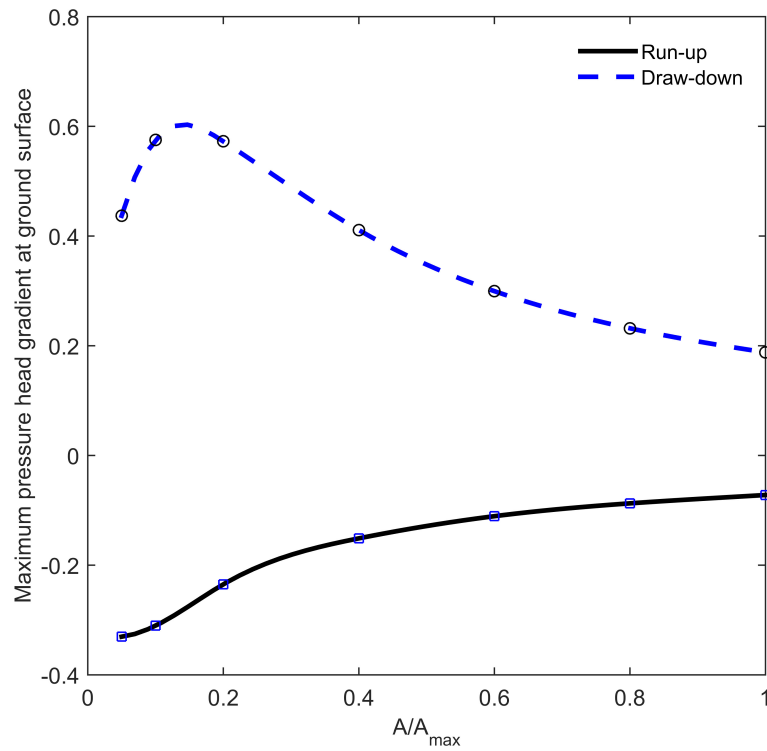


Figure 6.18: Maximum pressure head gradient at the ground surface for the fully saturated condition using nonlinear constitutive model, and the impermeable layer depth is at 50 m below ground surface.

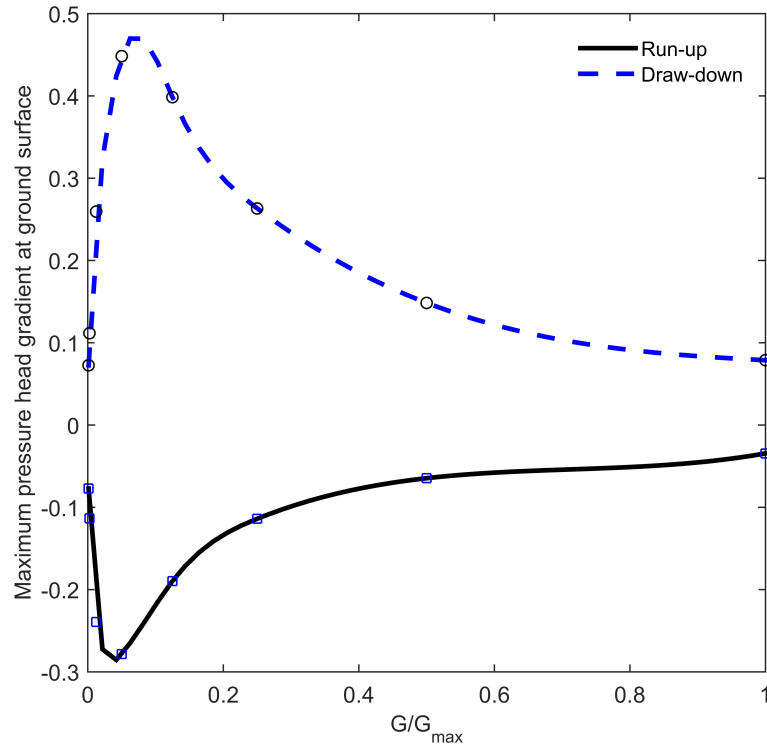


Figure 6.19: Maximum pressure head gradient at the ground surface for the fully saturated condition using linear constitutive model, and the impermeable layer depth is at 50 m below ground surface.

sensitivity analysis, which we assumed to be $G_{max} = 70MPa$. Note that herein, the G/G_{max} we predict is different from the typical G/G_{max} predicted for soil dynamics (e.g., Seed and Idriss, 1970). In this section, only G/G_{max} is used to normalize the shear modulus with the maximum assumed shear modulus. The shear modulus is assumed constant with depth.

The trend of variation of the maximum excess pore water pressure head gradient at the ground surface for the linear soil constitutive model is similar to the trend seen when the nonlinear soil constitutive model is used. As the shear modulus

increases, the absolute value of the maximum excess pore water pressure head gradient increases and then reduces. This trend refers to the two competing effect of soil stiffness on m_v and B value, as mentioned previously.

Figure 6.20 shows the variation of the maximum excess pore water pressure head gradient at the ground surface with the normalized diffusion coefficient using the assumptions that $\alpha = 1$, $\nu_u = 0.5$, and $B = 0$ (i.e., the uncoupled approach). In fact, the Yeh and Mason (2014) approach is used to estimate the excess pore water pressure head gradient at the ground surface. The absolute value of the maximum excess pore water pressure head gradient at the ground surface reduces as C_v^* increases, and the preceding change is larger for smaller values of C_v^* . The variation of the excess pore water pressure head gradient is very small for large values of C_v^* . Note that $C_{v,max}^* = 100,000 \text{ cm}^2/\text{s}$.

The calibration of the diffusion coefficient for different conditions is shown Figure 6.21. The calibration is based on the same value of the maximum excess pore water pressure head gradient at the ground surface.

6.5 Effects of entrained air bubbles

Field measurements by Okusa et al. (1984) indicate that seabeds are generally unsaturated due to the presence of gas, which is especially true at shallow depths, where the water pressure is not large enough to dissolve the small quantities of gas. As explained earlier, the air in water reduces the water's bulk modulus significantly; for instance, 3% of air in water reduces the water's bulk modulus from 2.2 GPa

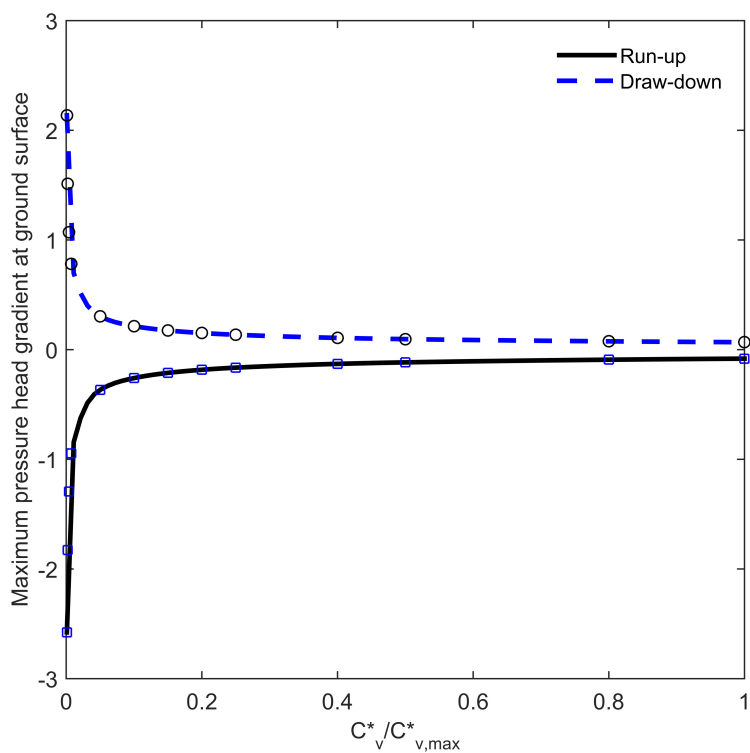


Figure 6.20: Maximum pressure head gradient at the ground surface for the fully saturated condition using Carslaw and Jaeger (1959) analytical solution. The diffusion coefficient is normalised with the maximum value of the $C_{v,max}^* = 100000 \text{ cm}^2/\text{s}$.

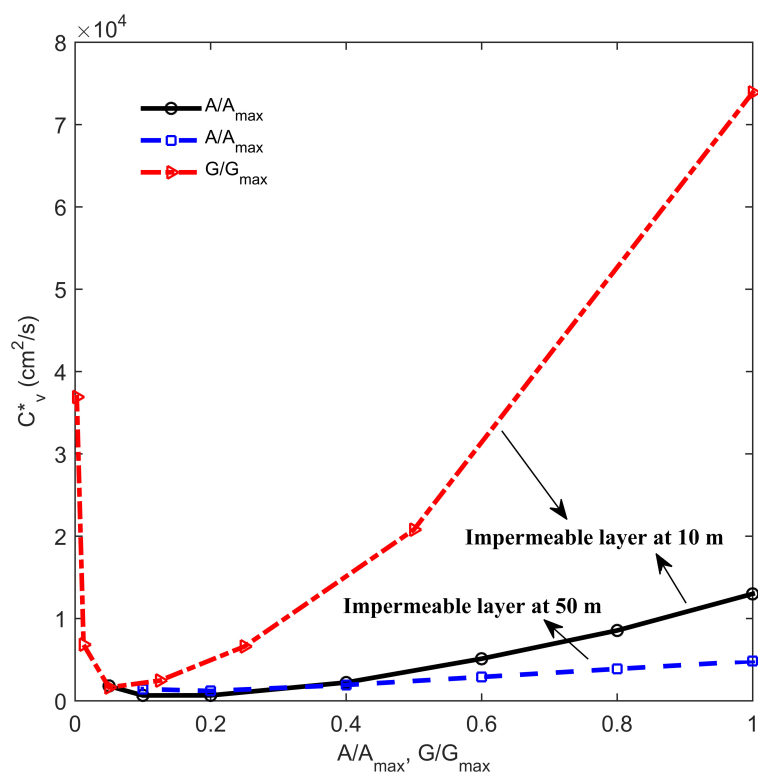


Figure 6.21: Calibration of the diffusion coefficient. The dotted line shows the relation between the diffusion coefficient and G/G_{max} where $G_{max} = 70$ MPa for the linear soil constitutive model, A/A_{max} where $A_{max} = 500$ for the nonlinear soil constitutive model. Note that the minimum value for G/G_{max} is 0.00125.

(i.e., de-aired water) to 4 MPa. Bonjean et al. (2004) reported the air content in within a beach sand from Capbreton, France in the depth range of 0 to 0.5 m, and they found an air content of up to 5%. Michallet et al. (2009) extrapolated the measurements performed by Bonjean et al. (2004) to a depth of 1.2 m. Herein, the extrapolated line from Michallet et al. (2009) is further extrapolated to a depth of 10 m, which is shown in Figure 6.22. Note that this is the only source we found regarding measuring the air content in the field. Note that Bonjean et al. (2004) did not measure the air in the water at shoreline, and they only used a camera to estimate the air bubbles in water. All cases examined in this section assume a fully saturated soil condition and the nonlinear soil constitutive model. The depth to impermeable layer is 10 m.

Herein, we consider a similar gas content distribution with depth at the shoreline (i.e. Figure 6.22) to model more realistic seabeds. Note that even in regions not influenced by beach draining during low tide, air exists in the seabed, so the problem we investigate is relevant to many beaches. The air/gas in the seabed can be related to the deterioration of organic material, to air trapped in the pores during a lower water level several thousand years ago, or the gas (i.e., methane) hydrates in seabed. According to McGinnis et al. (2006), most marine sources of the atmospheric methane are located in shallow oceans with water depth less than 100 m.

In this section, the gas content distribution with depth shown in Figure 6.22 is used to estimate the pore water pressure induced by tsunami loading. The pore water pressure changes during tsunami run-up and draw-down developed based on

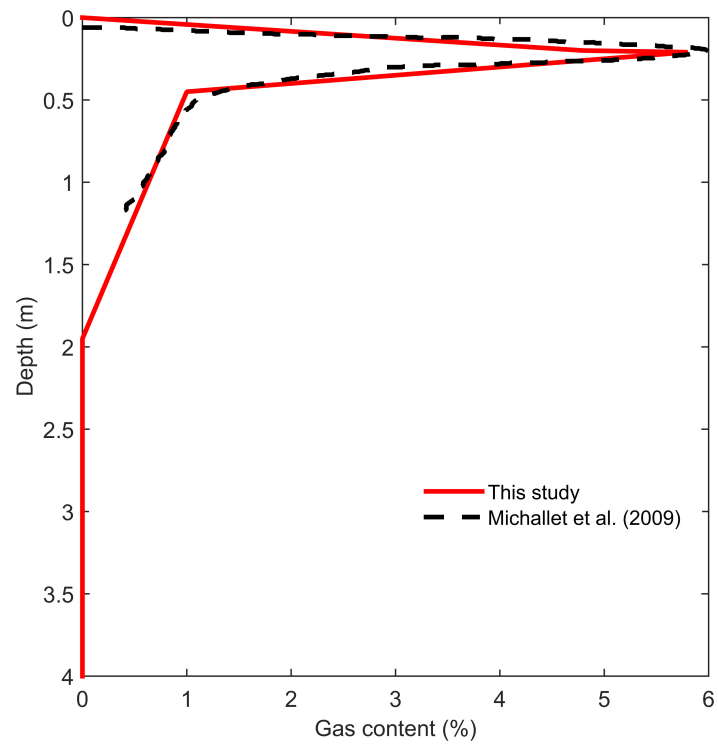


Figure 6.22: Variation of the gas content with depth, extrapolated from Bonjean et al. (2004) and Michallet et al. (2009).

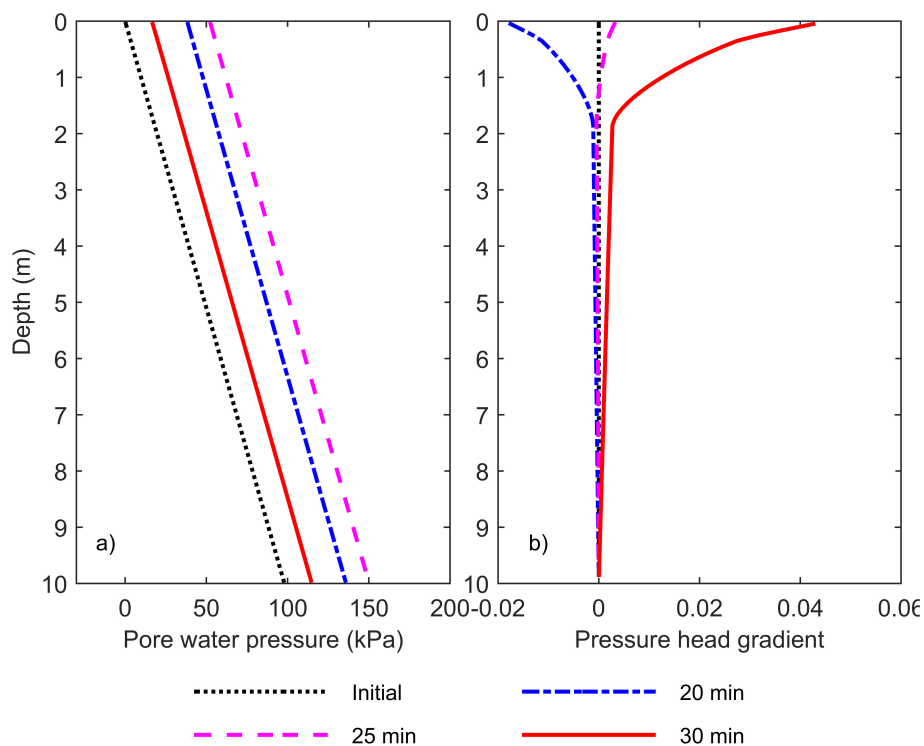


Figure 6.23: Effects of entrained air bubbles: a) the variation of the pore water pressure with depth at different times for the nonlinear soil constitutive model; b) the variation of the pore water pressure head gradient with depth at different times for nonlinear model. Note that the air content distribution with depth is shown in Figure 6.22.

Figure 6.22 are shown in Figure 6.23a. Figure 6.23b shows the the excess pore water pressure head gradient with depth at different times.

From Figure 6.23, the maximum excess pore water pressure head gradient at the ground surface during the draw-down is 0.0395, which is larger than the value obtained for the pure water case (i.e., 0.0032). However, this value is about ten times smaller than the condition where the entire 10 m soil layer is full of aired water (i.e., 0.1864).

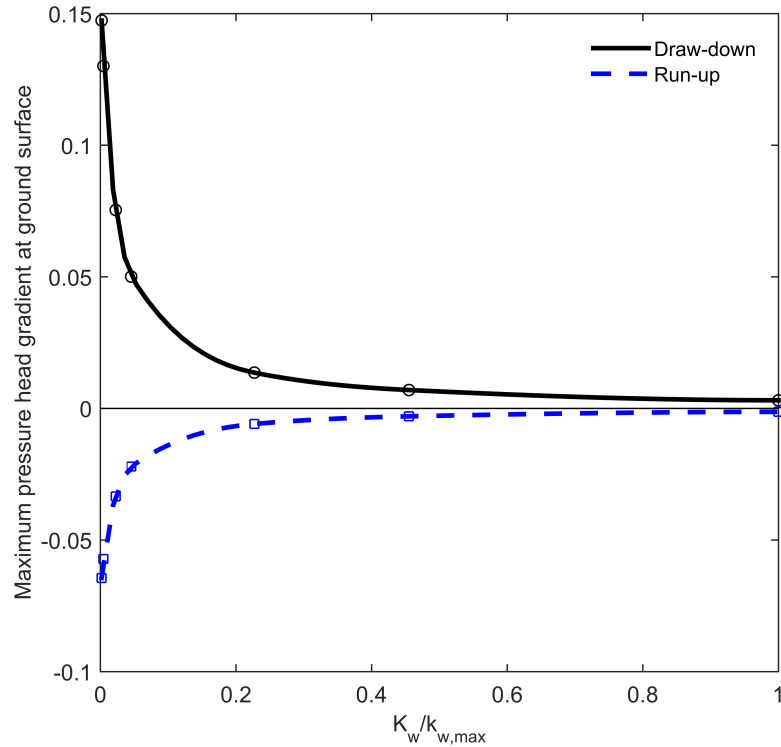


Figure 6.24: Variation of the excess pore water pressure head gradient with normalized fluid bulk modulus. Maximum bulk modulus is for pure water $K_{w,max} = 2.2 \text{ GPa}$. The solid line shows the maximum excess pore water pressure head gradient at the surface during draw-down and the dashed line shows the maximum absolute value of the excess pore water pressure head gradient during run-up.

Figure 6.24 shows the variation of the maximum excess pore water pressure head gradient at the ground surface with normalized water bulk modulus. The water bulk modulus is normalized by the maximum water bulk modulus ($K_{w,max} = 2.2 \text{ GPa}$). In Figure 6.24, the minimum $K_w/K_{w,max}$ represents the bulk modulus of 4 MPa. Accordingly, a small amount of air significantly increases the maximum excess pore water pressure head gradient at the ground surface. Note that the linear soil constitutive model is used to develop Figure 6.24.

Table 6.2: The maximum excess pore water pressure head gradient at the ground surface, $(\partial h/\partial z)_{z=0}$, caused by the different tsunamis shown in Figure 6.25. Note that Case 4 did not converge, which indicates that tsunami-induced liquefaction occurred.

| Case | $\max[(\partial h/\partial z)_{z=0}]$ |
|----------|---------------------------------------|
| 1 | 0.78 |
| 2 | 0.39 |
| 3 | 0.19 |
| 4 | - |
| 5 | 1.10 |
| 6 | 0.42 |

6.6 Initiation of liquefaction

To investigate the initiation of tsunami-induced liquefaction, six tsunamis with different heights and durations are used, which are shown in Figure 6.25. The computed values of the maximum excess pore water pressure head gradient induced by different tsunamis are shown in Table 6.2. For all cases examined in §6.6, the depth to the impermeable layer is 10 m, the soil constitutive model is nonlinear, and aird water is the pore fluid.

Recall from Chapter 1 that there are two definitions for liquefaction. The first definition of liquefaction is based on the excess pore water pressure gradient; i.e., when $\partial h/\partial z$ is equal or greater than i_{cr} , then liquefaction occurs. The second definition of liquefaction is based on total stress and total pore water pressure; i.e., when the total pore water pressure is greater than or equal to the total stress in the soil bed, then liquefaction occurs. The results shown in Table 6.2 indicate that for Case 5, liquefaction occurs at the ground surface (n.b., this observation

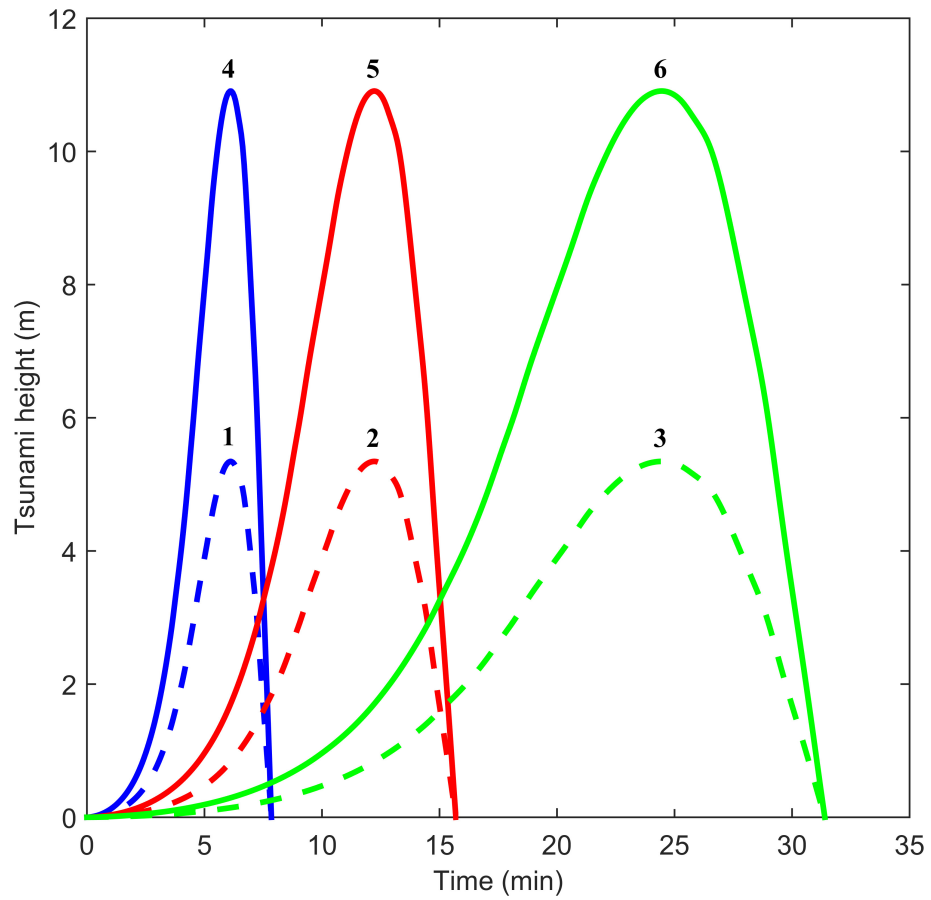


Figure 6.25: Six different tsunamis that are used to study the effect of tsunami-induced liquefaction.

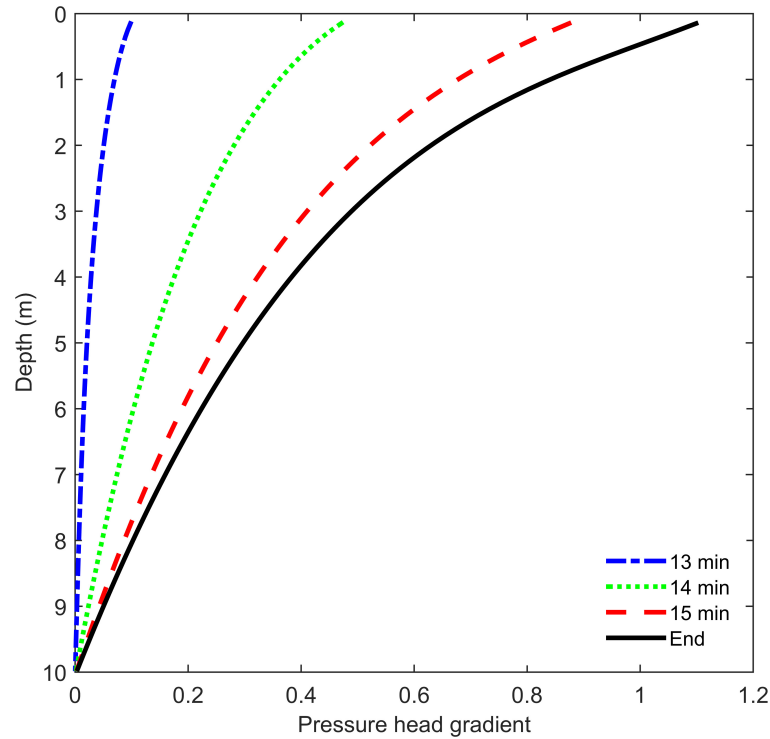


Figure 6.26: Case 5 from Table 6.2: variation of excess pore water pressure head gradient with depth at different times.

is based on the first definition of liquefaction). Figure 6.26 shows the variation of $\partial h/\partial z$ with depth at different times. Notably, $\partial h/\partial z$ reduces with depth from its maximum value at the ground surface. From Figure 6.26, it can be seen that when $t \geq 13$ min, the value of $\partial h/\partial z$ progressively increases. At the end of the tsunami, we see that the depth of liquefaction is about 1 m (i.e., the depth where $\partial h/\partial z \approx i_{cr}$).

Figure 6.27 shows the variation of pore water pressure and total stress with depth at the end of the tsunami for case 5. From Figure 6.27, we see that from the ground surface to a depth of approximately 1 m under ground, the total stress is

approximately equal to the pore water pressure (i.e., second definition of liquefaction). Note that the soil is still not fully liquefied based on the second definition of liquefaction for case 5. When the pore water pressure is equal to the total stress, the effective stress diminishes and the soil's modulus of elasticity becomes zero. From a mathematical point-of-view, the numerical formulation of the coupled seepage-deformation model corrupts. In other words, based on Equation 3.17, the shear modulus becomes zero and the deformation model is singular. Notably, in Figure 6.27, the effective stress does not quite reach zero (i.e., the total stress is slightly greater than the pore water pressure). For completeness, the excess pore water pressure and the pore water pressure at hydrostatic condition are also shown in Figure 6.27.

Liquefaction is initiated for Case 4. The values of $\partial h/\partial z$ versus depth are shown in Figure 6.28 for Case 4. As seen in Figure 6.28, the value of $\partial h/\partial z$ is still negative after 6 min. However, one minute later, the value of $\partial h/\partial z$ has increased significantly and is positive. As a result of the large value of $\partial h/\partial z$, the soil starts liquefying at a time between approximately 7 and 7.3 min (i.e., the first definition of liquefaction). Figure 6.29 shows the total pore water pressure and total stress versus depth for Case 4 (as well as the hydrostatic pore water pressure). It can be seen from Figure 6.29 that the second definition of liquefaction is also met (i.e., the total stress is equal to the total pore water pressure). This condition is met at approximately 7.3 min. In summary, for Case 4, liquefaction occurs because of the large value of $\partial h/\partial z$ earlier relative to second definition of liquefaction, which is based on total pore water pressure. After 7.3 min, the effective stress starts

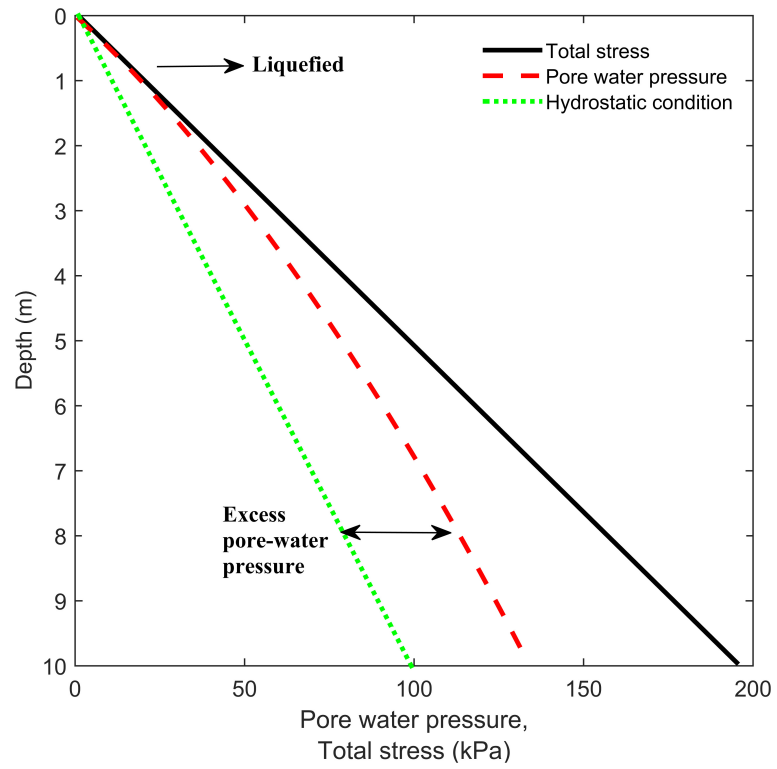


Figure 6.27: Case 5 from Table 6.2: variation of pore water pressure and total stress with depth at the end of the tsunami.

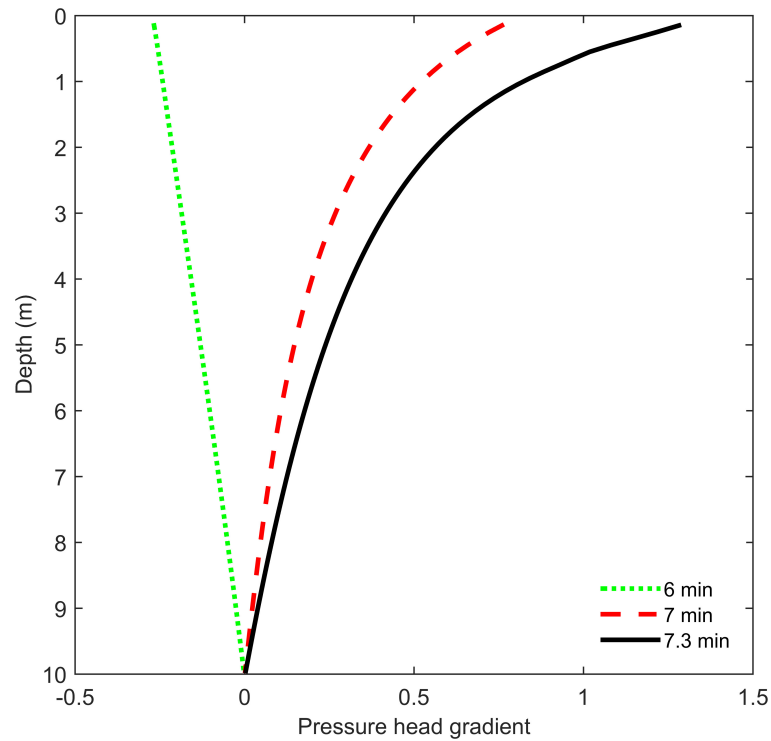


Figure 6.28: Case 4 from Table 6.2: variation of pore water excess pore water pressure head gradient with depth at different times.

becoming negative, and the value of $\partial h/\partial z$ becomes very large as a result. When this occurs, the nonlinear soil constitutive model collapses (i.e., $G \rightarrow 0$, and the porosity becomes very large).

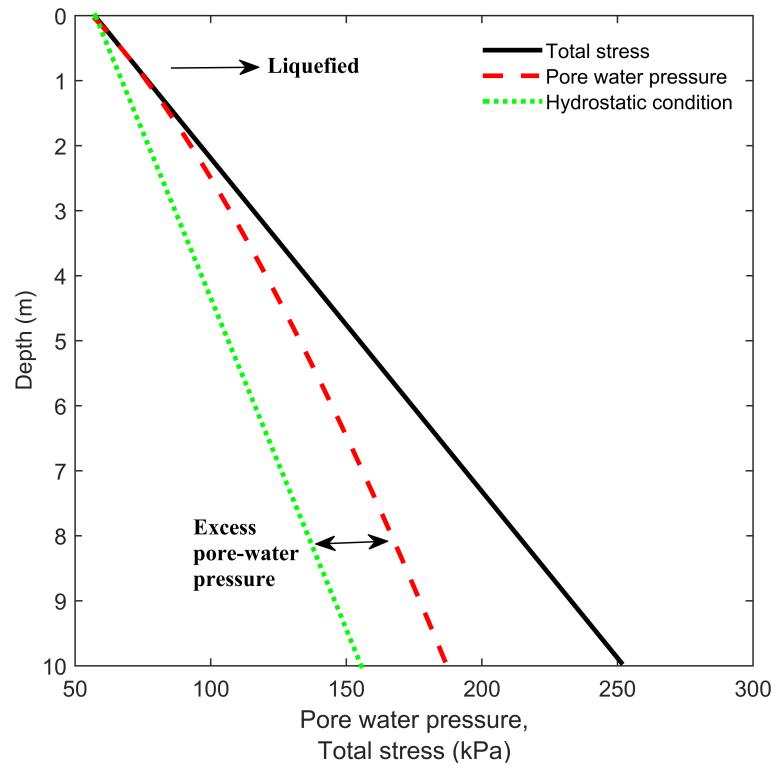


Figure 6.29: Case 4 from Table 6.2: variation of pore water pressure and total stress with depth at 7.3 min after the start of the tsunami.

6.7 Extension to two-dimensions

6.7.1 Two-dimensional formulation

The length scale along the shoreline is very large compared with the length scale perpendicular to the shoreline. In other words, during tsunami loading, the soil deformation along the shoreline is negligible compared to the soil deformation perpendicular to the shoreline; therefore, a two-dimensional model with a plain strain assumption is reasonable to model tsunami-induced soil instability. However, herein for the sake of simplicity, only the normal vertical stress induced by the tsunami is considered. The other component of normal stress and all the shear stresses induced by the weight of the tsunami are neglected, and a one-dimensional deformation model is used to estimate the deformation induced by the tsunami weight. Also, for the sake of simplicity, because the tsunami occurs quickly, it is assumed that the total stress changes on the soil surface resulting from the weight of the tsunami is equal to the tsunami height. Note that this assumption is acceptable, because the tsunami is a long wave. Equation 3.12 is used for the soil deformation model.

In addition to the stress deformation model, the Richards' equation, Equation 4.1, also needs to be considered to compute the seepage. Unlike the stress deformation equation, the seepage equation is modelled two-dimensionally; i.e., seepage can occur in vertical and horizontal directions.

The one-dimensional finite difference model can easily be generalized to the two-dimensional form. Similar to the one-dimensional model, the finite difference

approach is used to solve the coupled seepage-deformation equation for the two-dimensional model. The spatial domain is discretized by a rectangular uniform grid of size Δx and Δz with cell centers denoted by x_i and z_j , where, $i = 1, \dots, mx$ and $j = 1, \dots, mz$. mx and mz denote the number of the cells. Note that as it is shown in Figure 6.30, for the sloped beach condition, the effect of depth in z -direction is calculated and considered. Again, similar to the one-dimensional model, the fully implicit cell centered finite difference approach with Newton's iteration is implemented to solve the coupled seepage-deformation equation. At each iteration, the initial guess is extracted from previous steps. The Jacobian is computed analytically. Either a constant time step or a variable time step can be used in solution. The variable time step is controlled automatically depending on the success or failure of the Newton iteration. The finite difference form of the flow in unsaturated soil is (see §4.3),

$$R = \frac{(\rho_{w_{j,i}} \phi_{j,i} S_{j,i})^n - (\rho_{w_{j,i}} \phi_{j,i} S_{j,i})^{n-1}}{\Delta t} - \frac{1}{\Delta z_j} [Q_{j+1/2,i}^n - Q_{j-1/2,i}^n] - \frac{1}{\Delta x_i} [Q_{j,i+1/2}^n - Q_{j,i-1/2}^n] = 0, \quad (6.4a)$$

$$Q_{j+1/2,i}^n = \rho_{w_{j+1/2,i}} k_{r_{j+1/2,i}} T z z_{j+1/2,i} \cdot [p_{w_{j+1,i}}^n - p_{w_{j,i}}^n - \rho_{w_{j+1/2,i}} G (D_{j+1,i} - D_{j,i})], \quad (6.4b)$$

$$Q_{j-1/2,i}^n = \rho_{wj-1/2,i} k_{rj-1/2,i} Tz z_{j-1/2,i} \cdot [p_{w_{j,i}}^n - p_{w_{j-1,i}}^n - \rho_{wj-1/2,i} G(D_{j,i} - D_{j-1,i})], \quad (6.4c)$$

$$Q_{j,i+1/2}^n = \rho_{wj,i+1/2} k_{rj,i+1/2} Txx_{j,i+1/2} \cdot [p_{w_{j,i+1}}^n - p_{w_{j,i}}^n - \rho_{wj,i+1/2} G(D_{j,i+1} - D_{j,i})], \quad (6.4d)$$

$$Q_{j,i-1/2}^n = \rho_{wj,i-1/2} k_{rj,i-1/2} Txx_{j,i-1/2} \cdot [p_{w_{j,i}}^n - p_{w_{j,i-1}}^n - \rho_{wj,i-1/2} G(D_{j,i} - D_{j,i-1})], \quad (6.4e)$$

where,

$$Tz z_{j+1/2,i} = \frac{2}{\frac{\Delta z_{j,i}}{kvis_{j,i}} + \frac{\Delta z_{j+1,i}}{kvis_{j+1,i}}}, \quad (6.5a)$$

$$Tz z_{j-1/2,i} = \frac{2}{\frac{\Delta z_{j,i}}{kvis_{j,i}} + \frac{\Delta z_{j-1,i}}{kvis_{j-1,i}}}, \quad (6.5b)$$

$$Txx_{j,i+1/2} = \frac{2}{\frac{\Delta z_{j,i}}{kvis_{j,i}} + \frac{\Delta z_{j,i+1}}{kvis_{j,i+1}}}, \quad (6.5c)$$

$$Txx_{j,i-1/2} = \frac{2}{\frac{\Delta z_{j,i,j}}{kvis_{j,i}} + \frac{\Delta z_{j,i-1}}{kvis_{j,i-1}}}, \quad (6.5d)$$

$$kvis = \frac{k_{ab}}{\mu_w}. \quad (6.5e)$$

Also at the boundary (1) and $(nx + 1)$,

$$Tzz(1, i) = \frac{2}{\frac{\Delta z_1}{kvis_{1,i}}}, \quad (6.6a)$$

$$Tzz(mx + 1) = \frac{2}{\frac{\Delta z_{nz}}{kvis_{mz,i}}}, \quad (6.6b)$$

$$Txx(j, 1) = \frac{2}{\frac{\Delta x_1}{kvis_{j,1}}}, \quad (6.6c)$$

$$Txx(j, mx + 1) = \frac{2}{\frac{\Delta x_{mx}}{kvis_{j,mx}}}. \quad (6.6d)$$

The boundary condition on the top of the ground surface ($z = 0$) is Dirichlet, and the other boundary conditions at the left, right and the bottom boundaries is Neumann. One of the challenges about applying the finite difference to the problem is with the sloping boundary. Herein, a new rotated coordinate system is implemented, and the rotated coordinate system is shown in Figure 6.30. Note that in the rotated coordinate system, the gravitational acceleration has two components in both the x and z directions.

6.7.2 Numerical convergence and preliminary results

Due to the computational costs of two-dimensional modeling, a simple two-dimensional model is investigated herein. A soil section with a horizontal distance of 800 m and a depth of 10 m is considered. $x = 0$ is located 400 m offshore, $x = 800$ m is located 400 m onshore, and the shoreline is located at $x = 400$ m. It is assumed

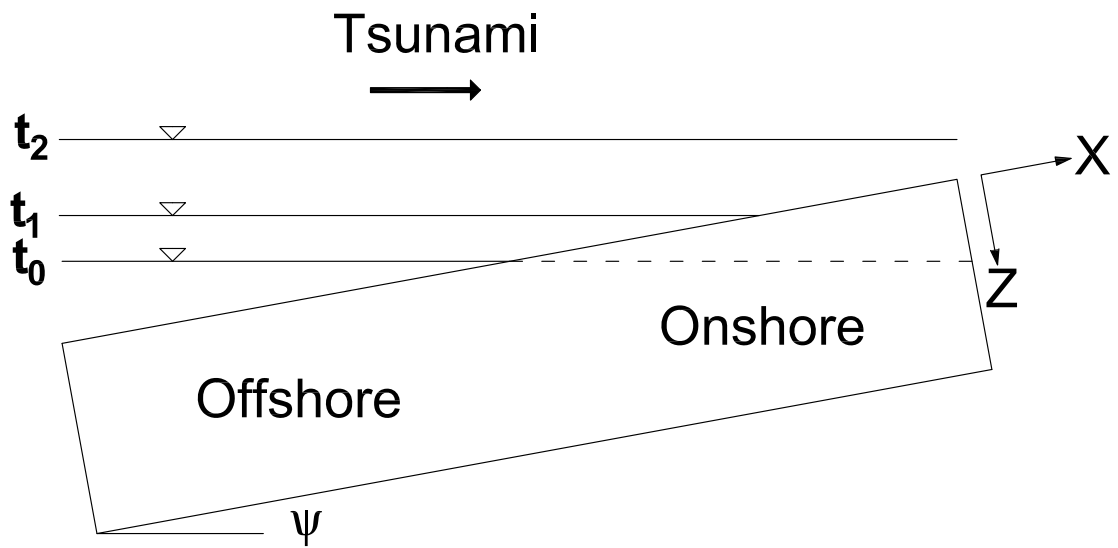


Figure 6.30: Schematic of rotated coordinate system for two-dimensional numerical experiments: Tsunami run-up on the plane slope.

that the ground water table is initially at the same level as t_0 in Figure 6.30. The soil is unsaturated above the ground water table. The maximum ground water table depth is 2 m at $x = 800$ m, and the maximum water depth is 2 m at $x = 0$. The beach slope is planar and is $\psi = 1/200$. The maximum tsunami height at the shoreline is 5 m; therefore, the maximum tsunami height at $x = 800$ is 3 m. A one meter mesh size in both the X and Z directions is used, and the time increment is assumed to be 1 s. A uniform sand is used, and the soil properties are the same as the one used for one-dimensional model.

To be able to compare the two-dimensional results with the one-dimensional model results and to simplify the problem, it is assumed that boundary condition at top of the soil stays Dirichlet throughout tsunami loading. In the other words, it is assumed that during the draw-down, after the water surface decreases, the pore water pressure at the soil surface is zero. Because only 400m of onshore soil is modelled and the results show that the unsaturated soil becomes fully saturated after run-up, the Dirichlet boundary condition assumption is reasonable. Note that, for comparison purposes, the same tsunami loading is applied to a one-dimensional soil layer in a fully saturated condition, which is a similar condition to the two-dimensional model of a soil column located at the shoreline.

The pore water pressure in the soil as a function of depth and horizontal distance at $t = 0$ is shown in Figure 6.32. Figures 6.33 to 6.38 show the pore water pressure at different depths perpendicular to shoreline at $t = 100$ s, $t = 200$ s, $t = 300$ s, $t = 400$ s, $t = 500$ s, $t = 600$ s, respectively. During run-up, the pore water pressure starts increasing from the ground surface to the bottom of the soil

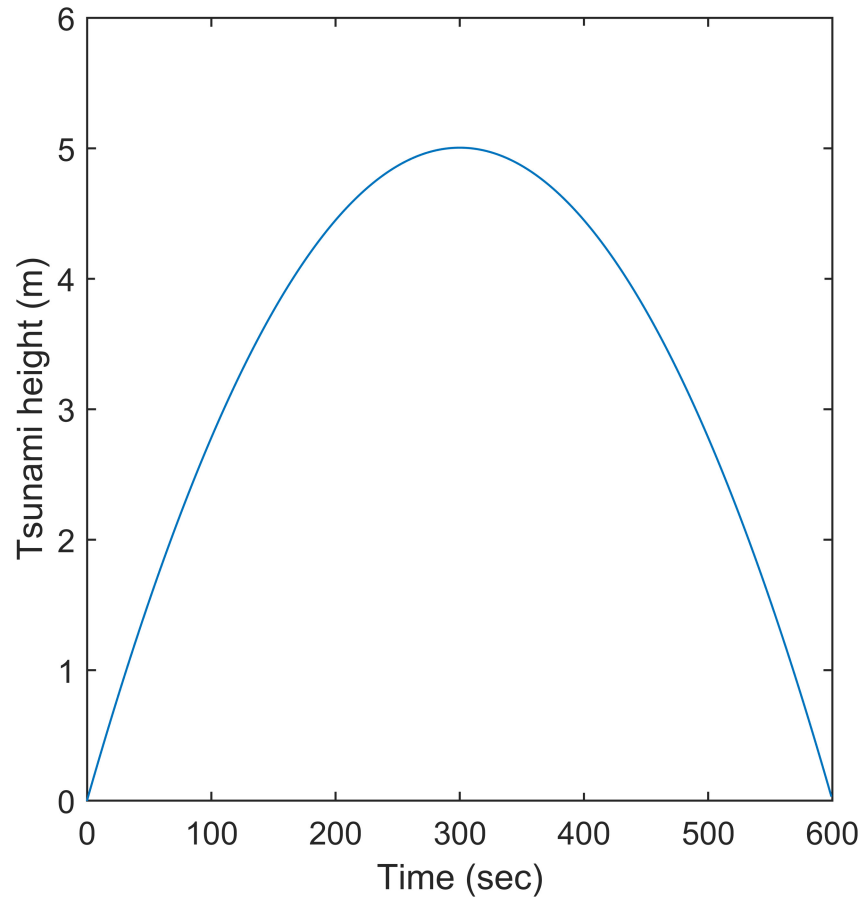


Figure 6.31: Hypothetical tsunami flow height-time series at the shoreline used for the two-dimensional numerical experiments.

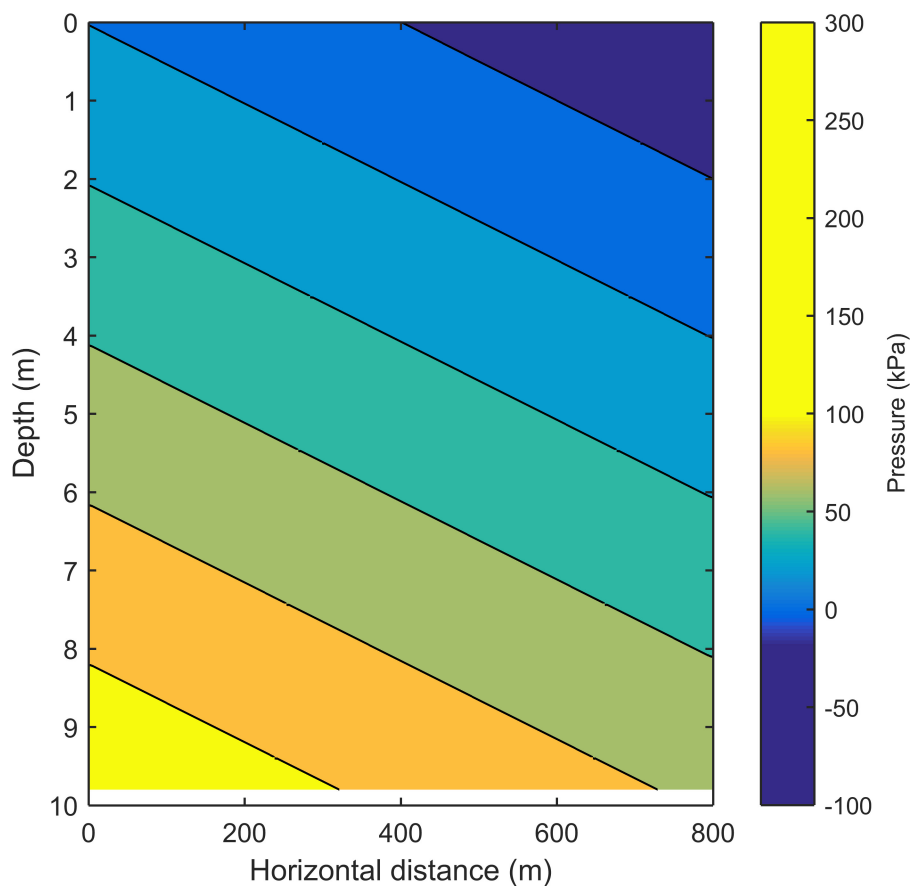


Figure 6.32: Pore water pressure response of the two-dimensional soil bed subjected to the tsunami loading shown in Figure 6.31 at the initial condition.

bed and from offshore to onshore. At the end of the tsunami, the soil bed is fully saturated and upward flow of pore water occurs within the entire soil bed. Figures 6.39 and 6.40 show the variation of pore water pressure at different times with horizontal distance at 1.2 m below ground surface and 4.2 m below the ground surface. During the tsunami draw-down, the upward flow of pore water induces soil instability.

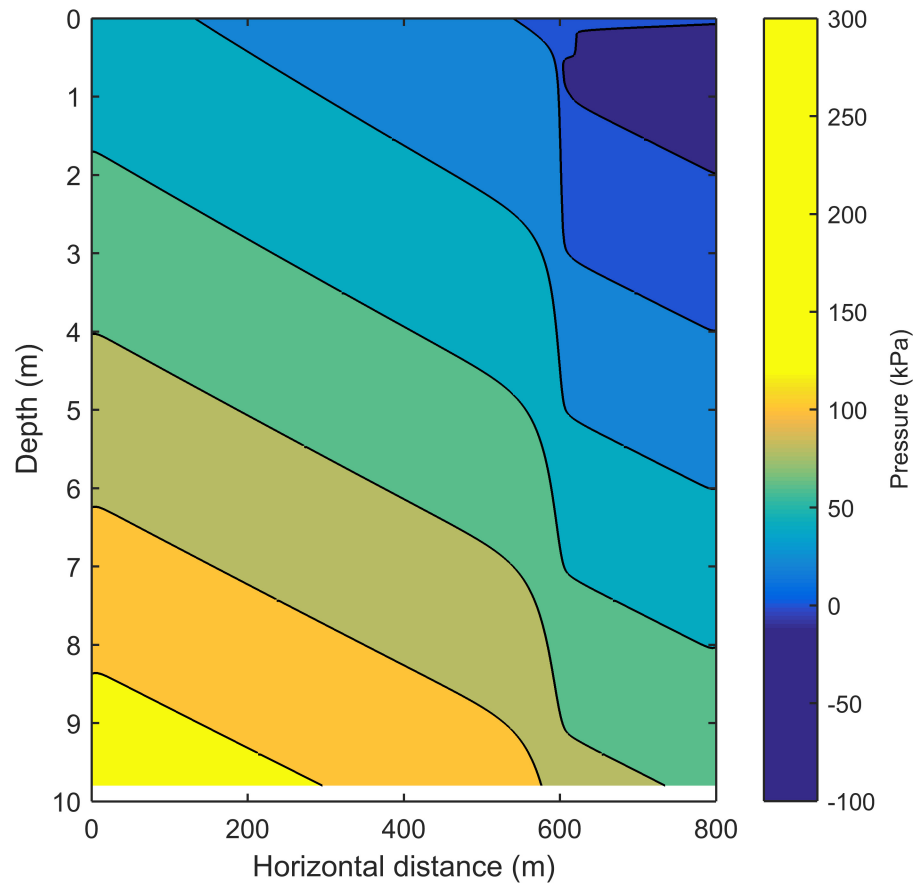


Figure 6.33: Pore water pressure response of the two-dimensional soil bed subjected to the tsunami loading shown in Figure 6.31 at $t=100$ s.

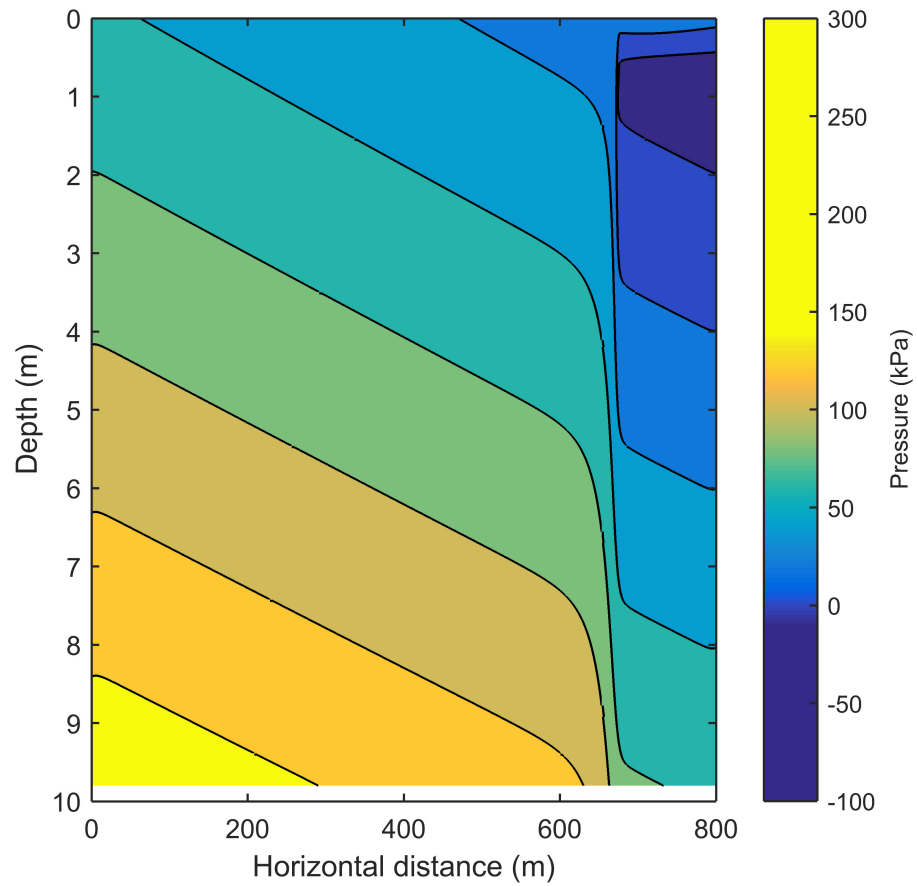


Figure 6.34: Pore water pressure response of the two-dimensional soil bed subjected to the tsunami loading shown in Figure 6.31 at $t=200$ s.

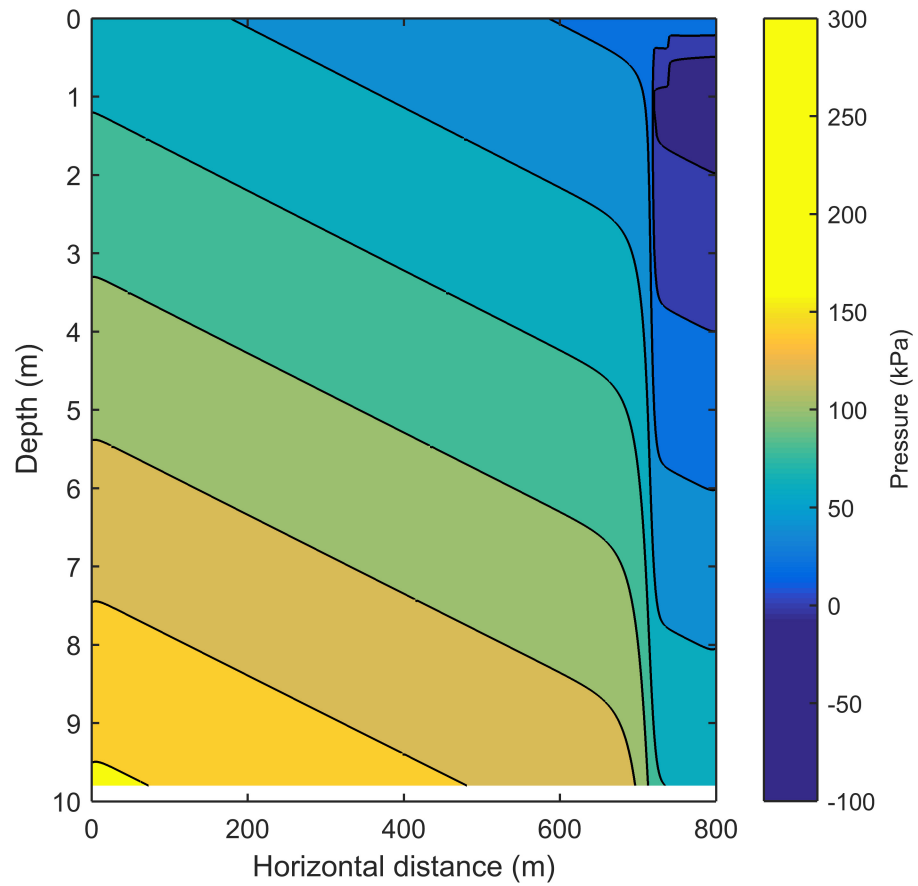


Figure 6.35: Pore water pressure response of the two-dimensional soil bed subjected to the tsunami loading shown in Figure 6.31 at $t=300$ s.

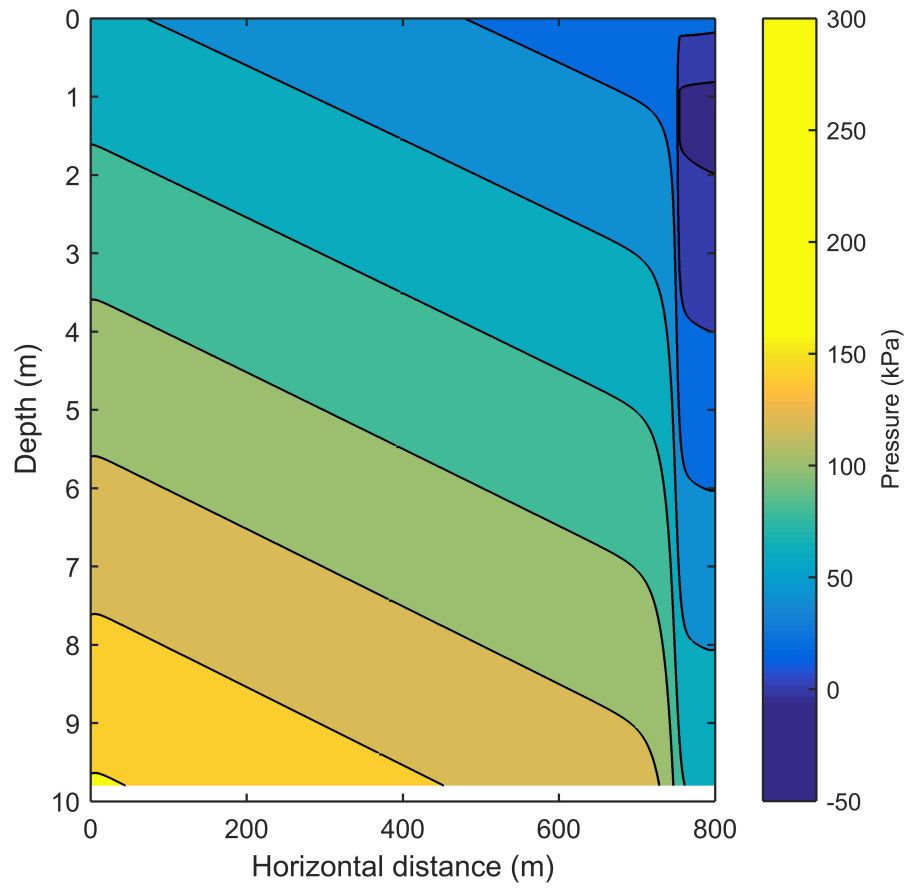


Figure 6.36: Pore water pressure response of the two-dimensional soil bed subjected to the tsunami loading shown in Figure 6.31 at $t=400$ s.

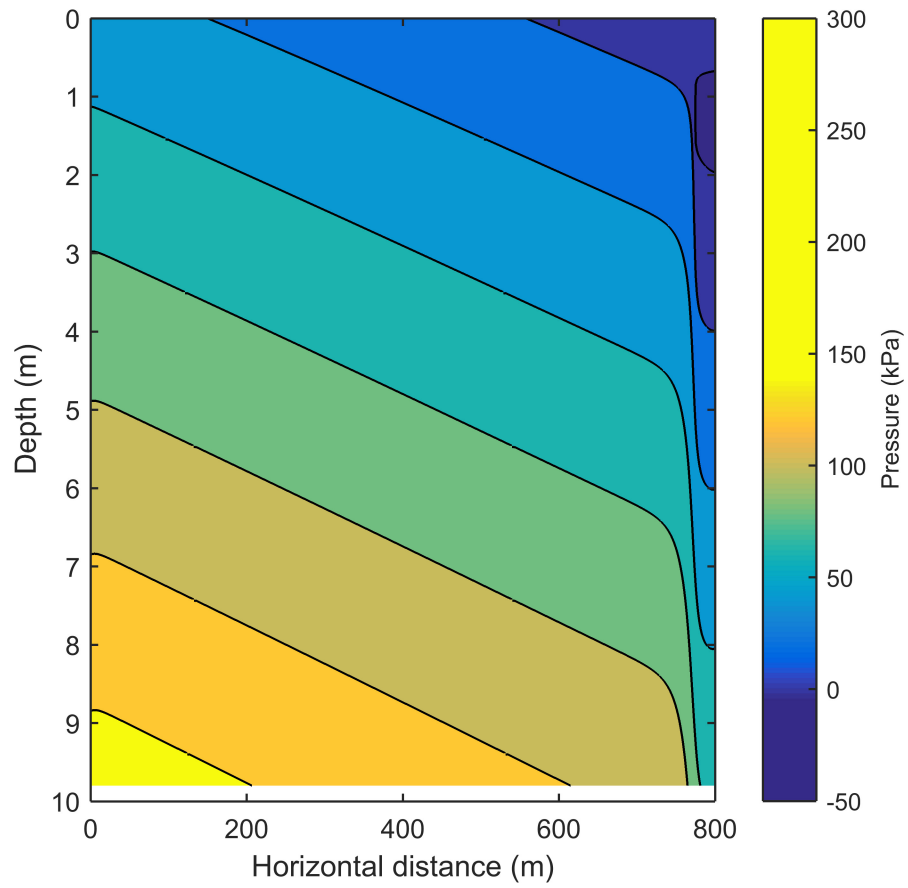


Figure 6.37: Pore water pressure response of the two-dimensional soil bed subjected to the tsunami loading shown in Figure 6.31 at $t=500$ s.

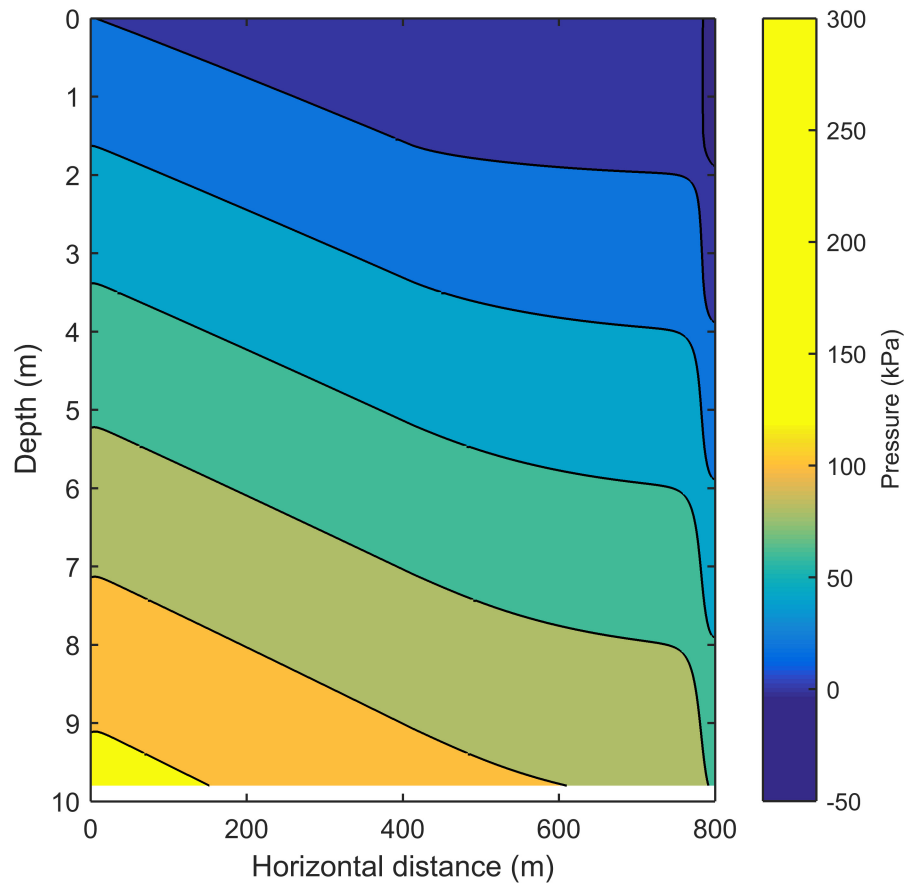


Figure 6.38: Pore water pressure response of the two-dimensional soil bed subjected to the tsunami loading shown in Figure 6.31 at the end of the tsunami loading.

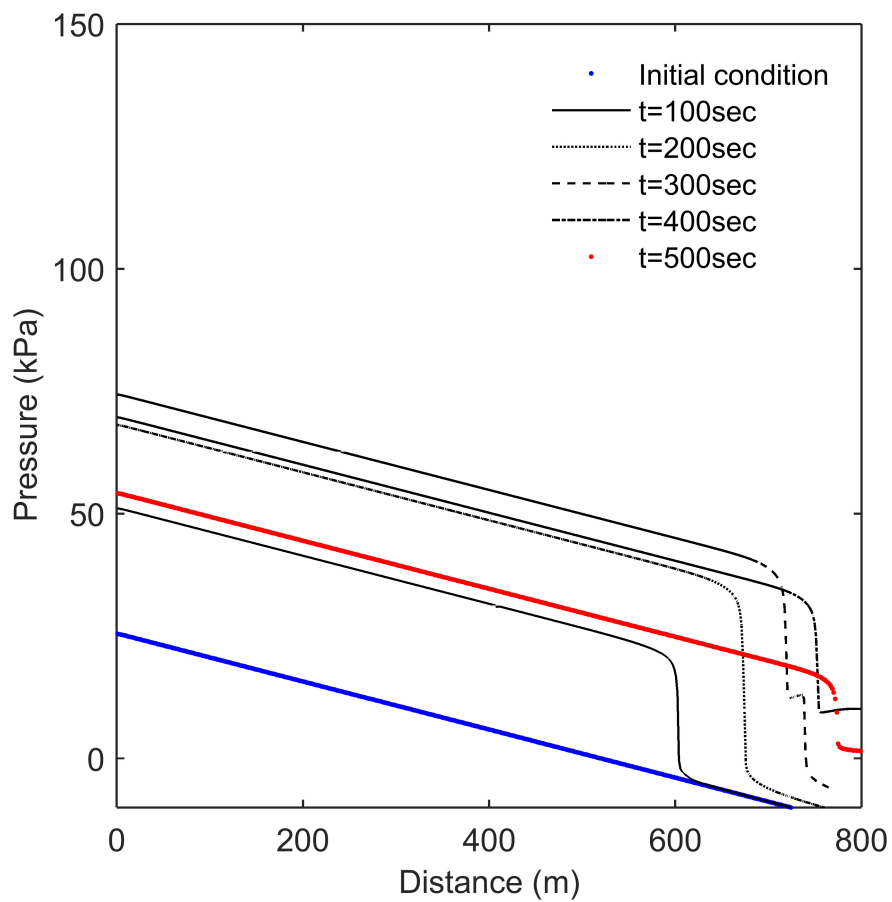


Figure 6.39: Pore water pressure at a depth of 1.2 m underground as a function of the horizontal distance at different times.

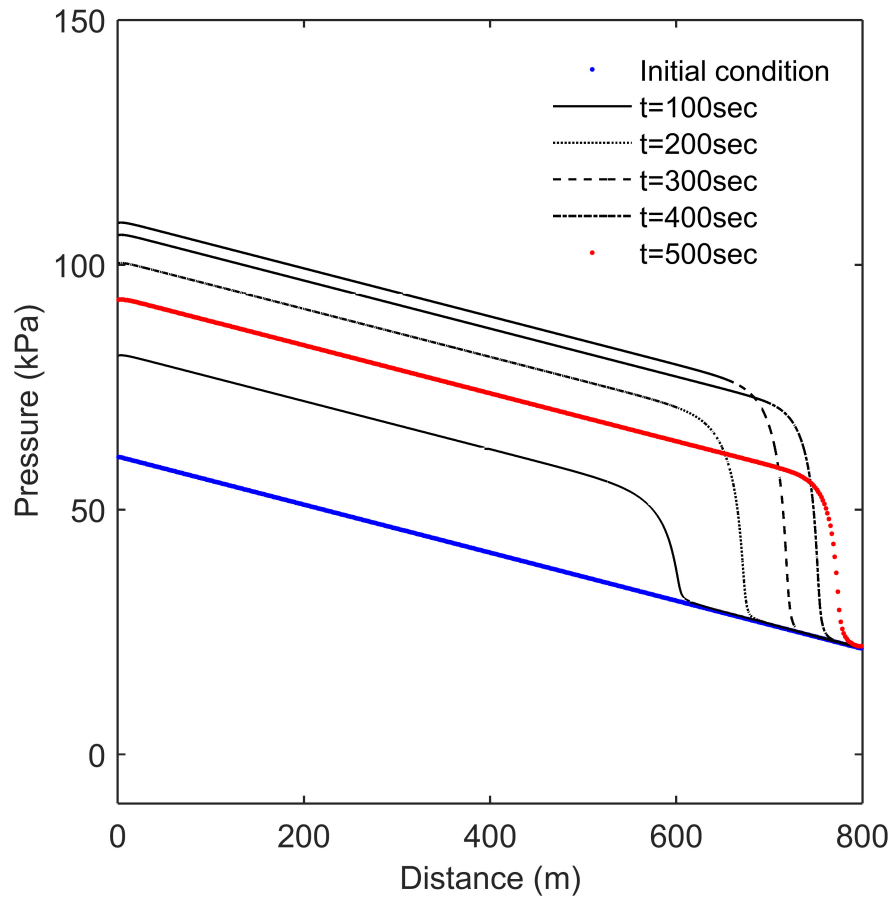


Figure 6.40: Pore water pressure at a depth of 4.2 m underground as a function of horizontal distance at different times.

Table 6.3: Summary of convergence studies with four different grids for the two-dimensional model. Δz is the cell size in the z -direction, Δx is the cell size in the x -direction, mz is the total number of cells in the z -direction, mx is the total number of cells in the x -direction, Δt is the time increment, and N is the total number of time increments.

| | Δz (m) | mz | Δx (m) | mx | Δt (s) | N |
|---------------|----------------|------|----------------|------|----------------|-----|
| Grid A | 2 | 5 | 8 | 100 | 10 | 60 |
| Grid B | 0.67 | 15 | 2.67 | 300 | 3.33 | 180 |
| Grid C | 0.4 | 25 | 1.6 | 500 | 2 | 300 |

The convergence studies for the two-dimensional model are performed using four different “grids,” which are shown in Table 6.3. Grid A is the “coarsest” grid, and the Grid C is the “finest” grid. The time step, Δt , varies as a function of the cell size, Δz .

Figure 6.41 and 6.42 show the convergence studies for the two-dimensional model for different grid sizes. As we see in the preceding figures, as the grid size reduces, the model converges and it predicts the pore water pressure induced by tsunami better. However, as the grid size reduces, the computational cost increases.

For the two-dimensional model, Grid C is selected and used for investigating the pore water pressure induced by tsunami loading. Figure 6.43 and 6.44 show the pore water pressure and excess pore water pressure head gradient at the shoreline with depth at different times. During tsunami run-up, the excess pore water pressure head gradient is negative, which indicates that downward seepage occurs, and during the tsunami draw-down, the excess pore water pressure head gradient is positive, which indicates that upward seepage occurs. A comparison of the excess pore water pressure head gradient resulting from one-dimensional model and the

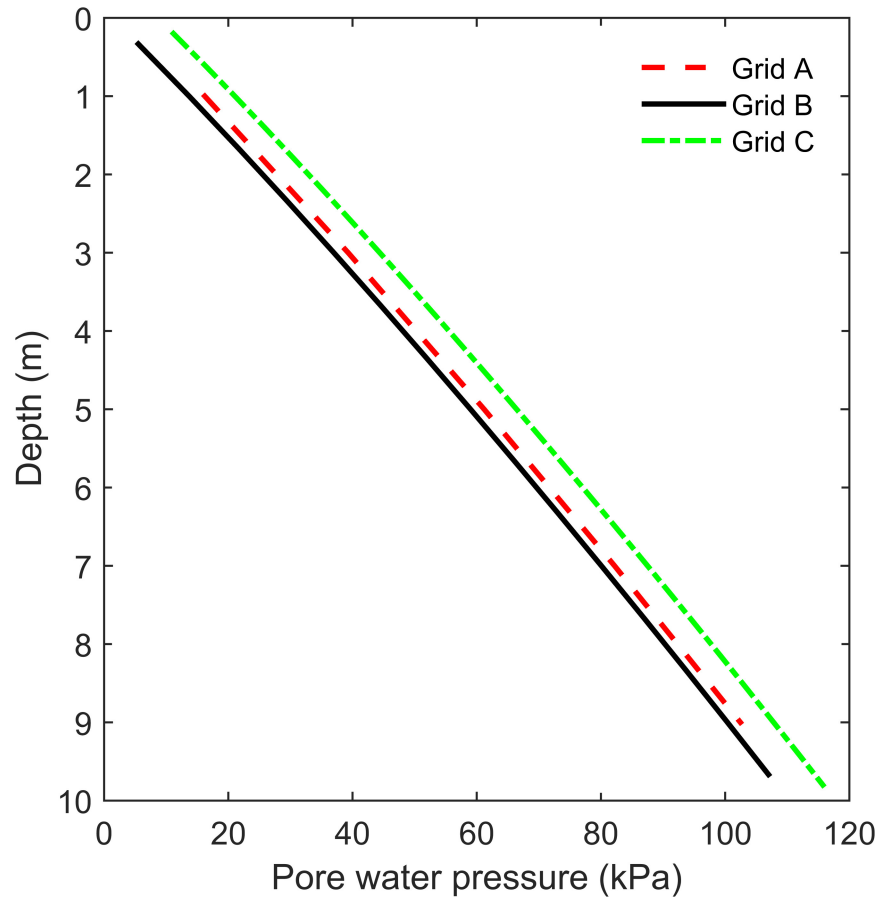


Figure 6.41: Convergence studies for two dimensional model at shoreline and at $t=600$ s.

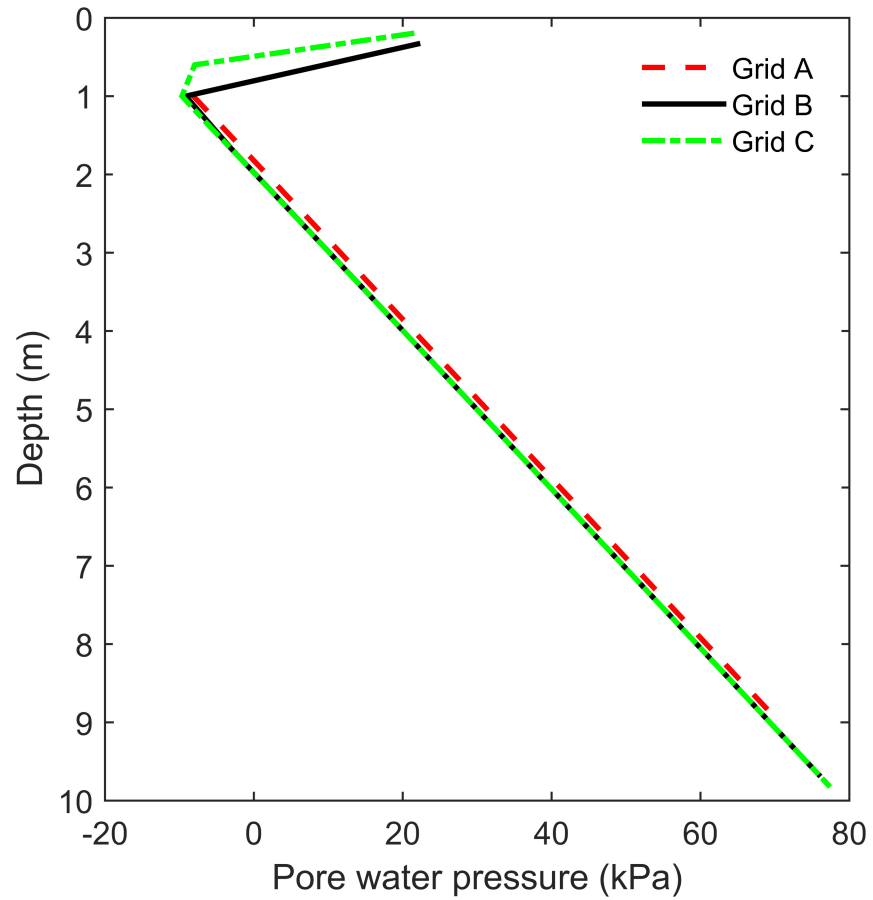


Figure 6.42: Convergence studies for two dimensional model at $x=800$ m and at $t=600$ s.

two-dimensional model shows that the excess pore water pressure head gradient induced by the tsunami loading is larger when the two-dimensional model is used. Note that the two-dimensional model is a more realistic model, and in fact, the one-dimensional model underestimates the excess pore water pressure head gradient induced by tsunami. In addition, for the examined two-dimensional cases, the horizontal excess pore water pressure head gradient is negligible, because the beach slope is very small. Accordingly, the comparisons herein are with respect to the vertical (i.e., defined z in Figure 6.30) excess pore water pressure head gradient component.

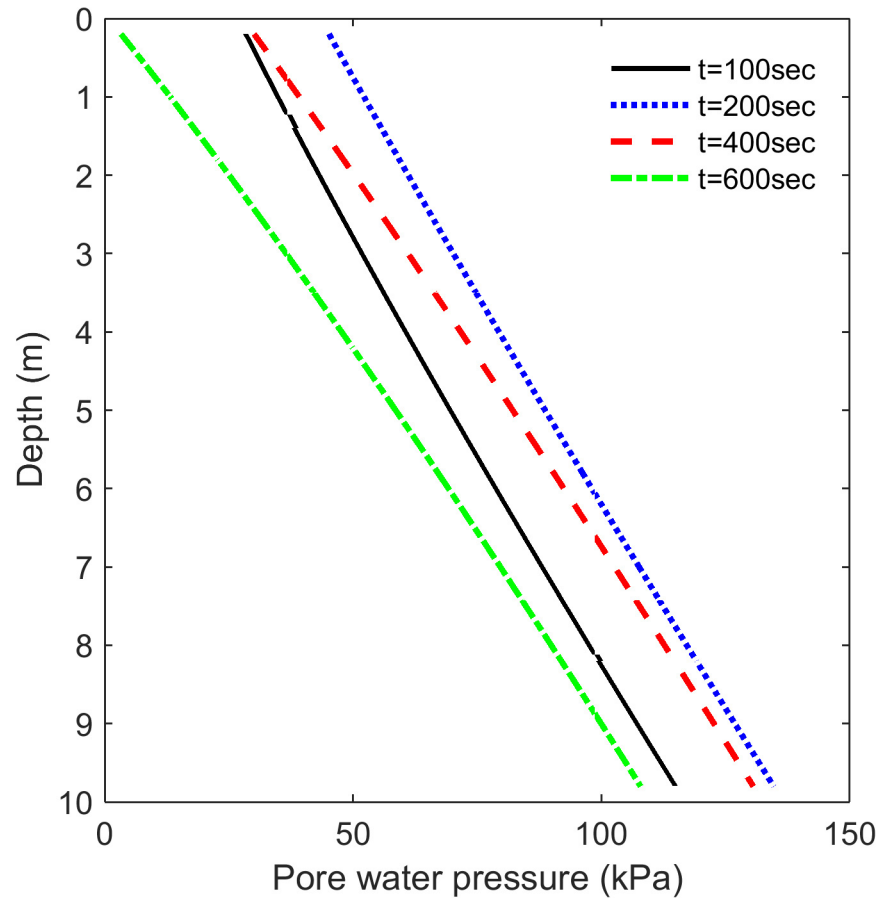


Figure 6.43: Pore water pressure at the shoreline for different times from two-dimensional analysis.

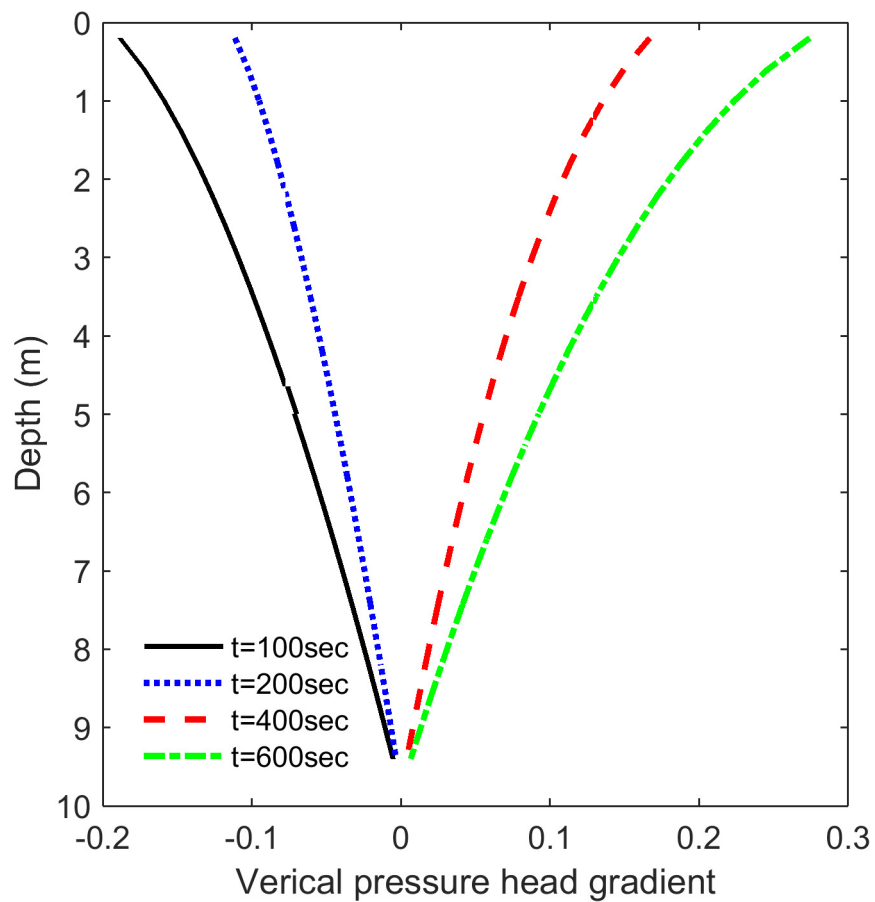


Figure 6.44: Vertical (i.e., z direction in Figure 6.30) excess pore water pressure head gradient at the shoreline for different times from two-dimensional analysis.

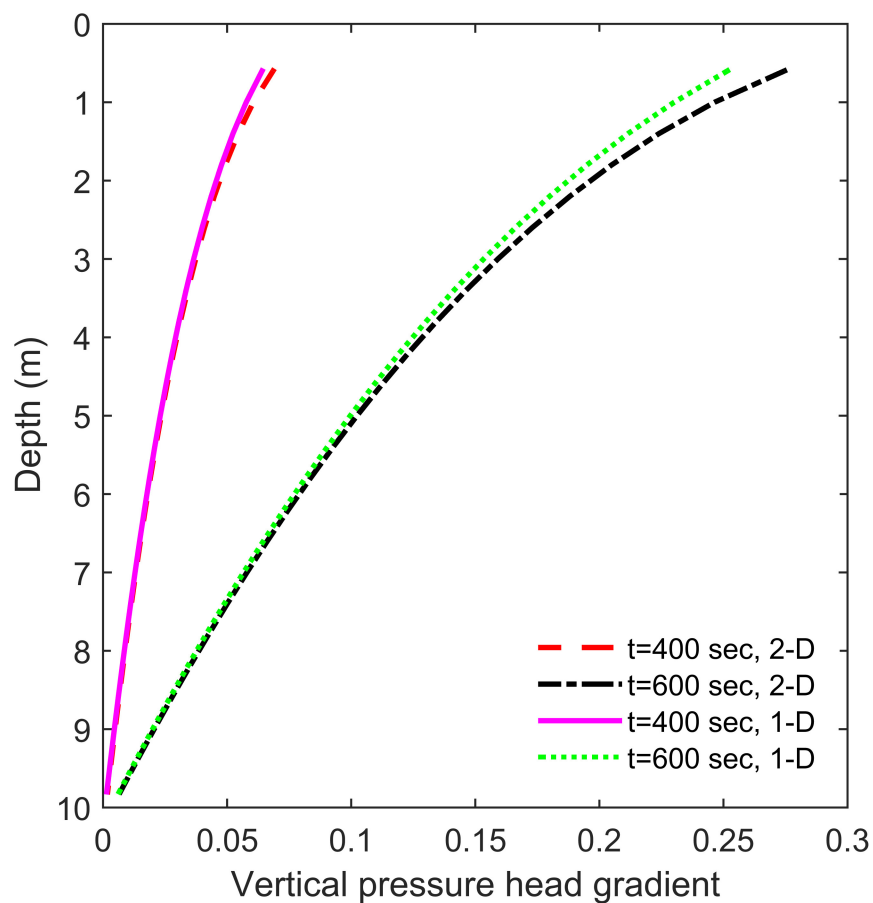


Figure 6.45: Comparison of the vertical (i.e., z direction in Figure 6.30) excess pore water pressure head gradient induced by the tsunami at the shoreline based on the one-dimensional and two-dimensional models, where for the two-dimensional model, $x=400$ m.

Chapter 7: Summary and conclusions

Coastal areas are vulnerable to the earthquake-tsunami multi-hazard, which can cause significant sediment instability near the shoreline, leading to potential damage or collapse of critical coastal infrastructure. During the earthquake, sediment instability can occur via residual liquefaction, and the water table can rise following the cessation of strong shaking (Abdollahi et al., 2017). During the tsunami, sediment instability can occur via the strong bed shear stresses (i.e., sediment transport) as well as the excess pore water pressure head gradient created in the soil bed by the inundation of the tsunami water during tsunami run-up followed by the relatively rapid draw-down of the tsunami water during tsunami draw-down. The focus herein was on the second part of the earthquake-tsunami multi-hazard problem (i.e., the tsunami), and more specifically, the work focused on the pore water pressure response of soil beds subjected to tsunami loading. The potential for sediment instability was discussed in a broad context, as it related to the pore water response in the examined soil beds. To understand the pore water response in soil beds, a coupled seepage-deformation model was created and numerically formulated using a finite difference approach. Numerical experimentation was performed on hypothetical soil beds using hypothetical tsunami loadings. In this Chapter, we provide a comprehensive summary of the performed work with conclusions. In addition, we provide some ideas for future related work.

7.1 Summary

Following the Introduction (Chapter 1), Chapter 2 contains the theory and background of different topics that are related to the concepts presented in Chapters 3 to 6. From the the previous researchers, we primarily found that the fully coupled transient seepage-deformation analysis is needed to estimate the pore water pressure induced by tsunami loading (i.e., a coupled model that accounts for pore water pressure changes due to both deformation of the soil bed and seepage of the overlying tsunami water into the soil bed). Note that tsunami loading on soil beds is related to the loading of porous media by fluids. We stated that the condition of tsunami loading on a soil bed is very similar to the rapid draw-down of water in embankment dams. However, the time scale of tsunami loading (both run-up and draw-down) is different than the time scale of rapid draw-down of water in embankment dams. More specifically, the rapid draw-down of water in embankment dams occurs at a rate of approximately 0.1 to 0.5 m/day, but in contrast, tsunami run-up and draw-down occurs on the order of minutes.

In short, to estimate the pore water pressure induced by tsunami loading, a coupled seepage-deformation model is needed to model the succeeding physical description. During tsunami run-up, the weight of the overlying tsunami water on the soil bed increases, and the pore water pressure in the soil bed increases quickly. However, the increased pore water pressure caused by the tsunami water weight is not considered excess pore water pressure, but rather, it is considered to be hydrostatic pore water pressure, and the excess pore water pressure is precisely

defined as the deviation of pore water pressure from the hydrostatic condition. Note that all the weight of the overlying tsunami water does not change to pore water pressure in the soil bed; i.e., only a portion of the tsunami water weight converts into pore water pressure. The other component of the pore water change during tsunami loading is caused by the infiltration of tsunami water into the soil bed, which increases the pore water pressure because of the pressure head gradient at the ground surface. For the tsunami draw-down, a similar physical scenario exists. Note that the tsunami loading of a soil bed is a “partial drainage” problem. The existing deformation models can not predict the pore water pressure induced by tsunami loading, and they can not separate the deformation induced by the weight of the tsunami water and the seepage-induced pore water pressure. Therefore, a new deformation model is needed that can model the partial drainage condition in the soil bed.

In Chapter 3, a deformation model is developed and proposed. Herein, we always assume that the soil bed is in equilibrium, and, we tried to apply “equilibrium soil parameters” to represent a transient scenario (i.e., tsunami loading). For example, to measure the Skempton’s B value, we assume that the soil bed can be represented by a small specimen in triaxial cell, and we measure the pore water pressure in the specimen after the confining pressure changes and after the specimen achieves a stable, equilibrium condition. In reality, for the case of tsunami loading, we are concerned with large regions (i.e., large soil beds), and the loading rate of the tsunami is not slow compared to typical geotechnical laboratory testing (i.e., the tsunami loading condition is transient, as previously mentioned).

The proposed deformation model has the ability to model the partial drainage condition. In fact, the B value controls the drainage potential of the soil bed. When $B = 1$, the condition is undrained and as the B value reduces, the drainage potential increases.

In Chapter 4, seepage flow through partially saturated porous media was described, and the flow through porous media equation (i.e., the Richards' equation) was coupled with the developed deformation model. A finite difference approach based on Newton's method was implemented in MATLAB to solve the coupled seepage-deformation model.

In Chapter 5, first the hypothetical tsunami waveforms were developed, and a suitable tsunami wave form was selected based on the Carrier et al. (2003) approach. A reasonable set of soil properties was selected for numerical experimentation, and the numerical experimentation plan was outlined. Then, numerical convergence was studied for two worst case scenarios. After the convergence study was performed, it was shown the maximum excess pore water pressure head gradient reduces linearly with the reduction of B value. The surface excess pore water pressure head gradient linearly changes with the B value for both the linear soil constitutive model and nonlinear soil constitutive model. As the B value decreases, the nonlinear soil constitutive model results in a larger excess pore water pressure head gradient at the ground surface compared with the linear soil constitutive model. Assuming de-aired water as the pore fluid results in negligible excess pore water pressure head gradients at the ground surface for both soil constitutive models. Comparison of the maximum excess pore water pressure head gradient

induced by tsunami loading for a soil bed saturated with de-aired water and 3% aired water showed that 3% of air in water can significantly increase the excess pore water pressure head gradient induced by tsunami loading.

In Chapter 6, we showed the results from further numerical experimentation. The effect of different impermeable layer depths on excess pore water pressure head gradient induced by tsunami loading was investigated. The results showed that the maximum excess pore water pressure head gradient increases as the depth to the impermeable layer increases up to a certain depth of impermeable layer.

The effect of tsunami properties (i.e, tsunami height and duration) was also studied in Chapter 6. The results showed that as the tsunami height increases, the excess pore water pressure head gradient at the ground surface also increases. For tsunamis with the same duration, the excess pore water pressure gradient at the ground surface increases linearly with an increase of tsunami height. For tsunamis with the same height and different durations, the results showed that the excess pore water pressure head gradient at the ground surface increases non-linearly with the decrease of tsunami duration. The variation of normalized maximum excess pressure head gradient with soil impermeable layer depth that is normalized with $\sqrt{C_{v0}T_d}$ showed that the initial coefficient of consolidation, C_{v0} , and tsunami duration, T_d , are terms that can be used to characterize the soil for modeling the excess pore water pressure head gradient induced by tsunami loading. The maximum excess pore water pressure head gradient at the ground surface was observed within the range of $z_i/\sqrt{C_{v0}T_d}$ equal to 1.5 and greater. It was shown that the critical depth of impermeable layer (i.e., the smallest depth that creates

the largest maximum excess pore water pressure head gradient; $z_i/\sqrt{C_{v0}T_d} \approx 1.5$) also decreases as T_d and C_{v0} decrease, which is a realistic situation for many plane beaches subjected to tsunami loading. Note that this result can be extended to other types of waves, such as storm waves (i.e., increase of wave frequency increase pore water pressure head gradient induced by waves). We showed that the time factor, T_v , which is used in theory of consolidation, can also be related to $z_i/\sqrt{C_{v0}T_d}$. We also showed the importance of the time lag between the tsunami flow height time series and the excess pore water pressure head gradient with depth. After tsunami draw-down starts, infiltration still occurs for some time and then upward seepage flow occurs. It was shown that the time lag increases with depth and decrease of tsunami duration.

In Chapter 6, sensitivity analyses performed for hydraulic conductivity showed that the maximum excess pore water pressure head gradient at ground surface reduces significantly with increase of hydraulic conductivity. Sensitivity analyses were also performed on soil bulk modulus. The trend of variation of the maximum excess pore water pressure head gradient at the ground surface for the linear model is similar to the nonlinear model. As the shear modulus increases the absolute value of the maximum excess pore water pressure head gradient increases and then reduces. This trend refers to the two competing effect of soil stiffness on m_v and B value.

During the tsunami, the pore water pressure changes from the ground surface to the within the ground. More specifically, the pore water pressure diffuses from the ground surface into the ground. The diffusion rate is governed by a diffusion

coefficient and the diffusion equation (n.b., the diffusion coefficient is different from the coefficient of consolidation). A new diffusion coefficient, C_v^* , was proposed and calibrated. The goal of the C_v^* calibration was to estimate the pore water pressure induced by tsunami loading with an uncoupled rapid draw-down of water approach. Therefore, the correlation between the soil stiffness and C_v^* was shown for both the linear and nonlinear soil constitutive models.

We used previous researchers measurement of entrained air to estimate the excess pore water pressure head gradient for a field case with real gas content measurements. The maximum excess pore water pressure head gradient at the ground surface during the tsunami draw-down is 0.0395, which is larger than the value obtained for the de-aired water case (i.e., 0.0032). However, this value is about ten times smaller than the condition where the entire 10 m soil layer is fully saturated with aired water (i.e., 0.1864). The reported values above are for a tsunami with medium duration and medium height. Sensitivity analysis for water bulk modulus showed that reduction of fluid bulk modulus can significantly increase pore water pressure head gradient induced by tsunami.

To investigate liquefaction potential, six tsunamis with different heights and durations were studied. The results showed that soil liquefaction potential increases with increase of tsunami height and reduces with increase of tsunami duration. Two definitions for tsunami-induced liquefaction were shown. It was shown that soil firstly liquefied locally, because of high excess pore water pressure head gradient (although the total stress is more than total pore water pressure). After that, the excess pore water pressure head gradient increases until the total pore water

pressure becomes equal to the total stress. For tsunami-induced liquefaction, the excess pore water pressure head gradient can become large (i.e., more than the critical gradient needed for sediment instability), and the effective stress can become negative (i.e., total pore water pressure is more than total stress in soil). Note that this condition does not occur for residual liquefaction. The current developed seepage-deformation model has the limitation that it can not predict the excess pore water pressure head gradient induced by tsunami loading after the total pore water pressure becomes larger than the total stress (i.e., effective stress becomes zero and soil stiffness diminishes).

At the end of Chapter 6, the coupled seepage-deformation model was extended to two dimensions. The convergence studies for two dimensional model showed that the numerical model converged. Comparison of one dimensional model with two dimensional model results show that the one dimensional model underestimates the pore water pressure head gradient induced by tsunami. Note that, testing in a two-dimensional flume is not the best method to separate residual liquefaction and momentary liquefaction for progressive waves and standing waves, because residual liquefaction and momentary liquefaction occur simultaneously during progressive wave and standing wave loading. Recall that momentary liquefaction occurs because of the seepage in the soil, and residual liquefaction occurs because of cyclic shear stress in the soil. Under the wave crest, pressure is higher than under the trough, which results in two-dimensional seepage within the soil bed. In other words, under the wave crest, a upward gradient exists, and under the wave trough, a downward gradient occurs. In addition, note that in the two-dimensional do-

main, for the sloped bed, the excess pore water pressure head gradient is affected by the gravitational acceleration component along bed, which is not considered during the one-dimensional modeling. The preceding point is significant for steep slopes; therefore, for fully saturated soil conditions on a sloped soil bed, momentary liquefaction is a two-dimensional problem rather than a one-dimensional problem. Based on the aforementioned discussion, the problem of pore water pressure changes during tsunami draw-down is a two-dimensional problem. Note that the mechanism of progressive wave and standing wave induced liquefaction is more akin to residual liquefaction. The preceding observation is supported by the experiments performed by previous researchers (i.e., explained in Chapter 2). For two dimensional model, cyclic deformation of soil generates pore water pressure. We believe that shear stress is not zero under the anti-nodes. Shear deformation exists, but in another plane and with a lower amount. The shear stress increases from anti-nodes towards the nodes. Note that the cyclic deformation of soil under wave loading (i.e., residual liquefaction) was not investigated herein; i.e., the focus was on momentary liquefaction.

Finally, we also want to mention that although we applied the developed seepage-deformation model to tsunami loading, it is not restricted to tsunami loading. It can be used for loading of soil by fluid in other scenarios. In other words, it can be used to study sediment instability caused by different types of waves, like standing waves and progressive waves.

7.2 Recommendations for future work

The developed seepage-deformation model is able to predict excess pore water pressure head gradients based on given modeling inputs. Moving forward, the developed seepage-deformation model needs to be calibrated and the results need to be compared with laboratory experimental results. Therefore, one-dimensional laboratory experiments investigating wave-induced pore water pressures in soil beds with impermeable bottoms should be performed to calibrate the seepage-deformation model. During the laboratory experiments, the B value and fundamental soil properties need to be measured.

It was shown that the developed seepage-deformation model is a function of the soil properties, and it was especially shown that the B value is an important parameter. Recall that the B value is a function of the relative stiffness of fluid and soil structure; accordingly, the existence of air can affect the B value significantly. More work needs to be completed to investigate the affect of air bubbles, dissolved air, and sand density on the B value.

Determining how the B value changes under different rates of loading for different soils is important and more laboratory experiments need to be performed to estimate B values for clay, silt, sand, gravel, and rock for different rates of loading. Note that in soil mechanics laboratory experiments, like triaxial testing, usually de-aired water with high back pressure is used to increase the B value. For the more realistic condition in the ocean for the surface soil, the B value is different from the laboratory determined value, because the laboratory-determined B value

is based on a stabilized, equilibrium condition. In other words, loading of porous media by waves is a dynamic and transient problem; therefore, the B value should be measured in a transient condition. In summary, more studies on how the load is shared between soil particle and water with time in sand during slow and fast loading (i.e., loading by fluid) rates should be performed.

New triaxial equipment should be designed to run unjacketed tests on sand. In unjacketed tests, there is no impermeable membrane around the soil specimen and fluid around the specimen has direct interaction with the soil. From the unjacketed test, the time lag between the pore water pressure changes and fluid pressure changes around the specimen can be estimated. Note that larger specimens result in more realistic results during unjacketed tests. Besides the B value, drained and undrained Poisson's ratio of sand measured during transient conditions in the unjacketed tests also needs to be studied.

The proposed seepage-deformation model can be improved by improving the deformation model. For example, there are several complex volume change models that should be investigated during future studies (e.g., Alonso et al., 1990; Bolzon et al., 1996; Gallipoli et al., 2003; Sheng et al., 2004). In the developed seepage-deformation model, the effect of air was neglected. Because the loading occurs quickly, it is suggested to consider the effect of air. Considering air pressure results in more accurate results and the fingering effect can be shown too by considering air pressure. Herein, the assumed soil water characteristic model neglects the hysteresis effect. In the future, the hysteresis effect in the soil characteristic curve models can be considered. In the developed seepage-deformation model, for the

two-dimensional model during the tsunami draw-down it was assumed that the pressure is atmospheric at the ground surface. In other words, it was assumed that after the soil is saturated during the tsunami run-up, the water table does not go below the ground surface. However, for large beach slopes, the dynamic boundary condition during the tsunami draw-down on the soil surface can be used. In other words, during tsunami draw-down, the boundary condition may change from Dirichlet to Neumann. We should also note that the generation of pore water pressure because of the cyclic deformation induced by the waves also needs to be considered for future analyses.

In addition to the aforementioned recommendations, more analysis should be performed to better understand the sediment behavior under tsunami loading. The effect of wave period, length, amplitude, and wave shape on pore water pressure distribution can be investigated. Herein, one type of soil was used for all the analyses; therefore, the effect of soil properties on pore water pressure distribution can be studied in future. For the two-dimensional model, the effect of slope, depth, wave period, wave length, amplitude, and soil properties on the excess pore water pressure head gradient in the soil bed needs to be investigated. An impermeable layer on the soil surface acting like a structure can be modeled. Then, the effect of the excess pore water pressure head gradient on the structure and the effect of structure on the pore water pressure distribution can be investigated. As stated in this study, tsunami attack occurs twenty to thirty minutes after earthquake. Earthquake changes the pore water pressure distribution in the soil. Therefore, the time lag between earthquake loading and tsunami loading on the pore water

pressure response in soil can be studied. Note that Abdollahi et al. (2017) contains more information about the effects of the time lag between earthquake loading and tsunami loading on the pore water pressure response of soil beds.

Finally, new models can be developed to study the pore water pressure induced by tsunami loading. Specifically, the new theory of porous media and mixture theory can be used to model the loading of porous media by fluid. In addition, superposition of two modes (i.e., mode 1: pore water pressure induced by tsunami weight, mode 2: pore water pressure induced by seepage) can be applied to model the pore water pressure induced by fluid.

Bibliography

- Abdollahi, A., Adams, R. K., and Mason, H. B., 2017. Earthquake-induced water level rise: Implications for tsunami-induced sediment instability in coastal areas. In *Proceedings of GeoCongress 2017*. Orlando, Florida.
- Abdoun, T., Gonzalez, M., Thevanayagam, S., Dobry, R., Elgamal, A., Zeghal, M., Mercado, V., and El Shamy, U., 2013. Centrifuge and large-scale modeling of seismic pore pressures in sands: Cyclic strain interpretation. *Journal of Geotechnical and Geoenvironmental Engineering* **139**, 1215–1234.
- Achenbach, J. D., 1975. *Wave Propagation in Elastic Solids*. 1st edn. Elsevier, Amsterdam.
- Adeyemo, M. D., 1968. Effect of beach slope and shoaling on wave asymmetry. In *Coastal Engineering 1968*, pp. 145–172. London.
- Alonso, E., Pérez de Agreda and Pinyol, N. M., Puigmartí, 2009. Slope stability under rapid drawdown conditions. In *First Italian Workshop on Landslides*, pp. 11–27.
- Alonso, E. E., Gens, A., and Josa, A., 1990. Constitutive model for partially saturated soils. *Géotechnique* **40**, 405–430.
- Alonso, E. E. and Pinyol, N. M., 2010. Landslides in reservoirs and dam operation. In *Proceedings of the 2nd International Congress on Dam Maintenance and Rehabilitation*, pp. 3–27. Zaragoza, Spain.
- Ammon, C. J., Lay, T., Kanamori, H., and Cleveland, M., 2011. A rupture model of the 2011 off the Pacific coast of Tohoku Earthquake. *Earth, Planets and Space* **63**, 693–696.
- Barden, L., 1965. Consolidation of clay with non-linear viscosity. *Géotechnique* **15**, 345–362.
- Bear, J., 1988. *Dynamics of Fluids in Porous Media*. 1st edn. Dover Publications, New York.

- Berilgen, M. M., 2007. Investigation of stability of slopes under drawdown conditions. *Computers and Geotechnics* **34**, 81–91.
- Bernard, E. N. and Robinson, A. R. (eds.), 2009. *Tsunamis*, vol. 15 of *The Sea*. Harvard University Press, Cambridge, Massachusetts.
- Biot, M. A., 1941. General theory of three-dimensional consolidation. *Journal of Applied Physics* **12**, 155–164.
- Bishop, A., 1959. The effective stress principle. *Teknisk Ukeblad* **39**, 859–863.
- Bishop, A. W., 1954. The use of pore-pressure coefficients in practice. *Géotechnique* **4**, 148–152.
- Bishop, A. W. and Henkel, D. J., 1962. *The Measurement of Soil Properties in the Triaxial Test*. 2nd edn. Edward Arnold Publishers, London.
- Bjerrum, L., 1973. Geotechnical problems involved in foundations of structures in the North Sea. *Géotechnique* **23**, 319–358.
- Bolzon, G., Schrefler, B., and Zienkiewicz, O., 1996. Elastoplastic soil constitutive laws generalized to partially saturated states. *Géotechnique* **46**, 279–289.
- Bonjean, D., Foray, P., Piedra-Cueva, I., Mory, M., Michallet, H., Breul, P., Haddani, Y., Abadie, S. et al., 2004. Monitoring of the foundations of a coastal structure submitted to breaking waves: Occurrence of momentary liquefaction. In *The Fourteenth International Offshore and Polar Engineering Conference*. International Society of Offshore and Polar Engineers.
- Bradford, S. F. and Sanders, B. F., 2002. Finite-volume model for shallow-water flooding of arbitrary topography. *Journal of Hydraulic Engineering* **128**, 289–298.
- Carrier, G. and Greenspan, H., 1958. Water waves of finite amplitude on a sloping beach. *Journal of Fluid Mechanics* **4**, 97–109.
- Carrier, G. F., Wu, T. T., and Yeh, H., 2003. Tsunami run-up and draw-down on a plane beach. *Journal of Fluid Mechanics* **475**, 79–99.
- Carrier, W. D., 2003. Goodbye, Hazen; hello, Kozeny-Carman. *Journal of Geotechnical and Geoenvironmental Engineering* **129**, 1054–1056.

- Carslaw, H. S. and Jaeger, J. C., 1959. Conduction of heat in solids. *Oxford: Clarendon Press, 1959, 2nd ed.* .
- Casulli, V., 1990. Semi-implicit finite difference methods for the two-dimensional shallow water equations. *Journal of Computational Physics* **86**, 56–74.
- Chowdhury, B., 2004. One dimensional study of wave-induced momentary liquefaction of the seabed. Master's thesis, National University of Singapore.
- Chowdhury, B., Dasari, G., and Nogami, T., 2006. Laboratory study of liquefaction due to wave–seabed interaction. *Journal of Geotechnical and Geoenvironmental Engineering* **132**, 842–851.
- Cryer, C., 1963. A comparison of the three-dimensional consolidation theories of Biot and Terzaghi. *The Quarterly Journal of Mechanics and Applied Mathematics* **16**, 401–412.
- De Boer, R., 2012. *Theory of Porous Media: Highlights in the Historical Development and Current State*. 1st edn. Springer, Berlin.
- Dean, R. G. and Dalrymple, R. A., 1991. *Water Wave Mechanics for Engineers and Scientists*. 1st edn. World Scientific, Singapore.
- Detournay, E. and Cheng, A. H.-D., 1993. Fundamentals of poroelasticity. In Hudson, J. A. (ed.), *Comprehensive Rock Engineering: Principles, Practice and Projects*, vol. 2, pp. 113–171. Pergamon Press, Oxford.
- Duncan, J. M., Wright, S., and Wong, K. S., 1990. Slope stability during rapid drawdown. In Duncan, J. M. (ed.), *H. Bolton Seed: Memorial Symposium Proceedings*, vol. 2, pp. 253–272. Bitech Publishers, Vancouver, Canada.
- Firoozabadi, A. and Katz, 1979. An analysis of high-velocity gas flow through porous media. *Journal of Petroleum Technology* **31**, 211–216.
- Fredlund, D. and Morgenstern, N., 1976. Constitutive relations for volume change in unsaturated soils. *Canadian Geotechnical Journal* **13**, 261–276.
- Fredlund, D. G. and Morgenstern, N. R., 1977. Stress state variables for unsaturated soils. *Journal of Geotechnical and Geoenvironmental Engineering* **103**, 261–276.

- Fredlund, D. G. and Rahardjo, H., 1993. *Soil mechanics for unsaturated soils*. John Wiley & Sons.
- Fredlund, D. G., Rahardjo, H., and Fredlund, M. D., 2012. *Unsaturated soil mechanics in engineering practice*. 1st edn. Wiley, Hoboken, New Jersey.
- Fredlund, M., Lu, H., and Feng, T., 2011. Combined seepage and slope stability analysis of rapid drawdown scenarios for levee design. In *Proceedings of Geo-Frontiers 2011*, pp. 1595–1604. Dallas.
- Fritz, H. M., Phillips, D. A., Okayasu, A., Shimosono, T., Liu, H., Mohammed, F., Skanavis, V., Synolakis, C. E., and Takahashi, T., 2012. The 2011 Japan tsunami current velocity measurements from survivor videos at Kesennuma Bay using LiDAR. *Geophysical Research Letters* **39**.
- Gallipoli, D., Gens, A., Sharma, R., and Vaunat, J., 2003. An elasto-plastic model for unsaturated soil incorporating the effects of suction and degree of saturation on mechanical behaviour. *Géotechnique*. **53**, 123–136.
- Garrison, T. and Ellis, R., 2016. *Essentials of Oceanography*. 8th edn. Cengage, Boston.
- Geo-Slope, 2013. Heave due to Infiltration. <http://downloads.geo-slope.com/geostudioresources/7/examples/Heave%20due%20to%20infiltration.pdf>. Accessed: 2017-03-06.
- Gratiot, N., Mory, M. et al., 2000. Wave-induced sea bed liquefaction with application to mine burial. In *The Tenth International Offshore and Polar Engineering Conference*. International Society of Offshore and Polar Engineers.
- Guppy, K. H., Cinco-Ley, H., and Ramey, H. J., 1982. Pressure buildup analysis of fractured wells producing at high flow rates. *Journal of Petroleum Technology* **34**, 2–656.
- Harbitz, C., 1992. Model simulations of tsunamis generated by the Storegga slides. *Marine Geology* **105**, 1–21.
- Hardin, B. O. and Richart, F. E. J., 1963. Elastic wave velocities in granular soils. *Journal of the Soil Mechanics and Foundations Division* **89**, 33–65.

- Hazen, A., 1892. Some physical properties of sands and gravels with special reference to their use in filtration. In *24th Annual Report*, pp. 539–556. Massachusetts State Board of Health, Boston.
- Helmig, R., 1997. *Multiphase Flow and Transport Processes in the Subsurface: A Contribution to the Modeling of Hydrosystems*. 1st edn. Springer-Verlag, Berlin.
- Holzbecher, E., 2016. Multiphysics modelling of the Mandel-Cryer effect. *International Journal of Multiphysics* **10**, 11–20.
- Hubbert, W. W., Rubey, 1960. Role of fluid pressure in mechanics of overthrust faulting a replay. *Geological Society of America Bulletin* **71**, 617–628.
- Idriss, I. and Boulanger, R. W., 2008. *Soil Liquefaction During Earthquakes*. 1st edn. Earthquake Engineering Research Institute, Oakland, California.
- Ishihara, K., 1996. *Soil Behaviour in Earthquake Geotechnics*. 1st edn. Clarendon Press, Oxford.
- Jaeger, H. M. and Nagel, S. R., 1992. Physics of the granular state. *Science* **255**, 1523–1531.
- Janbu, N., 1963. Soil compressibility as determined by oedometer and triaxial tests. In *Proceedings of the 2nd European Conference on Soil Mechanics and Foundation Engineering*, vol. 1, pp. 19–25. Wiesbaden, Germany.
- Khalili, N. and Khabbaz, M., 1998. A unique relationship for χ for the determination of the shear strength of unsaturated soils. *Géotechnique* **48**, 681–687.
- Kirca, V. O., Sumer, B. M., and Fredsøe, J., 2013. Residual liquefaction of seabed under standing waves. *Journal of Waterway, Port, Coastal, and Ocean Engineering* **139**, 489–501.
- Kokusho, T., 2000. Correlation of Pore-Pressure B-value with P-wave Velocity and Poisson's Ratio for Imperfectly Saturated Sand or Gravel. *Soils and Foundations* **40**, 95–102.
- Koshimura, S. and Hayashi, S., 2012. Tsunami flow measurement using the video recorded during the 2011 Tohoku tsunami attack. In *Geoscience and Remote Sensing Symposium (IGARSS), 2012 IEEE International*, pp. 6693–6696. IEEE.

- Krahn, J., 2004. *Stress and deformation modeling with SIGMA/W, an engineering methodology*. Tech. rep., GEO-SLOPE International Ltd, Calgary, Alberta.
- Kramer, S. L. and Seed, H. B., 1988. Initiation of soil liquefaction under static loading conditions. *Journal of Geotechnical Engineering* **114**, 412–430.
- Lambe, T. W. and Whitman, R. V., 1969. *Soil Mechanics*. 1st edn. John Wiley & Sons, New York.
- Laubscher, H. P., 1960. Role of fluid pressure in mechanics of overthrust faulting: discussion. *Geological Society of America Bulletin* **71**, 611–616.
- Liu, X., García, M. H., Muscari, R. et al., 2007. Numerical investigation of seabed response under waves with free-surface water flow. *International Journal of Offshore and Polar Engineering* **17**.
- Lowe, D. R., 1975. Water escape structures in coarse-grained sediments. *Sedimentology* **22**, 157–204.
- Lowe, J. and Karafiath, L., 1960. Effect of anisotropic consolidation on the undrained shear strength of compacted clays. In *Proceedings of the ASCE Research Conference on Shear Strength of Cohesive Soils*, pp. 837–858. Boulder, Colorado.
- Lu, N. and Kaya, M., 2013. Power law for elastic moduli of unsaturated soil. *Journal of Geotechnical and Geoenvironmental Engineering* **140**, 46–56.
- Lu, N. and Likos, W. J., 2004. *Unsaturated Soil Mechanics*. 1st edn. Wiley, Hoboken, New Jersey.
- Lu, N. and Likos, W. J., 2006. Suction stress characteristic curve for unsaturated soil. *Journal of Geotechnical and Geoenvironmental Engineering* **132**, 131–142.
- Mandel, J., 1953. Consolidation of soils (mathematical study). *Géotechnique* **3**, 287–299.
- Martins, J. P., Milton-Taylor, D., and Leung, H. K., 1990. The effects of non-Darcy flow in propped hydraulic fractures. In *SPE Annual Technical Conference and Exhibition*. New Orleans.

- Mason, H. B. and Yeh, H., 2016. Sediment liquefaction: A pore-water pressure gradient viewpoint. *Bulletin of the Seismological Society of America* **106**, 1908–1913.
- McGinnis, D. F., Greinert, J., Artemov, Y., Beaubien, S., and Wüest, A., 2006. Fate of rising methane bubbles in stratified waters: How much methane reaches the atmosphere? *Journal of Geophysical Research: Oceans* **111**.
- Mei, C. C. and Foda, M. A., 1981. Wave-induced responses in a fluid-filled poro-elastic solid with a free surface boundary layer theory. *Geophysical Journal International* **66**, 597–631.
- Merxhani, A. and Liang, D., 2012. Investigation of the poro-elastic response of seabed to solitary waves. In *The Twenty-Second International Offshore and Polar Engineering Conference*. Rhodes, Greece.
- Michallet, H., Mory, M., and Piedra-Cueva, I., 2009. Wave-induced pore pressure measurements near a coastal structure. *Journal of Geophysical Research: Oceans* **114**.
- Mitchell, J. K. and Soga, K., 2005. *Fundamentals of Soil Behavior*. 3rd edn. John Wiley & Sons, Hoboken, New Jersey.
- Miyamoto, S. S., J and Sekiguchi, H., 2003. Preshearing effect on the wave-induced liquefaction in sand beds. In *Proceedings of of Soil and Rock America*. Boston, pp. 1025–1032.
- Mongan, C. E., 1985. *Validity of Darcy's law under transient conditions*. *Tech. Rep. Professional Paper 1331*, United States Geological Survey, Washington, DC.
- Mori, N., Takahashi, T., Yasuda, T., and Yanagisawa, H., 2011. Survey of 2011 Tohoku earthquake tsunami inundation and run-up. *Geophysical Research Letters* **38**.
- Mualem, Y., 1976. A new model for predicting the hydraulic conductivity of unsaturated porous media. *Water resources research* **12**, 513–522.
- Murray, E. J., 2002. An equation of state for unsaturated soils. *Canadian Geotechnical Journal* **39**, 125–140.

- Naesgaard, E., Byrne, P. M., and Wijewickreme, D., 2007. Is P-wave velocity an indicator of saturation in sand with viscous pore fluid? *International Journal of Geomechanics* **7**, 437–443.
- Nakazawa, H., Ishihara, K., Tsukamoto, Y., and Kamata, T., 2004. Case studies on evaluation of liquefaction resistance of imperfectly saturated soil deposits. In *Proceedings of International Conference on Cyclic Behaviour of Soils and Liquefaction Phenomena, Bochum, Germany*, vol. 31, pp. 295–304.
- Nur, A. and Byerlee, J., 1971. An exact effective stress law for elastic deformation of rock with fluids. *Journal of Geophysical Research* **76**, 6414–6419.
- Oh, W. T., Vanapalli, S. K., and Puppala, A. J., 2009. Semi-empirical model for the prediction of modulus of elasticity for unsaturated soils. *Canadian Geotechnical Journal* **46**, 903–914.
- Okal, E. A., 2009. Excitation of tsunamis by earthquakes. In Bernard, E. N. and Robinson, A. R. (eds.), *Tsunamis*, vol. 15 of *The Sea*. Harvard University Press, Cambridge, Massachusetts.
- Okusa, S., Nakamura, T., and Fukue, M., 1984. Measurements of wave-induced pore pressure and coefficients of permeability of submarine sediments during reversing flow. In *Seabed Mechanics*, pp. 113–122. Springer.
- Olson, R. E., 1963. Effective stress theory of soil compaction. *Journal of the Soil Mechanics and Foundations Division* **89**, 27–46.
- Pariseau, W., Schmelter, S., and Sheik, A., 1997. Mine slope stability analysis by coupled finite element modeling. *International Journal of Rock Mechanics and Mining Sciences* **34**, 242.e1–242.e17.
- Peaceman, D. W., 1977. *Fundamentals of Numerical Reservoir Simulation*. 1st edn. Elsevier, New York.
- Peszyńska, M., Jenkins, E. W., and Wheeler, M. F., 2002. Boundary Conditions for Fully Implicit Two-Phase Flow. *Recent Advances in Numerical Methods for Partial Differential Equations and Applications: Proceedings of the 2001 John H. Barrett Memorial Lectures, Trends in Computational Mathematics, May 10-12, 2001, the University of Tennessee, Knoxville, TN* **306**, 85.

- Peszyńska, M. and Yi, S.-Y., 2008. Numerical methods for unsaturated flow with dynamic capillary pressure in heterogeneous porous media. *International Journal of Numerical Analysis and Modeling* **5**, 126–149.
- Pham, H. Q., Fredlund, D. G., and Barbour, S. L., 2005. A study of hysteresis models for soil-water characteristic curves. *Canadian Geotechnical Journal* **42**, 1548–1568.
- Pinyol, N. M., Alonso, E. E., and Olivella, S., 2008. Rapid drawdown in slopes and embankments. *Water Resources Research* **44**.
- Putnam, J., 1949. Loss of wave energy due to percolation in a permeable sea bottom. *Eos, Transactions American Geophysical Union* **30**, 349–356.
- Richards, L. A., 1931. Capillary conduction of liquids through porous mediums. *Journal of Applied Physics* **1**, 318–333.
- Sakai, T., Hatanaka, K., and Mase, H., 1992. Wave-induced effective stress in seabed and its momentary liquefaction. *Journal of Waterway, Port, Coastal, and Ocean Engineering* **118**, 202–206.
- Sakai, T., Hattori, A., and Hatanaka, K., 1991. Wave-induced transient pore-water pressure and seabed instability in the surf zone. In *Proceedings of International Conference on Geotechnical Engineering for Coastal Development-Theory and Practice on Soft Ground (Geo-Coast91)*, pp. 627–632.
- Santamarina, J. C., Klein, K. A., and Fam, M. A., 2001. *Soils and Waves*. 1st edn. John Wiley & Sons, Chichester, England.
- Sawangsurriya, A., Edil, T. B., and Bosscher, P. J., 2009. Modulus-suction-moisture relationship for compacted soils in postcompaction state. *Journal of Geotechnical and Geoenvironmental Engineering* **135**, 1390–1403.
- Scott, R. F., 1963. *Principles of Soil Mechanics*. 1st edn. Addison-Wesley Publishing Company, Reading, Massachusetts.
- Seed, H. B. and Idriss, I. M., 1970. *Soil Moduli and Damping Factors for Dynamic Response Analyses*. Tech. Rep. EERC 70-10, Earthquake Engineering Research Center, University of California, Richmond, California.

- Seed, H. B., Lysmer, J., and Martin, P. P., 1976. Pore-water pressure changes during soil liquefaction. *Journal of the Geotechnical Engineering Division* **102**, 323–346.
- Seed, H. B. and Rahman, M. S., 1978. Wave-induced pore pressure in relation to ocean floor stability of cohesionless soils. *Marine Georesources & Geotechnology* **3**, 123–150.
- Sheng, D., Sloan, S., and Gens, A., 2004. A constitutive model for unsaturated soils: thermomechanical and computational aspects. *Computational Mechanics* **33**, 453–465.
- Skempton, A., 1954. The pore-pressure coefficients A and B. *Géotechnique* **4**, 143–147.
- Skempton, A. W., 1984. Effective stress in soils, concrete and rocks. In Burland, J. B. (ed.), *Selected Papers on Soil Mechanics by A. W. Skempton, F. R. S.*, pp. 106–118. Thomas Telford, London.
- Stoker, J. J., 1957. *Water Waves*. 1st edn. Interscience Publishers, New York.
- Stoll, R. D. and Kan, T.-K., 1981. Reflection of acoustic waves at a water–sediment interface. *The Journal of the Acoustical Society of America* **70**, 149–156.
- Sumer, B., Hatipoglu, F., Fredsøe, J., and Kaan Sumer, S., 2006. The sequence of sediment behaviour during wave-induced liquefaction. *Sedimentology* **53**, 611–629.
- Sumer, B. M., 2014. *Liquefaction Around Marine Structures*. World Scientific, Singapore.
- Sumer, B. M. and Fredsøe, J., 2002. *The Mechanics of Scour in the Marine Environment*. World Scientific, Singapore.
- Sumer, B. M., Fredsøe, J., Christensen, S., and Lind, M., 1999. Sinking/floatation of pipelines and other objects in liquefied soil under waves. *Coastal Engineering* **38**, 53–90.
- Sumer, B. M., Sen, M. B., Karagali, I., Ceren, B., Fredsøe, J., Sottile, M., Zilioli, L., and Fuhrman, D. R., 2011. Flow and sediment transport induced by a plunging solitary wave. *Journal of Geophysical Research: Oceans* **116**.

- Tadepalli, R. and Fredlund, D., 1991. The collapse behavior of a compacted soil during inundation. *Canadian Geotechnical Journal* **28**, 477–488.
- Taylor, D. W., 1948. *Fundamentals of Soil Mechanics*. 1st edn. John Wiley & Sons, New York.
- Terzaghi, K., 1943. *Theoretical Soil Mechanics*. 1st edn. John Wiley & Son, New York.
- Terzaghi, K., Peck, R. B., and Mesri, G., 1996. *Soil Mechanics in Engineering Practice*. 3rd edn. John Wiley & Sons, New York.
- van Genuchten, M., 1980. A closed-form equation for predicting the hydraulic conductivity of unsaturated soils. *Soil Science Society of America Journal* **44**, 892–898.
- Vanapalli, S., Fredlund, D., Pufahl, D., and Clifton, A., 1996. Model for the prediction of shear strength with respect to soil suction. *Canadian Geotechnical Journal* **33**, 379–392.
- Vanapalli, S. and Oh, W., 2010. A model for predicting the modulus of elasticity of unsaturated soils using the soil-water characteristic curve. *International Journal of Geotechnical Engineering* **4**, 425–433.
- Vanapalli, S. K. and Mohamed, F. M., 2007. Bearing capacity of model footings in unsaturated soils. In Schanz, T. (ed.), *Experimental Unsaturated Soil Mechanics*, pp. 483–493. Springer, Berlin.
- VandenBerge, D. R., 2014. Total stress rapid drawdown analysis of the Pilarcitos Dam failure using the finite element method. *Frontiers of Structural and Civil Engineering* **8**, 115–123.
- VandenBerge, D. R., Duncan, J. M., and Brandon, T. L., 2013. Rapid drawdown analysis using strength reduction. In *Proceedings of the 18th International Conference on Soil Mechanics and Geotechnical Engineering*, pp. 829–832. Paris.
- Verruijt, A., 1969. Elastic Storage of Aquifers. In deWiest, R. M. (ed.), *Flow Through Porous Media*, pp. 331–376. Academic Press, New York.
- Vu, H. Q. and Fredlund, D. G., 2006. Challenges to modelling heave in expansive soils. *Canadian Geotechnical Journal* **43**, 1249–1272.

- Whitham, G. B., 1974. *Linear and Nonlinear Waves*. 1st edn. John Wiley & Sons, New York.
- Wijetunge, J. J., 2006. Tsunami on 26 December 2004: spatial distribution of tsunami height and the extent of inundation in Sri Lanka. *Science of Tsunami Hazards* **24**, 225–239.
- Wong, T. T., Fredlund, D. G., and Krahn, J., 1998. A numerical study of coupled consolidation in unsaturated soils. *Canadian Geotechnical Journal* **35**, 926–937.
- Woodward, C. S. and Dawson, C. N., 2000. Analysis of expanded mixed finite element methods for a nonlinear parabolic equation modeling flow into variably saturated porous media. *SIAM Journal on Numerical Analysis* **37**, 701–724.
- Yang, J., 2002. Liquefaction resistance of sand in relation to P-wave velocity. *Geotechnique* **52**, 295–298.
- Yang, J., 2005. Pore pressure coefficient for soil and rock and its relation to compressional wave velocity. *Géotechnique* **55**, 251–256.
- Yeh, H. and Mason, H. B., 2014. Sediment response to tsunami loading: mechanisms and estimates. *Géotechnique* **64**, 131–143.
- Yeh, H. and Sato, S., 2016. Tsunami Effects on Buildings and Coastal Structures (Special Issue on Uncertainties in Tsunami Effects). *Journal of Disaster Research* **11**, 662–669.
- Yeh, H., Tonkin, S., Heller, E., Arduino, P., Kato, F., and Sato, S., 2004. Mechanisms of scour induced by tsunami runup. In *Proceedings of Second International Conference on Scour and Erosion, Singapore*, vol. 2, pp. 464–471.
- Youd, T. L., Idriss, I. M., Andrus, R. D., Arango, I., Castro, G., Christian, J. T., Dobry, R., Finn, W. D. L., Harder Jr, L. F., Hynes, M. E., Ishihara, K., Koester, J. P., Liao, S. S. C., Marcuson III, W. F., Martin, G. R., Mitchell, J. K., Moriwaki, Y., Power, M. S., Robertson, P. K., Seed, R. B., and Stokoe II, K. H., 2001. Liquefaction resistance of soils: summary report from the 1996 NCEER and 1998 NCEER/NSF workshops on evaluation of liquefaction resistance of soils. *Journal of Geotechnical and Geoenvironmental Engineering* **127**, 817–833.
- Young, Y. L., White, J. A., Xiao, H., and Borja, R. I., 2009. Liquefaction potential of coastal slopes induced by solitary waves. *Acta Geotechnica* **4**, 17–34.

- Zarba, R. L., Bouloutas, E., and Celia, M., 1990. General mass-conservative numerical solution for the unsaturated flow equation. *Water Resources Research* **26**, 1483–1496.
- Zen, K. and Yamazaki, H., 1990a. Mechanism of wave-induced liquefaction and densification in seabed. *Journal of Soils and Foundations* **30**, 90–104.
- Zen, K. and Yamazaki, H., 1990b. Oscillatory pore pressure and liquefaction in seabed induced by ocean waves. *Journal of Soils and Foundations* **30**, 147–161.
- Zeng, Z. and Grigg, R., 2006. A criterion for non-Darcy flow in porous media. *Transport in Porous Media* **63**, 57–69.
- Zhang, L. L., Zhang, L. M., and Tang, W. H., 2005. Rainfall-induced slope failure considering variability of soil properties. *Géotechnique* **55**, 183–188.

APPENDICES

Appendix A: Pore water pressure and pore water pressure head
gradient for cases in Table 5.2

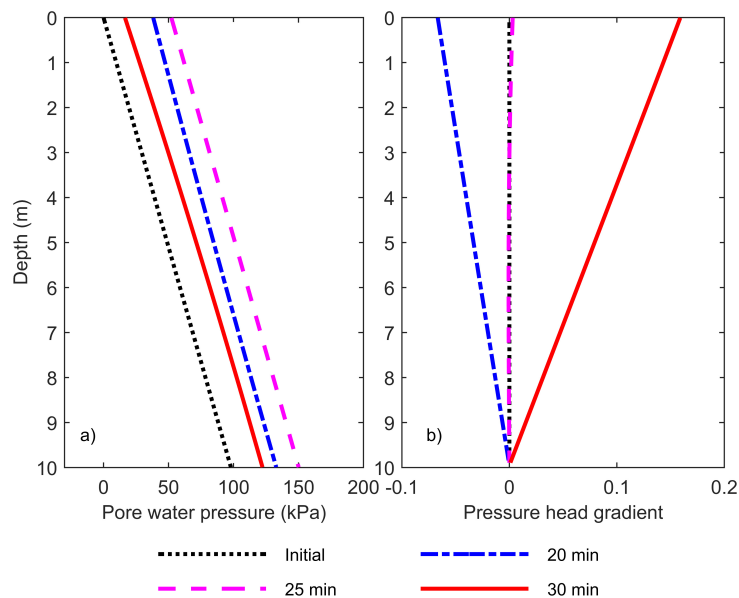


Figure A.1: Case S-LE-B(0): a) total pore water pressure at different time with depth for the saturated condition, assuming $B=0$, and considering linear constitutive model; b) pressure head gradient at different time with depth for the saturated condition, assuming $B=0$, and considering linear constitutive model.

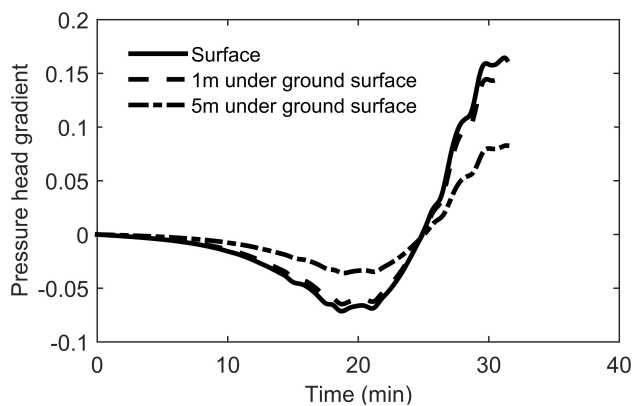


Figure A.2: Case S-LE-B(0): pressure head gradient changes with time at different depth for fully saturated linear model and $B=0$.

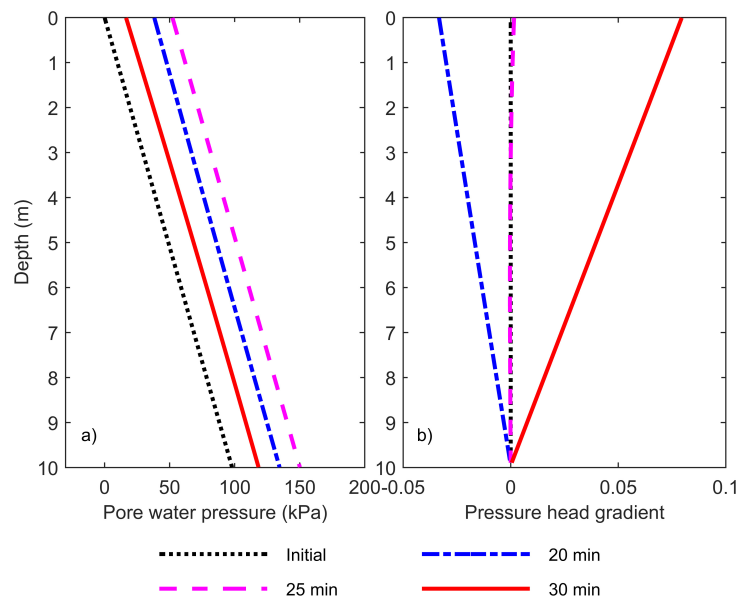


Figure A.3: Case S-LE-B(0.5): a) total pore water pressure at different time with depth for the saturated condition, assuming $B=0.5$, and considering linear constitutive model; b) pressure head gradient at different time with depth for the saturated condition, assuming $B=0.5$, and considering linear constitutive model.

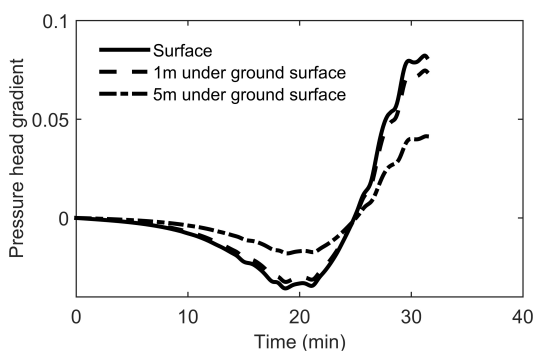


Figure A.4: Case S-LE-B(0.5): pressure head gradient changes with time at different depth for fully saturated linear model and $B=0.5$.

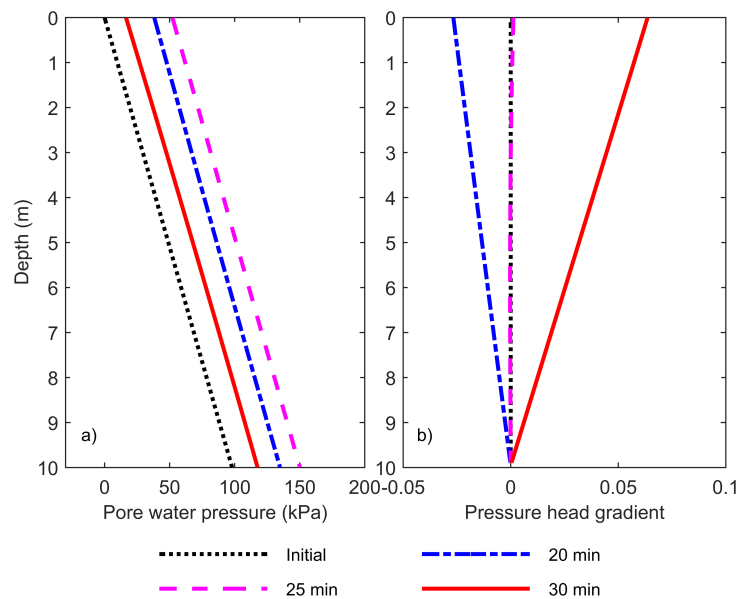


Figure A.5: Case S-LE-B(0.6): a) total pore water pressure at different time with depth for the saturated condition, assuming $B=0.5$, and considering linear constitutive model; b) pressure head gradient at different time with depth for the saturated condition, assuming $B=0.6$, and considering linear constitutive model.

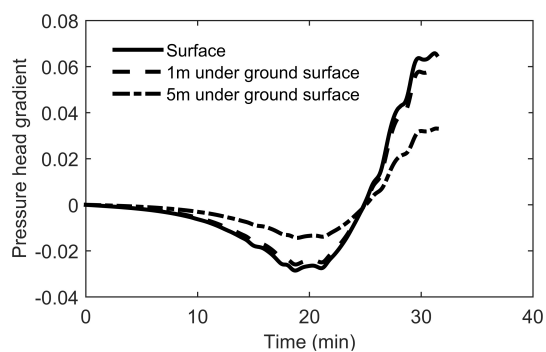


Figure A.6: Case S-LE-B(0.6): pressure head gradient changes with time at different depth for fully saturated linear model and $B=0.6$.

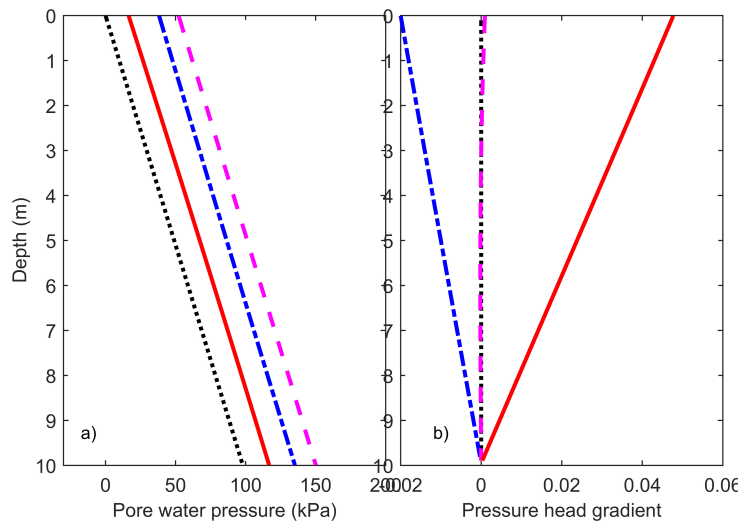


Figure A.7: Case S-LE-B(0.7): a) total pore water pressure at different time with depth for the saturated condition, assuming $B=0.7$, and considering linear constitutive model; b) pressure head gradient at different time with depth for the saturated condition, assuming $B=0.7$, and considering linear constitutive model.

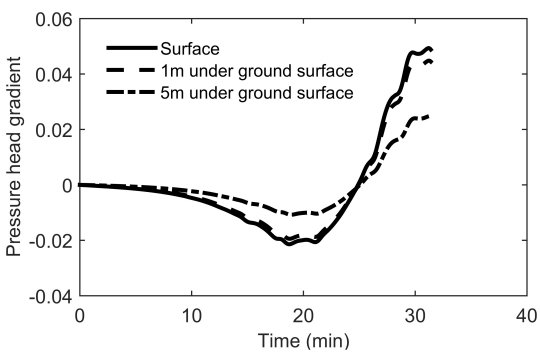


Figure A.8: Case S-LE-B(0.7): pressure head gradient changes with time at different depth for fully saturated linear model and $B=0.7$.

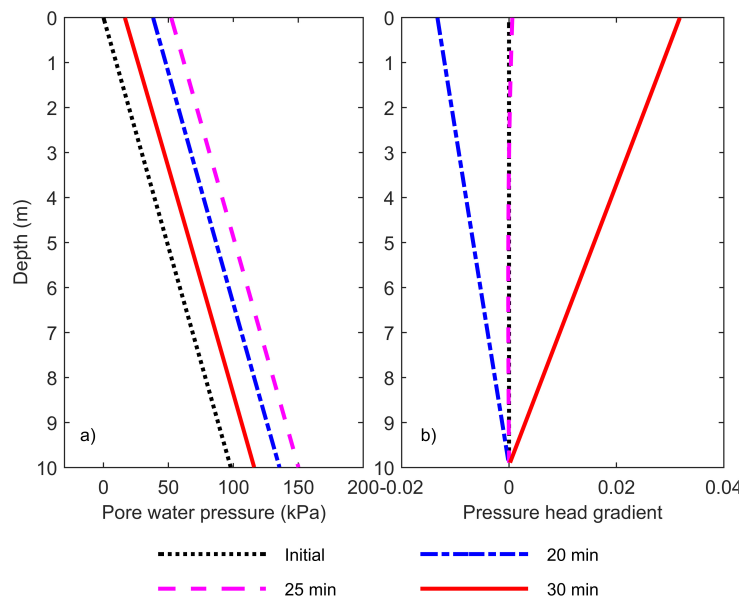


Figure A.9: Case S-LE-B(0.8): a) total pore water pressure at different time with depth for the saturated condition, assuming $B=0.8$, and considering linear constitutive model; b) pressure head gradient at different time with depth for the saturated condition, assuming $B=0.8$, and considering linear constitutive model.

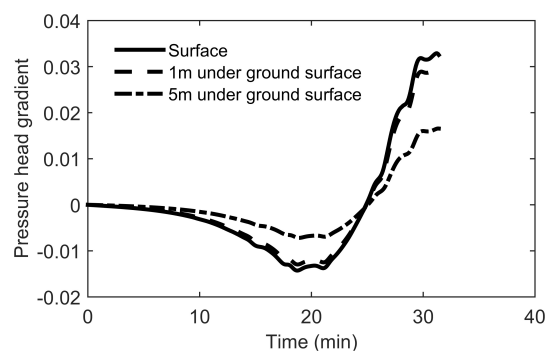


Figure A.10: Case S-LE-B(0.8): pressure head gradient changes with time at different depth for fully saturated linear model and $B=0.8$.

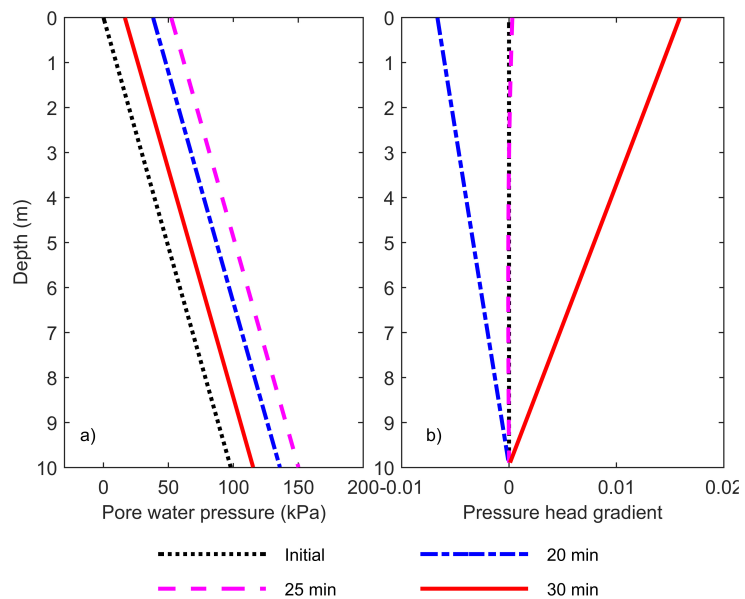


Figure A.11: Case S-LE-B(0.9): a) total pore water pressure at different time with depth for the saturated condition, assuming $B=0.9$, and considering linear constitutive model; b) pressure head gradient at different time with depth for the saturated condition, assuming $B=0.9$, and considering linear constitutive model.

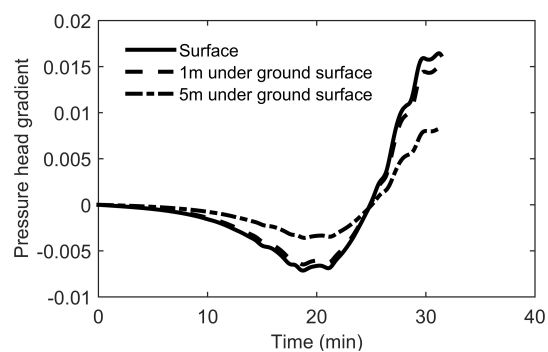


Figure A.12: Case S-LE-B(0.9): pressure head gradient changes with time at different depth for fully saturated linear model and $B=0.9$.

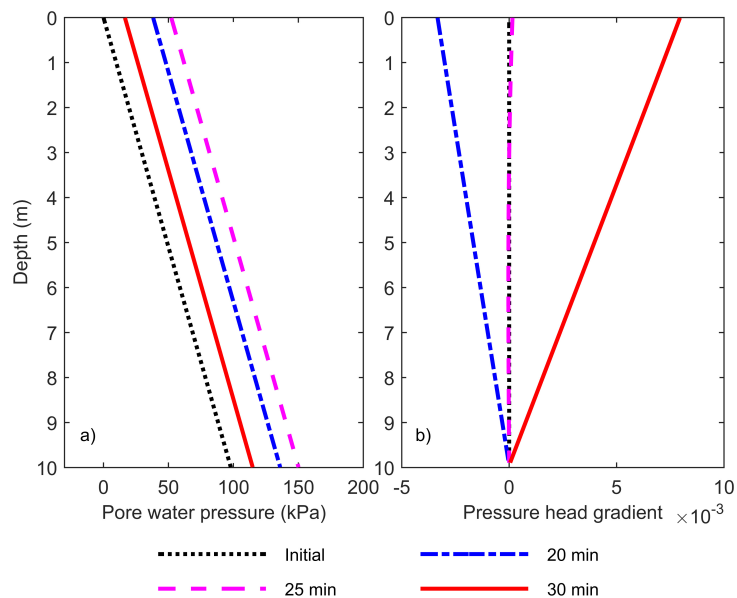


Figure A.13: Case S-LE-B(0.95): a) total pore water pressure at different time with depth for the saturated condition, assuming $B=0.95$, and considering linear constitutive model; b) pressure head gradient at different time with depth for the saturated condition, assuming $B=0.95$, and considering linear constitutive model.

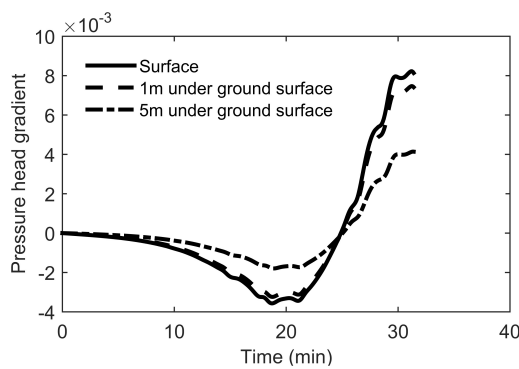


Figure A.14: Case S-LE-B(0.95): pressure head gradient changes with time at different depth for fully saturated linear model and $B=0.95$.

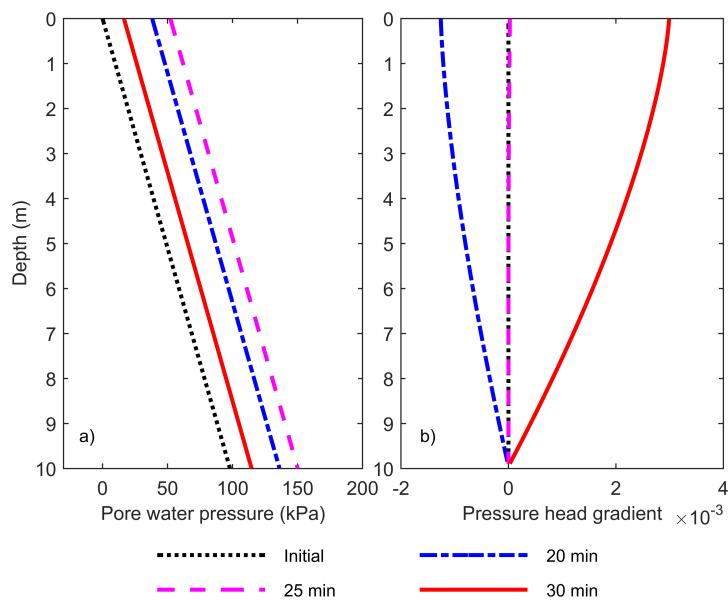


Figure A.15: Case S-LE-PW: a) total pore water pressure at different time with depth for the saturated condition, assuming pure water, and considering linear constitutive model; b) pressure head gradient at different time with depth for the saturated condition, assuming pure water, and considering linear constitutive model.

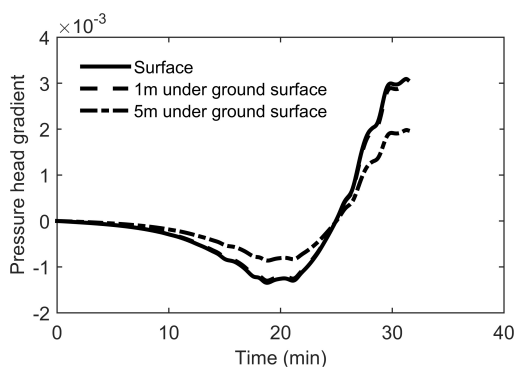


Figure A.16: Case S-LE-PW: pressure head gradient changes with time at different depth for fully saturated linear model and pure water.

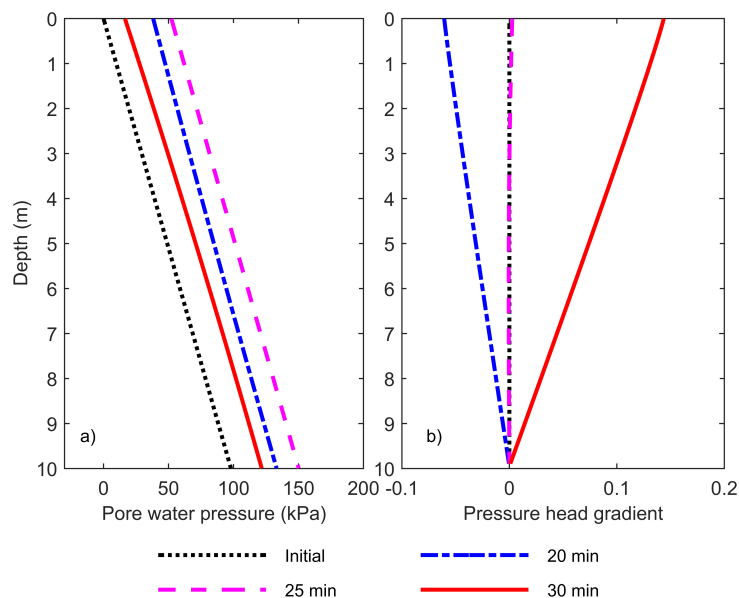


Figure A.17: Case S-LE-UW: a) total pore water pressure at different time with depth for the saturated condition, assuming aired water, and considering linear constitutive model; b) pressure head gradient at different time with depth for the saturated condition, assuming aired water, and considering linear constitutive model.

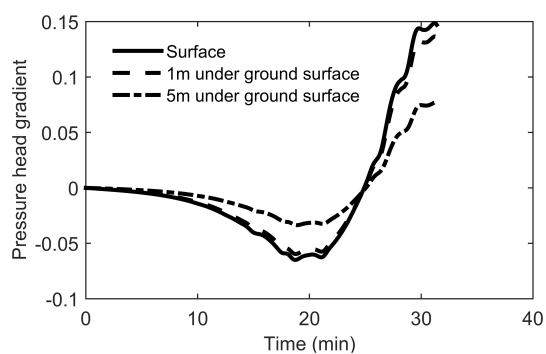


Figure A.18: Case S-LE-UW: pressure head gradient changes with time at different depth for fully saturated linear model and aired water.

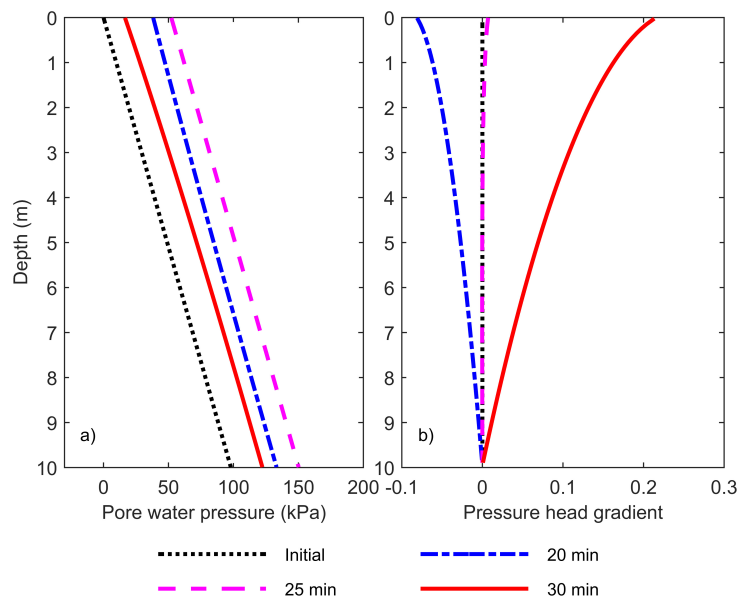


Figure A.19: Case S-NI-B(0): a) total pore water pressure at different time with depth for the saturated condition, assuming $B=0$, and considering nonlinear constitutive model; b) pressure head gradient at different time with depth for the saturated condition, assuming $B=0$, and considering nonlinear constitutive model.

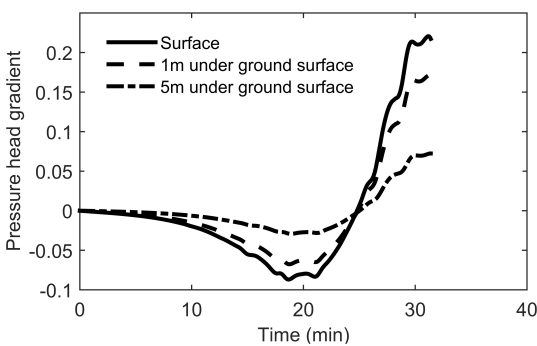


Figure A.20: Case S-NI-B(0): pressure head gradient changes with time at different depth for fully saturated nonlinear model and $B=0$.

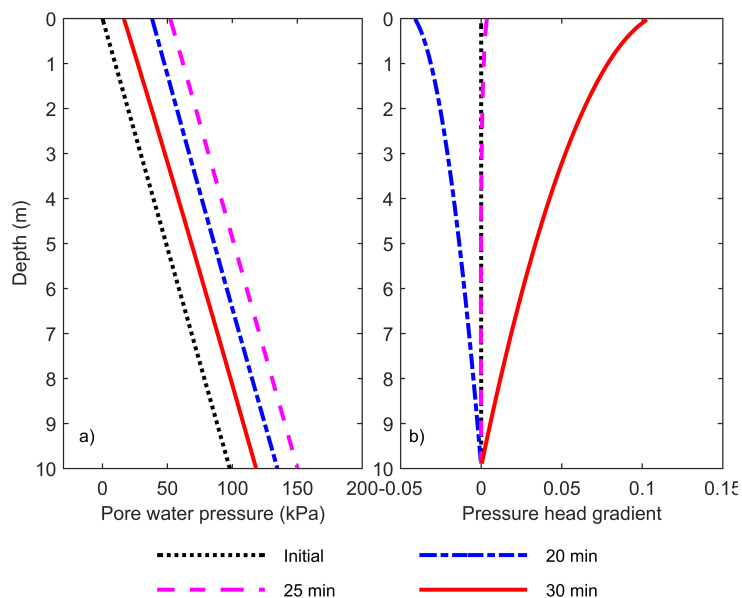


Figure A.21: Case S-NI-B(0.5): a) total pore water pressure at different time with depth for the saturated condition, assuming $B=0.5$, and considering nonlinear constitutive model; b) pressure head gradient at different time with depth for the saturated condition, assuming $B=0.5$, and considering nonlinear constitutive model.

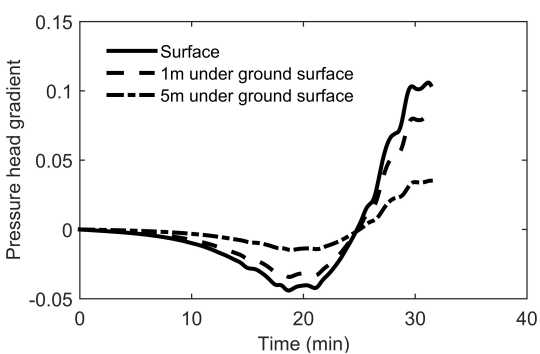


Figure A.22: Case S-NI-B(0.5): pressure head gradient changes with time at different depth for fully saturated nonlinear model and $B=0.5$.

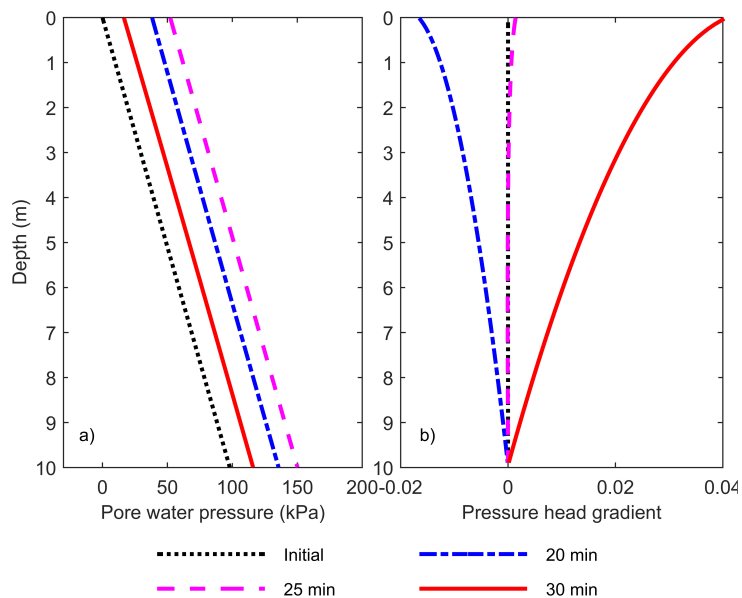


Figure A.23: Case S-NI-B(0.8): a) total pore water pressure at different time with depth for the saturated condition, assuming $B=0.8$, and considering nonlinear constitutive model; b) pressure head gradient at different time with depth for the saturated condition, assuming $B=0.8$, and considering nonlinear constitutive model.

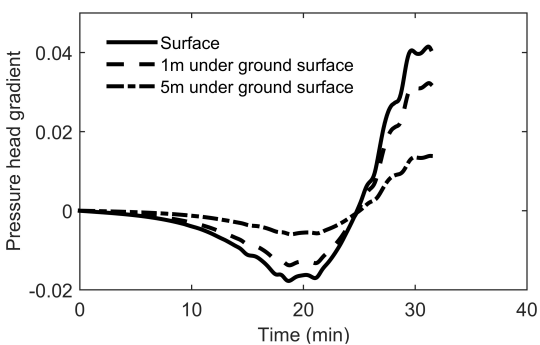


Figure A.24: Case S-NI-B(0.8): pressure head gradient changes with time at different depth for fully saturated nonlinear model and $B=0.8$.

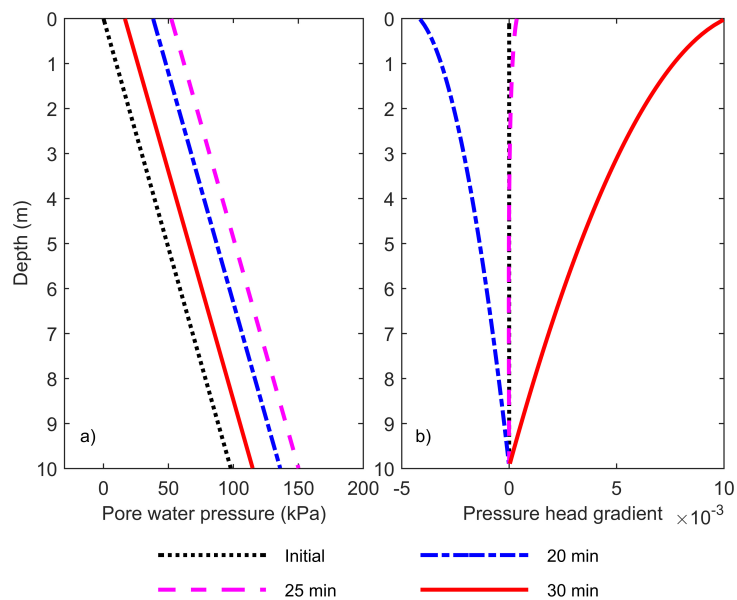


Figure A.25: Case S-NI-B(0.95): a) total pore water pressure at different time with depth for the saturated condition, assuming $B=0.95$, and considering nonlinear constitutive model; b) pressure head gradient at different time with depth for the saturated condition, assuming $B=0.95$, and considering nonlinear constitutive model.

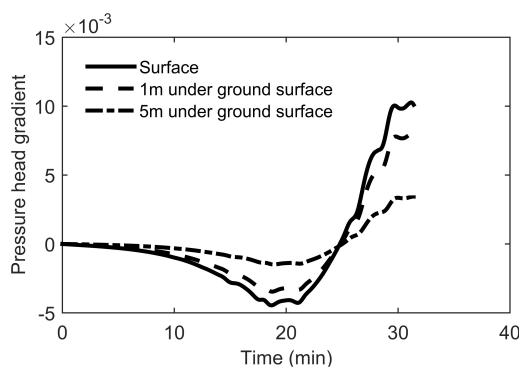


Figure A.26: Case S-NI-B(0.95): pressure head gradient changes with time at different depth for fully saturated nonlinear model and $B=0.95$.

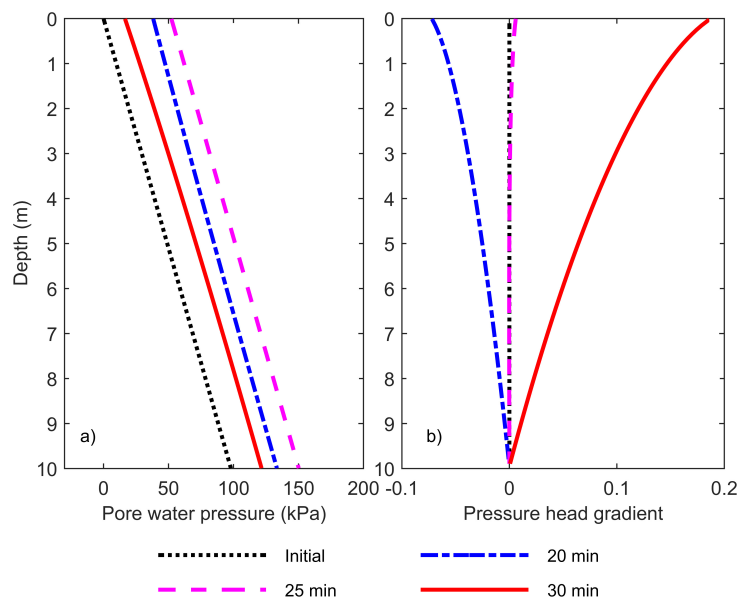


Figure A.27: Case S-NI-UW: a) total pore water pressure at different time with depth for the saturated condition, assuming aired water, and considering nonlinear constitutive model; b) pressure head gradient at different time with depth for the saturated condition, assuming aired water, and considering nonlinear constitutive model.

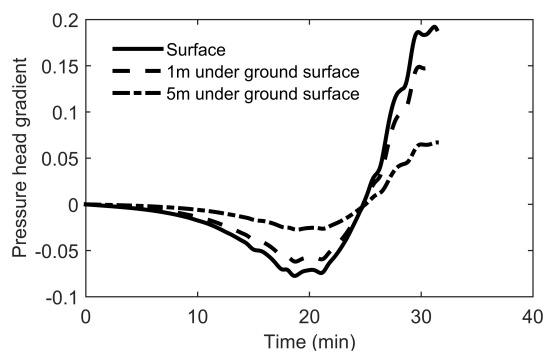


Figure A.28: Case S-NI-UW: pressure head gradient changes with time at different depth for fully saturated nonlinear model and aired water.

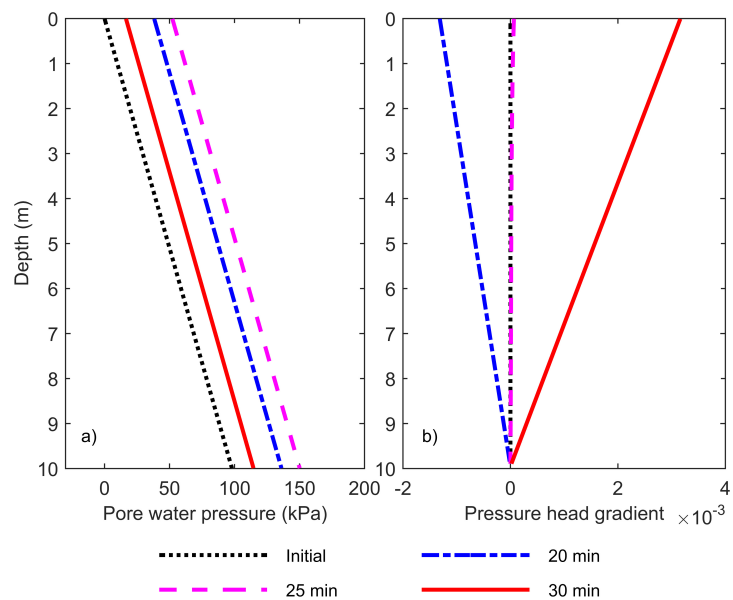


Figure A.29: Case S-NI-PW: a) total pore water pressure at different time with depth for the saturated condition, assuming pure water, and considering nonlinear constitutive model; b) pressure head gradient at different time with depth for the saturated condition, assuming pure water, and considering nonlinear constitutive model.

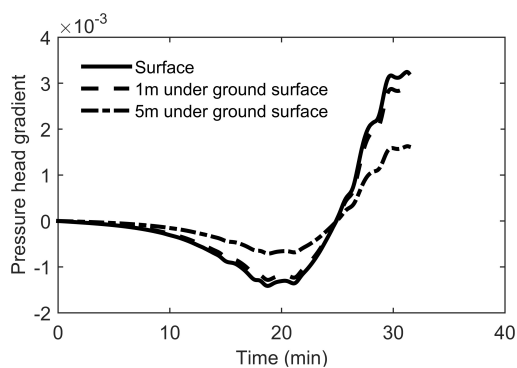


Figure A.30: Case S-NI-PW: pressure head gradient changes with time at different depth for fully saturated with nonlinear model and pure water.

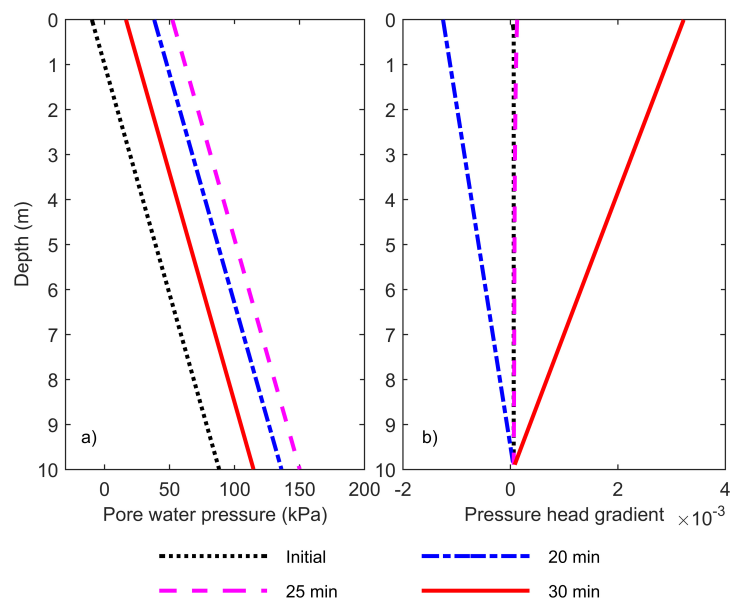


Figure A.31: Case UN-NI-PW(1m): a) pore water pressure changes with depth at different time for partially saturated condition when the water table is at 1 m, nonlinear model and pure water; b) pressure head gradient changes with depth at different time for partially saturated condition when the water table is at 1 m with nonlinear model and pure water.

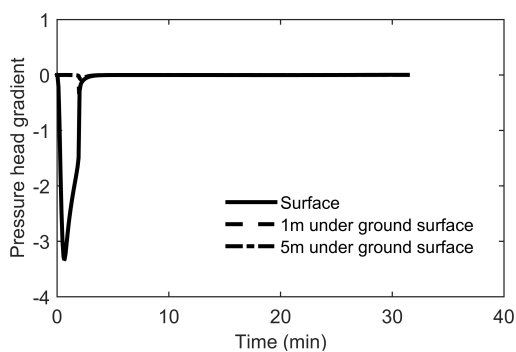


Figure A.32: Case UN-NI-PW(3m): pressure head gradient changes with time at different depth for when the water table is at 1 m with nonlinear model and pure water.

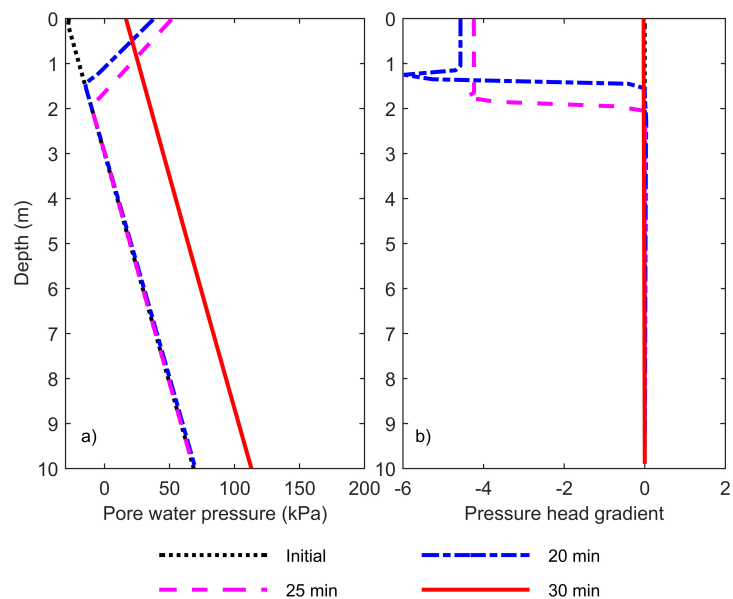


Figure A.33: Case UN-NI-PW(3m): a) pore water pressure changes with depth at different time for partially saturated condition when the water table is at 3 m, nonlinear model and pure water; b) pressure head gradient changes with depth at different time for partially saturated condition when the water table is at 3 m with nonlinear model and pure water.

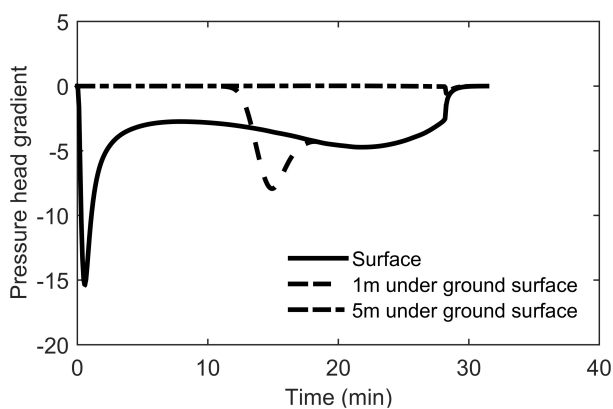


Figure A.34: Case UN-NI-PW(3m): pressure head gradient changes with time at different depth for when the water table is at 3 m with nonlinear model and pure water.

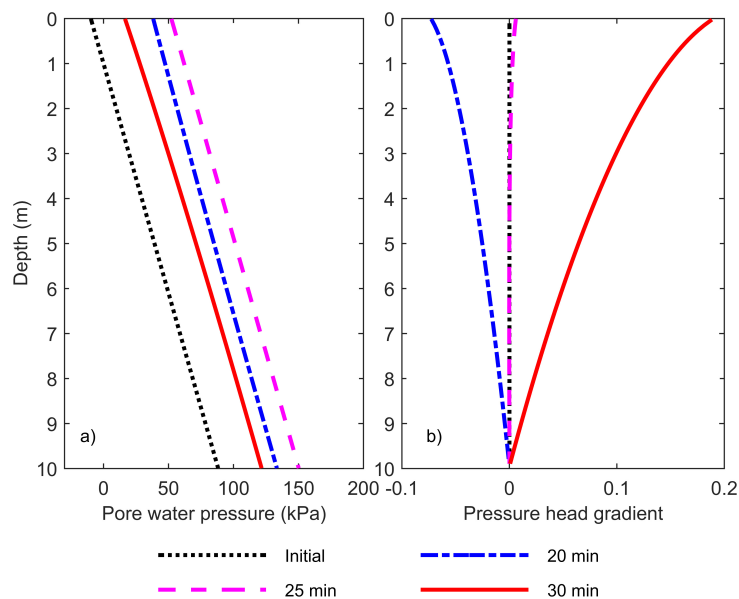


Figure A.35: Case UN-NI-UW(1m): a) pore water pressure changes with depth at different time for partially saturated condition when the water table is at 1 m, nonlinear model and aired water; b) pressure head gradient changes with depth at different time for partially saturated condition when the water table is at 1 m nonlinear model and aired water.

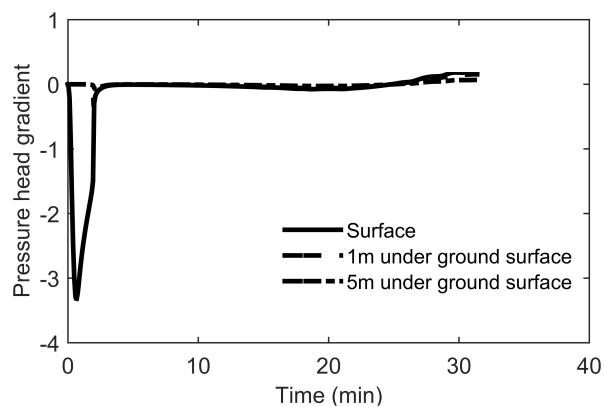


Figure A.36: Case UN-NI-UW(1m): pressure head gradient changes with time at different depth for when the water table is at 1 m with nonlinear model and aired water.

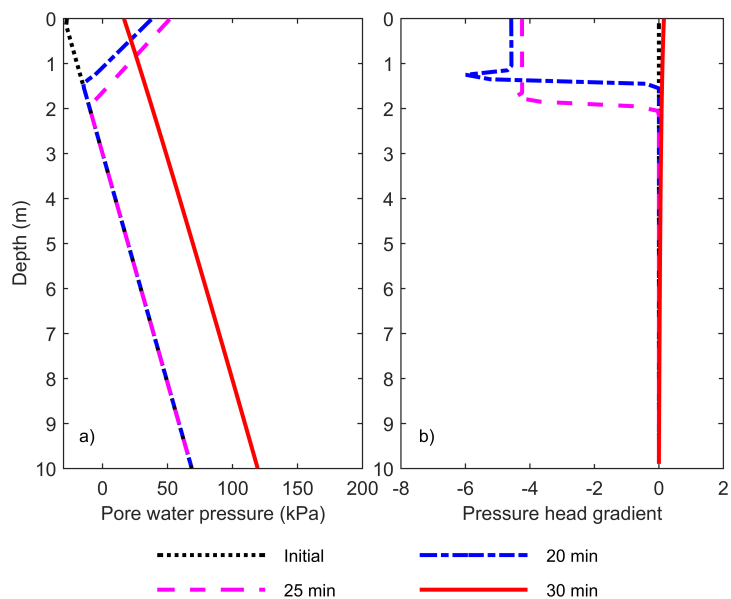


Figure A.37: Case UN-NI-UW(3m): a) pore water pressure changes with depth at different time for partially saturated condition when the water table is at 3 m, nonlinear model and aired water; b) pressure head gradient changes with depth at different time for partially saturated condition when the water table is at 3 m nonlinear model and aired water.

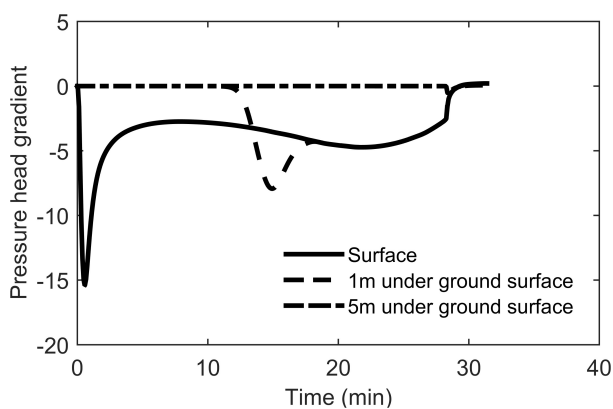


Figure A.38: Case UN-NI-UW(3m): pressure head gradient changes with time at different depth for when the water table is at 3 m with nonlinear model and aired water.

